CVR JOURNAL OF SCIENCE AND TECHNOLOGY

Vol.No. 24, June 2023
P-ISSN 2277 - 3916
DOI 10.32377/CVRJST24
E-ISSN 2581 - 7957

CVR COLLEGE OF ENGINEERING

In Pursuit of Excellence

PATRONS

Dr. Raghava V. Cherabuddi, President & Chairman

Dr. K. Rama Sastri, Director

Dr. K. Ramamohan Reddy, Principal

Editor : **Dr. K. Lal Kishore, Professor and Dean - Research, CVRCE**

Associate Editor : **Dr. S. Venkateshwarlu, Professor & Head, Dept. of EEE, CVRCE**

Technical support : **Mr. K. Veeranjaneyulu, Asst. Prof., Dept. of CSE, CVRCE**

Editorial Board :

Dr. M.V. Seshagiri Rao	Professor & Dean-Planning & Coordination, CVRCE
Prof. L.C. Siva Reddy	Professor & Vice-Principal, CVRCE
Dr. K.S. Nayanathara	Professor & Dean-Academics, CVRCE
Dr. T. Muralidhara Rao	Professor & Head, Dept. of Civil Engg., CVRCE
Dr. A. Vani Vathsala	Professor & Head, Dept. of CSE, CVRCE
Dr. K. Lalithendra	Professor & Head, Dept. of ECE, CVRCE
Dr. S. Harivardhagini	Professor & Head, Dept. of EIE, CVRCE
Dr. Bipin Bihari Jayasingh	Professor & Head, Dept. of IT, CVRCE
Dr. M. Venkata Ramana	Professor & Head, Dept. of Mech. Engg., CVRCE
Dr. H.N. Lakshmi	Professor & Head, Dept. of ET, CVRCE
Dr. G. Bhikshamaiah	Professor & Head, Dept. of H&S, CVRCE

International Review Board:

Prof. Tzung-Pei Hong	Chair Professor, Dept. of CSI Engg., AI Research Center National University of Kaohsiung 811, Taiwan
Dr. Tomonobu Senjyu	Professor, Department of Electrical Engineering, University of the Ryukyus, Nishihara-cho, Nakagami Okinawa, Japan
Dr. Masoud Mohammadian	Assoc. Professor, Faculty of Science and Technology, University of Canberra, Australia
Dr. Rubén Ruiz García	Full Professor, Head of the Applied Optimization Systems Group, Department of Applied Statistics, Universitat Politècnica de València, Camino de Vera, Spain
Dr. Ray-Hwa Wong	Professor, Department of Mech. Engg., Hwa-Hsia University of Technology, Taipei, Taiwan
Dr. Stefan Talu	Faculty of Mech. Engineering, DMCDI, The Technical University of Cluj-Napoca, B-dul Muncii Street, No. 103-105, Cluj-Napoca, 400641, Romania
Assoc. Prof. Ir. Dr. Norhaliza Abdul Wahab	Director, Control & Mechatronics Engg. Dept., Faculty of Electrical Engineering, UTM Skudai 81310 Johor
Dr. R. Venkata Rao	Professor, Department of Mech Engg., Sardar Vallabhbhai National Institute of Technology (SVNIT), Surat, Gujarat State – 395 007, India
Dr. Vijay Janyani	Professor Dept. of ECE, Malaviya National Institute of Technology (MNIT), Jaipur - 302017 (Rajasthan)
Dr. V. Prasanna Venkatesan	Prof. & Head, Department of Banking Technology, School of Management, R.V.Nagar, Kalapet, Pondicherry University, Puducherry

CVR JOURNAL
OF
SCIENCE AND TECHNOLOGY

Indexed by

- Google Scholar
- Directory of Research Journals Indexing (DRJI)
- Scientific Indexing Services (SIS)
- International Institute of Organised Research (I2OR)
- Scholar Impact - Journal Index
- Citefactor
- Member Crossref / DOI

Accredited by NAAC with 'A' GRADE

CVR COLLEGE OF ENGINEERING
(UGC Autonomous - Affiliated to JNTU Hyderabad)
Mangalpalli (V), Ibrahimpatnam (M),
R.R. District, Telangana. – 501510
http://cvr.ac.in

EDITORIAL

With great pleasure, the Editorial team of Biannual CVR Journal of Science and Technology is bringing out Volume 24, in time. All the members of the team thank authors, reviewers and others involved in this work. For the last 6 months, all of us have been working tirelessly to complete this task and bring out the Volume in time.

We are taking care to see that standard practices are followed in the publication of the Journal. Blind review is done, and a number of iterations are done till the reviewers are fully satisfied with the standard of the research paper. Senior faculty of English language Department, take care of the language issues. Template verification and typographical errors are checked before the articles go for publishing. Hope the researchers appreciate this effort. Many research articles published in the journal are being referred to by other researchers across the globe, as indicated by DOI, Crossref data.

This Volume covers research articles in the following disciplines:

CIVIL– 1, ECE–4, EIE–3, CSIT–1, CSE–5, EEE–1, MECH– 2, H & S(Maths)–1.

Students are being encouraged to publish research papers based on the project work done by them. Project work has such importance in the academic curriculum. P.G. students spend almost one year on the project work. So, this should result in significant work suitable for publication in a journal. Project supervisors guiding the students must give research orientation for the work of the students. Selected research papers of U.G. students are published in this volume. It is heartening to see that U.G. students are also showing enthusiasm for publishing papers. Four such papers are published in this volume- Hope this trend will continue.

This issue carries an interesting research paper on Hydraulic and Anti-clogging Performance Evaluation of a Novel Cylindrical Drip Emitter using CFD Techniques. A Rainwater Harvesting System using LabVIEW is proposed in one article. Another article on the design of Low Power RF Low Noise Amplifier Design for 5G applications is also published.

Undergraduate students contributed an article based on their project work with the help of their supervisor, on a Family health monitoring system using Python. Other articles related to biomedical applications are, An IoT based Saline bottle level monitoring, Automatic Non-Contact Temperature Detection for Health Monitoring, MLO Mammogram Pectoral Muscle Masking with Adaptive MSER. One more article on the Design and Analysis of a Switched Capacitor Inverter for EV applications is also published.

I am thankful to all the members of the Editorial Board for their help in reviewing and shortlisting the research papers for inclusion in the current Volume of the journal. I wish to thank **Dr. S. Venkateshwarlu, HOD, EEE** for the effort made in bringing out this Volume. Thanks are due to **HOD, H & S, Dr. G. Bhikshamaiah** and the staff of English Department for reviewing the papers. I am also thankful to **Smt. A. Sreedevi, DTP Operator** in the Office of Dean Research, for the preparation of research papers in Camera - Ready form.

For further clarity on waveforms, graphs, circuit diagrams and figures, readers are requested to browse the soft copy of the journal, available on the college website www.cvr.ac.in wherein a link is provided. Authors can also submit their papers through our online open journal system (OJS) www.ojs.cvr.ac.in or www.cvr.ac.in/ojs

Prof. K. Lal Kishore
Editor

Patrons:

Dr. Raghava V. Cherabuddi
President & Chairman
CVR College of Engineering,
Vastunagar, Mangalpalli (V),
Ibrahimpatnam (M)
Rangareddy (D),
Telangana 501 510.
E-mail: drcvraghava@gmail.com
Phone: 040-42204001, 02,03

Dr. K. Rama Sastri
Director
CVR College of Engineering,
Vastunagar, Mangalpalli (V),
Ibrahimpatnam (M)
Rangareddy (D), Telangana 501 510.
E-mail: director@cvr.ac.in
Phone: 08414-661666, 661601,661675

Dr. K. Ramamohan Reddy
Principal
CVR College of Engineering,
Vastunagar, Mangalpalli (V), Ibrahimpatnam (M)
Rangareddy (D), Telangana 501 510.
E-mail: principal@cvr.ac.in
Phone: 08414-661602, 661601,661675

Editor:

Dr. K. Lal Kishore
Professor and Dean Research
CVR College of Engineering
Vastunagar, Mangalpalli (V),
Ibrahimpatnam (M)
Rangareddy (D), Telangana 501 510.
E-mail: lalkishorek@gmail.com
lalkishore@cvr.ac.in
Mobile: +91 8309105423 , +91 9618023478
Phone: 08414-661658, 661601,661675

Associate Editor:

Dr. S. Venkateshwarlu
Professor & Head
Dept of Electrical and Electronics Engineering
CVR College of Engineering
Vastunagar, Mangalpalli (V),
Ibrahimpatnam (M)
Rangareddy (D), Telangana 501 510.
E-mail: svip123@gmail.com
hod.eee@cvr.ac.in
Mobile: +91 9490749568
Phone: 08414-661661

Technical support:

Mr. K. Veeranjaneyulu
Asst. Prof.
Dept. of Computer Science & Engineering
CVR College of Engineering
Vastunagar, Mangalpalli (V), Ibrahimpatnam (M)
Rangareddy (D),
Telangana 501 510.
E-mail: kveeru876@gmail.com
Mobile: +91 9177462507

Editorial Board:

Dr. M.V. Seshagiri Rao
Professor & Dean-Planning & Coordination
CVR College of Engineering
Vastunagar, Mangalpalli (V),
Ibrahimpatnam (M)
Rangareddy (D),
Telangana 501 510.
E-mail:
rao_vs_meduri@yahoo.com
sheshagiri.rao@cvr.ac.in
Mobile: +91 9440361817
Phone:08414-661617

Prof. L.C. Siva Reddy
Professor & Vice-Principal
CVR College of Engineering
Vastunagar, Mangalpalli (V),
Ibrahimpatnam (M)
Rangareddy (D),
Telangana 501 510.
E-mail: siva_reddy@cvr.ac.in
Mobile: +91 9885806151
Phone:08414-661656

Dr. K.S. Nayanathara Professor & Dean-Academics
CVR College of Engineering
Vastunagar, Mangalpalli (V),
Ibrahimpatnam (M)
Rangareddy (D),
Telangana 501 510.
E-mail:
ksattirajunayanathara@gmail.com

Mobile: +91 9502335871
Phone:08414-661667

Dr. T. Muralidhara Rao
Professor & Head
Dept. of Civil Engineering
CVR College of Engineering
Vastunagar, Mangalpalli (V),
Ibrahimpatnam (M)
Rangareddy (D),
Telangana 501 510.
E-mail:
tmuralidhararao@gmail.com
tmuralidhararao@cvr.ac.in
Mobile: +91 9989214274
Phone:08414-661655

Dr. A. Vani Vathsala
Professor & Head
Dept. of Computer Science & Engineering
CVR College of Engineering
Vastunagar, Mangalpalli (V),
Ibrahimpatnam (M)
Rangareddy (D),
Telangana 501 510.
E-mail: atlurivv@yahoo.com
vani_vathsala@cvr.ac.in
Mobile: +91 9866586106
Phone:08414-661697

Dr. K. Lalithendra
Professor & Head
Dept. of Electronics and Communication Engineering
CVR College of Engineering
Vastunagar, Mangalpalli (V),
Ibrahimpatnam (M)
Rangareddy (D),
Telangana 501 510.
E-mail: lkurra@gmail.com
lalithendra@cvr.ac.in
Mobile: +91 9871483379
Phone:08414-661660

Dr. S. Harivardhagini
Professor & Head
Dept of Electronics and Instrumentation Engineering
CVR College of Engineering
Vastunagar, Mangalpalli (V),
Ibrahimpatnam (M)
Rangareddy (D),
Telangana 501 510.
E-mail:
Harivardhagini@gmail.com
Mobile: +91 9985147962
Phone:08414-661653

Dr. Bipin Bihari Jayasingh
Professor & Head
Dept. of Information Technology
CVR College of Engineering
Vastunagar, Mangalpalli (V),
Ibrahimpatnam (M)
Rangareddy (D),
Telangana 501 510.
E-mail:
bipinbjayasingh@cvr.ac.in
Mobile: +91 9440476544
Phone:08414-661664

Dr. M. Venkata Ramana
Professor & Head
Dept. of Mechanical Engg
CVR College of Engineering
Vastunagar, Mangalpalli (V),
Ibrahimpatnam (M)
Rangareddy (D),
Telangana 501 510.
E-mail:
vramanamaringanti@cvr.ac.in
Mobile: +91 9948084192
Phone:08414-661689

Dr. H. N. Lakshmi
Professor & Head
Dept. of Emerging Technology
CVR College of Engineering
Vastunagar, Mangalpalli (V),
Ibrahimpatnam (M)
Rangareddy (D),
Telangana 501 510.
E-mail: hn.lakshmi@cvr.ac.in
Mobile: +91 9849698045

Dr. G. Bhikshamaiah
Professor & Head
Dept. of Humanities and Science
CVR College of Engineering
Vastunagar, Mangalpalli (V),
Ibrahimpatnam (M)
Rangareddy (D),
Telangana 501 510
E-mail: gbcvr17@gmail.com
hod.hns@cvr.ac.in
Mobile: +91 9949565350
Phone:08414-661631

International Review Board:

Prof. Tzung-Pei Hong
Chair Professor
Department of Computer Science and Information Engineering
AI Research Center
National University of Kaohsiung
No. 700, Kaohsiung University Road, Nan-Tzu District
Kaohsiung 811, Taiwan
Tel:(07)5919191, 5919398
Fax:(07)5919049
Email: tphong@nuk.edu.tw
Website: tphong.nuk.edu.tw

Dr. Tomonobu Senjyu
Professor
Department of Electrical Engineering
University of the Ryukyus,
Nishihara-cho,
Nakagami Okinawa, Japan
Tel:(+81-98-895-8686)
Email: b985542@tec.u-ryukyu.ac.jp

Dr. Masoud Mohammadian
Associate Professor
Faculty of Science and Technology
University of Canberra ACT 2601
Phone: +61 (0)2 6201 2917
Fax: +61 (0)2 6201 5231
Email:masoud.mohammadian@canberra.edu.au
Website:https://researchprofiles.canberra.edu.au/en/persons/masoud-mohammadian

Dr. Rubén Ruiz García
Full Professor. Head of the Applied Optimization Systems Group
Department of Applied Statistics, Operations Research and Quality
Universitat Politècnica de València
Camino de Vera s/n, Edificio 7A, 46022, Valencia, Spain
rruiz@eio.upv.es
http://soa.iti.es/rruiz

Dr. Ray-Hwa Wong
Professor
Department of Mechanical Eng.,
Hwa-Hsia University of Technology, Taiwan,
111 Gong Jhuan Rd., Chung Ho,
Taipei, Taiwan, R.O.C.
E-mail : rhwong@cc.hwh.edu.tw
Phone / Mobile Number : +886-2-8941-5129 ex 2108/+886-918-706-985

Dr. Stefan Talu
DMCDI
The Technical University of Cluj-Napoca
Faculty of Mechanical Engineering,
B-dul Muncii Street, No. 103-105, Cluj-Napoca, 400641,
Romania
http://research.utcluj.ro.
E-mail(uri) stefanta@mail.utcluj.ro, stefan_ta@yahoo.com
Telephone(s) Fixed line phone: 004 0264 401 200.
Mobile phone: 004 0744263660

Assoc. Prof. Ir. Dr Norhaliza Abdul Wahab
Director,
Control & Mechatronics Engineering Department
Faculty of Electrical Engineering
UTM Skudai 81310 Johor
Malaysia
Phone: +607-5557023, 012-5444297 (HP)
Email: aliza@fke.utm.my
URL: http://norhaliza.fke.utm.my/

Dr. R. Venkata Rao
Professor, Department of Mechanical Engineering
Sardar Vallabhbhai National Institute of Technology (SVNIT), Surat
Ichchanath, Surat, Gujarat State – 395 007, India,
Contact Nos.: 02612201982(O), 02612201661(R), 9925207027(M)
Email ID: ravipudirao@gmail.com, rvr@med.svnit.ac.in
Website: http://svnit.ac.in/facup/5274Rao-Resume.pdf

Dr. Vijay Janyani
Professor
Dept. of Electronics and Communication Engineering
Malaviya National Institute of Technology (MNIT)
Jaipur - 302017 (Rajasthan)
India.
www.mnit.ac.in
Email ID: vijay.janyani@ieee.org

Dr. V. Prasanna Venkatesan
Prof. & Head
Department of Banking Technology,
School of Management, R.V.Nagar,
Kalapet, Pondicherry University,
Puducherry – 605014,
India.Telephone No: 0413 - 2654 652
Mobile No: 0091-9486199939
Email: prasanna.btm@pondiuni.edu.in, prasanna_v@yahoo.com

CONTENTS

Page No.

E-ISSN 2581 – 7957
P-ISSN 2277 – 3916

CVR Journal of Science and Technology, Volume 24, June 2023
DOI: 10.32377/cvrjst2401

Hydraulic and Anti-clogging Performance Evaluation of a Novel Cylindrical Drip Emitter using CFD Techniques

Ramamohan Reddy Kasa[1] and Venkata Ramamohan Ramachandrula[2]
[1]Professor, CVR College of Engineering/Civil Engg. Department, Hyderabad, India.
Email: kasarammohan@gmail.com
[2]Executive Director, Water and Livelihoods Foundation, Hyderabad, India.
Email: ramamohan.ramachandrula@gmail.com

Abstract: **An inline cylindrical drip emitter of 4 Lh-1 design flow rate is developed incorporating favourable geometric features against the physical clogging. The emitter model, with one-outlet and two-outlet variants, was tested for its hydraulic and anti-physical-clogging performance using Ansys Fluent 2022 software. The simulated flow rate of 3.988 and 3.992 Lh-1 is found to be very close to the design flow rate. The emitter exponent values of 0.4351 and 0.4406 for the one-outlet and two-outlet variants, respectively, are found to be within the stipulated limit of 0.5 by Bureau of India Standards (BIS) guidelines.**

The discrete particle modelling (DPM) simulation revealed that 100% of the particles entering the inlets of the emitter variants are escaping within an average residence time of 0.3779-1.036 s for the one-outlet variant and 0.2044-1.005 s for the two-outlet variant. The average residence time increased with increase in the particle size from 0.1 µm to 100 µm, however the same is not affected by the mass flow rate of particles. Overall, the novel cylindrical emitter developed is found to be satisfactory in its hydraulic and anti-physical-clogging performance.

Index Terms: **CFD, DPM, Ansys fluent, Drip Emitter, Anti-clogging, SST, k-ω Turbulence Model.**

I. INTRODUCTION

Drip irrigation is widely known for its beneficial aspects, such as, improved water use efficiency and uniform application of water, resulting in better water and crop productivity. However, clogging of drip emitters is a major problem that occurs and increases with prolonged use of the drip systems. The emitter clogging affects the emitter flow rate, uniform delivery of irrigation water over the farmland and ultimately, its functional life. The composite clogging of emitters generally involves formation of physical, chemical, and biological deposits. In case of irrigation using groundwater pumped from wells, physical clogging due to the suspended solids (SS) in water and the chemical clogging due to the precipitation of dissolved chemicals (such as, salts of Ca, Mg, Fe etc.) in water are two major concerns.

Conventionally, the emitter clogging is addressed by frequent flushing of lateral pipes; periodic cleaning of disk or screen filter; treatment of laterals with acid for removing the chemical deposits; and chlorination to remove bacteriological clogging. IS 13487, IS 13488 and IS 14791 by Bureau of Indian Standards (BIS) elaborate on the methods of testing emitters, assessing clogging hazards of irrigation water and treatments against clogging (BIS 2015; BIS 2008; BIS 2016).

Drip emitters are primarily of two types, viz., (i) cylindrical and (ii) flat, based on the geometric features. Also, each of them may be classified as (i) regulated and (ii) unregulated emitters, depending on the pressure-flow rate relationship. While irrigation water quality plays a key role in the degree of emitter clogging, the geometric design of emitters is also found to be playing a significant role. Several researchers studied and suggested improved labyrinth path geometries for better anti-clogging performance. In this article, a novel anti-physical-clogging emitter design is proposed, and its performance is analysed using Computational Fluid Dynamics (CFD) techniques.

II. LITERATURE REVIEW

Recent advances in CFD software opened a new possibility of visualizing the fluid flow as well as particle tracks as they pass through the emitter flow paths. Also, CFD facilitated testing and simulation of hydraulic performance of emitters by varying different geometric features and inlet pressure.

[16] studied labyrinth flow paths of emitters and proposed pressure loss coefficient (PLC) as the index for evaluation of their hydraulic performance. [12] applied standard k-ε and large eddy simulation (LES) methods for CFD simulation of flow through the labyrinth path of a cylindrical drip emitter. The anti-clogging performance of the emitter flow path was studied using the velocity distribution at different sections. [7] analysed the hydraulic and anti-clogging abilities of a flat type drip emitter, using CFD simulations and improved digital particle image velocimetry (DPIV) equipment in the laboratory settings. [10] analysed a trapezoidal labyrinth flow path of a flat emitter, by varying the values of dent spacing and dent angle. It was found that, for a given length of flow path, increase in dent spacing increased the flow rate and increase in dent angle reduced the pressure sensitivity of the emitter. [14] coupled the discrete element method (DEM) with the CFD to model the movement of tiny physical particles of size 65, 100 and 150 µm in the emitter labyrinth path. The study found that larger sized particles are more prone to be caught in the vortex areas of the labyrinth, resulting in eventual settlement, and clogging of the emitter. [2] studied four cylindrical emitter models having circular,

Received on 03-04-2023, Revised on 01-05-2023, Accepted on 11-05-2023.

rectangular, triangular and trapezoidal labyrinth paths and found that triangular one has got the least flow rate and most pressure drop for a given inlet pressure.

CFD modelling not only eased the comparative study of existing emitters, but also facilitated anti-clogging geometric improvements to the emitters. Few researchers optimize the labyrinth flow path of the flat emitters by appropriately altering one or more flow path width, dent angle, dent spacing and boundary features. Few other researchers came up with entirely novel designs of emitters that incorporated new features into the labyrinth paths, such as, divided-flow emitters, pit structure emitters etc.

[6] studied a flat type drip emitter with various combinations of dent height (h), flow path width (D) and dent angle (ɵ). Larger dent angle was found to favour pressure insensitivity of the emitters, and boundary optimization helped in improved anti-clogging performance. [1] designed an online anti-clogging drip emitter consisting of connected cones and labyrinth flow path, improving the hydraulic and physical particle flow dynamics through the emitter. [11] designed a divided flow emitter path and optimized its geometric dimensions. The optimal channel had an emitter exponent of 0.515 and a particle passing rate of 88.5%.

[7] optimized the flow path boundary with a curvature of ½ of the flow path width, creating the washing-the-effect leading to improved particle excretion performance. [15] analysed the hydraulic performance and sand particle movement in a labyrinth channel at different dentation angles of 90°, 60°, 45° and 30°. The study recommended dentation angle range of 60° to 90° and a higher velocity level for optimum hydraulic and anti-clogging performance. [9] devised a novel type of stellate water-retaining labyrinth channel structure with optimum emitter exponent value. [13] developed a pit drip irrigation emitter by optimizing the vortex formation areas of the labyrinth path. The flow index and energy dissipation coefficient obtained from CFD simulations were compared with the experimental investigations.

Though most of these works mainly focused on either optimizing the trapezoidal labyrinth path or proposed novel flow path structures, there are none that attempted to optimize the whole emitter geometry. Current work addresses this gap and proposes a novel cylindrical emitter and analyses its hydraulic and anti-physical-clogging performance using CFD techniques.

III. MATERIALS AND METHODS

A cylindrical emitter model of 4 Lh-1 design flow rate was prepared using AutoCad Fusion 360 software in STEP file format. The emitter model has the option of using one outlet hole or two outlet holes on the lateral pipe. For carrying out Computational Fluid Dynamics (CFD) analysis, the flow path geometries were separated from the emitter models using Ansys SpaceClaim 2022 software (Fig.1).

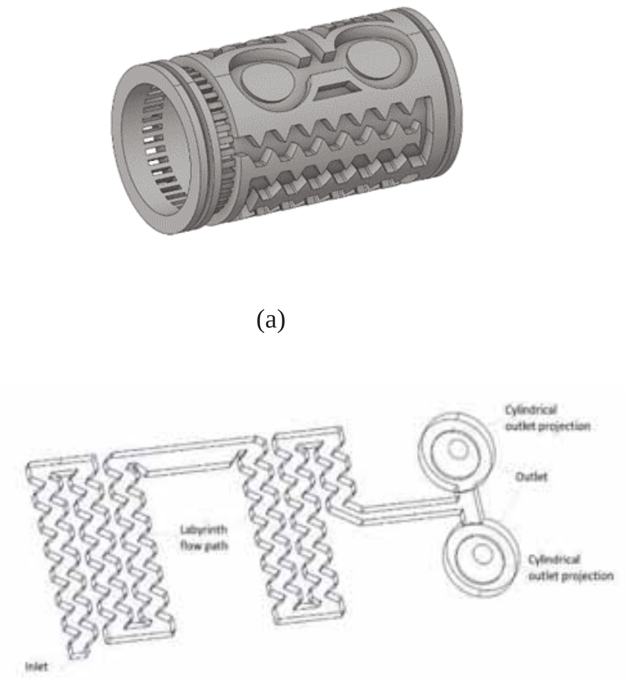

(a)

(b)

Figure1. CAD Models of (a) Cylindrical Emitter, (b) Unwrapped Flow Path

The performance of the novel emitter model developed was tested in terms of its hydraulic and anti-physical-clogging performance, as described below.

A. *Hydraulic Performance of Emitter Variants*

Ansys Fluent 2022 student software was used to conduct hydraulic performance studies on the four flow path variants. The flow rate of the emitter models is assessed under steady state flow conditions through the flow paths. Both inlet and outlet(s) are set as pressure boundaries. The two-equation Shear Stress Transport (SST) k-ω turbulent flow model is used for the simulation. The outlet gauge pressure was set as 0 m (= atmospheric pressure). The outlet flow rate measurement was done for the inlet gauge pressure of 100 KPa (10.2 m). In case of two outlet model variant, the flow rates from individual outlets were added for calculating the total flow rate of the emitter. In order to find the emitter exponent in the exponential pressure-flow rate relationship, the outlet flow rate was measured at eight pressure points by varying the inlet pressure between 20-200 KPa. The values of emitter exponent ‘m’ in the pressure-flow rate relationship for different variants were determined and compared with the recommended values by [5].

B. *Anti-physical-clogging Performance*

Using the Discrete Particle Modelling in Ansys Fluent, a simulation was done to check the size and quantity of particles that escaping through the emitter outlets. This analysis was carried out on the two emitter flow path variants having one outlet and two outlets respectively. Particles of ‘anthracite’ material that are ‘inert’ were selected. Eight streams of particle input with randomized starting point were given as input normal to the inlet face.

The inlet velocity of the particles is assumed to be equal to that of the fluid inflow. The simulations were run for the two flow path variants, by taking the combination of five different particle sizes (0.0001, 0.001, 0.005, 0.01 and 0.1 mm) and three particle flow rates (1e-10, 1e-6 and 1e-5 kg/s). For each of the simulations, a particle track graph was generated by taking the 'particle residence time' as the parameter to colour the tracks. Finally, the 'average residence time' and the 'escape flow rate' of the particles were recorded.

IV. RESULTS AND DISCUSSION

The hydraulic and anti-physical-clogging performance assessment results of the novel cylindrical emitter are presented below.

A. Hydraulic Performance

The volume flow rate of 4 Lh-1 through emitter from one or two outlets is between 3.95 to 4.00 Lh-1 for an inlet pressure of 10.2 m (100 KPa), which is very close to the design flow rate (Table 1). While the velocity at the outlet increased compared to the inlet velocity in case of one-outlet variant, the same got reduced substantially to 0.311-0.324 ms-1 in the case of two-outlet variant.

TABLE I.
VELOCITY AND FLOW RATE OF EMITTER VARIANTS

Flow Path	**Inlet Velocity (ms^{-1})**	**Outlet1 Velocity (ms^{-1})**	**Outlet2 Velocity (ms^{-1})**	**Outlet1 Flow Rate (Lh^{-1})**	**Outlet2 Flow Rate (Lh^{-1})**	**Total Flow Rate (Lh^{-1})**
One-outlet variant	0.522	0.677	--	3.988	--	3.988
Two-outlet variant	0.527	0.324	0.311	2.080	1.913	3.992

The velocity vector graphs show maximum velocity in the zig-zag flow path at the tip of the dents combined with clear turbulent vortex formation on both the side walls, facilitating the flushing of any physical particles settled in the labyrinth zig-zag path (Fig.2a). There is helical flow formation at each outlet due to the circular shape of the outlet and the presence of cylindrical-shaped outlet projection (Fig.2b). This helical motion of flowing water is expected to dislodge and excrete the tiny physical particles that tend to settle at the outlets.

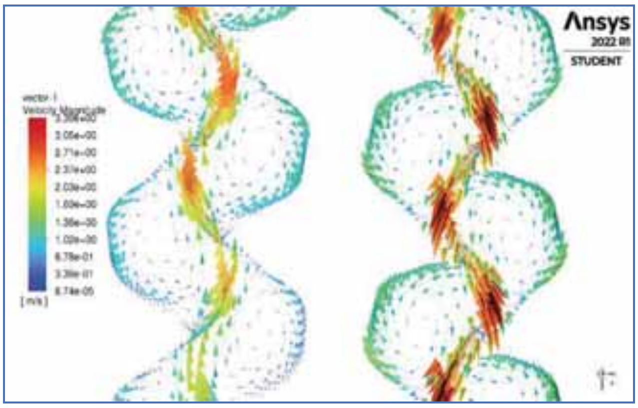

(a)

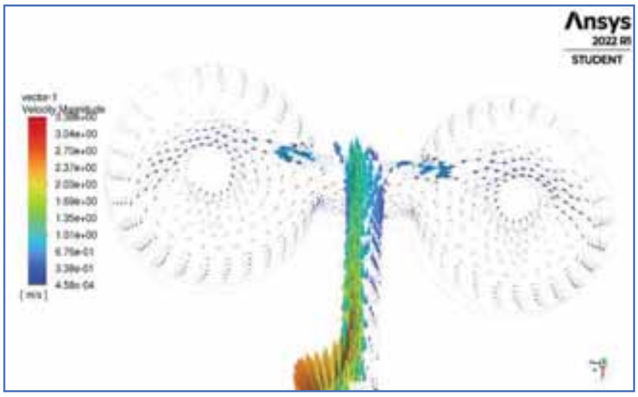

(b)

Figure 2. Velocity Field, (a) in the Labyrinth Path, and (b) at the Outlets

The pressure (p)-flow rate (q) relationship plotted for the 4 Lh-1 emitter paths indicated that the emitter exponent 'm' is well below the 0.5 limit recommended by the [5]. The regression coefficient values are > 0.95 indicating a good fit of the simulation data to the exponential regression model (Fig.3).

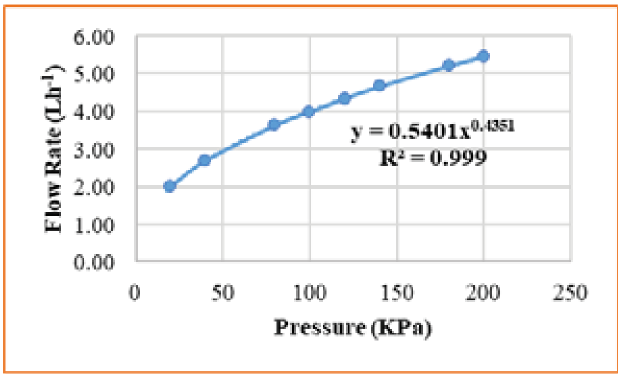

(a)

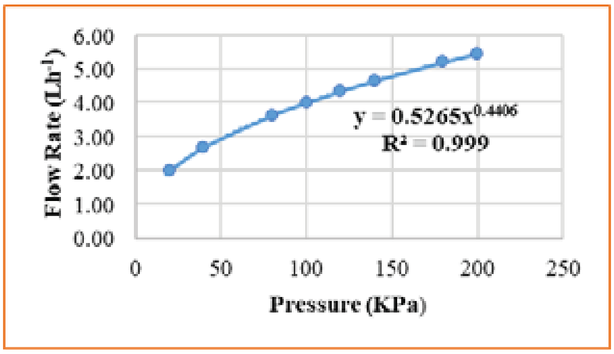

(b)

Figure 3. p-q relationship of, (a) one-outlet variant, and (b) two-outlet variant

B. *Anti-physical-clogging Performance*

Table 2 and Table 3 present the DPM results for one-outlet and two-outlet emitter variants, respectively. The residence time of the particles in the flow paths increased with increasing size of the particles, from 0.1 micron (0.0001 mm) to 100 micron (0.1 mm). However, varying the particle mass flow rate at the inlet (from 1e-9, 1e-6 and 1e-5 kg/s) did not affect any change in the particle residence time. For all the particle sizes and flow rate combinations, the particle escape rate is found to be 100%. The average particle residence time was 0.3779-1.036 s for the one-outlet variant and 0.2044-1.005 s for the two-outlet variant.

TABLE II.
AVG. RESIDENCE TIME AND % ESCAPE RATE OF PARTICLES FOR ONE-OUTLET VARIANT

Particle Flow Rate (kgs^{-1})	**Parameter**	**Particle Size**				
		0.1 µm	**1**	**5**	**10**	**100**
		0.0001 mm	**0.001**	**0.005**	**0.01**	**0.1**
$1.00e^{-09}$	Avg. residence time	0.378	0.317	0.286	0.396	1.036
	% Escape rate	100	100	100	100	100
$1.00e^{-06}$	Avg. residence time	0.378	0.317	0.286	0.396	1.036
	% Escape rate	100	100	100	100	100
$1.00e^{-05}$	Avg. residence time	0.378	0.317	0.286	0.396	1.036
	% Escape rate	100	100	100	100	100

Large number of inlet vents, compared to the conventional cylindrical emitter designs, facilitate entry of water to the emitters even if some vents get clogged over time. Further, the helical motion created at the outlets ‘lifts’ the particles to be flushed out through the outlet holes. Thus, it is found that the proposed emitter designs are 100% efficient in excretion of physical particles in the size range of 0.1 to 100 microns. The particle tracks in the flow path indicated the residence time and the pattern of their movement along with the flowing water. Fig.4a presents the particle’s tracks coloured by their residence time for the one-outlet variant. Similarly, Fig.4b presents the particle tracks through the flow path of the two-outlet variant. Both Fig.4a and Fig.4b are generated for the particle mass flow rate of 1.00e-05 kgs-1 and the particle size of 100 µm. These particle tracks clearly indicated that their movement is helical at the outlets. Some of the particles moved away from the high-velocity mainstream flow, expending more time in circular motion near walls in the labyrinth path. However, this phenomenon was not observed in case of particle size less than 100 µm.

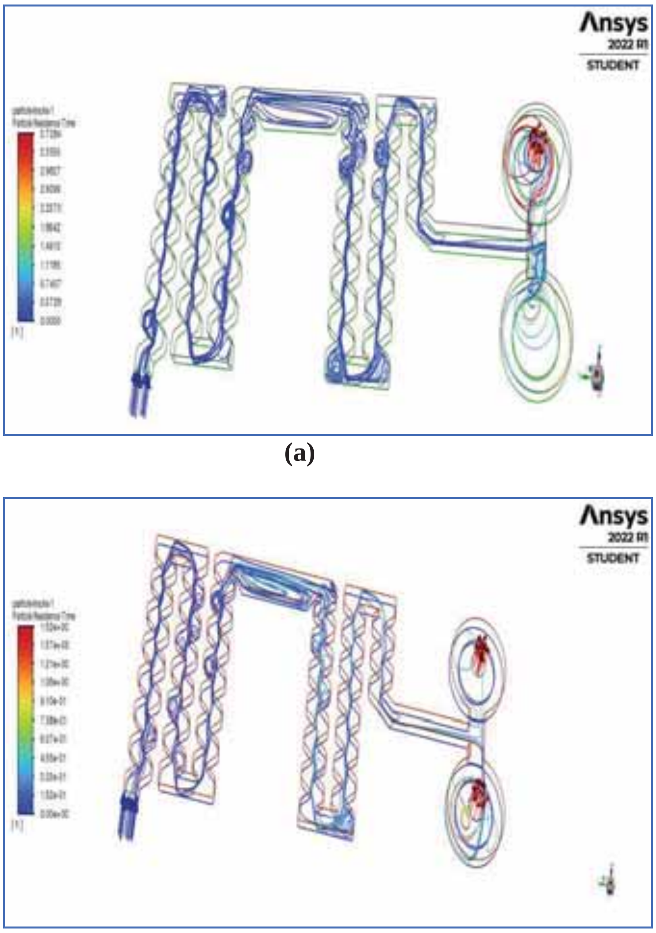

(a)

(b)

Fig.4: Particle tracks coloured by their residence time in the flow path, (a) one-outlet variant, and (b) two-outlet variant

TABLE III.
AVG. RESIDENCE TIME AND % ESCAPE RATE OF PARTICLES FOR TWO-OUTLET VARIANT

Particle Flow Rate (kgs^{-1})	**Parameter**	**Particle Size**									
		0.1 µm		**1**		**5**		**10**		**100**	
		0.0001 mm		**0.001**		**0.005**		**0.01**		**0.1**	
		Outlet1	**Outlet2**	**Outlet1**	**Outlet2**	**Outlet1**	**Outlet2**	**Outlet1**	**Outlet2**	**Outlet1**	**Outlet2**
$1.00e^{-09}$	Avg. residence time (s)	0.204	0.350	0.286	0.580	0.29	0.408	0.272	0.47	0.472	1.005
	% Escape rate	16.67	83.33	50.00	50.00	50.00	50.00	33.33	66.67	16.67	83.33
$1.00e^{-06}$	Avg. residence time (s)	0.204	0.350	0.286	0.580	0.29	0.408	0.272	0.47	0.472	1.005
	% Escape rate	16.67	83.33	50.00	50.00	50.00	50.00	33.33	66.67	16.67	83.33
$1.00e^{-05}$	Avg. residence time (s)	0.204	0.350	0.286	0.580	0.29	0.408	0.272	0.47	0.472	1.005
	% Escape rate	16.67	83.33	50.00	50.00	50.00	50.00	33.33	66.67	16.67	83.33

V. CONCLUSIONS

The novel emitter, with a design flow rate of 4 Lh^{-}1 and helical flow at the outlets, proved to be efficient in hydraulic and anti-physical-clogging performance. The simulation flow rates of 3.988 and 3.992 Lh^{-1} are very close to the design flow rate. The emitter exponent values of the one-outlet and two-outlet variants are 0.4351 and 0.4406 respectively, which are well below the [5] stipulated limit of 0.5. While both the one-outlet and two-outlet variants were found with 100% particle escape rate, the average particle residence time was insignificantly higher (0.3779-1.036 s) for the one-outlet variant, compared to the 0.2044-1.005 s in case of two-outlet variant. Therefore, both the variants of the novel emitter developed are found to perform satisfactorily in terms of hydraulic and anti-clogging parameters. Laboratory testing of physical emitter models for validation of these simulation results forms the future scope of work.

REFERENCES

[1] Ali, A.A.M. (2013). Anti-clogging drip irrigation emitter design innovation. European International Journal of Science and Technology, 2(8), 154-160.

[2] Bhagel, Y.K., Kumar, J., and Patel, V.K. (2021) CFD analysis of the flow characteristics of in-line drip emitter with different labyrinth channels, Journal of Institution of Engineers Ser. A, 102 (1), 111-119. https://doi.org/10.1007/s40030-020-00499-5

[3] BIS (2008) Indian Standard IS 13488 Irrigation Equipment – Emitting Pipe Systems – Specifications. Bureau of Indian Standards, New Delhi.

[4] BIS (2015). Indian Standard IS 14791 Prevention and treatment of blockage problem in drip Irrigation system – Code of Practice. Bureau of Indian Standards, New Delhi.

[5] BIS (2016). Indian Standard IS 13487 Irrigation Equipment – Emitters. Bureau of Indian Standards, New Delhi.

[6] Dazhuang, Y., Peiling, Y., Shumei, R., Li, Y. and Tingwu, X. (2007) Numerical study on flow property in dentate path of drip emitters, New Zealand Journal of Agricultural Research, 50(5), 705-712. https://doi.org/10.1080/00288230709510341

[7] Feng, J., Sun, H. and Li, Y. (2013) Visualizing particles movement characteristics in drip irrigation emitters with digital particle image velocimetry. Transactions of the CSAE, 29(13), 90-96. https://doi.org/10.3969/j.issn.1002-6819.2013.13.013

[8] Feng, J., Li, Y., Wang, W. and Xue, S. (2018) Effect of optimization forms of flow path on emitter hydraulic and anti-clogging performance in drip irrigation system. Irrigation Science, 36, 37–47. https://doi.org/10.1007/s00271-017-0561-9

[9] Li, Y., Feng, X., Liu, Y., Han, X., Liu, H., Sun, Y., Li, H. and Xie, Y. (2022) Research on hydraulic properties and energy dissipation mechanism of the novel water-retaining labyrinth channel emitters. Agronomy, 12, 1708. https://doi.org/10.3390/agronomy12071708

[10] Reethi, K., Mallikarjuna and Vijaya Raghu, B. (2015) Analysis of flow through a drip irrigation emitter. International Journal of Modern Engineering Research, 5(11), 57-64

[11] Weijing, Y., Zhengying, W., Huali, C. and Shengli, M. (2014) Optimal design and experiment for divided-flow emitter in drip irrigation. Transactions of the Chinese Society of Agricultural Engineering, 30(17), 117-124. https://doi.org/10.3969/j.issn.1002-6819.2014.17.016

[12] Wu, D., Li, Y., Liu, H., Yang, P., Sun, H. and Liu, Y. (2013) Simulation of the flow characteristics of a drip irrigation emitter with large eddy methods. Mathematical and Computer Modelling,58(3-4),497-506. https://doi.org/10.1016/j.mcm.2011.10.074

[13] Xu, T., Zhi, S., Yu, Q. and Zheng, E. (2022) Hydraulic performance and energy loss effect of pit structure optimized

drip irrigation emitter. Nature Environment and Pollution Technology, 21(2), 487-496.

[14] Yu, L., Li, N., Long, J., Liu, X. and Yang, Q. (2018) The mechanism of emitter clogging analyzed by CFD–DEM simulation and PTV experiment. Advances in Mechanical Engineering, 10(1), 1-10. https://doi.org/10.1177/1687814017743025

[15] Yu, L., Li, N., Liu, X., Yang, Q., Li, Z. and Long, J. (2019) Influence of dentation angle of labyrinth channel of drip emitters on hydraulic and anti-clogging performance. Irrigation and Drainage, 68, 256–267. " https://doi.org/10.1002/ird.2304

[16] Zhang, J., Zhao, W. and Lu, B. (2011) New Method of hydraulic performance evaluation on emitters with labyrinth channels. Journal of Irrigation and Drainage Engineering, 137, 811-815. http://dx.doi.org/10.1061/(ASCE)IR.1943-4774.0000365

E-ISSN 2581 – 7957
P-ISSN 2277 – 3916

CVR Journal of Science and Technology, Volume 24, June 2023
DOI: 10.32377/cvrjst2402

Low Power RF Low Noise Amplifier Design for 5G Wi-Fi Receiver

T.D.V.A Naidu[1] and K. Lal Kishore[2]
[1]Assoc. Professor, Satya Institute of Technology and Management/ECE Department, Vizianagaram, Andhra Pradesh, India
Email: teludamodar@gmail.com
[2]Professor, CVR College of Engineering/ECE Department, Telangana, India
Email: lalkishorek@gmail.com

Abstract: **This paper presents the design of a differential Low Noise Amplifier (LNA) for a 5th generation Wi-Fi Receiver. The circuit is implemented with 90nm transistors using CMOS technology. The proposed differential LNA for 5G Wi-Fi (IEEE 802.11ac) is designed by combining two single-ended 5G Wi-Fi LNAs with optimized design values. The gate and source degenerated inductance values are optimized to achieve a 5GHz frequency of operation. Noise neutralization capacitors of 10pF are used to reduce the channel noise in the MOSFETs used in the circuit. The differential LNA achieves 93.6% input matching, an input impedance of 45.94Ω, a transducer gain of 25.76dB, a noise figure of 1.52dB, P_{1dB} of -11.7dBm and IIP3 of 3.17dBm.**

Index Terms: **CMOS, Noise Figure, 1dB compression point (P_{1dB}), Third Order Input Intercept Point (II3), harmonic signal, ISM Band**

I. INTRODUCTION

IEEE 802.11ac standard is known as 5G Wi-Fi. Modern Wi-Fi technology uses 2.4GHz and 5GHz frequencies. The design of LNA is mainly important in the performance of the overall receiver chain. The noise performance of the LNA should be critical because the same noise is amplified in the succeeding stages. To control the noise in the subsequent stages, LNA gain should be very high. The design of LNA should balance the Gain, Input impedance, Noise Figure and Power Consumption. To design LNA for a 5GHz Wi-Fi receiver, the design factors for LNA are shown in Table 1.

TABLE I.
RF LNA DESIGN FACTORS

Parameter	Value/Range
Input Resistance(R_{in})	=50Ω
Transducer Gain (G_T)	15dB-20dB
Noise Figure(NF)	<=3dB
1-dB compression point (P_{1dB})	>-30dBm
Third-order Intermodulation Intercept Point (IIP3)	>-20dBm
Power Consumption (P_{static})	<5mw
Frequency of operation (f_r)	5 GHz
Input Reflection Coefficient (S_{11})	<-15dB

The inductive degeneration technique is implemented in distributed amplifier design to reduce the noise figure under low power operation state. A common-source amplifier is cascaded to the distributed amplifier to progress the gain at high frequency and encompass the bandwidth [1]. A two-stage ultra-wide-band CMOS LNA is designed with the common-gate configuration as the input stage, the broad-band input matching is obtained, and the noise does not increase rapidly at higher frequencies. By merging the common-source (CS) and common-gate (CG) stages, the broad-band characteristic can be achieved by using two inductors [2]. A CG amplifier combined with a CS amplifier through a current mirror can achieve a high gain due to the additional current amplification. Low noise figure (NF) due to the thermal noise cancellation can be attained with low power consumption without degrading the input matching. The linearity can be improved with low power consumption, a multiple-gated transistor technique for cancelling the IM3 distortion [3]. The T-match technique is applied to achieve simultaneously wideband input and output impedance matching, wideband power gain and a wideband NF [4].

A concurrent dual-band LNA is designed to achieve concurrent gain and impedance matching at both bands. Input and output matching is realized using two-pole matching and LC resonant network [5]. Series inductive peaking in the feedback loop can be implemented to enhance the bandwidth and noise performance of the LNA [6]. The dual-loop feedback configuration can stabilize the LNA's input return loss (S11) at Very High-Frequency (VHF) with small dc blocking capacitors. The body bias control technique is helpful to reduce the power consumption in the inverter-based resistive feedback amplifier [7].

A couple of CS stages are stacked to share the current, and the double transformers are implemented as an RF signal path between the CS stages to improve the gain and stability [8]. Four common-source stages and three transformers are used to connect the drains of the former transistors and the sources of the following transistors to boost the transconductance of the transistors. Consequently, the gain of the circuit is effectively amplified. The NF can be reduced due to the noise contributions of the following stages being further suppressed by the application of the transformers [9].

This paper uses a Cascoded common source topology to avoid Miller's effect and improve the LNA's gain. The various existing impedance matching techniques, such as resistive matching, shunt feedback, common gate input matching and inductive source degeneration techniques, are reviewed [15]. The proposed differential LNA design uses the inductive source degeneration to transfer maximum power from the antenna to LNA. The gain improvement techniques are reviewed, such as Inter Stage Inductive Coupling, Transconductance (g_m) boosting, Partial Positive Feedback, and Cascoding strategies [13]. The cascoding technique is used to design the proposed LNA with optimized design values to achieve the desired gain and improved NF.

Received on 02-05-2023, Revised on 07-05-2023, Accepted on 18.05.2023.

The wireless receiver front end consists of a Low Noise Amplifier (LNA), Mixer and Voltage Controlled Oscillator (VCO). According to the National Frequency Allocation Plan (NFAP), it operates from several MHz to GHz frequencies. In NFAP, 2.4GHz-2.4835GHz frequency is the unlicensed band used for ISM (4G) applications such as Wi-Fi, Bluetooth, Zigbee etc. Similarly, the 5GHz-5.8GHz band is allocated for 5th generation (5G) Wi-Fi IEEE 802.11ac [10]. The present work generally relates to radio frequency (RF) frontend receiver circuit, and in specific relates to a low noise amplifier and mixer circuit design for use in radio frequency (RF) frontend receivers that reduce power consumption without affecting the overall gain of the circuit [16]. Single-ended and staggered-tuned four-stage LNA circuits can work at $f_{max}/2$ frequencies [18].

Wireless receives the signal and converts them into the necessary form with amplification. Typically, LNA is the first block of the receiver chain in a radio frequency system, the first block decides the performance of the remaining receiver chain, and hence LNA plays a crucial role in the receiver front-end design. The front-end block is formed by a Low Noise Amplifier (LNA) and a mixer block for mixing a signal amplified by the LNA with a local oscillator signal, to down-convert the amplified signal to an intermediate frequency. The thermal, flicker and gate-induced noise degrades the noise performance of the circuit [19].

II. CIRCUIT DESIGN

The main objective of this work is to provide a new and improved merged LNA-Mixer circuit with a low power consumption for a Wi-Fi/radio front-end receiver. Figure 1 (Ckt 1) is RF LNA for the 5G Wi-Fi receiver front end.

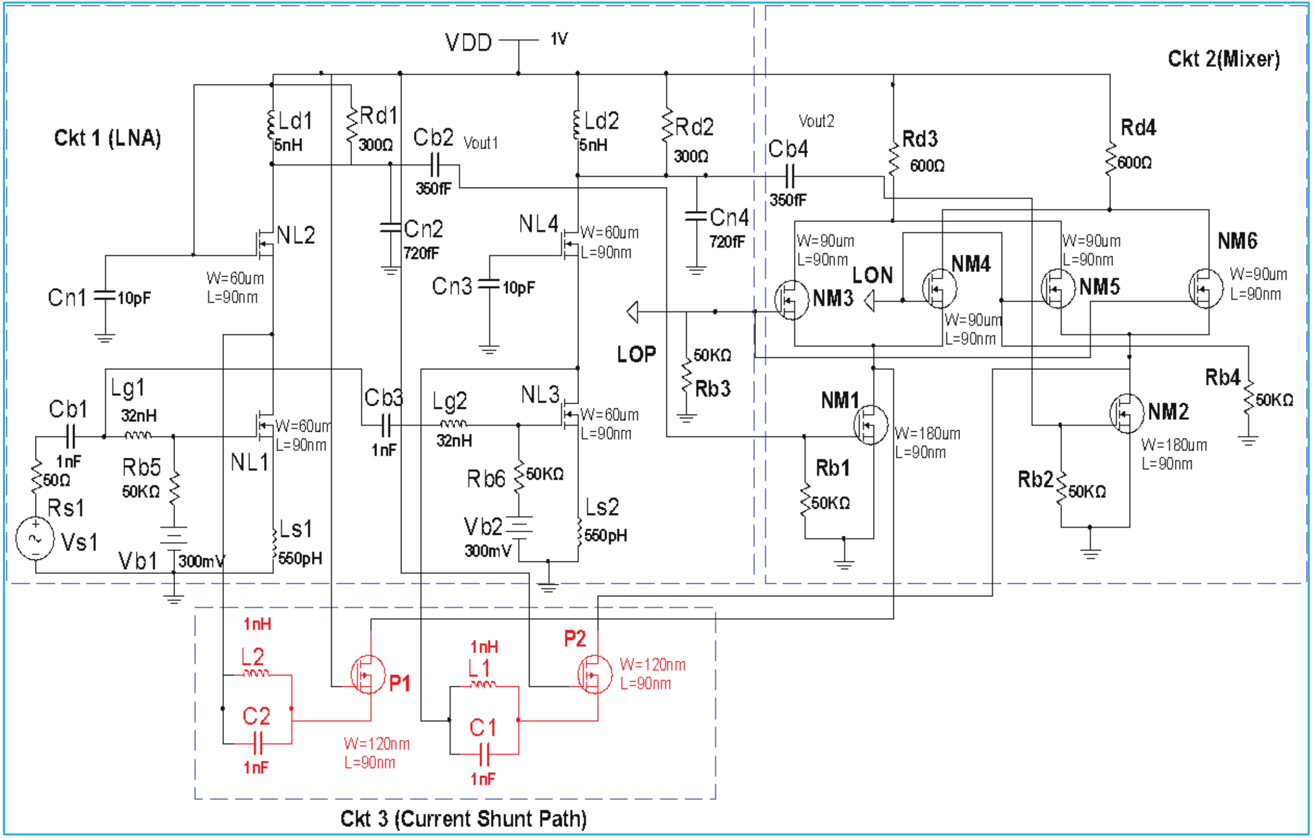

Figure 1. Proposed Novel merged LNA mixer using creative current recycle technique

In Fig 1 (Ckt 1), the Input port source resistance is 50Ω. Coupling Capacitors C_{b1}, C_{b2}, $C_{b3,}$ and C_{b4} are coupling capacitors that couple the a.c input to the MOSFET. Noise Cancellation Capacitors C_{n1}, C_{n2}, C_{n3}, and C_{n4} are used to cancel the noise. R_{d1} and R_{d2} act as load resistors, and R_{b1} and R_{b2} act as biasing resistors. Gate Inductors L_{g1} and L_{g2}, source degenerated inductors L_{S1} and L_{S2} and drain Inductors and $L_{d1,}$ and L_{d2} can series RLC network and be used to provide additional gain to LNA. Here the source degeneration technique is used to achieve impedance matching.

$$Z_{in} = \frac{g_m L_S}{C_{gs}} + j\omega L_S + \frac{1}{j\omega C_{gs}} \quad (1)$$

$$R_{in} = \frac{g_m L_S}{C_{gs}} \quad (2)$$

Differential Cascode Common Source LNA with inductive source degeneration and noise neutralization capacitors shown in Figure 1 (Ckt 1), is used for impedance matching and Gain improvement. The input transistors NL1 and NL3 convert the input voltage into drain current (I_{DS}). The drain current I_{DS} is flowing through a low impedance node available at the source of NL1 and NL3 to cascode transistors NL2 and NL4 to output inductive loads Ld1 and Ld2. The output inductive loads convert this I_{DS} into an output voltage V_{out1} and V_{out2}. In Figure 1(Ckt 1), V_{S1} is the source signal voltage received from the antenna, R_{S1} is the source resistance, the gate bias voltage is V_{dc1}, and the supply voltage is V_{DD}. From the mathematical analysis, the gate-to-source capacitance and the quality factor can be represented as shown in equations 3 and 4 respectively.

$$C_{gs1} \approx \frac{2}{3}WLC_{ox} + C_{OV} \tag{3}$$

$$Q_S = \frac{1}{2R_S\omega_r C_{gs1}} \tag{4}$$

From the R_{d1}, L_{d1}, C_{b2}, C_{n2} and parasitic capacitances C_{gd2}, C_{db2} a parallel resonant circuit is formed at the output of the LNA circuit. The resonant frequency at the output is shown in Equation 6. C_{gd2} is the gate to drain capacitance, and C_{db2} is the drain to bulk capacitance of MOSFET NL2. C_{n2} is the noise neutralization capacitor and C_{b2} blocking capacitor of NL4. The resonant frequency (ω_r) is shown in Eqn 5.

$$\omega_r = \frac{1}{\sqrt{(L_{d1})(C_{gd2}+C_{db2}+C_{n2}+C_{b2})}} \tag{5}$$

Z_{in} is resistive at resonant frequency (ω_r) with the input resistance (R_{in}) shown in equation 2 by choosing good g_m, L_S and C_{gs} values. So that, the impedance can be achieved is $R_{in} = 50\Omega$. C_{gs} depend upon the MOSFET device dimensions and frequency of operation. Choose the value of L_s according to g_m and C_{gs}. Here L_s is an on-chip inductor, and L_g is an off-chip inductor. The frequency of operation can be represented as shown in equation 6.

$$\omega_r = \frac{1}{\sqrt{(L_g+L_s)C_{gs}}} \tag{6}$$

The gain of the common source or common gate amplifiers can be improved by increasing the transconductance or the output resistance. The output of the common source amplifier is connected to a common gate amplifier known as cascoding, which improves the gain of the circuit. Miller effect can be reduced by using a cascoding structure. The g_m can be improved by increasing the μ_n or C_{ox} or W/L ratio or $I_{DS,}$ as shown in equation 7. An increase in μ_n or C_{ox} or W/L ratio will tend to increase the I_{DS}, which increases the voltage drop across R_D, which reduces the output voltage swing of the circuit. Hence the g_m should be increased without affecting the circuit's gain.

$$g_m = \sqrt{2\mu_n C_{ox}\frac{W}{L}I_{DS}} \tag{7}$$

The typical receiver noise figure is 6 to 8 dB, in that the antenna switch or duplexer contributes about 0.5 to 1.5 dB, the LNA about 2 to 3 dB, and the remainder of the chain about 2.5 to 3.5 dB [12]. While these values provide a good starting point in the receiver design, the exact partitioning of the noise is flexible and depends on the performance of each stage in the chain. The total noise figure of LNA and Mixer is represented in equation 5, where NF_{LNA} is the noise figure of LNA, $\underline{v_{n,mix}}^2$ is mean square noise voltage of mixer, A_{LNA} is the gain of the LNA.

$$NF_{Total} = NF_{LNA} + \frac{\overline{v_{n,mix}^2}}{A_{LNA}^2}\cdot\frac{1}{4kTRs} \tag{8}$$

The linearity is represented in terms of 1-dB compression point (P_{1dB}) and Third order Intermodulation Intercept Point (IIP3). Non-linearity in the RF circuits creates harmonic distortion, gain compression, Intermodulation, and cross-modulation [12]. The typical value of 1dB compression point is in the range of -20dBm to -25dBm, of IIP3 of LNA, is -10dBm to -16dBm to achieve better linearity in the LNA design. The nonlinearity expression in a cascaded LNA-Mixer circuit is defined as shown in equation 9, where $V_{IP3,LNA}$ is the third harmonic frequency signal voltage generated by LNA, A_{LNA} is the gain of the LNA and $V_{IP3,mix}$ is the third harmonic frequency signal voltage generated by a mixer. From mathematical analysis, LNA gain and noise factor is represented in equation (10) and (11) respectively.

$$\frac{1}{V_{IP3,tot}^2} = \frac{1}{V_{IP3,LNA}^2} + \frac{A_{LNA}^2}{V_{IP3,mix}^2} \tag{9}$$

$$A_V = \frac{-R_{d1}}{2\omega_r L_{S1}} \tag{10}$$

$$F = 1 + \gamma g_{m1} R_S \left(\frac{\omega_r}{\omega_T}\right)^2 + \frac{4R_S}{R_{d1}}\left(\frac{\omega_r}{\omega_T}\right)^2 \tag{11}$$

The differential LNA design values for 5G Wi-Fi receiver are shown in Table II [11]. From Table II the input port resistance of LNA is 50Ω.

TABLE II.
DIFFERENTIAL 5G WI-FI (5GHZ) LNA DESIGN VALUES

Input Port (P_{in1}) Source Resistance	50Ω
Coupling Capacitors (C_{b1} & C_{b2})&(C_{b3} & C_{b4})	1nF &350fF
Noise Cancellation Capacitors (C_{n1} & C_{n3})	10pF
Noise Cancellation Capacitors (C_{n2} & C_{n4})	720fF
Load Resistors (R_{d1} & R_{d2})	300Ω
Biasing resistors (R_{b1} & R_{b2})	50KΩ
Gate Inductors (L_{g1} & L_{g2})	32nH
Source degenerated inductors (L_{S1} & L_{S2})	550pH
Drain Inductors (L_{d1} & L_{d2})	5nH
Length of NL1, NL2, NL3 & NL4	90nm
Width of NL1, NL2, NL3 & NL4	60um

The Proposed Mixer circuit without shunt paths is shown in Fig 1 (Ckt 2) and is implemented with 'NM1', 'NM2' are RF transistors that convert RF voltage into current [17]. This current is steered by LO transistors 'NM3', 'NM4', 'NM5' and 'NM6'. Then this steered current is converted into IF voltage using 'R_{d3}' & 'R_{d4}'. Here 'NM3', 'NM4', 'NM5' and 'NM6' transistors are known as switching quad [14]. At the RF port V_{RF+} and V_{RF-} represent the different phases of RF input. The conversion gain (G_C) of the proposed mixer without shunt paths is shown in Equation 12. It can be defined as the ratio of the IF can be defined as the ratio of the IF voltage (V_{IF}) at the output to RF voltage (V_{RF}) at the input, where g_{m1} transconductance of 'NM1' and 'Rd3' is the load resistor.

$$G_C = \frac{2}{\pi}.g_{m1}.R_{d3} \tag{12}$$

The Proposed Merged LNA-Mixer with current shunt paths is shown in Fig 1. A feedback connection shown in Fig 1 (Ckt 3) is given from the mixer drain terminals of 'NM1' and 'NM2' to LNA drain terminals of 'NL1' and 'NL3' using PMOS current sources ('P1' and 'P2') and two LC tank circuits. The LC tank circuit provides high input resistance from LNA to Mixer, such that the drain current of LNA cannot be entered into Mixer.

III. SIMULATION RESULTS AND ANALYSIS

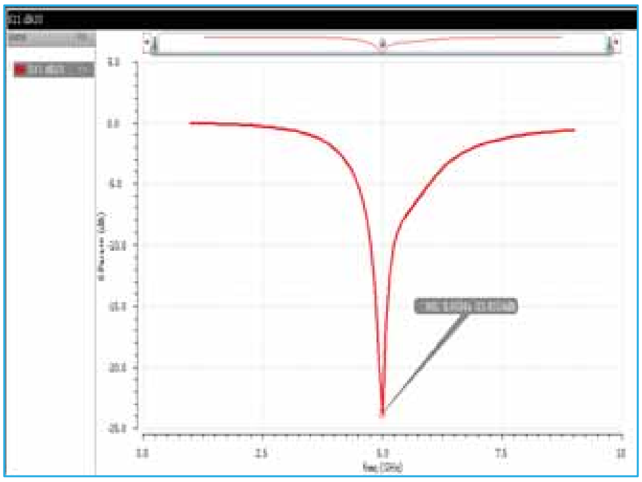

Figure 2. S_{11} of differential 5G Wi-Fi LNA

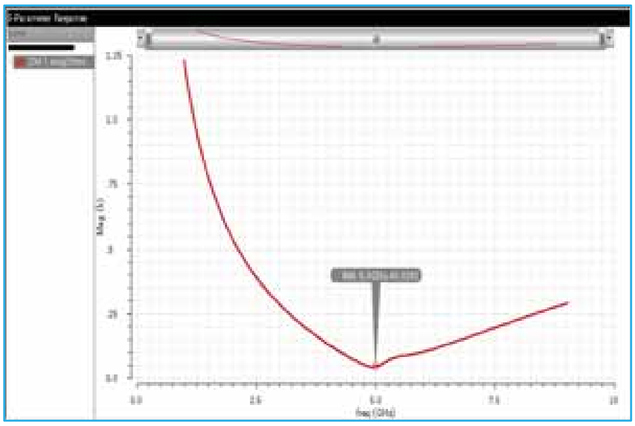

Figure 3. R_{in} of differential 5G Wi-Fi LNA

From Fig 2, the input reflection coefficient is -23.831dB. From that it can be said that in the proposed differential 5G Wi-Fi, LNA delivers 93.6% of input signal to the circuit and 6.4% of incident wave is reflected back as shown in Fig 2. From the port input impedance Z_{M1}=45.94Ω at 5 GHz frequency as shown in Fig 3. From this, it can be said that 91.88% matching occurs at the input of LNA**.**

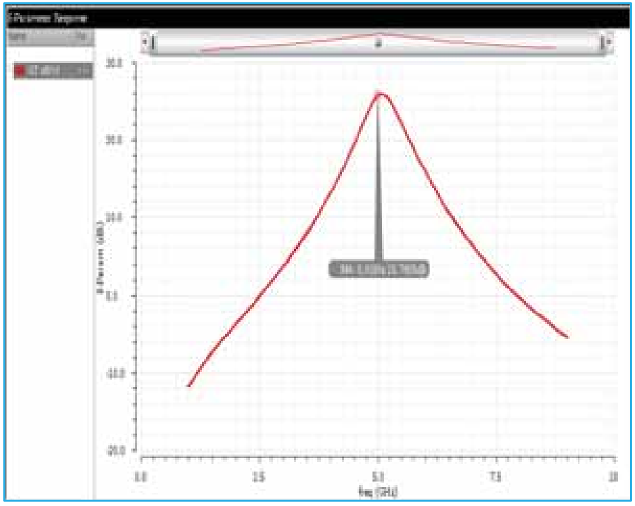

Figure 4. G_T of differential 5G Wi-Fi LNA

The achieved transducer gain is 25.76dB at 5GHz frequency for Differential LNA shown in Fig 1 (Ckt 1).

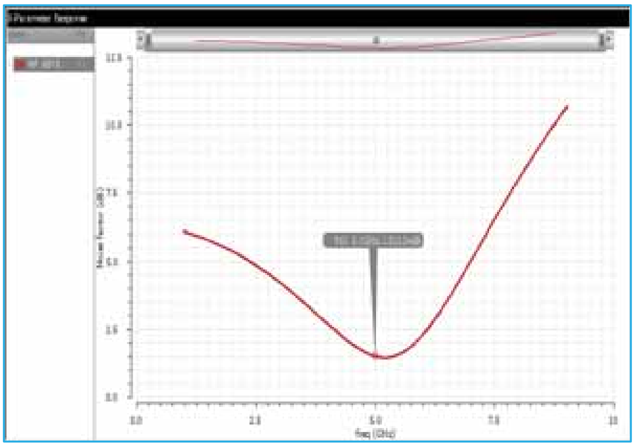

Figure 5. NF of differential 5G Wi-Fi LNA

The target Noise Figure is <3dB and the achieved Noise Figure =1.52dB in Differential LNA shown in Fig 1 (Ckt 1) as shown in Fig 5.

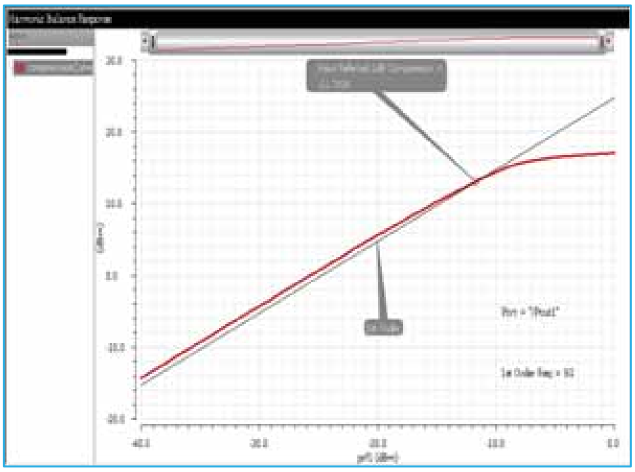

Figure 6. P_{1dB} of differential 5G Wi-Fi LNA

LNA gain in Differential LNA shown in Fig 1 (Ckt 1) is compressed by 1dB from actual value at -11.7dBm i.e. when the input signal power attained to value of 67µW as shown in Fig 6.

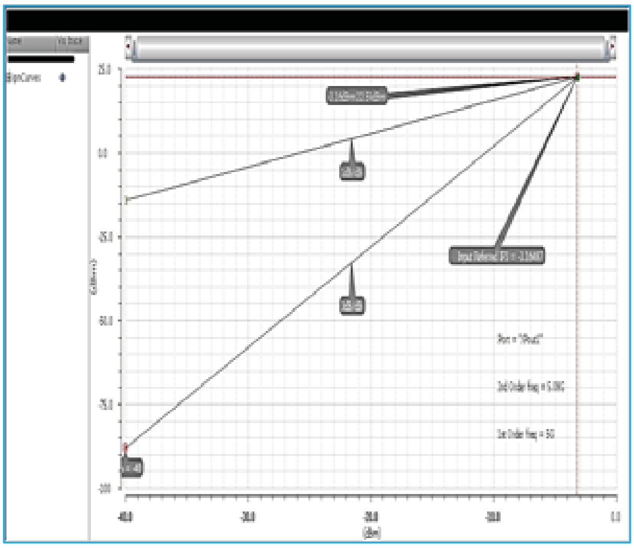

Figure 7. IIP3 of differential 5G Wi-Fi LNA

IIP3= -3.17dBm of Differential LNA shown in Fig 1 (Ckt 1), when the input signal power reached to -3.17dBm (i.e.) 481µW, the third harmonic signal power meets the input signal power as shown in Fig 7.

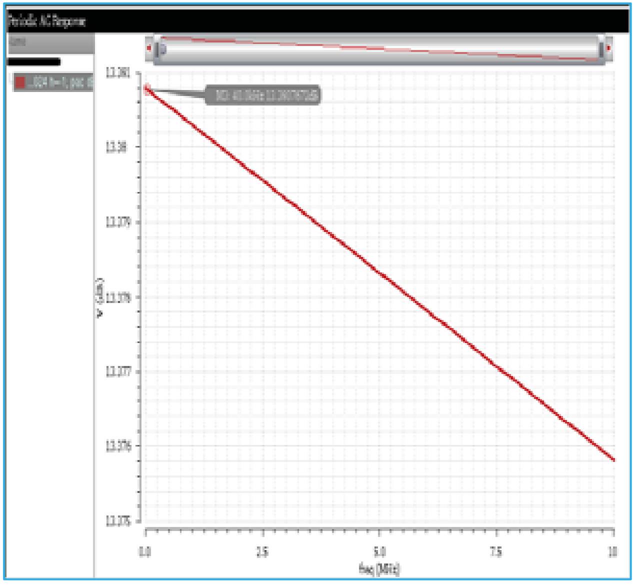

Figure 8. Mixer Conversion Gain

In Table III, the biasing voltages for RF and LO transistors are taken as 300mV. The proposed mixer voltage conversion gain of the Mixer circuit shown in Fig 1 (Ckt 2) is 13.38 dB at 5 GHz frequency. The current flowing through the transistors, drain to source voltages of transistors used in the mixer part and power calculations of proposed merged Differential LNA-Mixer with shunt paths in Fig 1 (Ckt 2) are shown in Table III. The static power consumed in the mixer part of Fig 1 is 1.276mW.

TABLE III.
POWER CALCULATIONS OF PROPOSED LNA-MIXER WITH SHUNT PATHS (MIXER PART)

Parameter	Value
Biasing voltages [$V_{b(RF)}$ & $V_{b(LO)}$]	300mV
Current through N_{M1}&N_{M2}	0.687mA
Current through N_{M3}, N_{M4}, N_{M5} & N_{M6}	0.317mA
Drain to Source Voltage of N_{M1}&N_{M2}	70.13mV
Drain to Source Voltage of N_{M3}, N_{M4}, N_{M5} & N_{M6}	548.9mV
Power consumed by R_{d3} & R_{d4} branch	0.484mW
Power consumed by N_{M1}&N_{M2}	0.096mW
Power consumed by N_{M3}, N_{M4}, N_{M5} & N_{M6}	0.696mW
Static power Consumption in merged LNA-Mixer with current shunt paths (Mixer Part)	1.276mW

The biasing voltage of differential LNA is taken as 300mV. The current flowing through the transistors, drain to source voltages of transistors used in the LNA part and power calculations of proposed merged Differential LNA-Mixer with shunt paths in Fig1 (Ckt 1) are shown in Table IV. The static power consumed by the differential LNA part in Fig 1 is 2.26mW.

TABLE IV.
POWER CALCULATIONS OF PROPOSED LNA-MIXER WITH SHUNT PATHS (LNA PART)

Parameter	Value
Biasing voltages [V_{b1}&V_{b2}]	300mV
Current through N_{L1}, N_{L2}, N_{L3} & N_{L4}	1.13mA
Drain to Source Voltages of N_{L1} & N_{L3}	618.13mV
Drain to Source Voltage of N_{L2} & N_{L4}	381.87mV
Power consumed by N_{L1} & N_{L3}	1.397mW
Power consumed by N_{L2} & N_{L4}	0.863mW
Static power Consumption in merged LNA-Mixer with current shunt paths (LNA Part)	2.26mW

TABLE V.
POWER CALCULATIONS OF PROPOSED LNA-MIXER WITH SHUNT PATHS (SHUNT PATH PART)

Parameter	Value
Current through P1 & P2	0.053mA
Drain to Source Voltages of P1 & P2	548 mV
Power consumed by P1 & P2	0.058mW

The current flowing through the transistors P1 and P2, drain to source voltages of transistors used in shunt paths and power calculations of proposed merged Differential LNA-Mixer with shunt paths in Fig 1 (Ckt 3) are shown in Table V. The static power consumed by LNA, Mixer and shunt path parts and the total static power consumed in Merged Differential LNA-Mixer with current shunt paths in Fig 1 is shown in Table VI.

TABLE VI.
POWER CONSUMPTION IN PROPOSED DIFFERENTIAL LNA-MIXER WITH CURRENT SHUNT PATHS

Parameter	Value
Static power Consumption in LNA part	2.26mW
Static power Consumption in Mixer part	1.276mW
Static power Consumption in current shunt paths	0.058mW
Total Static power Consumption in Merged LNA-Mixer with current shunt paths	**3.594mW**

The transducer gain (G_T) of LNA and the conversion gain (Gc) of the Mixer, the total gain and the total static power consumed in proposed Merged LNA-Mixer (Fig 1) are shown in Table VII.

TABLE VII.
TOTAL STATIC POWER CONSUMPTION AND THE CONVERSION GAIN OF PROPOSED DIFFERENTIAL LNA-MIXER

Result Parameter	Value
Transducer Gain (G_T) of LNA	25.76dB
Conversion Gain (G_C) of Mixer	13.38dB
Total Gain of in proposed LNA-Mixer	39.14dB
Power Consumption in LNA	2.172mW
Power Consumption in Mixer	1.336mW
Power Consumption in proposed LNA-Mixer	3.594mW

TABLE VIII.
COMPARISON OF THE LNA CIRCUIT IN PROPOSED DIFFERENTIAL LNA-MIXER

Parameter/Reference	**LNA design factors**	**REF [10]**	**REF [15]**	**Proposed LNA**
f_r	5GHz	5.2GHz	5.2GHz	5GHz
S_{11}	<-15dB	-15dB	-10.5dB	-23.8dB
G_T	25.76dB	15.5dB	8.22dB	25.8dB
NF	<=3dB	4.5dB	3.7dB	1.5dB
IIP3	>-20dBm	5.6dBm	4dBm	-3.16dBm
P_{static}	<5mW	10mW	7.6mW	3.594mW

The comparison of the existing LNAs with the LNA circuit in the proposed differential LNA-Mixer circuit in Fig 1 (Ckt 1) is shown in Table VIII. Table VIII compares the results of the existing 5GHz proposed differential LNA with REF [22] and REF [23] and with the LNA design factors. From Table VIII, the input reflection coefficient (S_{11}) of the LNA part is -23.8dB, the Transducer gain (G_T) of the LNA part is 25.88, Noise Figure (NF) is 1.5dB, IIP3 is -3.16dBm and the static power consumed (P_{static}) is 3.594mw are superior to REF [10] and [15].

III. CONCLUSIONS

The differential LNA for 5G wi-fi and mixer circuit can be merged to achieve larger gains. This is a useful feature for the subsequent blocks in the 5G Wi-Fi receiver design. The source degeneration technique is beneficial to achieve impedance matching at the input side of the circuit. The cascoding of a common source amplifier with a common gate amplifier will improve the gain of the circuit while avoiding the Miller effect in common source amplifiers. Cascoding Technique is not only used to improve the gain, but also to improve the noise figure and linearity. The linearity of the LNA can also improve by choosing the differential structures in LNA circuit design. The PMOS transistors are used in current shunt paths. The current shunt paths are used to connect the mixer circuit with LNA to reduce the power consumption without affecting the gain in future.

REFERENCES

[1] Yueh-Hua Yu, Yi-Jan Emery Chen and Deukhyoun Heo, "A 0.6-V Low Power UWB CMOS LNA," *IEEE Microwave and Wireless Components Letters*, Vol. 17, No. 3, pp. 229-231, March 2007.

[2] Ke-Hou Chen, Jian-Hao Lu, Bo-Jiun Chen, and Shen-Iuan Liu, "An Ultra-Wide Band 0.4–10 GHz LNA in 0.18µm CMOS," *IEEE Transactions on Circuits and Systems-II: Express Briefs*, Vol. 54, No. 3, pp. 217-221, March 2007.

[3] Donggu. Im, I. Nam and K. Lee, "A Low Power Broadband Differential Low Noise Amplifier Employing Noise and IM3 Distortion Cancellation for Mobile Broadcast Receivers," in IEEE Microwave and Wireless Components Letters, vol. 20, no. 10, pp. 566-568, Oct. 2010.

[4] Y.-S. Lin, G.-L. Lee, " Low-power 77–81 GHz CMOS LNA with excellent matching for automotive radars", in Electronics Letters 30th January 2014 Vol. 50 No. 3 pp. 207–209.

[5] Y.J. Hong, S.F. Wang, P.T. Chen, Y.S. Hwang and J.J. Chen, "A concurrent dual-band 2.4/5.2 GHz low-noise amplifier using gain enhanced techniques," 2015 Asia-Pacific Symposium on Electromagnetic Compatibility (APEMC), Taipei, Taiwan, 2015, pp. 231-234.

[6] M. Parvizi, K. Allidina and M. N. El-Gamal, "A Sub-mW, Ultra-Low-Voltage, Wideband Low-Noise Amplifier Design Technique," in IEEE Transactions on Very Large-Scale Integration (VLSI) Systems, vol. 23, no. 6, pp. 1111-1122, June 2015.

[7] D. Im and I. -Y. Lee, "A High IIP2 Broadband CMOS Low-Noise Amplifier with a Dual-Loop Feedback," in IEEE Transactions on Microwave Theory and Techniques, vol. 64, no. 7, pp. 2068-2079, July 2016.

[8] S. Kong, H. D. Lee, M. -S. Lee and B. Park, "A V-Band Current-Reused LNA With a Double-Transformer-Coupling Technique," in IEEE Microwave and Wireless Components Letters, vol. 26, no. 11, pp. 942-944, Nov. 2016.

[9] Y. Yu, H. Liu, Y. Wu and K. Kang, "A 54.4–90 GHz Low-Noise Amplifier in 65-nm CMOS," in IEEE Journal of Solid-State Circuits, vol. 52, no. 11, pp. 2892-2904, Nov. 2017.

[10] Khosravi, S. Zandian, A. Bijari and N. Kandalaft, "A Low Power, High Gain 2.4/5.2 GHz Concurrent Dual-Band Low Noise Amplifier," 2019 IEEE 9th Annual Computing and Communication Workshop and Conference (CCWC), Las Vegas, NV, USA, 2019, pp. 0788-0792 To-Po Wang "A Low-Voltage Low Power K-Band CMOS LNA Using DC-Current-Path Split Technology" IEEE Microwave and Wireless Components Letters, Vol. 20, No. 9, Sept. 2010, pp. 519-521.

[11] Behzad Razavi, "Cognitive Radio Design Challenges and Techniques" IEEE Journal of Solid-State Circuits", Vol. 45, No. 8, Aug. 2010, pp. 1542-1553.

[12] Ehsan Kargaran, and Bahman Madadi, "Design of a Novel Dual-Band Concurrent CMOS LNA with Current Reuse Topology," 2010 International Conference on Networking and Information Technology, Date of Conference: 11-12 June 2010, INSPEC Accession Number: 11432175, pp. 386-388.

[13] Ehab Ahmed Sobhy, Ahmed A. Helmy, Sebastian Hoyos, Kamran Entesari, and Edgar Sánchez-Sinencio, "A 2.8-mW Sub-2-dB Noise-Figure inductorless Wideband CMOS LNA Employing Multiple Feedback," IEEE TRANSACTIONS ON MICROWAVE THEORY AND TECHNIQUES, VOL. 59, NO. 12, DECEMBER 2011, pp. 3154-3161.

[14] A. V. Do, C. C. Boon, M. A. Do, K. S. Yeo and A. Cabuk, "A Weak Inversion Low-Power Active Mixer for 2.4 GHz ISM Band Applications," in IEEE Microwave and Wireless Comps Letters, vol. 19, no. 11, pp. 719-721, Nov. 2009.

[15] Yu-Jun Hong, San-Fu Wang, , Po-Tsung Chen, Yuh-Shyan Hwang and Jiann-Jong Chen, "A Concurrent Dual-Band 2.4/5.2 GHz Low-Noise Amplifier Using Gain Enhanced Techniques" APEMC 2015.

[16] S. K. Hampel, O. Schmitz, M. Tiebout and I. Rolfes, "Inductor less Low-Voltage and Low-Power Wideband Mixer for Multistranded Receivers," in IEEE Transactions on Microwave Theory and Techniques, vol. 58, no. 5, pp. 1384-1390, May 2010.

[17] M. Kim, H. An, Y. Kang, J. Lee, and T. Yun, "A Low-Voltage, Low-Power, and Low-Noise UWB Mixer Using Bulk-Injection and Switched Biasing Techniques," in IEEE Transactions on Microwave Theory and Techniques, vol. 60, no. 8, pp. 2486-2493, Aug. 2012.

[18] S. P. Singh, T. Rahkonen, M. E. Leinonen and A. Parssinen, "Design Aspects of Single-Ended and Differential SiGe Low-Noise Amplifiers Operating Above fmax/2 in Sub-THz/THz Frequencies," in IEEE Journal of Solid-State Circuits, doi: 10.1109/JSSC.2023.3264475.

[19] A. Michailidis, T. Noulis and K. Siozios, "CMOS Noise Analysis and Simulation from Low Frequency and Baseband to RF and Millimeter Wave," in IEEE Access, vol. 11, pp. 39807-39823, 2023, doi: 10.1109/ACCESS.2023.3268821.

E-ISSN 2581 – 7957
P-ISSN 2277 – 3916

CVR Journal of Science and Technology, Volume 24, June 2023
DOI: 10.32377/cvrjst2403

Breaking the Boundaries using DNA Technologies to Advance Computing

A. Kunchala Krishna[1] and B. Jonnala Sai Maneesh Kumar[2]
[1]UG Scholar, CVR College of Engineering /ECE Department, Hyderabad, India
Email: kunchalakrishna9951@gmail.com
[2]UG Scholar, CVR College of Engineering /ECE Department, Hyderabad, India
Email: maneeshjonnala@gmail.com

Abstract: **Innovative technology known as "DNA computing" uses the chemical characteristics of DNA strands to carry out intricate calculations. DNA base pairing characteristics are taken advantage of in DNA computing models to encode data and carry out computations. Numerous industries could benefit from DNA computing, including molecular automation, bioinformatics, optimization, and encryption. This paper provides a general summary of DNA computing, including its background, benefits, and drawbacks. Additionally, this paper provides the contemporary DNA computing models, such as Adleman's, Winfree's, and Rothemund's models, and give instances of how they are used. This paper provide potential of DNA computing as well as the chances and difficulties facing future study and development. In concluded DNA computing has the potential to revolutionize the computing sector and challenge established computing approaches as a unique computing strategy. It has the potential to result in significant advances in computing technology.**

Index Terms: **DNA Computing, Rothemud's Model, conventional computing, molecular automation.**

I. INTRODUCTION

A. *Overview of DNA Computing*

An interdisciplinary field known as DNA computing has developed at the nexus of computer science, molecular biology, and chemistry. DNA molecules are used as information storage and processing units at the heart of DNA computing. Due to its capacity to store enormous amounts of information in a small, robust form, DNA molecules are especially well-suited for computation. Information is represented in DNA computing as a sequence of nucleotides, the components of DNA. Adenine, guanine, cytosine, and thymine are the four nucleotides that can be combined in any way to make a distinctive sequence that stands in for a particular piece of information. In the lab, DNA sequences can be created and modified using methods like PCR, gel electrophoresis, and hybridization.

The capacity of DNA computing to handle data in a massively parallel manner is one of its main features. Through the use of PCR, DNA molecules can be reproduced and amplified, enabling the processing of numerous distinct sequences at once. Because of this, DNA computing is especially well suited for tasks requiring extensive data processing, such as genome sequencing and data encryption. The capacity of DNA computing to function in situations hostile to conventional computer equipment is another benefit. As DNA molecules are immune to radiation, heat, and chemical deterioration, they are perfect for use in severe situations. As a result, several applications, such as environmental monitoring and biological diagnostics, can now be served by DNA-based sensors and detectors.

Despite its potential benefits, DNA computing still has several issues that need to be solved before it can be extensively used as a technology. The high cost of DNA synthesis and sequencing as well as the difficulty in inventing and putting into practice efficient DNA computing algorithms are some of these difficulties. Overall, DNA computing is an area that is expanding quickly and has the potential to completely change how the data is processed and stored. DNA computing will likely find novel applications in a variety of disciplines with further study and development.[1] [8]

B. *Brief history of DNA Computing*

Leonard Adleman originally proposed the idea of DNA computing in 1994 when he showed how DNA molecules may be utilized to solve a computational issue. Adleman solved a particular instance of the Hamiltonian route problem, which entails locating a path through a graph that precisely visits each vertex, using a process known as DNA hybridization. Researchers in the area started to investigate the possibility of DNA computing for a range of applications after Adleman's pioneering work. Paul Rothemund developed a technique for building precise nanoscale structures using DNA molecules in 1997, opening the door for the creation of DNA-based molecular motors and robotics.

The methods and algorithms utilized in DNA computing kept being improved in the years that followed. Erik Winfree developed a framework in 2002 that has now become a common tool in the industry for instructing DNA molecules to carry out intricate computations. Since its beginnings, DNA computing has been used to solve a wide range of issues in industries including biology, optimization, and cryptography. DNA molecules have been employed in cryptography to encrypt and decrypt secret communications, providing a potential substitute for established encryption techniques. Large genetic data sets have been analyzed in bioinformatics using DNA computing, providing new insights into the biology of illness.

Despite its potential uses, DNA computing still has several obstacles to overcome. The high cost of DNA synthesis and sequencing, the difficulty of inventing and putting into practice efficient algorithms, and the requirement for specialized laboratory tools and knowledge are some of the difficulties. Overall, DNA computing has

Received on 31-03-2023, Revised on 26-04-2023, Accepted on 13-05-2023.

seen a history of quick innovation and advancement, with researchers consistently pushing the limits of what is feasible with this cutting-edge technology. It is conceivable that DNA computing will find novel applications in a variety of industries, including health, materials science, and artificial intelligence, with continuing study and development.

C. Importance of DNA Computing

DNA computing offers several advantages over conventional computing techniques and has the potential to change the way information is processed and retained. DNA coding offers several important advantages, including:

- ***Massive parallel processing:*** PCR's ability to duplicate and amplify DNA molecules enables the processing of numerous distinct patterns at once. Because of this, DNA computing is especially well adapted for tasks requiring extensive data processing, like gene decoding and data encryption.
- ***Energy efficiency:*** Since DNA computing doesn't use electricity or any other exterior energy sources, it is naturally energy-efficient. This makes it a potential replacement for conventional processing techniques, which can be energy- and environment-intensive.
- ***Robustness:*** DNA strands can withstand high temperatures, radiation harm, and chemical deterioration, making them perfect for use in extreme conditions. As a result, a variety of uses, such as environmental tracking and biomedical tests, can now be served by DNA-based sensors and detectors.
- ***New applications:*** DNA computing has already been used to solve a range of issues in industries like biology, optimization, and encryption. New and creative uses in disciplines like artificial intelligence, materials science, and medicine are likely to appear as technology advances.

Despite its potential benefits, DNA computing still has several issues that need to be solved before it can be extensively used as a technology. The high cost of DNA synthesis and sequencing as well as the difficulty in inventing and putting into practice efficient DNA computing algorithms are some of these difficulties.

Overall, DNA computing is significant because it has the potential to change how information is processed and stored while providing several advantages over current computing techniques. DNA computing is projected to become a more vital tool in a variety of industries, including medical, environmental monitoring, and national security, with sustained study and development.

II. PRINCIPLES OF DNA COMPUTING

A. DNA Structure and Properties

As they support DNA molecules' capacity to store and process information, DNA's structure and physical characteristics are crucial to the area of DNA computing. Fig.1 shows the structure of DNA. Deoxyribonucleic acid, or DNA, is a double-stranded, helical molecule with the genetic code for all living things. The two strands of DNA are made up of nucleotides, which are the substances that gives DNA its structure. Each nucleotide comprises a sugar molecule (deoxyribose), a phosphate group, and a nitrogenous base. The nitrogenous bases adenine (A), thymine (T), guanine (G), and cytosine (C) are the four types that make up DNA (C). Each organism's genetic code is determined by the arrangement of these bases, and each arrangement represents a particular mix of genetic data.

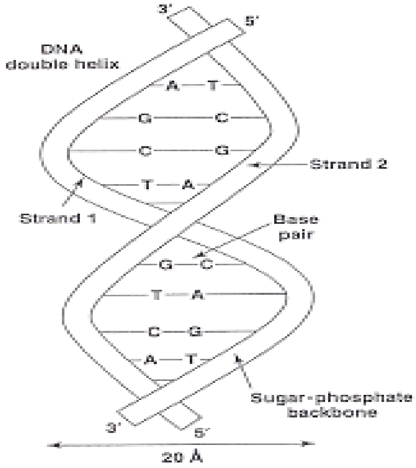

Figure 1. DNA structure [14]

The nitrogenous bases form hydrogen bonds with one another, holding the two DNA strands together. Particularly, adenine (A-T) and guanine (G-C) always pair with thymine (T-T) (G-C). Since it enables DNA replication and transcription, this base pairing is essential for DNA's capacity to store and process information.

The physical and chemical characteristics of DNA are another way to describe it. The capacity of DNA to undergo strand separation, which takes place when the hydrogen bonds between the nitrogenous bases are broken, is one of its most crucial characteristics. Several methods, such as heat, chemicals, or enzymes, might cause this. The ability to access and copy the genetic information encoded in DNA makes strand separation a critical stage in the replication and transcription of DNA. The capacity of DNA to hybridize, or to establish stable base-pairing connections with complementary DNA or RNA sequences is another crucial characteristic of DNA. The invention of DNA-based logic gates and algorithms is only one example of how this characteristic has been used in DNA computing.

In conclusion, as they allow DNA molecules to store, process, and transfer information, DNA's structure and physical characteristics are crucial to DNA computing. DNA's capacity to serve as a computing substrate is significantly influenced by its double-stranded helical structure, nitrogenous base composition, and capacity for strand separation and hybridization. [12]

B. DNA sequence Design

As DNA sequence design affects how well DNA molecules can store and process information, it is a crucial component of DNA computing. To encode specific information, nucleotides must be carefully chosen and arranged. Physical and chemical characteristics that influence how DNA molecules behave must also be taken into account when designing DNA sequences. The selection of the proper nucleotide sequence to encode a certain piece of information is a crucial factor in DNA sequence design. This may entail selecting a particular nitrogenous base sequence that maps to a certain gene or protein or creating a sequence that can serve as a trigger for a certain reaction or activity.

The optimization of physical and chemical characteristics that have an impact on how DNA molecules behave is a key component of DNA sequence design. For instance, the durability, melting temperature, and hybridization effectiveness of DNA sequences can be influenced by their length and base makeup. So, to assure the best performance in a given application, these qualities are frequently optimized during the construction of DNA sequences. DNA sequence design entails not only choosing and refining nucleotide sequences but also taking into account other elements that may have an impact on how DNA molecules behave. For instance, adding methyl groups or phosphorothioate linkages to DNA molecules might increase their stability or specificity, while labeling DNA with fluorescent dyes or other substances can make it easier to identify and analyze DNA molecules. [10]

Overall, the process of designing DNA sequences is intricate and multidimensional, requiring careful consideration of several variables. DNA sequence design plays a crucial role in enabling the use of DNA as a computational substrate in a variety of applications, including data storage, cryptography, and molecular sensing. This involves the selection and optimization of nucleotide sequences as well as the consideration of physical and chemical properties. Unlocking the full potential of this fascinating technology will depend on the development of fresh, cutting-edge techniques for DNA sequence design as the area of DNA computing continues to advanced.

C. DNA Hybridization

A crucial step in DNA computing is the development of permanent base-pairing connections between complementary DNA or RNA sequences, a process known as DNA hybridization. Since it permits the selective identification and binding of particular DNA sequences, hybridization is a crucial technique by which DNA molecules may be employed to store, process, and transfer information. The complementary base-pairing rules, which state that adenine (A) pairs with thymine (T) and guanine (G) pairs with cytosine (C), regulate the process of DNA hybridization (C). Sequence-complementary DNA or RNA strands will hybridize when they come into contact, creating a double-stranded structure that is supported by hydrogen bonds between the complementary bases.

DNA hybridization's specificity, which enables the selective identification and binding of particular DNA sequences, is one of its main benefits. The complementary base-pairing rules, which guarantee that only complementary sequences will establish stable base-pairing interactions, control this specificity. In light of this, DNA hybridization is a potent tool for the development of DNA-based sensors, detection assays, and computing systems. DNA hybridization is distinguished by its sensitivity, which enables the detection and measurement of minute quantities of DNA, in addition to its specificity. This sensitivity results from the fact that the stability of the hybridized structure might be compromised by just one base-pair mismatch between the two complementary sequences. Hence, DNA hybridization may be utilized to detect certain DNA or RNA sequences with great sensitivity and precision.

The speed of the process, which may be altered by a variety of circumstances, is another significant component of DNA hybridization. For instance, the DNA sequences' length and base composition, as well as the existence of secondary structure or other types of interference, might influence the pace and effectiveness of hybridization. Designing and refining DNA-based sensing and computing systems depend critically on understanding and improving the kinetics of DNA hybridization.

Overall, DNA hybridization is a crucial technique in DNA computing because it allows for the very precise and sensitive binding and selective detection of particular DNA sequences. The creation of novel and creative methods for DNA hybridization will be crucial to realizing the full potential of this formidable technology as the area of DNA computing continues to advance.[2]

D. Enzymatic Reactions and DNA Polymerase Chain Reaction (PCR)

The modification and amplification of DNA sequences are made possible by enzymatic reactions and DNA polymerase chain reaction (PCR), two crucial procedures in DNA computing. These procedures enable the selective amplification, alteration, and analysis of certain DNA sequences, which is essential for the implementation of many DNA-based computer and sensing devices. Enzymes are often used to catalyze particular chemical processes involving DNA or RNA molecules. DNA polymerases, which are in charge of creating new DNA strands, are one significant family of enzymes employed in DNA computation. Using a complementary DNA template strand as a guide, DNA polymerases are highly specialized enzymes that can add nucleotides to a developing DNA strand in a sequence-specific way. [11]

DNA polymerases are used in the potent PCR method to selectively amplify certain DNA sequences. A reaction mixture including the target DNA sequence, DNA polymerase, and certain primers that bind to and delineate the boundaries of the target sequence is heated and cooled repeatedly during the PCR process. The primers attach to the complementary target sequences during the chilling stage, enabling the DNA polymerase to synthesize new DNA strands. During the heating process, the DNA strands are denatured, or separated, into single strands. The number of copies of the desired DNA sequence can then be produced exponentially by using the generated DNA strands as templates for more amplification. The selective amplification of particular DNA sequences for a variety of applications, including DNA-based sensing, diagnostics, and data storage, has made PCR become a frequently used method in DNA computing. DNA sequences may be altered and analyzed in several circumstances by combining PCR with other enzymatic processes like restriction digestion or ligation.

Enzymatic reactions and polymerase chain reactions (PCR) are crucial procedures in DNA computing because they allow for the selective modification and amplification of particular DNA sequences. The creation of fresh, cutting-edge enzymatic and PCR-based methods will be crucial for realizing the full promise of this fascinating technology as DNA computing advances.

E. DNA Computing algorithms

DNA strands are used as the computing medium in DNA computing algorithms, which are computational operations. Fig.2 shows the process of DNA Computing. These algorithms may be used to carry out a variety of computing tasks, including sorting, searching, and pattern recognition. They are usually based on the concepts of DNA hybridization and enzymatic processes. Strand displacement-based algorithms are a significant class of DNA computing techniques. These algorithms make use of DNA strands that have been engineered to hybridize with other DNA strands in a certain order, dislodging existing strands and forming new DNA structures. As well as for the identification and diagnosis of illnesses, strand displacement-based algorithms have been utilized for several computing tasks, including the sorting and counting of DNA strands.[3]

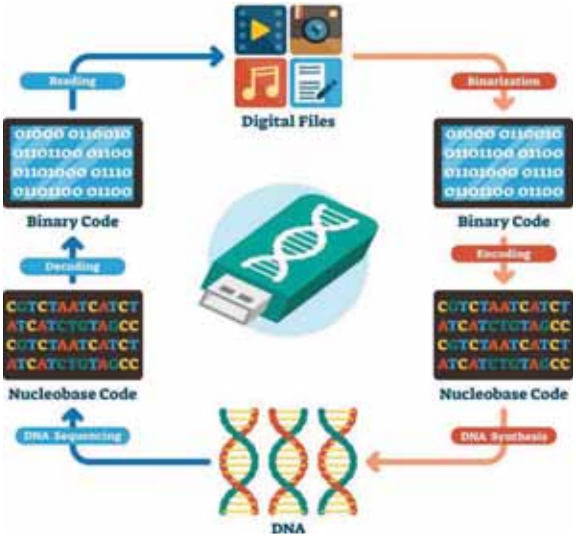

Figure 2. DNA computing process [19]

Tile-based algorithms are a significant subset of DNA computing algorithms. These algorithms employ tiny DNA tiles that are intended to self-assemble into predetermined patterns using the concepts of DNA hybridization. Many computational challenges, like finding the shortest way through a maze and modeling the behavior of cellular automata, have been solved using tile-based techniques. To develop hybrid computational systems with distinctive features and capabilities, DNA computing algorithms can also be integrated with other computational approaches like microfluidics or optical computing. For instance, portable diagnostic systems for the detection of infectious illnesses have been created by integrating DNA computing algorithms with microfluidic devices. One of the main benefits of DNA computing algorithms is their parallelism and scalability, which enables the quick execution of computational tasks by processing several DNA strands at once. Furthermore, DNA computer algorithms are very versatile and simple to reprogram or alter to carry out various jobs.

Overall, DNA computing algorithms are a fascinating and quickly growing topic with a wide range of possible applications in computer science, biology, and sectors like medicine. The potential for this technology to transform computing and data processing will keep growing as researchers work to create fresh and creative DNA computing algorithms.

III. DNA COMPUTING MODELS

A. Adleman's Model

Leonard Adleman's approach, which he initially suggested in 1994, is the most well-known example of DNA computing. The Hamiltonian Path Problem, a well-known computational issue in graph theory, is one of the computational problems that Adleman's model uses DNA molecules to resolve. To find a path that precisely reaches each vertex of a graph is to solve the Hamiltonian Path Problem. According to Adleman's model, the graph was converted into a DNA sequence and then chemically produced in the lab. The path that passed through every vertex of the graph was then determined by subjecting the DNA molecules to a series of enzyme reactions and DNA hybridization processes.[4]

In Adleman's concept, shorter DNA sequences served as the graph's vertices, while longer DNA sequences with complementary "sticky ends" served as the graph's edges. The DNA sequences were able to hybridize and create a route that passed through every vertex of the network thanks to the sticky ends. Adleman's model's primary benefit is its capacity for massively parallel calculations employing a sizable number of DNA molecules. The model's strong scalability enables the effective resolution of challenging computational issues. The fundamental drawback of Adleman's model is its high error rate, which can lead to inaccurate computational problem solutions.

Adleman's concept, despite its flaws, has had a considerable influence on DNA computing and has sparked the creation of a broad variety of DNA computing models and algorithms. Adleman's concept has also paved the way for discoveries in the domains of molecular biology and nanotechnology, as well as novel methods for employing DNA molecules to carry out computations.

B. Winfree's Model

In 1998, Erik Winfree published "Winfree's model," a DNA computing theory. This model employs DNA molecules to do computations by utilizing the ideas of programmable DNA interactions and molecular self-assembly. Winfree's theory makes use of very small DNA molecules known as "DNA tiles." These "DNA tiles" may self-assemble into larger, more intricate structures through interactions between complementary base pairs. DNA tiles may be constructed so that they interact with one another in certain ways, allowing the construction of complex DNA structures with specific characteristics.[15]

In Winfree's approach, "algorithmic crystals," which are substantial, crystalline structures that contain computational information, are built from DNA tiles. The algorithmic crystals may be created to carry out particular computations, including pattern recognition or sorting. The primary benefit of Winfree's concept is its capacity to run complex computations in parallel utilizing a huge number of DNA molecules. The model's strong scalability enables the effective resolution of challenging computational issues. Moreover, the utilization of programmable DNA interactions enables the creation of extremely unique computing systems with distinct features and capabilities.

However, the fundamental drawback of Winfree's methodology is the challenge of designing and producing massive, intricate DNA structures. Moreover, the model needs exact control over how DNA tiles interact with one another, which can be difficult in practice. Winfree’s concept, despite its flaws, has had a considerable influence on DNA computing and has motivated the creation of new DNA computing models and algorithms. The model has also opened up new directions for study in the disciplines of molecular biology and nanotechnology as well as the development of new concepts and methods for employing DNA molecules to carry out computing tasks.[4]

C. Rothe mund’s Model

Paul Rothemund proposed Rothemund's model in 2006. It is a DNA computing paradigm. In this model, DNA molecules are used to create intricate forms and patterns using the technique known as "DNA origami“.By employing short, "staple" DNA strands to keep the larger DNA molecule in place, a technique known as DNA origami may be used to fold DNA molecules into precise shapes and patterns. The method enables the precise nanoscale creation of intricate two-dimensional and three-dimensional structures.

In Rothemund's approach, "tiles" that encode computational information are built using DNA origami. The ability to create larger, more intricate structures that are capable of carrying out computational tasks is made possible by the tiles' ability to interact with one another in specified ways. The main benefit of Rothemund's approach is its capacity for exact control of shape and geometry when building intricate, microscopic structures. The model's strong scalability enables the effective resolution of challenging computational issues. However, the fundamental drawback of Rothemund's paradigm is the challenge of designing and producing vast, intricate DNA structures. Moreover, the model needs exact control over how DNA tiles interact with one another, which can be difficult in practice.

Despite its drawbacks, Rothemund's model had a big influence on DNA computing and served as an inspiration for the creation of other DNA computing models and algorithms. The model has also opened up new directions for study in the disciplines of molecular biology and nanotechnology as well as the development of new concepts and methods for employing DNA molecules to carry out computing tasks.

D. Examples of DNA Computing Models

Throughout the years, a variety of distinct DNA computer models have been created, each with its special advantages and drawbacks. DNA computer modeling examples include:

- ***The Adleman's model:*** This model searches for a certain sequence of DNA molecules that satisfies a set of requirements to employ DNA molecules to solve computational problems. Adleman's concept makes use of PCR to amplify and identify DNA sequences and is based on the principles of DNA hybridization. [13]
- ***Winfree's model:*** In this approach, massive, crystalline structures that contain computational information are built using DNA tiles. The ability to design the tiles' interactions with one another enables the creation of intricate DNA structures with predetermined features.[17]
- ***Rothemund's model:*** In this model, intricate two- and three-dimensional structures that contain computational information are built using DNA origami. Larger, more intricate structures that can carry out computational tasks can be built by carefully planning the interactions between the structures.
- ***Lipton's model:*** In this model, DNA molecules are used to simulate the action of biological neurons to carry out computational tasks. The input and output of neurons are represented by DNA molecules in the model, and the interactions between neurons are simulated via DNA hybridization.
- ***Soloveichik's model:*** In this model, parallel calculations are carried out utilizing DNA molecules using a method known as "chemical reaction networks." The model simulates the interactions between molecules by using DNA hybridization and DNA molecules to represent the molecules involved in chemical processes.

These are only a handful of the several DNA computer models that have been created throughout the years. Each model has certain advantages and disadvantages, and scientists are always looking for novel applications for DNA molecules in computation.

IV. APPLICATIONS OF DNA COMPUTING

A. Cryptography

Secure communication in the presence of adversaries is practiced through the use of cryptography. It includes converting plaintext into ciphertext, which can only be decoded by authorized users who have access to a secret key, using mathematical techniques and protocols. Cryptography has grown in importance as the digital era and contemporary communication have increased the need for information security. For cryptography, DNA computing has several benefits, including great storage density, huge parallelism, and high mistake tolerance. DNA molecules are a perfect contender for storing and transferring massive amounts of encrypted data because they can pack a huge quantity of information into a little amount of space. DNA computing can do calculations concurrently, enabling quick encryption and decryption of huge volumes of data. [9]

The "millionaire's dilemma," which includes two billionaires wishing to compare their wealth without disclosing their true net worth, is one of the most well-known applications of DNA computing in cryptography. This issue can be resolved with DNA computing by recording each millionaire's net worth as a series of DNA molecules, which can then be combined and compared using PCR. Without disclosing any private information, the two parties may decide who is wealthier by measuring the quantity of DNA that corresponds to each millionaire's net worth. DNA computing has been utilized to carry out the millionaire's problem as well as other cryptographic tasks including creating secure keys, encrypting communications, and performing secure multiparty calculations. By encoding random DNA molecule sequences that are shared by two parties, DNA computing, for instance, may be used to generate secure keys. Then, by encrypting and decrypting messages using these keys, sensitive information may be protected from unauthorized users.[5]

With several benefits over conventional cryptographic techniques, DNA computing has considerable potential for the area of cryptography overall. Researchers are always looking for new ways to utilize DNA molecules to enhance the security and privacy of digital communication, even though there are still numerous obstacles to be solved.

B. *Bioinformatics*

With the use of computer tools and methods, bioinformatics analyses and interprets biological data, such as DNA sequences, protein structures, and genetic networks. Because of their shared interest in the modification and study of DNA sequences, DNA computing, and bioinformatics naturally complement one another. Designing DNA microarrays, which are used to study the patterns of gene expression in cells, is one of the main uses of DNA computing in bioinformatics. A DNA microarray is made up of several DNA molecules, each of which is associated with a different gene. Researchers can concurrently evaluate the expression levels of thousands of genes by hybridizing a sample of RNA isolated from cells to the microarray. This makes it possible to find the genes that change their expression in response to diverse stimuli like medications, poisons, or diseases.

Other bioinformatics activities including sequence alignment, motif discovery, and phylogenetic analysis may also be carried out using DNA computing. To find regions of similarity and divergence across various species, researchers can utilize DNA computing, for instance, to align several DNA molecule sequences. The creation of phylogenetic trees and the inference of evolutionary links are therefore possible using this knowledge. The prediction of protein structures and interactions is a significant use of DNA computing in bioinformatics. The amino acid sequences of proteins may be encoded by DNA molecules, which can then be folded into their natural conformations via computer simulations. This can give important information on how proteins interact with other molecules and how they maintain their stability.

Ultimately, DNA computing has the potential to completely transform the discipline of bioinformatics by allowing scientists to study and comprehend biological data more quickly and accurately than previously. The creation of new DNA-based computational tools and algorithms will probably have a significant influence on our comprehension of biological systems and the illnesses that affect them, even if there are still numerous obstacles to be overcome.

C. *Optimization*

Finding the optimal answer to a problem within a set of restrictions is the process of optimization. Many optimization issues, including the well-known Traveling Salesman Problem (TSP) and more challenging issues involving numerous objectives and constraints have been tackled using DNA computing.The intrinsic parallelism of DNA computing is one of its benefits for optimization. At a fraction of the time needed by conventional optimization techniques, a huge number of potential solutions may be simultaneously explored and the best answer can be found by encoding them in a DNA sequence. In the instance of the TSP, DNA computing has been utilized to find the quickest path between several cities while accounting for variables like distance, travel time, and cost. The best path has been quickly identified by encoding every potential path in a DNA sequence, followed by a series of hybridization and enzymatic processes.

The optimization of intricate biological processes like metabolic pathways or gene regulatory networks is another area where DNA computing has shown potential. The best conditions for each reaction may be determined, and the yield of a desired product can be increased, by encoding the reactions as DNA sequences and simulating them in vitro.In fields including logistics, manufacturing, and transportation, DNA computing has been used to optimize scheduling and resource allocation issues. It is feasible to determine the ideal timetable or allocation method that optimizes efficiency and reduces costs by encoding the characteristics of the problem as DNA sequences and modeling the interactions between them.

Therefore, DNA computing has the potential to transform the area of optimization by making it possible to quickly explore sizable search spaces and find the best answers to challenging issues. The creation of novel DNA-based optimization algorithms and methodologies is anticipated to significantly influence various sectors and applications, even though there are still numerous obstacles to be solved.

D. *Molecular Robotics*

The goal of the rapidly expanding area of molecular robotics, which uses DNA as a fundamental building element, is to create molecular-scale machines and robots. By enabling the exact control of DNA-based structures and the integration of complex molecular systems, DNA computing has significantly contributed to the advancement of molecular robotics. DNA computing's capacity to encode complicated behaviors and functionalities into DNA-based structures is one of its primary benefits for molecular robots. It is possible to control the building and motion of molecular-scale structures by encoding certain sequences and instructions into DNA. This enables the creation of intricate molecular machines and robots.

For instance, using DNA computing, scientists have created molecular walkers that can travel along a DNA track just like a real motor protein. The walker may follow a predefined course and carry out certain duties, like transferring goods or starting a reaction, by embedding a series of instructions in the DNA sequence. Moreover, DNA-based sensors and actuators that can adapt to changes in their environment and carry out certain tasks have been designed and constructed using DNA computing. Researchers have created DNA-based sensors, for instance, that can recognize particular compounds, like glucose or toxins, and cause a reaction, such as the release of a medication or the activation of a signalingpathway. The creation of self-assembling structures and materials is a further application of DNA computing in molecular robotics. It is feasible to control the construction of intricate three-dimensional structures and materials, such as DNA origami and nanotubes, by programming particular sequences and interactions into DNA.

Overall, DNA computing and molecular robotics have the potential to transform the area of nanotechnology by making it possible to design and build intricate molecular machines and devices that have a variety of uses, from materials research to medicine. The creation of new DNA-based tools and approaches will probably result in significant advancements in the sector in the years to come, even if there are still numerous obstacles to be addressed.

E. Other Applications

There is a wide range of other possible uses for DNA computing, in addition to its current applications in molecular robotics, bioinformatics, optimization, and cryptography. These are a few instances:

- ***Data storage:*** Due to its great storage density and long-term stability, DNA has been suggested as a viable medium for digital data storage. Data backup and long-term archiving may benefit from the capacity to encode and recover information using DNA-based storage devices, which has been proven by researchers.
- ***Nanoscale computing:*** DNA computing has the potential to make it possible to design and build nanoscale computing circuits and devices, which might be applied to a variety of tasks, from calculation to sensing. For instance, scientists have created DNA-based logic gates and circuits that are capable of carrying out basic computing operations.
- ***Drug delivery:*** DNA-based devices and structures may be utilized for targeted drug delivery, in which medications are only released in response to particular bodily signals or circumstances. In reaction to the presence of particular biomarkers, researchers have created DNA-based nanorobots that can target cancer cells and deliver medications.
- ***Environmental monitoring:*** DNA-based sensors may be employed in environmental monitoring to identify and measure pollutants, poisons, and other environmental constituents. As an illustration, scientists have created DNA-based sensors that can find heavy metals in both water and the air.
- ***Synthetic biology:*** By enabling the exact control and manipulation of DNA-based systems and organisms, DNA computing has the potential to transform the area of synthetic biology. For instance, scientists have created synthetic gene networks using DNA computing that are capable of carrying out sophisticated tasks like controlling gene expression or detecting environmental cues.

Overall, DNA computing has a wide range of possible applications, and the discipline is still in its infancy. Anticipating many more cutting-edge uses of this technology in the years to come as researchers continue to create new instruments and methods for working with DNA.

V. ADVANTAGES AND CHALLENGES OF DNA COMPUTING

A. Advantages of DNA Computing

DNA computing benefits include:

- ***High Parallelism:*** DNA computing's capacity to carry out a huge number of computations in parallel is one of its key features. This demonstrates how much quicker DNA computing can tackle complicated issues than conventional computers.
- ***Huge Data Storage:*** With the enormous quantity of information that DNA molecules are capable of storing, DNA computing is a promising technique for data storage and retrieval. One exabyte of data may be stored in one gram of DNA molecules.
- ***Energy Efficiency:*** Since DNA computing works at the molecular level, it uses a lot less energy than conventional computers do. It is an energy-efficient technology since the amount of energy needed to conduct a DNA computation is proportional to the volume of operations being carried out.
- ***Fault Tolerance: DNA computing is intrinsically error-tolerant, which*** means it can carry on even when there are mistakes. Duplicate calculations can be used to repair errors and guarantee the accuracy of the final result.
- ***New Computing Paradigms:*** DNA computing provides new paradigms that may be more effective for addressing particular sorts of issues, including optimization, cryptography, and biology. Problems that are challenging or impossible to address using conventional computer techniques can also be solved with DNA computing.
- ***Nanoscale Computing:*** As DNA acts at the nanoscale, it may be utilized to create incredibly tiny machines that can carry out sophisticated computations. Because of this, DNA computing holds great promise for the creation of nanoscale devices and sensors.
- ***Environmentally Friendly:*** DNA computing doesn't emit any trash or pollutants, making it an ecologically responsible device. Because renewable materials can be used to create DNA strands, this technology is also environmentally friendly.

In conclusion, high parallelism, enormous data storage, energy economy, failure tolerance, innovative computing models, nanoscale computing, and environmental friendliness are some of the benefits of DNA computing. For a variety of uses, including data storing, encryption, bioinformatics, and nanoscale computing, DNA computing is a hopeful tool because of these benefits.

B. Challenges of DNA Computing

Challenges of DNA Computing:

Despite all of its benefits, DNA computing has several issues that must be resolved before it can reach its maximum potential. These difficulties include:

- ***Complexity:*** DNA computing needs a high level of knowledge in molecular biology, chemistry, and computer science. It is a complicated technology. The synthesis and modification of DNA molecules also need specialist tools and resources.
- ***Error Rates:*** During calculation, DNA strands may experience mutations or harm that can affect the end outcome. Despite the intrinsic fault tolerance of DNA computing, techniques for mistake discovery and correction are still necessary to guarantee the precision of the outcomes. [3]
- ***Scalability:*** Because DNA computing is still in its infancy, it will be difficult to scale up the technology to manage larger and more complicated computations. DNA computing's ability to scale is also constrained by the expense of synthesizing and working with vast quantities of DNA strands.
- ***Integration with Conventional Computing:*** DNA computing is a complementary technology that can be used with conventional methods to handle complicated issues rather than as a substitute for them. It is still difficult to develop techniques for combining DNA computing with conventional computing techniques.
- ***Ethical and Legal Concerns:*** The application of DNA computing poses ethical and legal concerns, especially in the fields of security and privacy. Regulations are also required to guarantee the responsible and secure application of DNA computing technology.
- ***Education and Training:*** DNA computing needs specialized knowledge and expertise, so education and training programmers are required to create a population with the necessary level of expertise.

The intricacy, error rates, scalability, integration with conventional computing, moral and legal concerns, and education and training problems are, in summation, the difficulties of DNA computing. For DNA computing technology to be developed and used successfully, these issues must be resolved.[6]

C. Comparison of DNA Computing with Traditional Computing

The use of DNA computing is compared to traditional computing.

DNA computing differs from traditional computing methods in both its advantages and disadvantages. The similarities between DNA computing and traditional computing highlighted the following key distinctions:

- ***Speed:*** Electronic computations take only a few microseconds or less, whereas DNA reactions usually take hours or days to finish. As a result, DNA computing is slower than conventional computing techniques. However, DNA computing may be able to carry out several calculations concurrently, which may be advantageous for some uses.
- ***Memory Capacity:*** DNA is capable of storing enormous amounts of data in a very tiny quantity of area and has a very high data storage capacity. Because of this, it is a desirable choice for data storage apps, particularly for big data sets.
- ***Energy Efficiency:*** DNA computing employs chemical processes, which require very little energy, to carry out calculations, making it one of the most energy-efficient forms of computing. In comparison, the energy needed to operate electronic devices in conventional computing techniques is substantial.
- ***Programmability:*** By encoding DNA sequences with particular commands, DNA computing can be made to execute specific calculations. However, this computing necessitates a specialized understanding and proficiency in chemistry and molecular biology.
- ***Scalability:*** Due to the specialized tools and resources needed for the synthesis and handling of DNA strands, DNA computing is not yet as scalable as conventional computing techniques. Its capacity to manage complicated calculations and uses is thus constrained.
- ***Error Rates:*** Because DNA sequence mistakes can be fixed through self-replication and self-assembly processes, DNA computing is naturally fault-tolerant. Traditional computing techniques, on the other hand, are susceptible to mistakes brought on by faulty gear or software.
- ***Price:*** Due to the high expense of synthesizing and modifying DNA strands, DNA computing can be costly. On the other hand, traditional processing techniques are now more reasonably priced as a result of technological advancements and efficiencies of scale.

In conclusion, DNA computing has several benefits over conventional computing techniques, such as high data storage capability, energy economy, and fault tolerance. However, its scalability and greater price are presently limiting factors. DNA computing is a complementary technology that can be used with conventional computing techniques to tackle challenging issues, not a replacement for them.[6]

D. Comparison of DNA Computing between different methods

The most well-known DNA computing models are those created by Adleman, Winfree, and Rothemund. Although they have certain things in common, they also have some significant distinctions.

The DNA computing pioneer Adleman's paradigm is predicated on the notion of employing DNA strands as a computational tool. Adleman's model uses DNA strands to represent a graph, and a sequence of DNA manipulations, including PCR amplification, gel electrophoresis, and restriction enzyme digestion, are utilized to solve the computational problem. Adleman's model has the advantage of being able to tackle NP-complete problems, but because DNA changes are so intricate, it can be slow and prone to mistakes.

On the other hand, Winfree's paradigm is predicated on the notion of exploiting DNA as a programmable molecular fabric. According to Winfree's concept, a sequence of hybridization processes is used to create DNA strands that are intended to self-assemble into specific forms and patterns. Although Winfree's model has the benefit of parallel computations, which help speed up the process, designing and optimizing DNA sequences to create the desired structure can be difficult.

The concept behind Rothemund's model, commonly referred to as DNA origami, is to use DNA strands to fold into intricate two- and three-dimensional forms. Using shorter DNA strands, referred to as "staple strands," Rothemund's model describes how a lengthy single-stranded DNA molecule is folded into a predefined form. The ability to produce complex and programmable nanostructures is a benefit of Rothemund's concept, but designing and optimizing the DNA sequences to get the required form may be difficult and time-consuming.

In conclusion, DNA strands are used in Adleman's model to solve computational issues, DNA strands self-assemble in Winfree's model to produce predetermined shapes and patterns, and DNA strands are folded into complex, programmable nanostructures in Rothemund's model. The choice of the model relies on the particular application needs. Each model has benefits and drawbacks.[17]

VI. FUTURE OF DNA COMPUTING

A. *Current Research and Development*

The performance and dependability of DNA computing models are currently being optimized, and novel uses for the technology are being investigated. Among the study topics being pursued at the moment are:

- ***DNA computing algorithm optimization:*** To facilitate quicker and more accurate issue solving, researchers are trying to increase the effectiveness and accuracy of DNA computing algorithms.[7]
- ***DNA molecule design and synthesis:*** DNA computing heavily relies on DNA molecule design and synthesis, and scientists are currently working on improved methods for synthesizing and building DNA strands.
- ***Integration of DNA computing with other technologies:***To build more potent computing systems, researchers are looking into integrating DNA computing with other cutting-edge technologies like quantum computing and machine learning.
- ***DNA computing in biology and medicine:*** By facilitating more effective drug discovery and personalized medicine, DNA computing has the potential to revolutionize biology and medicine. In these areas, researchers are looking into novel uses for DNA intelligence.
- ***Creation of fresh DNA computing models:*** New DNA computing models are being created by researchers, and they will be able to handle larger and more complicated issues. This includes models that integrate other kinds of molecules, such as RNA and enzymes, as well as models that employ DNA-based logic circuits.

In general, DNA computing research and development is geared towards enhancing the technology's powers and broadening its uses. DNA coding has the potential to develop into a potent instrument for tackling some of the most difficult issues of our time with further developments.

B. *Potential of DNA Computing*

The promise of DNA computing is enormous because it provides a special collection of benefits over conventional computing techniques. The following are some possible uses for DNA computing:

- ***Effective issue handling:*** DNA computing can be more effective than conventional computing techniques at solving complex problems. This is possible because DNA can hold a tonne of data in a tiny quantity of area and carry out extremely complex parallel computations.
- ***Secure data storage:*** Due to its durability and resilience to deterioration, DNA has the potential to be used as a secure data storage medium. It is a desirable choice for long-term storage because it can hold a large quantity of data in a small area.
- ***Personalized medicine:*** By facilitating quicker and more effective medication finding, DNA coding has the potential to revolutionize personalized medicine. Personalized therapy strategies based on a person's genetic makeup can also be developed using it.
- ***Environmental tracking:*** DNA coding can be used for pollution identification and environmental monitoring. This is due to the high precision and sensitivity with which DNA can be used to identify particular environmental toxins and pathogens.
- DNA computing is extremely energy-efficient, making it a desirable choice for uses where energy usage is a worry. It also can provide affordable, environmentally friendly working options.

Overall, DNA computing has enormous promise and has a special set of benefits over conventional computing techniques. DNA computing has the potential to revolutionize a variety of sectors and find solutions to some of the most difficult issues of our time with ongoing study and development.

C. Future Challenges and Opportunities

DNA computing will eventually encounter several difficulties and possibilities, just like any other new technology. The expensive expense of synthesizing and sequencing DNA, which can restrict its use in practical uses, is one of the major challenges. Additionally, it may be challenging for academics to work together and exchange information due to the absence of standard methods and tools for DNA computing.

The requirement to create more dependable and effective techniques for DNA production presents another difficulty. The polymerase chain reaction (PCR), one of the contemporary techniques for DNA synthesis, has constraints in terms of precision and scalability and has the potential to incorporate errors into DNA sequences.

Despite these difficulties, DNA computing has a wide range of possible uses, from bioinformatics and encryption to drug discovery and molecular automation. In the future, DNA computing may revolutionize industries like biotechnology and personalized medicine by enabling more specialized and tailored illness therapies. [16]

Additionally, DNA computing has the potential to be combined with other technologies, such as machine learning and artificial intelligence, to produce even more effective and sophisticated systems. For instance, DNA computing could be combined with machine learning techniques to create more precise predictive models for the detection and management of diseases.

Overall, there are many possibilities and obstacles in the future of DNA computing. It can revolutionize many fields and have a major effect on society with ongoing study and development and collaboration between scientists and researchers from various disciplines.

VII. CONCLUSIONS

A. Summary of the Importance and Potential of DNA Computing

In conclusion, DNA computing is a rapidly developing field that, by utilizing the ability of biological molecules to carry out sophisticated computations, has the potential to revolutionize computing. Its significance stems from its capacity to carry out massively parallel calculations and resolve intricate issues that are challenging or unattainable to resolve using conventional computing techniques. The promise of DNA computing is enormous, with uses in everything from molecular robotics and optimization to bioinformatics and encryption.

The creation of new algorithms, methods, and models that enable faster and more accurate computations has enabled advancements in DNA computing. DNA computing has gained new opportunities thanks to the ability to precisely create and modify DNA sequences.

The possible advantages of this technology are substantial, despite the difficulties that must be surmounted in the development of DNA computing, such as the expense and duration of DNA synthesis and the requirement for specialized laboratory tools. The possible uses of DNA computing are anticipated to grow as this field of study advances, making it an interesting field of study for both computer scientists and biologists.

B. Results and Outcome of DNA Computing

Clear objectives and anticipated results are crucial while undertaking research in the field of DNA computing. However, in other circumstances, especially in exploratory or speculative research, it may not be practical or acceptable to suggest precise conclusions or outcomes.

In the early phases of a new subject or technology, exploratory research is frequently carried out with the goal of developing fresh concepts and investigating prospective applications. In these circumstances, the research might not have a clear hypothesis or research topic, and the results can be random or unknowable. On the other hand, exploratory research looks at concepts or hypotheses that might not have enough empirical data to back them up.

In either situation, the absence of anticipated consequences or findings does not automatically imply that the study is not worthwhile or significant. Instead, it could encourage more creative investigation with a wider range of possibilities, which could result in unforeseen findings or breakthroughs. Additionally, speculative and exploratory research can act as a springboard for more targeted and concentrated study, where projected aims and results can be more precisely specified.

Even in exploratory or speculative research, a defined study plan and technique should still be in place. By doing this, you can make sure that the study is methodical, exacting, and founded on scientific standards. Additionally, to encourage cooperation and expand on the findings, the study should be thoroughly recorded and distributed to others in the area.

Here are some obvious results.

- DNA computing holds the promise of huge parallelism and biocompatibility, which could lead to advancements in sectors like drug development, materials research, and encryption.
- Anticipating the construction of more complex models and applications as DNA computing research develops, which could ultimately result in the development of whole new computer paradigms.
- Although DNA computing is still in its infancy, it has already shown that it has the potential to be an effective tool for dealing with practical issues. Anticipating more complex and varied uses of DNA computing as research in this area advances.
- The development of molecular machines and DNA-based nanorobots may make it possible to build intricate nanoscale systems for a variety of uses, such as targeted medicine delivery and environmental monitoring.
- The potential of DNA computing ultimately resides in its capacity to push the boundaries of computing and open up fresh opportunities for research and technological advancement. [18]

In conclusion, DNA computing is a fascinating and quickly developing field of study that has the potential to revolutionize how biology, computer, and technology are viewed. DNA computing has the potential to revolutionize a variety of sectors and spur new developments in science and engineering with ongoing investment and research.

REFERENCES

[1] Adleman, L. M. (1994). Molecular computation of solutions to combinatorial problems. Science, 266(5187), 1021-1024.

[2] Qian, L., Winfree, E., & Bruck, J. (2011). Neural network computation with DNA strand displacement cascades. Nature, 475(7356), 368-372.

[3] Seelig, G., Soloveichik, D., Zhang, D. Y., & Winfree, E. (2006). Enzyme-free nucleic acid logic circuits. Science, 314(5805), 1585-1588.

[4] Stojanovic, M. N., & Stefanovic, D. (2003). A deoxyribose-based molecular automaton. Nature Biotechnology, 21(9), 1069-1074.

[5] Zhang, D. Y., & Seelig, G. (2011). Dynamic DNA nanotechnology using strand-displacement reactions. Nature Chemistry, 3(2), 103-113.

[6] Zadeh, J. N., Steenberg, C. D., Bois, J. S., Wolfe, B. R., Pierce, M. B., Khan, A. R., ... & Winfree, E. (2011). NUPACK: analysis and design of nucleic acid systems. Journal of computational chemistry, 32(1), 170-173.

[7] D. Reinsel, J. Gantz and J. Rydning, Data Age 2025, IDC white paper, April 2017.

[8] An introduction to DNA data storage, white paper, 2021.

[9] A. Fernandez, From DNA Synthesis on Chips to DNA Data Storage SDC 2021, September 2021.

[10] J. Eid et al., "Real-Time DNA Sequencing from Single Polymerase Molecules", *Science*, vol. 323, pp. 133-138, 5910.

[11] S. Brooking, "Putting DNA Synthesis in the Hands of every researcher", *Innovation in Pharmaceutical Technology*, Nov. 2020.

[12] N. C. Seeman, "DNA in a material world", *Nature*, vol. 421, pp. 427-431, Jan. 2003.

[13] L. M. Adleman, "Computing with DNA", *Sci. Amer.*, vol. 279, no. 2, pp. 54-61, 1998.

[14] Zhang, D. Y., &Turberfield, A. J. (2017). DNA computing goes deep. Nature Nanotechnology, 12(8), 737-739.

[15] Qian, L., & Winfree, E. (2015). Scaling up digital circuit computation with DNA strand displacement cascades. Science, 332(6034), 1196-1201.

[16] Zhang, D. Y., & Chiu, D. T. (2012). Using DNA to build nanostructures for synthetic biology: linking topology to function. Current Opinion in Biotechnology, 23(4), 547-553.

[17] Kim, J., & Winfree, E. (2011). Synthetic in vitro transcriptional oscillators. Molecular Systems Biology, 7(1), 465.

[18] Li, S., Jiang, S., & Song, Y. S. (2018). DNA computing: emerging trends and diverse applications. Chemical Reviews, 118(13), 6056-6109.

[19] Raphael Kim, Larissa Pschetz, Conor Linehan, Chang Hee Lee, Stefan Poslad,June 2021, ‘Archives in DNA: Workshop Exploring Implications of an Emerging Bio-Digital Technology through Design Fiction

E-ISSN 2581 – 7957
P-ISSN 2277 – 3916

CVR Journal of Science and Technology, Volume 24, June 2023
DOI: 10.32377/cvrjst2404

Design and ASIC Implementation of Modified Shift-and-Add Algorithm using Redundant Arithmetic Integrator Adder and Subtractor

T. Subha Sri Lakshmi
Asst. Professor, CVR College of Engineering/ECE Department, Hyderabad, India
Email: rupashubha@gmail.com

Abstract: **Shift and Add Algorithm, also referred to as Volder's algorithm and the digit-by-digit technique. This is a specialized digital computer designed for airborne real-time processing. To calculate the trigonometric relationships involved in a plane coordinate rotation and conversion from rectangular to polar coordinates, a specific computational technique is used in this case. Additionally, the shift and add algorithm apply to modern systems, square roots, logarithms, and exponential expressions. Trigonometric functions are highly important in computation units; currently, many mathematical functions Sine, Cosine, Tangent, etc., by applying this approach, it is very simple to compute. Redundant arithmetic is used to lower the delay and boost the speed of operation. The adders play a significant part in the shift and add algorithm and carry propagation in adders causes the delay to increase quickly and slow down the speed of operation. Carry-propagation chains are produced by conservative operations like addition, multiplication, and subtraction. To rectify this issue, redundant number schemes are used. Using redundant numbers by speeding up mathematical operations. This technique is applied in signal processing and other areas. In this paper, an efficient and modified shift-and-add algorithm is designed, which is used to minimize the rotation angles. The main idea of the algorithm is to replace the carry select adder with an Integrated Redundant Arithmetic adder and subtractor, to achieve better latency and maximum throughput. By using redundant adders, the algorithm can be implemented with high speed and low power.**

Index Terms: **Shift and Add algorithm, Carry Select Adder (CSLA), Redundant Arithmetic Adder (RAA), rotation angles, Cadence-Innovus.**

I. INTRODUCTION

A common shift and add approach is used to compute a variety of arithmetic, logarithmic, trigonometric, and hyperbolic functions [1, 2]. The Shift and Add technique, which lowers complex multiplication and significantly reduces overall hardware complexity, is very straightforward and iterative. It is now a common option when a designer seeks to balance hardware requirements with latency. As a result, it was used in a wide range of industries including communications, multimedia, robotics, and the internet of things [3].

When compared to the traditional shift and add method, several variants have been suggested in the literature for an efficient shift and add implementation with the fewest repetitions. The reverse angle recoding is employed to get rid of the redundant shift and add elementary rotation [4]. The shift and add algorithm determine the number of iterations to do and compute the necessary angle using the fewest possible iterations. A redesigned shift and add architecture were presented that uses a new set of angles to split the rotational angles into smaller angles and calls for the least number of adders possible [5]. New, better designs were also suggested [6], replacing the regular adders in the architecture with area-efficient carry-select adders. With the enhanced power control and the hardware reduction approaches, a low-power and high-speed shift and add (LH-SAA) design is presented to produce a high-speed or the architecture of low latency VLSI for the shift and add algorithm [7].

In order to reduce the number of iterations and power consumption, hardware reduction techniques are proposed in this study along with an enhanced shift and add design that makes use of an integrated adder subtractor. The primary goal of the shift and add algorithm being suggested is to achieve low latency and high-speed VLSI design. The Hcub algorithm and the Canonical Signed-Digit (CSD) approach are used to reduce the number of shifters and adders/subtractors. These strategies are employed to carry out complicated processes. CSD implements the extension circuit's non-zero combination operations. Instead of being restricted by a constant bit, it creates a multiplier block out of the group of constants. The main contribution of the paper is an enhanced shift and add design that makes use of the built-in adder and subtractor.

II. RELATED WORK

The revised shift and add algorithm, which replaces the shifts and adds micro-rotation by a new angle set, was introduced by Garrido et. al. [5]. Three new sorts of rotators are used in their novel strategy: friend angles, USR Shift & add, and nano-rotations. The proposed shift and add algorithm use the fewest adders among shift and add algorithms too far owing to the proposed micro-rotations.

Even though the new design has additional advantages, demonstrated in earlier research [6, 7] that it may still be improved architecturally by employing cutting-edge methods. Making the entire design power efficient with the architecture of the friend angles (5 Adder, 7 MUX, and 9) was the focus of the work's primary sections.

A shift and add with low power and high speed (LH-shift and add) is designed. A proposed design [7] for enhanced power control and hardware optimization methods is implemented using the Canonical Signed digit.

Received on 10-10-2022, Revised on 11-12-2022, Accepted on 02-03-2023.

The (CSD) approach and the Hcub algorithm are utilized to calculate the size of the shifter. The Advanced Boolean Logic (ABL) technique used in the design of the adders blends the two binary adders into one, allowing for component sharing, especially during the preprocessing and sum computation phases. These three methods are utilized to restructure the complete shift and incorporate logic stages which [5], results in low power consumption and increased throughput.

The primary concept behind this suggested approach is that redundant arithmetic adders can be employed in place of a traditional CSLA adder. Due to no carry propagation chains; this adder may perform quick arithmetic operations in a variety of data processing approaches. Due to the aforementioned feature, this adder is mostly utilized for minimizing area and power dissipation. The carry propagation delay can be reduced by manipulating CSLA in various computational structures, but it cannot be eliminated entirely [13]. Compared to standard binary representation, a redundant binary representation is effective for accelerating arithmetic operations even on FPGA/ASIC. Redundant binary representation accelerates addition, subtraction, and multiplication. The price for the speed is frequently reasonable when you realize how crucial timing is when creating digital filters.

III. PROPOSED ALGORITHM

The shift-and-add algorithm is designed in hardware using the proposed method, which uses an integrated adder and subtractor to simplify the hardware implementation. Because it combines numerous adders/subtractors into a small one, the integrated adder/subtractor uses minimum adder, and subtractor for the computation of addition, subtraction, carry, and borrow. To calculate the nano-rotations, it makes use of some of the resources from the shift-and-add method and goes through multiple rotational steps. Each level in this series differentiates itself from the others based on the input angle for the shift-and-add nano-rotations. Instead, then using traditional logic gates, the proposed solution employs redundant arithmetic gates to produce the correct performance of addition and subtraction operations.

A. Integrator Adder and Subtractor

Using a shift-and-add algorithm, you can simplify long-term arithmetic operations by integrating the adder and subtractor. If more than two bits are added or subtracted, the binary full adder/subtractor will fail to work [8]. It can handle only one bit per input with output carry and borrow. A different kind of computer arithmetic that is appropriate for applications with a lot of numbers is provided by Redundant Number Systems (RNS). The ability of RNS is to catch or prohibit carry propagation [9], which results in parallel adders with constant delay regardless of the operand word length, is a key feature. As a result, RNS format results are produced with reduced latency. It uses 1.4 times less power and memory while reducing the number of adders and subtractors that are utilized in the shift-and-add architecture.

In numerically demanding applications, the usage of redundant number systems can greatly enhance computational performance. However, because each symbol requires numerous bits, the architecture of their arithmetic circuits is typically expensive [9]. The redundant arithmetic integrator has two types of circuits i.e., Redundant Arithmetic - Plus Plus Minus (RA-PPM) adder, and Redundant Arithmetic - Minus Minus Plus (RA-MMP) Subtractor. An integrated adder/subtractor consists of two RA-PPM and two RA-MMP gates with redundant arithmetic logic architecture as shown in Fig. 1.

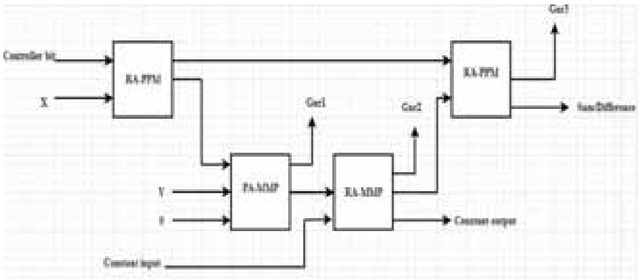

Figure 1. Redundant Arithmetic Integrator Adder & Subtractor

Three inputs—X, Y, and a constant input—are used, and the output is the sum or difference. When the control bit is set to zero, the circuit performs an addition operation. If the value is set to one, the circuit performs a subtraction operation. In this circuit, there is only one garbage input, which is represented by the logical zero. Gar1 through Gar3 refers to the three garbage outputs [10]. The third and the fourth inputs to the RA-MMP gate are the output from RA-PPM gates, constant inputs, and B value. Two split equivalent outputs are managed by A, the second input to the RA-PPM gate.

The selection input represents the constant input which is taken into consideration for addition and subtraction. The input indicates whether the operand is a 2'complement and whether it follows a critical path. Utilizing this shift-and-add architecture's combined adder and subtractor the complexity of addition and subtraction has been lowered, and the need for adders and subtractors was also decreased. In this study, the shift-and-add architecture [11, 12] is a simplified, fully integrated adder/subtractor, which increased architecture performance and reduced power consumption.

B. Improved Shift-and-Add Architecture

The improved shift-and-add algorithm's rotation stages are organized as shown in Fig.2 below, and Table 1 provides detailed information on each stage. The shift-and-add Rotator rotates the input vector by any necessary angle to produce a new vector with the x-axis. The result of the vectoring procedures and the original vectors' scaled magnitude is the rotation angle. When six stages of architecture is taken into consideration it may not be suitable for all kinds of applications because of slight latency increases which may not be majorly suitable for battery-operated devices. The six stages are Trival rotations, friend angle rotation, USR Cordic, traditional Cordic (2 stages), and Nano rotator. The Trivial Rotation stage measures the trivial rotations by ±180 and ±90 in the range of ±45 to set the remaining angle apart from this any other angle set cannot be assigned. The friend angle rotation stage will rotate the entire kernel with a reduced input angle set. In the USR Cordic stage, the angle value will be further reduced by changing the shifter and reducing the number of iterations. A comparison of two angle sets which are coming from the friend angle and USR rotor will be compared and finally, that will be given to the nano rotation stage. The output of this stage will have a very minute angle value. The CORDIC algorithm, where it is bigger than out of the preceding stage for every stage, provides the convergence of circumference. Finally, the presentation of the angle in the range of [0, 1]. By eliminating the 4th and 5th stages angle minimization is happening but latency is slightly increasing due to its traditional architectural structure of Cordic which is designed using carry save adders and no. of iterations. When iterations are going on increasing the area of architecture is slightly increasing due to an increase in adders and shifters. The main goal of architecture is to minimize the angle and to get in range of [0, 1] so the 4th and the 5th stages are eliminated and slightly modify the architecture of the nano-rotor with different shifter sizes, and a few multiplexers are added.

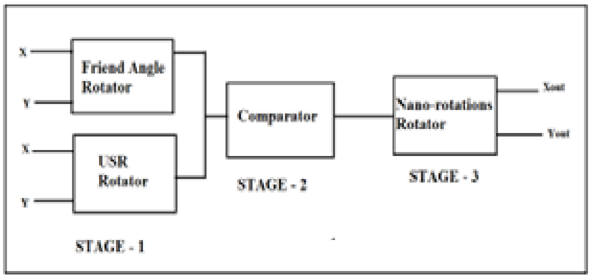

Figure 2. The architecture of the Improved Shift-and-Add Algorithm

TABLE I.
ROTATION STAGES AND THEIR DESCRIPTION

Stage Index	Input Angle	Output Angle
1	±180°	±46°
2	±48.105	±11.305
3	±11.67	±4.635
4	±4.56	±2.79
5	±2.79	±0.986

At each rotation of the angle, the function of the vectoring uses the least significant components of the residual vector. The sign of the residual component determines the next rotational direction of the rotator. The angle accumulator is first initialized to zero, and the traversed angle specifies the end of each repetition.

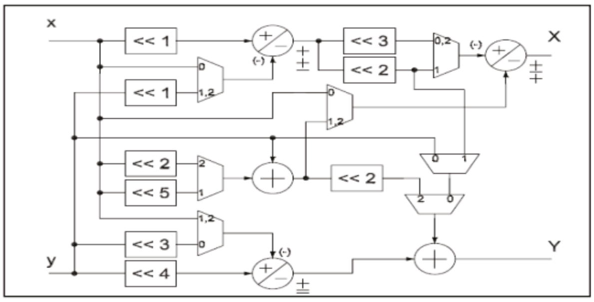

Figure 3. Architecture of Friend Angle Rotator

The canonical signed digit, which subdivides the original angle into several smaller angles, is used to extract the rotational quantization process of the angle. These sub-angles reduced the angle quantization error and are roughly closer than that of the original rotational angle. In the initial phase, friend angle and USR [11] are used. The hardware architecture is presented in Fig. 3. It has seven 2:1 multiplexers and five adders. Depending on how the multiplexers are set up, it can calculate all the kernel rotations. The kernel is also defined by the user. The Rotator architecture of the USR is depicted in Fig. 4. The only way to implement this architecture is by using two adders and two 2:1 multiplexers.

The friend angle and USR inputs in STAGE-1 are both presented in rectangular form. The outputs of the Friend angle rotator and USR rotator are compared using two 16-bit comparators as shown in Fig. 5 in STAGE-2. Separate comparisons are made between the Friend angle rotator's output x out and y out and the USR.

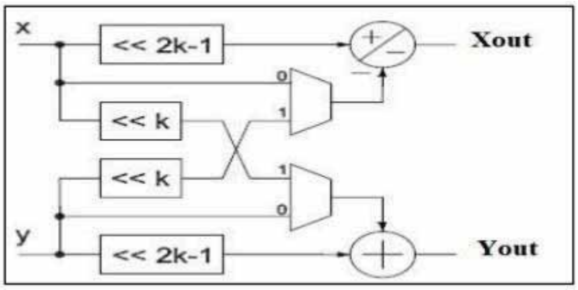

Figure 4. The architecture of the USR Rotator

The friend angle and USR inputs in STAGE-1 are both presented in rectangular form. The outputs of the Friend angle rotator and USR rotator are compared using two 16-bit comparators as shown in Fig. 5 in STAGE-2. Separate comparisons are made between the Friend angle rotator's output x out and y out and the USR.

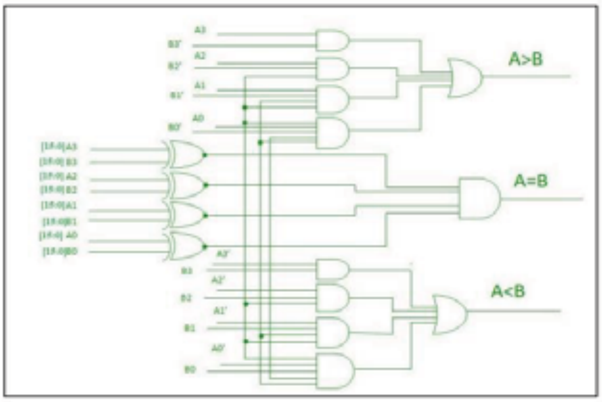

Figure 5. Design Structure of 16-bit Comparator

This level employs a rotator with nano-rotations as shown in Fig. 6. First, β_M must be chosen to construct the rotator taking into account the range of input angles.

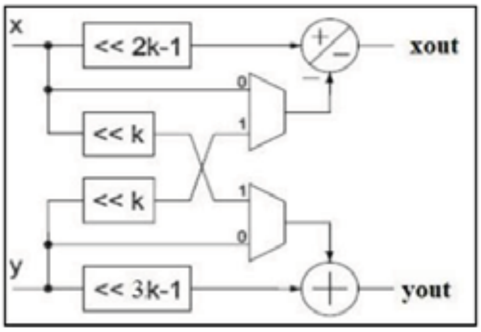

Figure 6. Architecture of Nano-Rotations

The output of the comparator is used as input to the Nano rotator. Depending on the situation, the user can select either the value A>B or AB. The user can use AB if he only wants a very small angle. The output is also reliant on the 2:1 multiplexer's selection line.

IV. EXPERIMENTAL RESULTS & DISCUSSION

The Carry Select Adder (CSLA), which mandates that the carrying extend from the LSB to the MSB, is the foundation of the improved Shift-and-Add architecture. As a result, as word length rises, so do the flaws in the breakdown process and the execution of the sub functions [12]. Because of this, there are various critical routes for various stages, which cause distinct clock cycles. The core's general working frequency is therefore determined by the system's slowest arrangement, which is a factor. The proposed redundant arithmetic adder (RA-PPM) is significantly less complicated, requiring only bit-by-bit XOR, NAND, and INV as shown in Fig. 7, as well as synchronous activities to make the limitation in the disintegration of a level planning reaction and primarily reducing long carry prorogation chains.

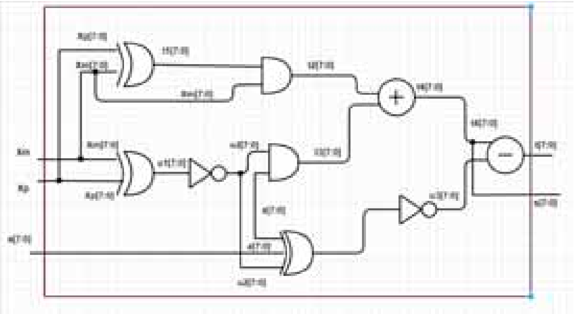

Figure 7. RTL Schematic of RA-PPM adder

The CSLA logic is created with the use of parallel carry chains. The suggested RA-PPM adder structure [12] and traditional structures, such as the CSLA [12], are compared in terms of various area execution parameters, including the number of cells, I/O ports, and nets in addition to a logic latency (ns), path latency (ns), and highest combinational delay (ns) shown in Fig. 8. In Fig. 9, the power usage of two designs is displayed. Compared to the CSLA structure, the suggested RA-PPM structure dissipates less power (Fig. 9). A superfluous mathematical idea diminished the strength of the suggested method. In addition, the suggested Shift-and-Add use little hardware, leading to increased on-chip control dispersion. It is obvious that the planned Shift-and-Add is practical to enforce when it comes to the planning reaction of the suggested Shift-and-Add structure.

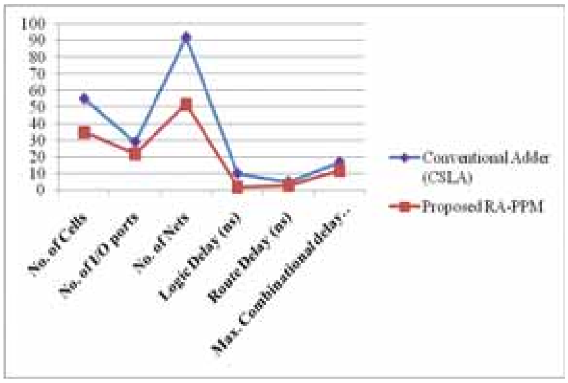

Figure 8. Comparison of CSLA and RA-PPM in terms of area

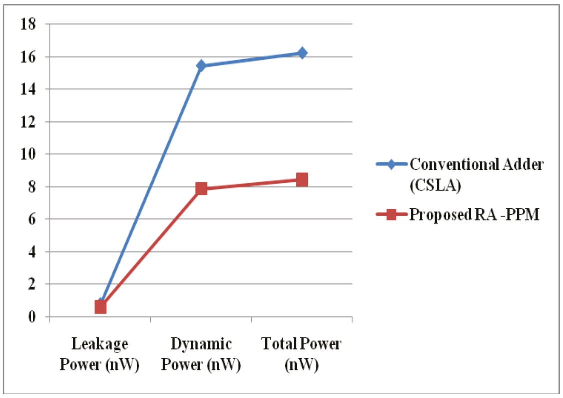

Figure 9. Comparison of CSLA and RA-PPM in terms of power

RTL schematic of the RA-MMP subtractor is shown in Fig. 10.

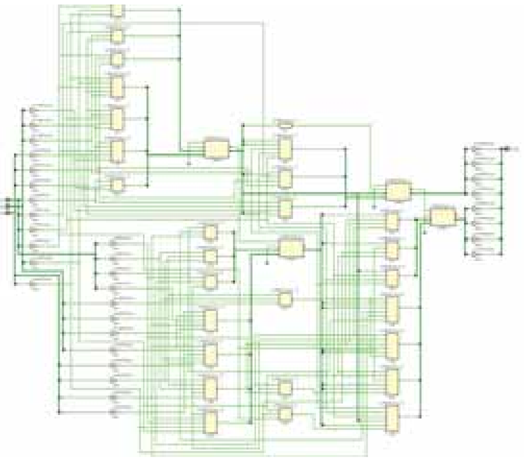

Figure 10. RTL Schematic of RA-MMP subtractor

The rectangular shape of the input angle is taken. Specifically, x+ iy = 25+ i500 = 85.120 (angle). In stage 1, the input is provided to the buddy angle rotator and USR. The 2:1 MUX selection line of the rotators control output of stage 1. Then, in stage 2, the comparator compares the outputs of the two rotators, and the lowest value of x + iy is taken into account. The nano-rotation rotator receives the lowest value in stage 3.

CASE 1:
INPUT: x+ iy = 25+ i500 = 85.12° (angle)
Selection lines of 2:1 MUX of all rotators = s = 1
OUTPUT: Stage -1: Friend angle: 625+ i10425
USR CORDIC: 3175+ i64500
Stage-2: compare 625, 3175 and 10425, 64500.
Stage-3: lowest value of comparator is input to nano-rotator.
x+ iy = 625+ i10425
Finally, the output of the nano-rotation rotator is.
x+ iy = 49551 + i3257 = 3.76° (angle)

CASE 2:
INPUT: x+ iy = 25+ i500 = 85.12° (angle)
Selection lines of 2:1 MUX of all rotators = s = 0
OUTPUT: Stage -1: Friend angle: 5500+ i16200
USR CORDIC: 60736+ i64400
Stage-2: compare 5500, 60736, and 16200, 64400.
Stage-3: lowest value obtained by the comparator is the input to the nano-rotation rotator
x+ iy = 5500+ i16200
Finally, the output of the nano-rotation rotator is.

x+ iy = 19456 + i57344 = 71° (angle). The RTL schematic of redundant integrator adder and subtractor-based improved shift-and-add architecture is shown in Fig. 11.

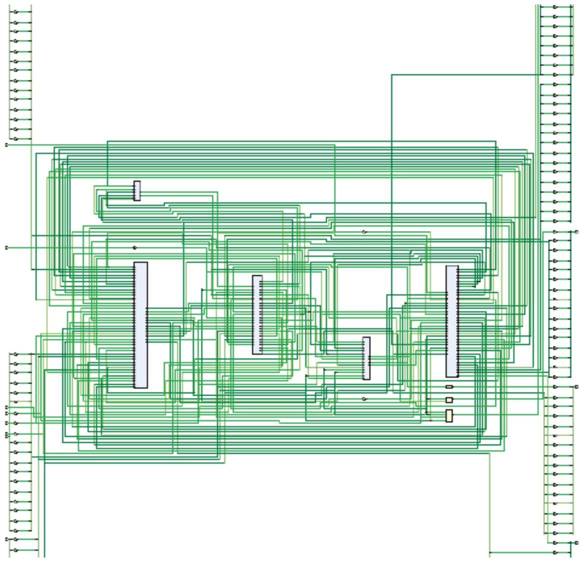

Figure 11. RTL Schematic of Improved Shift-and-Add architecture.

As it is designed using the suggested RA-PPM adder, it delivers lower hardware utilization and power consumption when compared to typical architectures. The input signal "Clk," along with all other input signals, is rotated at a 45-degree angle as one example. Sine values are discrete, while cosine values are discrete. The addresses are kept in predetermined Shift-and-Add algorithm slant values. Shift-and-Add architecture with the suggested adder is laid out in Fig. 12.

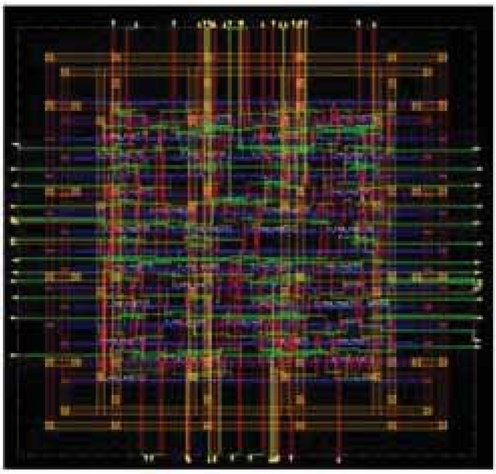

Figure 12. Physical Layout of Improved Shift-and-Add architecture.

Digital signal processing techniques typically call for a lot of multiplications. Consider a FIR filter with 32 taps as a basic example. A single sample of the filter output requires 16 multiplications, which becomes easy when it uses symmetry in the filter coefficients. These multiplications may take a while, depending on the number of bits used to represent the input samples and the filter coefficients. Over the years, there has been a lot of interest in the design of hardware-efficient multipliers, and adders, and substantial research has produced several solutions. The fundamental ideas of canonical signed digit (CSD) representation are reviewed in this article. When multiplying an input signal by a constant multiplicand, such as when designing an FIR filter where we have some fixed coefficients, CSD is an intriguing method for creating efficient multipliers. The arithmetic procedure known as Multiple Constant Multiplications (MCM) multiplies a group of fixed-point constants by the same fixed-point variable X. Costly multipliers must be avoided for MCM to be applied effectively. Hardware substitutions that solely do adds, subtraction, and shifts are required to be multiplier-less. As a result, the process of determining the least amount of addition/subtraction operations is how the MCM problem is described. It is hypothesized that MCM's computational complexity is NP-hard. Table II bounds have been precisely determined by the average, added cost, and adder depth additions for various algorithms. Compared to all algorithms CSD looks better for both serial and parallel adder design depths.

TABLE II.
COMPARISON OF VARIOUS ALGORITHMS IN TERMS OF ADDER COST

Algorithm	Adder-Cost	Serial-Adder Depth		Parallel-Adder Depth	
		Max.	Avg.	Max.	Avg.
CSD	12	10	8.33	4	4.00
HCUB	13	11	7.33		
MCM	19	8	6.33	4	4.00

V. CONCLUSIONS

In this study, a hardware reduction technique-enhanced shift-and-add design with an integrated adder and subtractor using a redundant arithmetic concept is proposed. An integrated adder/subtractor, or CSD approach, reduces the number of adders, subtractors, and shifters and by using RA-PPM adders and RA-MMP subtractors the latency is reduced, and throughput increases due to no carry propagation chain. ASIC-Cadence tools are used to implement the proposed and enhanced shift-and-add architecture. When compared to the existing methodologies, the performance of the suggested method performs better in terms of area, power consumption, and frequency. All the designs are designed using Verilog HDL, simulated using the NCHDL simulator, and synthesized using the genus synthesis tool, and finally, physical design is performed using the Cadence Innovus tool to generate a graphic data stream II file. When compared to the shift-and-add algorithm's conventional way, the simulation results reveal that the proposed method uses 12.11% less power, operates at a higher frequency of 33.3%, and occupies 14% less space.

REFERENCES

[1] J. E. Volder, “The CORDIC trigonometric computing technique,” IRE Transactions on Electronic Computers, vol. 8, no. 3, pp. 330–334, 1959.

[2] J. S. Walther, “A unified algorithm for elementary functions,” in Proceedings of the AFIPS Spring Joint Computer Conference, pp. 379–385, May 1971.

[3] P. K. Meher, J. Valls, T. Juang, K. Sridharan, and K. Maharatna, "50 Years of CORDIC: Algorithms, Architectures, and Applications," in IEEE Transactions on Circuits and Systems I: Regular Papers, vol. 56, no. 9, pp. 1893-1907, Sept. 2009.

[4] Parfieniuk, Marek, and Sang Yoon Park. "Sparse-iteration 4D CORDIC algorithms for multiplying quaternions." IEEE Transactions on Computers 65.9 (2015): 2859-2871.

[5] Mario Garrido, Petter Källström, Martin Kumm, and Oscar Gustafsson, “CORDIC II: A New Improved CORDIC Algorithm”, IEEE Transactions on Circuits and Systems—II: Express Briefs, vol. 63, no. 2, February 2016.

[6] Sharath Chandra Inguva, Dr. J. B. Seventline, “Implementation of Area Efficient CORDIC for QPSK Modulation”, Journal of Engineering Science and Technological Review, Volume 11, Issue 2, Pg:96- 102,2018.

[7] Sharath Chandra Inguva, Dr. Joseph Beatrice Seventiline. "LHCORDIC: Low Power FPGA Based Implementation of CORDIC Architecture", International Journal of Intelligent Engineering and Systems, Vol.12, No.2, 2019.

[8] Madhavi, Hossein, and Somayeh Timarchi. "Area-Time-Power Efficient FFT Architectures Based on Binary-Signed-Digit CORDIC." IEEE Transactions on Circuits and Systems I: Regular Papers (2019).

[9] Kamp W., Smith A. B., Hayes M.,‖ Efficient Implementation of Fast Redundant Number Adders for Long Word-lengths in FPGAs,‖ International Conference on Field-Programmable Technology, 2009.

[10] Nupur Jain, Biswajit Mishra, and Peter Wilson, "A Low gate count Reconfigurable architecture for biomedical signal processing applications", SN Applied Sciences (A Springer Nature Journal), 3:439, 2021.

[11] Adam Wilson J, Gerwin Schalk, and Justin Williams, "A Procedure for Measuring Latencies in Brain-Computer Interfaces, IEEE Transactions on Biomedical Engineering", 57(7), pp: 1785 - 1797, 2010.

[12] Subha Sri Lakshmi. Thiruveedhi, P. Radhika Yedukondalu Kamatham," Performance Analysis of Shift-And-Add Architecture Using RBA Adder for Low Latency Biomedical Signal Processing Applications ", 2nd International Conference on Intelligent Technologies (2nd CONIT 2022) Technical Co-sponsored by IEEE Bangalore Section, K. L. E Institute of Technology, Hubballi, Karnataka, India, 24th – 26th June 2022.

[13] Mr. Sharath Chandra Inguva, Dr. J. B. Seventline, “Enhanced CORDIC Algorithm using an Area Efficient Carry Select Adder”, International Conference on Intelligent Sustainable Systems (ICISS 2017), 978-1-5386-1959-9/17/$31.00, 2017 IEEE.

E-ISSN 2581 – 7957
P-ISSN 2277 – 3916

CVR Journal of Science and Technology, Volume 24, June 2023
DOI: 10.32377/cvrjst2405

Family Health Monitoring System using Python for Biomedical Applications

Anjali Chindham[1], Sabavath Virisha[2], Rakesh Donthagani[3], Racha Ganesh[4] and K. Lal Kishore[5]
[1] UG Student, CVR College of Engineering/ECE Department, Hyderabad, India.
Email: anjalichindam153@gmail.com[1]
[2] UG Student, CVR College of Engineering/ECE Department, Hyderabad, India.
Email: sabavathvirisha@gmail.com[2]
[3] UG Student, CVR College of Engineering/ECE Department, Hyderabad, India.
Email: rakesh45roshan@gmail.com[3]
[4]Assoc. Professor, CVR College of Engineering/ECE Department, Hyderabad, India.
Email: rachaganesh@gmail.com[4]
[5]Professor, CVR College of Engineering/ECE Department, Hyderabad, India.
Email: lalkishore@cvr.ac.in[5]

Abstract: **In the present world nothing is more important than one's health. Good health is necessary for human satisfaction and well-being, and it contributes significantly to prosperity, wealth, and even economic growth. Hence, there is a huge necessity for healthy populations in the present real-time world for a better society and a longer human life cycle. Now a days people are becoming vulnerable due to climate changes, industrialization, and lack of physical activities. Everyone needs to monitor their health conditions regularly and take precautionary measures before it is too late. This precautionary measurement results in lower morbidity and longer life span of human beings. There are four basic and important parameters for every individual, that are checked to evaluate certain aspects of human health i.e., Body temperature, Pulse rate, Respiratory Rate, and Blood Pressure. All these human health parameters are collected from the various sensors and these sensors' information is given to a health monitoring system that is designed using Python. These health parameters are analyzed for different age groups of human beings for their health monitoring conditions for a better life. The age groups are considered as infant, adolescent. Middle age, and old age based on the age group. This designed system also gives the health condition parameters range and health status in terms of abnormality. Using these output values, proper suggestions, precautions, physical activities, and medications will be suggested in the form of health reports. With all these output parameters the health conditions of present human beings will be properly monitored for better survival.**

Index Terms: **Health System, Body Temperature, Blood Pressure Pulse Rate, Respiratory Rate, Python.**

I. INTRODUCTION

The current state of the healthcare system is disintegrated due to poor patient-doctor communication. Therefore, information technology using software languages becomes necessary to solve this issue. IoT-enabled medical equipment can significantly improve healthcare services. There is a big possibility of saving lives by implementing IoT concepts in healthcare [1]. In this study, a customized sensor is utilized to track the patient's breathing rate, bodily movement, body temperature, and heart rate. The Raspberry Pi is one of the most important IoT learning platforms. Due to its ability to provide a full Linux server on a tiny platform for a very low price, the Raspberry Pi is a popular platform. The general purpose I/O pins on the Raspberry Pi can be used to connect to services and actuators as well.

The integration of Raspberry Pi with IoT creates a cutting-edge medical solution [2,3]. Multi parameter displays, which can track and display different parameters simultaneously, are becoming more and more popular these days. Pulse oximetry, ECG, blood pressure, and temperature are among the parameters that are measured with a thermoelectric transducer [4]. The Internet of Things (IoT) is a network of actual physical things that use embedded technology to communicate, detect, or respond to internal conditions or environmental changes. "Things on the Internet of Things" refers to any form of object, whether it is a smart gadget with higher artificial intelligence that can communicate with other objects very effectively or a dumb object without any communication skills [5]. Previously, it was difficult for a doctor to keep a check on a patient in a remote location during an emergency. To allow the doctor to continuously access the data and to alert the career when the patient is in a severe condition, a system is developed which can continuously monitor the patient's status and automatically sends the data to a server [6]. In the past, only various devices for various metrics could be used to monitor the patient. Therefore, it is recommended to combine various equipment into a single module to monitor the patient's necessary circumstances [7]. Each sensor's data was recorded and uploaded to the server. The data was retrieved from numerous devices connected to the internet using secure login information [8]. It is a significant problem for the providers to effectively handle the massive amounts of information and data produced by these interconnected IoT devices [9]. Internet of Things Analytics (IoT) is a technology used to address this issue of storing and analyzing enormous amounts of data [10, 11].

The healthcare sector has experienced considerable expansion in recent years and has significantly increased both employment and revenue [12]. A few years ago, a physical examination in the hospital was required to diagnose diseases and other abnormalities in the human body [13, 14]. Most of the patients had to remain in the hospital for the duration of their therapy. This has increased healthcare costs and put pressure on healthcare facilities in rural and isolated areas [15].

Received on 31-03-2023, Revised on 09-05-2023, Accepted on 14-05-2023.

For a long time, traditional checkups in a specialist medical facility were the norm for determining blood sugar, blood pressure, and heart rate [16]. Today's patients may take their vital signs every day because of the wide range of sensors that are available to read vital signs, including blood pressure cuffs, glucose meters, heart rate monitors, and electrocardiograms [17,18].

In present world, the health related issues are the major reason for increasing human death rate. Due to the statistics of different surveys, every day around 1,51,600 people are losing their lives because of these health issues. Modernization and precaution measurements of health care system can reduce this people’s death rate per day. In the Conventional health care systems, the health care professions play a primary role for health monitoring of human beings. [19]. But, nowadays, there are a lot of old people who are living alone at home, and they may not have access to the hospitals for regular medical care. Hence, there is a requirement of health monitoring system which will help every human being in examining all health parameters. The FPGA is used to create this monitoring system, which will examine heart rate, temperature and processes the data at high speed [20].

The health monitoring system can be designed by adding different sensors to a human being to monitor different health parameters. These sensors data outputs are processed by using data aggregator, communication link and processing unit. A specialized gadget and/or personal computer may serve as the data aggregator and processing unit. [21].

The physiological parameters of human beings need to be monitored by the healthcare monitoring system are different for different age groups. For instance, the criteria for constant monitoring system of the pregnant woman consists of monitoring the status of Blood Pressure (BP), heart rate, and movements of the developing foetus etc. Similarly, it is a challenging task to monitor a patient's health if they have a chronic illness or physiological issue. The challenge is that the doctor must frequently visit the patient and evaluate their condition by examining the recorded physiological measures, such as body temperature and blood pressure etc. [22] Most of the health monitoring systems uses microcontrollers for their implementation, but in this design, FPGA is used because of the advantages in terms of reconfigurability, flexible functionality and adoption for advanced technologies. This FPGA based design is also used for better power efficiency, small operations at precise timings, real-time and improved performance applications. [23].

Health related issues are the major problem for human society in the entire world. Hence, there is a requirement of design in the technique and a system which allows a person to remotely measure the vital indicators at any time. This type of system will help the people who are constantly busy in their routine life and busy schedule. Due to this busy daily schedule of activities people are becoming physically and mentally susceptible. This results in time constraints for their families and to maintain the level of fitness needed for healthy survival. The fundamental tenet of healthcare is "appropriate care for the right person at the right time," which results in more acceptable outcomes, improvements in terms of healthcare dependency and cost-effective solutions.

The intense demand on urban healthcare administration has spurred technological development to produce the right solutions to the problems that are emerging. The challenge is that a patient must regularly visit the doctor to monitor their health status using the observed data, such as Body temperature, Pulse rate, Respiration rate and Blood pressure. Hence, the proposed health monitoring system is suggested by combining monitoring of different health parameters into a single module. The design of the proposed system is accomplished with the aid of Python-based real-time monitoring system for Bio-medical applications.

In this paper, section 2 covers the information and design methodology about the design of existing and proposed Health Monitoring systems. Section 3 covers the information about hardware and software components by using the flow chart and algorithms of Health Monitoring system. Section 4 covers the Result analysis. Section 5 shows the Conclusion followed by References.

II. DESIGN METHODOLOGY

There are different health monitoring systems to support Body Temperature, Pulse Rate, Respiratory Rate and Blood Pressure are available with certain advantages and limitations as discussed below.

The Body Temperature Monitoring System [24] essentially measures and senses body temperature. This generates a sound alarm system when a patient's temperature changes quickly and turns on an LED when a patient's temperature is expected to worsen soon. To measure the patient's actual body temperature, an LM35 temperature sensor must be inserted into the patient's body cavity. For further analysis, the data must be gathered and preserved. Any machine learning technique may forecast the temperature measurements for every half-hour or hour using this data. It is possible to establish upper and lower threshold limitations. As a result, two tasks will be completed simultaneously. This continuous monitoring will be helpful in analyzing the predicted and actual values with the threshold ranges. A positive signal will be given to alarms if there is any discrepancy.

The Heart Rate Monitoring system using IoT [25] project is made up of several parts, including LCD display, Wi-Fi module, receiver module, heartbeat sensor, and 5V Regulated Power Supply. The microcontroller serves as the project's central processing unit and keeps track of the patient's heart and pulse rates. The patient's temperature is calculated by a temperature sensor, and the patient's heart rate is monitored by a heart rate sensor. One can measure the heart rate with the help of the lights on the heart rate sensor module. The amount of blood in the capillaries is represented by the reflected light when the finger is placed on the pulse sensor.

The Respiratory Monitoring System for Asthma Patients based on IoT [26] uses Ethernet shield to display the respiration rate number in a web browser, clinicians can easily access the patient's information from anywhere in the hospital. The patient's health status can then be determined without the aid of medical personnel by applying data mining techniques. Early disease identification is made feasible by this system. Future data retrieval processes will take advantage of wireless technologies, cloud storage, and big data analytics.

The IoT blood pressure monitoring system [27], which is implemented by using both software and hardware. The system's block diagram represents and shows that Raspberry Pi can recognize data from the blood pressure device and send it over the internet. Because of this the users may view the monitoring results using Telegram and mail applications. These results are accessible for anyone who has the authority to access the data and information.

To overcome all the limitations of these existing systems, a new health monitoring system is designed with all the four health conditioning parameters and their age groups to support the entire family health care monitoring. This system also provides proper medication as a suggestion if abnormal cases exist. The suggested data is stored in the form of reports, so that people can be aware of their health status and can be in regular contact with their physical body for a proper healthy lifecycle. This system will monitor the health of various family members by taking four important measurements: body temperature, pulse rate, respiratory rate, and blood pressure. This approach evaluates each of these four variables based on their age. While there are some existing devices to monitor each of these four factors separately up to this point, this proposed method is using different standard values for different age groups. These values are taken from different sensors, and they are given as inputs to the health monitoring system. These inputs will be analyzed for the human body's typical ranges for each of their age groups using Python. Finally, a report with the measured values and the human body's standard values will be produced.

The block diagram of proposed health monitoring system is shown in Figure 1. The different health parameters like body temperature, pulse rate, respiratory rate and blood pressure of a human are collected from different sensors. Their values are given to the Python based Health monitoring system.

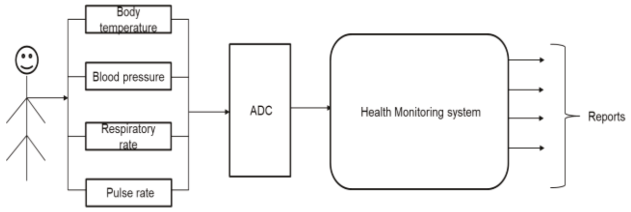

Figure 1. Block diagram of Health Monitoring System

The values of different age groups and corresponding health parameter values ranges are shown in Table 1.

The age of human being will be taken as first input, then based on this age value, there are four sub age groups. They are classified as child age (3-16), young age (17-25), middle age (26-45) and old age (>45) groups. Each age group has the corresponding standard for health parameters in terms of Body temperature, Pulse rate, Respiratory rate, and Blood pressure. The health conditioning and report generating will be done as per the selected age group based on flow chart and design algorithms.

TABLE I.
PARAMETER RANGES

Health parameters	Child Age (3 - 15 years)		Young Age (16 - 25 years)		Middle Age (25 - 45 years)		Old Age (> 45 years)	
Body Temperature	96.6 F - 98 F		95.3 F – 98.4 F		95.5 F – 98.2 F		96 F – 97.4 F	
Pulse Rate	75 – 120		60 – 100		90 – 140		75 – 136	
Respiratory Rate	20 – 30		16 – 25		12 – 20		16 - 25	
Blood Pressure	Systolic	Diastolic	Systolic	Diastolic	Systolic	Diastolic	Systolic	Diastolic
	97-112	56-76	112-128	66-80	122-124	74-77	95-145	70-90

Flow Chart and Algorithms of Health Monitoring System

The flow chart of the Family health monitoring system is shown in Figure 2.

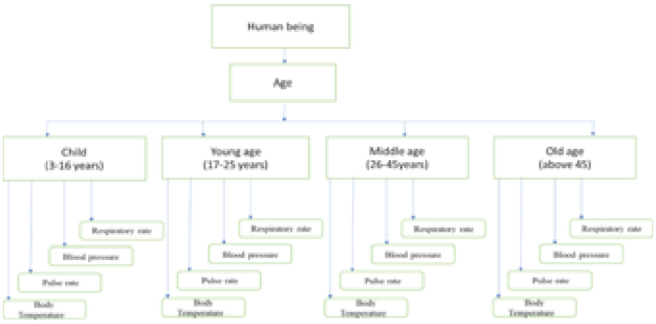

Figure 2. Flow chart of Family Health Monitoring System

This flowchart considers the human being age with the allotted age groups for child age (3-16), young age (17-25), middle age (26-45) and old age. All these age groups are deeply analyzed with health monitoring parameters for proper health condition status and report generation using their design algorithms.

III. DESIGN ALGORITHMS

The design algorithms for the proposed health monitoring system are specified for different age groups like Child age, young age, middle age, and old age groups are discussed below.

Algorithm for Child Age Group

Figure 3 describes the algorithm for the child age group. The four health parameters that are given as input will be analyzed with the moderate values of those respective health parameters as shown in table1. If the input parament values are in the range of the moderate health parameters, the system displays normal. If the parameter value is higher than the moderate range the system displays that respective parameter value of the human being is high and if the parameter value is lower than the moderate range the system displays that respective parameter value of the human being is low.

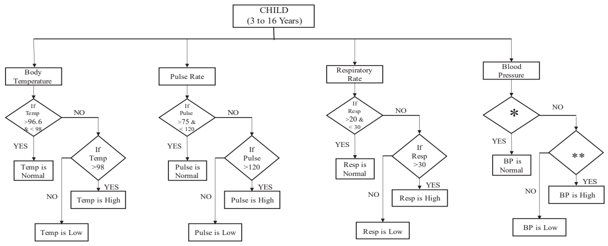

- * = If (SP >97 & <112) and (DP>56 & <76)
- ** =If (SP >112) OR (DP>76)

Figure 3. Algorithm for Child Age Group

Algorithm for Young Age Group

Figure 4 describes the algorithm for the young age group. The four health parameters that are given as input will be analyzed with the moderate values of those respective health parameters as shown in Table 1. If the input parament values are in the range of the moderate health parameters, the system displays normal. If the parameter value is higher than the moderate range the system displays that respective parameter value of the human being is high and if the parameter value is lower than the moderate range, then the system displays that respective parameter value of the human being is low.

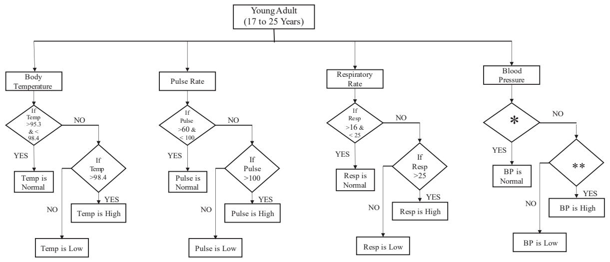

- * = If (SP >112 & <128) and (DP>66& <80)
- ** =If (SP >128) OR (DP>80)

Figure 4. Algorithm for Young Age Group

Algorithm for Middle Age Group

Figure 5 describes the algorithm for the middle age group. The four health parameters that are given as input will be analyzed with the moderate values of those respective health parameters as shown in Table 1. If the input parament values are in the range of the moderate health parameters, the system displays normal. If the parameter value is higher than the moderate range the system displays that respective parameter value of the human being is high and if the parameter value is lower than the moderate range the system displays that respective parameter value of the human being is low.

Algorithm for Old Age Group

Figure 6 describes the algorithm for the old age group. The four health parameters that are given as input will be analyzed with the moderate values of those respective health parameters as shown in Table 1. If the input parament values are in the range of the moderate health parameters, the system displays normal. If the parameter value is higher than the moderate range the system displays that respective parameter value of the human being is high and if the parameter value is lower than the moderate range the system displays that respective parameter value of the human being is low.

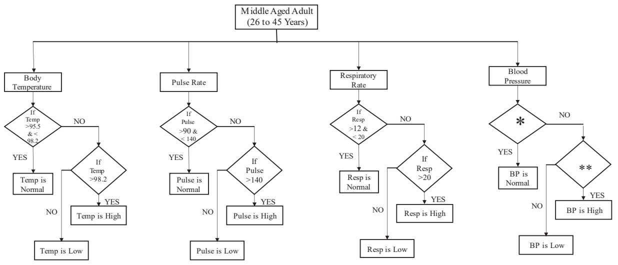

- * = If (SP >122 & <124) and (DP>74 & <77)
- ** =If (SP >124) OR (DP>77)

Figure 5. Algorithm for Middle Age Group

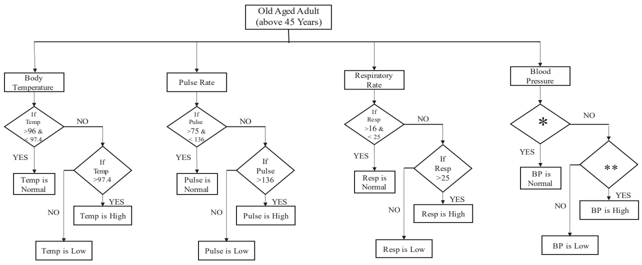

- * = If (SP >95 & <145) and (DP>70 & <90)
- ** =If (SP >145) OR (DP>90)

Figure 6. Algorithm for Old Age Group

IV. RESULT ANALYSIS

This section gives information about the results of the family health monitoring system. This system is designed by using Python with different age groups and different health monitoring parameters. This system is deeply analyzed by using their design algorithms and verified for proper health condition status.

Here is an example of a family containing four family members i.e., Ganesh, Rakesh, Virisha and Anjali. In the proposed system first, the system will ask for number of family members in a particular family, as in this case there were four family members, the system will take four as input. The different test cases and reports for four family members using the proposed health monitoring system are shown as different cases like case1, case2, case3 and case4 for child age, young age, middle age and old age are shown below.

Test Case 1: Health Monitoring of Child Age Group

Now the system asks for their name, age, temperature, bp systolic, bp diastolic, pulse rate and respiratory of the fourth family member i.e., Anjali. After that it analyses the given data based on the age of Anjali (15). As her body temperature is 96 which is less than moderate range for her age, the output is generated as "body temperature is low". As her pulse rate is 85 which is in moderate range for her age, the output is generated as "pulse rate is normal". As her respiratory rate is 33 which is more than moderate range for her age, the output is generated as "respiratory rate is high". As bp systolic and diastolic is 115 and 77 respectively which is greater moderate range for her age, the output is generated as "bp is high". and attached report 1 for her health status.

The generated report for child age group and health parameters of Anjali is shown in Figure 7.

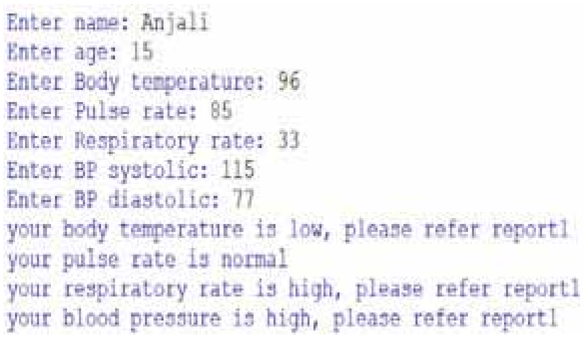

```
Enter name: Anjali
Enter age: 15
Enter Body temperature: 96
Enter Pulse rate: 85
Enter Respiratory rate: 33
Enter BP systolic: 115
Enter BP diastolic: 77
your body temperature is low, please refer report1
your pulse rate is normal
your respiratory rate is high, please refer report1
your blood pressure is high, please refer report1
```

Figure 7. Report of Family Health Monitoring System for child age group

Test Case 2: Health Monitoring of Young Age Group

Now the system asks for their name, age, temperature, bp systolic, bp diastolic, pulse rate and respiratory of the third family member i.e., Virisha. After that it analyses the given data based on the age of Virisha (21). As her body temperature is 98 which is in moderate range for her age, the output is generated as "body temperature is normal". As her pulse rate is 69 which is in moderate range for her age, the output is generated as "pulse rate is normal". As her respiratory rate is 20 which is in moderate range for her age, the output is generated as "respiratory rate is normal". As bp systolic and diastolic is 97 and 65 respectively which is less than moderate range for her age, the output is generated as "bp is low" and attached report 2 for her health status.

The generated report for young age group and health parameters of Virisha is shown in Figure 8.

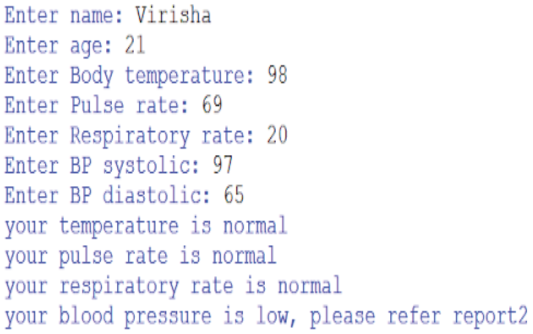

```
Enter name: Virisha
Enter age: 21
Enter Body temperature: 98
Enter Pulse rate: 69
Enter Respiratory rate: 20
Enter BP systolic: 97
Enter BP diastolic: 65
your temperature is normal
your pulse rate is normal
your respiratory rate is normal
your blood pressure is low, please refer report2
```

Figure 8. Report of Family Health Monitoring System for young age group

Test Case 3: Health Monitoring of Middle Age Group

Now the system asks for their name, age, temperature, bp systolic, bp diastolic, pulse rate and respiratory of the second family member i.e., Rakesh. After that it analyses the given data based on the age of Rakesh(30). As his body temperature is 98.1 which is in moderate range for his age, the output is generated as "body temperature is normal". As his pulse rate is 89 which is not in moderate range for his age, the output is generated as "pulse rate is low". As his respiratory rate is 18 which is in moderate range for his age, the output is generated as "respiratory rate is normal". As bp systolic and diastolic is 100 and 78 respectively which is not in moderate range for his age, the output is generated as "bp is low" and attached report 3 for his health status.

The generated report for middle age group and health parameters of Rakesh is shown in Figure 9.

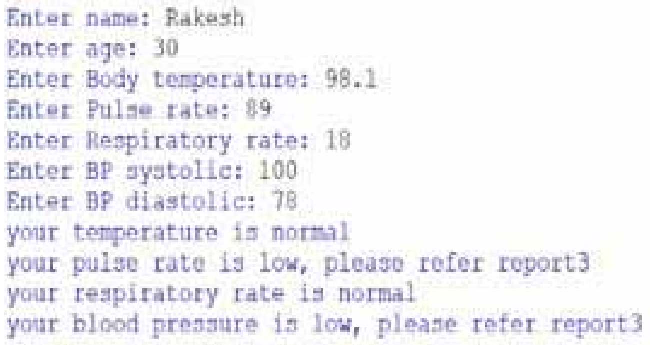

```
Enter name: Rakesh
Enter age: 30
Enter Body temperature: 98.1
Enter Pulse rate: 89
Enter Respiratory rate: 18
Enter BP systolic: 100
Enter BP diastolic: 78
your temperature is normal
your pulse rate is low, please refer report3
your respiratory rate is normal
your blood pressure is low, please refer report3
```

Figure 9. Report of Family Health Monitoring System for middle age group

Test Case 4: Health Monitoring of Old Age Group

The system asks for their name, age, temperature, bp systolic, bp diastolic, pulse rate and respiratory of the first family member i.e., Ganesh. After that it analyses the given data based on the age of Ganesh (49). As his body temperature is 99 which is not in moderate range for his age, the output is generated as "body temperature is high". As his pulse rate is 100 which is in moderate range for his age, the output is generated as "pulse rate is normal". As his respiratory rate is 29 which is less than moderate range for his age, the output is generated as "respiratory rate is low". As bp systolic and diastolic is 100 and 80 respectively which is in moderate range for his age, the output is generated as "bp is normal" and attached report 4 for his health status. The generated report for old age group and health parameters of Ganesh is shown in Figure 10.

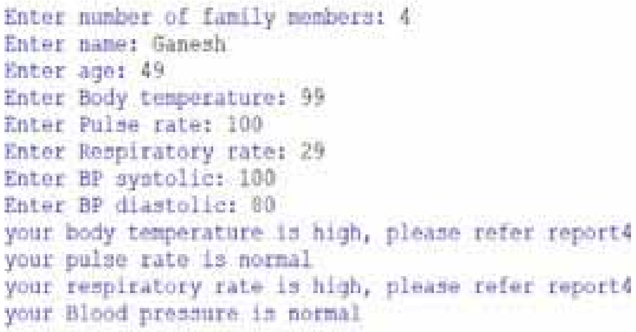

```
Enter number of family members: 4
Enter name: Ganesh
Enter age: 49
Enter Body temperature: 99
Enter Pulse rate: 100
Enter Respiratory rate: 29
Enter BP systolic: 100
Enter BP diastolic: 80
your body temperature is high, please refer report4
your pulse rate is normal
your respiratory rate is high, please refer report4
your Blood pressure is normal
```

Figure 10. Report of Family Health Monitoring System for old age group

V. CONCLUSIONS

The main idea of this device is to provide better and efficient health services to the human beings. Now a days health marketing is becoming the major aspect, in which there is a huge growth of population. So, everyone can afford a health monitoring device which keeps us in regular update with our body. The health care market is one of the majors in which there is a huge growth, the future of health care will be more reliable on this device and also it is very helpful for our upcoming generations. This device takes less than a minute to compute the result of body such as Blood Pressure, heart rate, body temperature, and respiratory rate and also its help's the patients to easily carry this device with them wherever they go and it is also useful for project developers of biomedical device systems.

The above parameters data is stored inside the cloud, so that the experts and doctors could make use of this data and provide a fast and an efficient solution. It allows the objects to be sensed and controlled remotely and it provides the information through smart objects. This device will give a health report of a person which tells us about the person's health condition. Finally, it displays the health status of a human being whether the person is normal or abnormal. Based on this health report a doctor can examine his patient from anywhere and anytime. Continuous monitoring of health and cost-effective disease management is the only way to ensure economic viability of the healthcare system.

REFERENCES

[1]. Nor Shahanim Mohamad Hadis , Muhammad Nazri Amirnazarullah, Muhammad Mahdi Jafri, Samihah Abdullah, "IoT Based Patient Monitoring System using Sensors to Detect, Analyse and Monitor Two Primary Vital Signs" , Journal of Physics: Conference Series, DOI: 10.1088/1742-6596/1535/1/012004.

[2]. K. Arshak, E. Jafer and C. S. Ibala, "FPGA Based System design suitable for Wireless Health Monitoring Employing Intelligent RF module," SENSORS, 2007 IEEE, Atlanta, GA, USA, 2007, pp. 276-279, doi: 10.1109/ICSENS.2007.4388390.

[3]. Narasimha Rao Jasti Madhu, "IoT based Remote Patient Health Monitoring System". B.E., DR AIT, India, 2010

[4]. Thirumalasetty Sivakanth and S. Kolangiammal, "Design of Iot Based Smart Health Monitoring and Alert System," I J C T A, 9(15), 2016, pp. 7655-7661

[5]. Jorge Gómez , Byron Oviedo , Emilio Zhuma., "Patient Monitoring System Based on Internet of Things" Procedia Computer Science 83 (2016) 90 – 97

[6]. Punit Gupta, Deepika Agrawal, Jasmeet Chhabra, Pulkit Kumar Dhir, "IoT based Smart HealthCare Kit", 2016 International Conference on Computational Techniques in Information and Communication Technologies (ICCTICT).

[7]. Archit Sharma, Ruqaiya Khanam, Akriti Kumari, Subham Singh, "A Smart Patient Health Monitoring System Using Raspberry Pi 3", JETIR (ISSN-2349-5162), October 2017, Volume 4, Issue 1

[8]. Mohammad Salah Uddin, Jannat Binta Alam, and Suraiya Banu, "Real Time Patient Monitoring System based on Internet of Things", Proceedings of the 2017 4th International Conference on Advances in Electrical Engineering (ICAEE),Page No-516-521.

[9]. Amandeep Kaur, Ashish Jasuja , "Health Monitoring Based on IoT using RASPBERRY PI", International Conference on Computing, Communication and Automation (ICCCA2017), ISBN:978-1-5090-6471-7/17, Page No-1335-1340.

[10]. K. Mohanraj, N. Balaji, R. Chithrakkannan "IoT Based Patient Monitoring System Using Raspberry Pi 3 and LabVIEW", Pak. J. Biotechnol. Vol. 14 (3) 337-343 (2017).

[11]. Shafaque Nasruddin Soparkar, Dr. Lochan Jolly, "Improved Medical Healthcare System Based On IoT," Vol. 6, Issue 8, August 2017

[12]. Sangle Sagar D, Deshpande Niranjan R, Vadane Pandurang M,Dighe M. S, "IoT Based Health-Care System Using Raspberry Pi," International Research Journal of Engineering and Technology (IRJET), Volume: 04 Issue: 04 | Apr -2017,e-ISSN: 2395 -0056.

[13]. "An FPGA Implementation of Health Monitoring System using IoT" A. Jhansi Naga Sai Surekha,D. Archana,N. Hannah Priyanka, S. Munavvar Hussain in International Journal of Creative Research Thoughts Volume-6, Issue-2, April-2018

[14]. D.Shiva Rama Krishnan, Subhash Chand Gupta, Tanupriya Choudhury, "An IoT based Patient Health Monitoring System", 2018 International Conference on Advances in Computing and Communication Engineering (ICACCE-2018), Paris, France 22-23 June 2018.

[15]. Sunilkumar Laxmanbhai Rohit and Bharat V. Tank, "IOT Based Health Monitoring System Using Raspberry Pi-Review", Proceedings of the 2nd International Conference on Inventive Communication and Computational Technologies (ICICCT 2018), IEEE Xplore Compliant - Part Number: CFP18BAC-ART; ISBN:978-1-5386-1974-2, Page No-997-1002.

[16]. Gutte, A., & Vadali, R. (2018). IoT Based Health Monitoring System Using Raspberry Pi. 2018 Fourth International Conference on Computing Communication Control and Automation (ICCUBEA), 1-5.

[17]. Yedukondalu Udara, Srinivasarao Udara, Harish H M, Hadimani H C " Health Monitoring System Using IoT," International Journal of Engineering and Manufacturing Science, ISSN 2249-3115 Volume 8, Number 1 (2018) pp. 177-182

[18]. Thirumalasetty Sivakanth and S. Kolangiammal, "Design of Iot Based Smart Health Monitoring and Alert System," I J C T A, 9(15), 2016, pp. 7655-7661

[19]. Perumalla Srinivasa Rao, Kamatham Yedukondalu & Racha Ganesh (2021) FPGA implementation of digital 3-D image skeletonization algorithm for shape matching applications, International Journal of Electronics, 108:8, 1326-1339, DOI: 10.1080/00207217.2020.1859143

[20]. Tamilselvi, V., Sribalaji, S., Vigneshwaran, P., Vinu, P., & Geetharamani, J. (2020). IoT Based Health Monitoring System. 2020 6th International Conference on Advanced Computing and Communication Systems (ICACCS), 386-389.

[21]. Bikash Pradhan ,Saugat Bhattacharyya ,and Kunal Pal "IoT-Based Applications in Healthcare Devices" Hindawi Journal of Healthcare Engineering Volume 2021, Article ID 6632599, 18 pages https://doi.org/10.1155/2021/6632599

[22]. Badiganti, P. K.; Peddirsi, S.; Rupesh, A. T. J.; Tripathi, S. L.., "Design and Implementation of Smart Healthcare Monitoring System Using FPGA", first International Conference on Computational Electronics for Wireless Communications, ICCWC 2021 ; 329:205-213, 2022

[23]. Mohammad Monirujjaman Khan, Turki M. Alanazi, Amani Abdulrahman Albraikan and Faris A. Almalki, "IoT-Based Health Monitoring System Development and Analysis" Volume 2022, Article ID 9639195, 11 pages

[24]. Gourab Banerjee, " Body Temperature Monitoring System"

[25]. Harshavardan K, Aravind S, Maanashaswaruban M," Heart Rate Monitoring System Using IoT", International Research Journal of Engineering and Technology (IRJET)

[26]. A.Raji, P.Golda Jeyaseeli, "Respiratory Monitoring System for Asthma Patients based on IoT"

[27]. Norlezah Hashim, Nurbahirah Norddin, Fakrulradzi Idris, Siti Nur Ilmani Mohd Yusoff, Madiha Zahari, "IoT Based Blood Pressure Monitoring System", Indonesian Journal of Electrical Engineering and Computer Science, Vol.19, No.3, ISSN2502-4752http://doi.org/10.11591/ijeecs.v19.i3.pp1384-1390.

E-ISSN 2581 – 7957
P-ISSN 2277 – 3916

CVR Journal of Science and Technology, Volume 24, June 2023
DOI: 10.32377/cvrjst2406

Development of Ultrasound Image Detection System based on Chirp-Coded Excitation

C. Pramod Kumar[1] and Narendra. B. Mustare[2]
[1]Sr. Asst. Professor, CVR College of Engineering/ EIE Department, Hyderabad, India
Email: Pramod.kumar@cvr.ac.in
[2]Professor, CVR College of Engineering/ EIE Department, Hyderabad, India
Email: narendra@cvr.ac.in

***Abstract:* In addition to enhancing contrast for imaging, high-frequency ultrasound with contrast agents also supports regional genomics research and may be used for medication administration. The possible signal-to-noise ratio (SNR) and depth of penetration of high-frequency ultrasound are important constraints. However, using chirped pulses as trigger signals and a cardinal frequency of 30 MHz, we created a novel ultrasound system in this work that uses chirp-coded-excitation ultrasound imaging. A home-made expander that used a novel peep pulse with contrast agents to reduce pulse compression and energy decay in human tissue improved the signal-to-noise ratio (SNR) by 20dB for high-frequency ultrasound flow imaging of the zebrafish heart, and the penetration depth increased to 2.2mm. Yet, a microbubble experiment that used variable echo signal concentrations was successful in distributing a variety of microbubble types as anticipated. Using the setup that we developed, we can demonstrate experimentally that chirp-encoded excitation reduces the signal-to-noise ratio (SNR) by about 43dB compared to unipolar and bipolar pulse excitation.**

***Index Terms:* SNR, High-frequency ultrasound, Chirped pulses, Image detection system, Microbubble**

I. INTRODUCTION

Chirp-coded excitation has recently been discovered to offer the potential to increase local medication administration and improve imaging. In the human body, ultrasonic frequency directly correlates to attenuation. The degree of ultrasonic attenuation through tissue increases with ultrasound frequency. As a result of this lessening impact, the ultrasonic energy of a high-recurrence signal is ordinarily lower than that of a low-recurrence signal. Moreover, the signal-to-noise ratio (SNR) and sensitivity of a high-frequency ultrasonic signal are limited because it is more susceptible to interference from internal and external systems. We can raise the SNR of a high-frequency ultrasound imaging system by maintaining a consistent level of system noise. [1]. There are two ways to increase the trigger signal's power. The first strategy is to boost the trigger signal's loudness for greater system sensitivity. In most cases, the maximum mechanical index has already been reached for the pulse amplitude of commercial ultrasound devices (MI). The second technique is to prolong the signal's transmission time to boost the trigger signal's average power. A coded waveform is the name for this processed signal. It is suggested that the coded waveform be used to improve the ultrasound system's SNR and depth of penetration. The pulse duration might, however, be lengthened. Keep in mind that the duration of the sent signal is what ultimately decides the axial resolution. The axial goal of pictures is re-established with the assistance of the trill-coded excitation procedure by changing the normal force of the coded waveform into the immediate force of a short heartbeat, thus expanding the sign plentifulness. In this review, we utilized a peep signal excitation strategy to help the sign strength of the reverberation signal, considering higher spatial goal in the resulting images. The echo signal is then pulse compressed to restore the axial resolution. To compare the properties of the coded waveform with those of a brief pulse, we employ phantoms and wire phantoms. Then, in contrast imaging, the coded excitation is used to improve the picture quality [2].

The SNR and axial resolution of an ultrasound picture is impacted by the chirp-coded excitation method. SNR and penetration depth are both negatively impacted by a brief pulse. Despite this, a brief pulse has a broad bandwidth and a high axial resolution. A longer pulse with more energy has better entrance profundity and SNR, however less hub goal because of its restricted band. One sort of extensive heartbeat is a coded signal. Coded excitation pushes the limits of this compromise by working on the SNR proportion and the infiltration profundity by fitting coding on the communicating part and deciphering on the getting side. Single-communicate codes simply need a solitary succession to be packed by a channel. Conversely, in different send frameworks, compression can only be achieved by combining two or more courses. Biphasic is one of the most often used phase-modulated codes, and the illustrative waveforms are Barker and Golay codes with symbols ±1.

The swept-frequency chirp is the most prevalent kind of frequency modulation. It is known that the chirp's immediate frequency varies linearly with time [3]. This chirp's pulse is longer than that of other chirps, such as the Gaussian chirp, in the same bandwidth. A longer pulse has more energy. As a result, it is challenging to attenuate such a pulse, which ultimately results in an increase in SNR. Regrettably, the axial resolution is decreased even more due to the overlapping of echo signals caused by a longer pulse. When this is the case, a pressure channel is utilized to abbreviate a long heartbeat into numerous more limited heartbeats to work on the hub goal. The ideal chirp has qualities like; long pulse length and increase in instantaneous frequency of chirps over time [4,5]. As the excitation signal, we choose the chirp whose frequency varies over time. It can precisely match the frequency response of sensors. The next pulse compression enables effective transmission of the trigger

Received on 15-03-2023, Revised on 14-04-2023, Accepted on 25-04-2023.

signal and the elimination of the nonlinear phase [6]. The arbitrary waveform generator's output seen in figure 1(a).

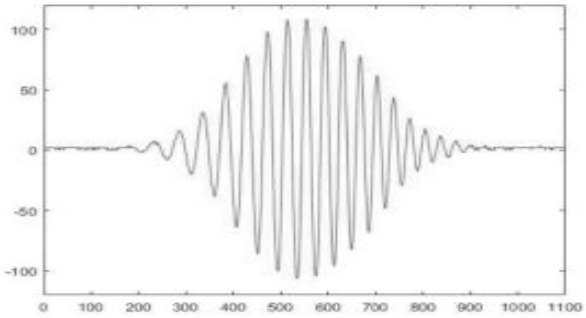

Figure 1(a). Simulated single RF-line data of chirp.

As can be seen in Fig. 1(b), the chirp signals exceeding 100 V are amplified by the power amplifier before being sent as trigger signals to the trigger sensor.

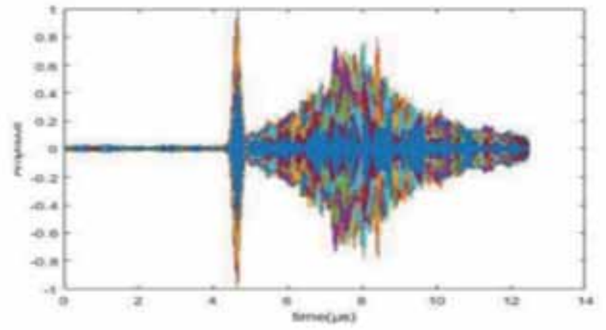

Figure 1(b) . Chirp after amplification with no attenuation.

With the goal of increasing both the average signal intensity,SNR and penetration depth of the proposed framework, we fostered an ultrasonic framework that involves the tweet waveform as the trigger sign. Figure 2 shows a block diagram of the chirp coded-excitation ultrasonic system, demonstrating the various components of the system[7]. These components include the inconsistent waveform generator and the erratic waveform power amplifier.

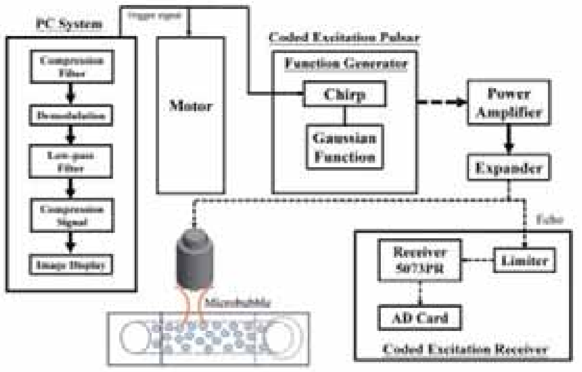

Figure 2.A functional block diagram of a chirp-coded-excitation ultrasound system.

II. METHODOLOGY

A. Coded Excitation Signal

A commercial ultrasonic pulse system's trigger signal is amplified to its maximum MI to enhance the device's efficiency when used in an ultrasound imaging system. Ultrasound produces high instantaneous pressure, which may cause tissue injury through overheating and cavitation effects if not properly mitigated by limiting the transmitted signal energy. The average power of the trigger signal is not relevant for defining short-pulse energy; rather, the power amplitude of the signal is. [8,9]. Chirp-coded excitation may boost SNR and depth of penetration by increasing the signal's average energy without changing the loudness of the trigger signal [10].

A shorter pulse has a smaller bandwidth envelope in the spectrum than a longer one. Because of this, the axial resolution would not be recovered from a long-pulse echo using a compression filter. Using a chirp as a carrier, we were able to get the bandwidth of a long pulse down to the same level as a short pulse in this study. Since that chirp frequency grows with time, its bandwidth is much larger than that of a constant-frequency sine wave carrier. When a lengthy pulse is carried by a chirp, the bandwidth is increased, and the echo is compressed [11]. A chirp is described as

$$c(t) = w(t)\cos\left[2\pi\left(f_0 - \frac{\Delta f}{2}t + \alpha t^2\right)\right],\ 0 \le t \le T, \qquad (1)$$

At some time in the future, where w(t) is a window of Gaussian distribution, f_o is the carrier frequency, f is the bandwidth, T is the signal length and frequency increment rate (=2f/T). The compression ratio function controls how long the chirp signal is played. A Gaussian pulse is the product of a chirp signal with a Gaussian envelope. Altering the chirp duration of a Gaussian chirp pulse yields signals of varying lengths while maintaining consistent bandwidths [12].

B. System Descriptions

An ultrasonic transducer with a 30 MHz central frequency and a 6 mm element diameter was used in this investigation.Fig.3(a) shows a typical acquired echo waveform.

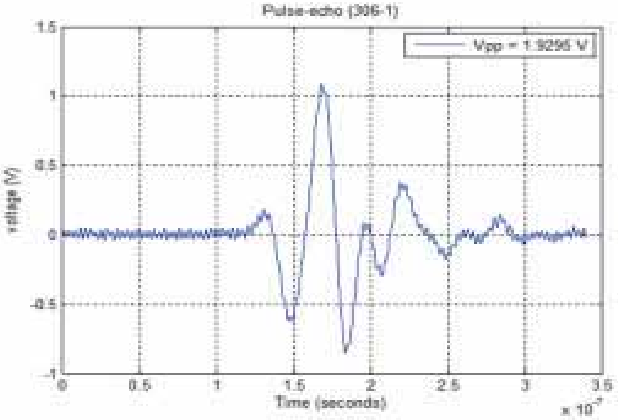

Figure 3. (a) Waveform of a pulse echo

As we can see in Fig.3(a), the transducer generates a signal of 1.92V peak to peak and with a delay of 1.4 microseconds, and frequency of 30 million cycles per second [13]. Higher frequencies generally provide better resolution and are suitable for imaging shallow structures or fine details. The emitted pulse is having a pulse duration of about 0.7 microsecond which improves axial resolution to distinguish between closely spaced reflectors along the path of the ultrasound beam. We can also see the leading edge of the echo is having a rapid rise time that allows for accurate determination of the time of flight for the ultrasound pulse, which is used to calculate the distance to the target.

Fig.3(b) explains the frequency response of the ultrasound transducer that we are using in our experiment. For an ultrasound transducer with a centre frequency of 30 MHz, the frequency response is typically like a bell-shaped curve centred around 30 MHz. The exact shape and width of the curve will depend on various factors, including the design of the transducer, the materials used, and the application for which it is intended [14]. The width of the frequency response curve, often referred to as the bandwidth, is relatively narrow, typically ranging from a few megahertz below to a few megahertz above the center frequency.

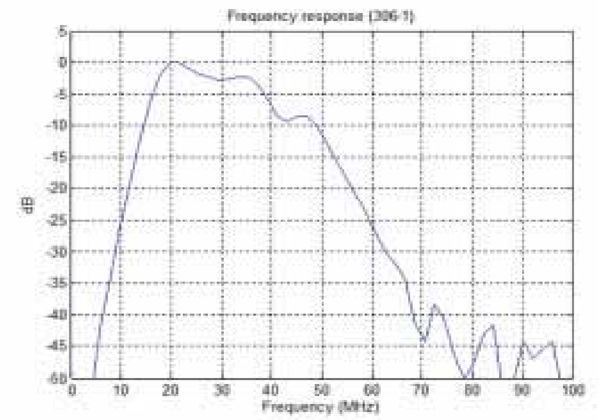

Figure 3. (b) Frequency Response

Both the transducer and the brass enclosure are coated with a protective parylene-c layer, which also serves as a matching layer. Transmission efficiency and ultrasonic reflectivity back to the sensor are both improved by adding this layer [15].

Both a function generator operating at 240 MHz sample/s and an arbitrary waveform power amplifier were part of the pulse system. The arbitrary waveform generator takes its input from computer-generated waveforms that are sent by the spatial programming. The AWG may subsequently give an extensive variety of helpful transmission signals. The increase of a 325LA is ostensibly 50 dB, with a gain fluctuation of 1.5 dB at most. In addition, the frequency response of the input voltages of the 325LA is flat from 250 kHz to 125 MHz input voltages over the peak voltage may cause irreparable harm to the instrument. A 5073PR ultrasonic receiver is used in this research, with a maximum bandwidth of 1 kHz to 75 MHz There is a 7 V peak-to-peak spread in the receiver's noise floor. As the function generator's trigger signal input, the MATLAB-edited chirp waveform is amplified by the power amplifier to produce a high-voltage pulse. The trigger signal is expanded by a diode circuit (expander) to remove noise; this is necessary because the power amplifier amplifies any noise that may be present in the trigger signal; finally, the trigger signal activates the high-frequency transducer, which sends out the ultrasound signal [16]. To shield the receiver's sensitive electronics from the high-voltage trigger signal, the reflected signal is routed via a second diode circuit (limiter) before it reaches the receiver. When the echo signal has been picked up, the 5073 PR receiver will boost it to the correct levels. After that, signal processing is used to convert the echo signal into visuals. A transducer for imaging scanning is mounted in the stationary section, and motion is generated in all three dimensions. The x-axis is steered by an HR8 ceramic linear servo motor, the main scan control motor. Both the y- and z-axis movements are controlled by high-precision stepper motors. The position may be fixed in space in all three dimensions thanks to the three-dimensional motion system. Specifications of the three-dimensional motion system are shown in Table 1.

TABLE I.
THREE-DIMENSIONAL MOTION SYSTEM'S SPECIFICATIONS.

Axis	Stroke (mm)	Count (µm)	Load (kg)	Velocity (mm/s)
x	150	0.1	2	150
y	300	0.8	10	100
z	50	0.6	2	50

C. Signal Processing

There are two distinct components to ultrasound signal processing and imaging. In the first, the echo signal is compressed to reduce its phase difference and concentrate its energy to restore its axial resolution. This study's compression filter of choice is a matched filter. An optimum ultrasonic signal is applied with the matching filter. Hence, pulse compression is accomplished by concentrating the echo signal's energy. Demodulation makes up the second phase. Using an ultrasonic transducer, the echo signal is demodulated to filter the carrier and diversify the wave crest. To create B-mode pictures, the compressed signal will next be converted. The trigger signal for the ultrasound system's imaging scans is produced by an arbitrary waveform generator. To activate the transducer to generate an ultrasonic signal, the trigger signal is amplified using an arbitrary waveform amplifier. The receiver picks up the echo signal, suitably amplifies it, and then feeds it to the oscilloscope for visual display. The experimental system is presented using a test block diagram. Oscilloscope results from the system test demonstrate that it is challenging to see the echo signal when it is obscured by noise. To identify and eliminate the noise source, each instrument's output signal is analysed. To increase the SNR, the right receiver is selected.

Schottky diodes are used in a traditional radar and ultrasound system to reduce nonlinear noise, improving the system SNR and spatial resolution at the same time. Expanders are produced using standard Schottky diodes, such as 1N4148 and 1N914. A trigger signal (30 MHz) is used to set the echo signal to 0.5 V chirp, and the echo signal's SNR is then measured. Three different kinds of expanders are related to the power amplifier. Table 2 displays the calculated findings. Expanders may lessen the power amplifier's noise in both commercial and homemade fashion. To effectively increase the SNR of the echo signal, the sound is reduced to 0.04 V. In this investigation, expander 1N4148 will be utilised to minimise noise since its SNR for the echo signal is superior to that of the other expanders.

TABLE II.
ECHO SIGNAL MEASUREMENTS WITH VARIOUS EXPANDER

Measured Results	1N4148 Expander	Commercial Expander	Handmade Expander
Peak Voltage	1.42 V	1.38 V	1.38 V
Noise Voltage	0.04 V	0.04 V	0.04 V
SNR	31dB	30.75 dB	30.75 dB

D. Microbubble Imaging

A discussion of microbubble concentration is essential when using them. The scatter signal will be insufficient to improve picture contrast if the microbubble concentration is too low. Interestingly, if the microbubble focus is too high, the ultrasonic sign will be a lot more fragile, and it won't be possible to picture the object's back. The shielding effect refers to this. Thus, it is necessary to determine the proper microbubble concentration. The selection of the proper microbubble concentration is crucial given that microbubbles will also be employed for in vitro research. Little animals' blood circulation will dilute microbubbles administered to them, decreasing the scatter signal's strength. Nevertheless, thrombosis will happen if tiny animals get an excessive number of microbubbles by injection. So, the microbubbles may keep their enormous scattering capability and not cause thrombosis if they are at a concentration that can be diluted by an animal's blood circulation. The microbubble sizes employed in this research are C3F8 1.1 m, C3F8 2 m, C4F10 1.1 m, and C4F10 2 m.

Suppose that the blood circulation will eventually dilute the microbubbles put into a tiny animal. The concentration of microbubbles drops by 10–100% in stages of 10%. The ultrasonic scanner receives the injection of the diluted microbubbles into an acrylic phantom. The photos are scanned with a Terason model T3000 from Teratech Company in the United States. The suitable concentration ranges for four distinct kinds of microbubbles are discovered based on the brightness of photographs with various microbubble concentrations. To improve the signal of the blood zone and identify micro perfusion, ultrasound contrast ants are intravenously administered into the bloodstream. Information on the characteristics of microbubble destruction and the distribution of size of microbubbles following disintegration is crucial for medication release. The visual contrast increases as the signal frequency approaches the resonant frequency. The microbubble size must be smaller than 1 m, which is uncommon since the trigger capability in the peep coded-excitation ultrasound framework has a high recurrence. As a result, little microbubbles continue to exist and improve the contrast of the picture while giant microbubbles are eliminated. Three acoustic pressures (0.2, 0.4, and 0.6 MPa) and three signal cycles make up the characteristics of the destruction signal (100, 500, and 1000 cycles). On the ultrasound scan, microbubbles do not continue to be of the same size. With the transition of positive or negative voltage, microbubbles expand or compress, accordingly. As a result, various acoustic pressures are established to track the size distribution of destroyed microbubbles. Indicator cycles influence the time at which microbubbles oscillate. Whenever a certain threshold is reached in the number of signal cycles, a microbubble will break apart into multiple smaller microbubbles. The quantity of microbubbles will then rise as their size declines. To track variations in the quantity of microbubbles, various signal cycle counts are specified. Injection of the microbubbles into an acrylic phantom. The parameters are utilised to produce a destruction signal using the function generator. To create the signal that kills microbubbles, the signal is fed to a 1 MHz transducer (model V303, Panametrics, Waltham, MA) after passing via a power amplifier to amplify it. 1 Hz is the pulse repetition frequency (PRF), and 30 s is the destruction time.

III. EXPERIMENTAL RESULTS

A. Image Phantom Fabrication

Imaging phantom, or simply phantom, is a specially designed object that is scanned or imaged in the field of medical imaging to evaluate, analyze, and tune the performance of various imaging devices. A phantom is more readily available and provides more consistent results than the use of a living subject or cadaver, and likewise avoids subjecting a living subject to direct risk. In electrical engineering, a wire phantom is an electrical circuit derived from suitably arranged wires with one or more conductive paths being a circuit and at the same time acting as one conductor of another circuit. Ultrasound imaging studies might benefit from using the wire phantom as a reference phantom for analysing axial and lateral resolutions, system noise, and dynamic range. To assess the picture resolution, a wire phantom made up of five tungsten wires with a diameter of 20 m is employed. With axial and lateral spacing's of 1 and 2 mm, respectively, the cables are diagonally aligned. As a result, the efficacies of scanning pictures with unipolar pulse, bipolar pulse, and chirp-coded excitations are compared. Images of wire phantoms with various excitations are shown in Figure 4.

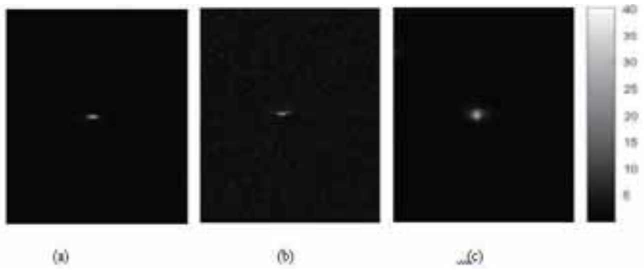

Figure 4. Pictures of a wire phantom:(a) Imaging with unipolar pulses (b) Imaging using bipolar pulses (c) Imaging using chirp-coded excitation

The size of the resonation signal from the wire around the middle point for brief vibration and trill coded excitation is shown in Figure 5. SNRs for short pulses and coded excitation are 31 dB and 43 dB, respectively. Hence, the

SNR of the proposed system increased to 12 dB in the case of chirp-coded excitation in compared to the SNR of the commercial ultrasonic pulse system.

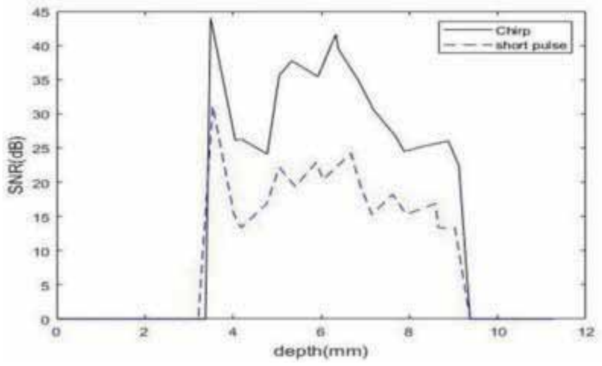

Figure 5.SNR for chirp-coded and short pulse excitation as a function of depth

The wire of the wire phantom should look circular in the photos; however, this is not the case since the cable is out of the focus point, causing distortion in the wire images. To indicate the degree of deformation in a certain point as a function of depth, the deformed wire pictures' minor axis to major axis ratio is a parameter. Increases in deformation cause a corresponding increase in the distance between the wire and the focal point. A brief pulse causes more deformation than coded excitation does, which is more severe. The findings were contrasted with an ultrasound picture for a different sort of stimulation. Hence, a soft tissue phantom (8 cm long, 5 cm wide, and 1.5 cm high) was employed to imitate the actual circumstances in which the ultrasound would be delivered. To scan the tissue phantom, a brief pulse with a trigger signal (30 MHz) and chirp-coded excitation were utilised. The tissue phantom pictures acquired using various forms of coded excitation are shown in Figure 6. As a result of the coded stimulation, the penetration depth increased to two mm, as compared to the unipolar pulse excitation.

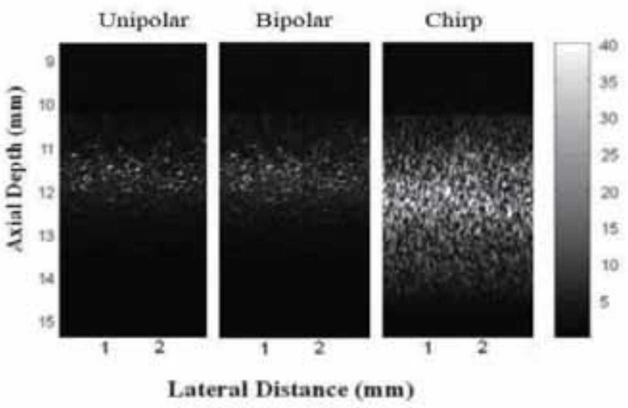

(a) (b) (c)

Figure 6. Ultrasound phantom images (a) Excitation of unipolar pulses (b) Excitation of a bipolar pulse (c) Excitation using chirp-codes.

B.. *Microbubble imaging*

In this study, four different kinds of microbubbles were employed. Choosing the right concentration range avoids the microbubble concentration from being too high, which would significantly attenuate the ultrasonic signal, or too low, which would improve the picture contrast. As a result, ten concentrations of the four different kinds of microbubbles are created.

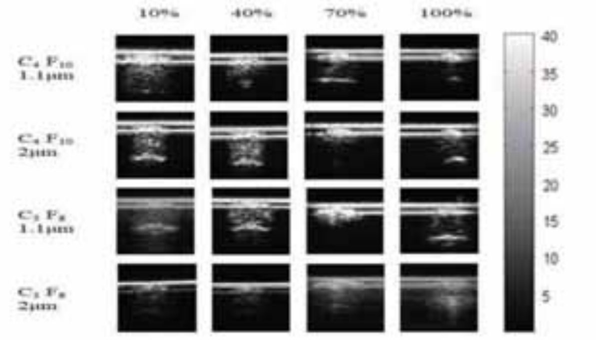

Figure 7. Contrast images for four microbubble concentrations: C3F8 1.1 μm, C3F8 2 μm, C4F10 1.1 μm, and C4F10 2 μm.

Figure 7 above displays contrast pictures of four distinct kinds of microbubbles at various intensities. The ultrasonic chirp coded-excitation system is activated by a radio frequency signal. The visual contrast is much stronger when the signal frequency is nearer to the resonance frequency of microbubbles. Yet, the relationship between the resonant frequency and the size of the microbubbles is inverse. The resonance frequency rises as the microbubble size decreases. In contrast, the resonance frequency decreases as the size of the microbubbles increases. Lately, the zebrafish heart has emerged as a potent model for comprehending the capacity for self-healing, making the zebrafish an essential component of regenerative medicine. As a result, microbubbles are employed to improve the visual contrast while observing zebrafish. Figure 8 shows a comparison of the zebrafish heart before and after microbubble injection.

Figure 8(a) depicts the zebrafish heart without microbubbles; all that can be seen is the shape of the breast. The zebrafish heart is seen in Figure 8(b) after microbubble injection. The heart's atrium and ventricle are visible.

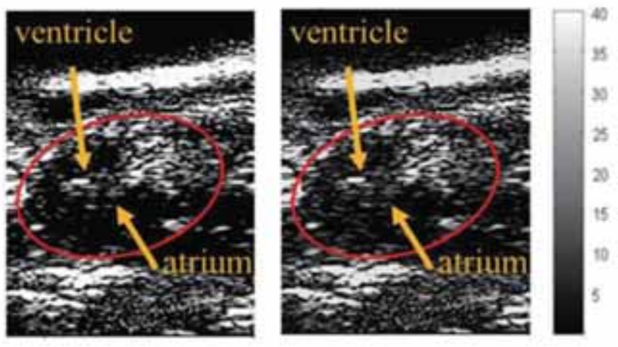

Figure 8. (a) Zebrafish heart devoid of microbubbles. (b) Zebrafish heart after injection of microbubbles

IV. CONCLUSIONS

In this work, we assessed how well the high-frequency ultrasonic detection method performed when contrast chemicals were used. Hence, we were able to demonstrate numerically and subjectively that chirp-coded excitation results in an SNR enhancement of roughly 12 dB over short-pulse excitation when employing the proper receiver and homemade expander. Nevertheless, in the view, injection of four different kinds of microbubbles revealed the following suitable concentration ranges from the microbubble imaging experiment.: C3F8, 1.1 μm from 20 to 40%; C3F8, 2 μm from 80 to 100%; C4F10, 1.1 μm from 20 to 40%; and C4F10, 2 μm from 30 to 50%. The dispersion of microbubble sizes shrank with the precise setting of the destruction signal. Hence, the image contrast is enhanced when the signal frequency is close to the resonance frequency of the microbubbles. The microbubbles were injected into zebrafish, and the fish were then subjected to an ultrasound examination utilising a chirp-coded-excitation system to detect and analyse cardiac alterations before and after the microbubble injection. An excitation-coded ultrasound system using microbubbles could one day be used to examine tumours in small animals without the need for necropsy. Since chirps have more energy and may thus achieve greater penetration and SNR, they may potentially be utilised as carriers for medications that are burst to release them at a specified location.

REFERENCES

[1] Chaturvedi P., Insana M.F., Hall T.J. 2-D companding for noise reduction in strain imaging. IEEE Trans. Ultrason. Ferroelectr. Freq. Control. 1998;45:179–191. doi: 10.1109/58.646923. [PubMed] [CrossRef] [Google Scholar]

[2] Behar V, Adam D. Parameter optimization of pulse compression in ultrasound imaging systems with coded excitation. Ultrasonics. 2004;vol. 42:1101–1109. [PubMed] [Google Scholar]

[3] Peng H., Liu D.C. Chirp-coded pulse excitation for ultrasound elasticity imaging; Proceedings of the 2010 4th International Conference on Bioinformatics and Biomedical Engineering (iCBBE); Chengdu, China. 18–20 June 2010; pp. 1–4. [Google Scholar]

[4] O'Donnell M. Coded excitation system for improving the penetration of real-time phased-array imaging systems. IEEE Trans. Ultrason. Ferroelectr. Freq. Control. 1992;39:341–351. doi: 10.1109/58.143168. [PubMed] [CrossRef] [Google Scholar]

[5] Chiao RY, Hao X. Coded excitation for diagnostic ultrasound: a system developer's perspective. IEEE Trans Ultrason Ferroelectr Freq Control. 2005;vol. 52:160–170. [PubMed] [Google Scholar]

[6] Gennisson J.L., Deffieux T., Fink M., Tanter M. Ultrasound elastography: Principles and techniques. Diagn. Interv. Imaging. 2013;94:487–495. doi: 10.1016/j.diii.2013.01.022. [PubMed] [CrossRef] [Google Scholar]

[7] Liu J., Insana M.F. Coded pulse excitation for ultrasonic strain imaging. IEEE Trans. Ultrason. Ferroelectr. Freq. Control. 2005;52:231–240. [PMC free article] [PubMed] [Google Scholar]

[8] Peng H., Liu D.C. Enhanced ultrasound strain imaging using chirp-coded pulse excitation. Biomed. Signal Process. Control. 2013;8:130–141. doi: 10.1016/j.bspc.2012.09.002. [CrossRef] [Google Scholar]

[9] Qiu W., Yu Y., Tsang F.K., Zheng H., Sun L. A novel modulated excitation imaging system for microultrasound. IEEE Trans. Biomed. Eng. 2013;60:1884–1890. [PubMed] [Google Scholar]

[10] C. Yoon, W. Lee, J. H. Chang, T.-K. Song, and Y. Yoo, "An efficient pulse compression method of chirp-coded excitation in medical ultrasound imaging," IEEE Trans. Ultrason., Ferroelect., Freq. Control, vol. 60, no. 10, pp. 2225–2229, Oct. 2013.

[11] P. Song, M. W. Urban, A. Manduca, J. F. Greenleaf, and S. Chen, "Coded excitation plane wave imaging for shear wave motion detection," IEEE Trans. Ultrason., Ferroelect., Freq. Control, vol. 62, no. 7, pp. 1356–1372, Jul. 2015.

[12] J. Song, J. H. Chang, T.-K. Song, and Y. Yoo, "Coded tissue harmonic imaging with nonlinear chirp signals," Ultrasonics, vol. 51, no. 4, pp. 516–521, May 2011

[13] J.-M. Girault, F. Ossant, A. Ouahabi, D. Kouame, and F. Patat, "Timevarying autoregressive spectral estimation for ultrasound attenuation in tissue characterization," IEEE Trans. Ultrason., Ferroelect., Freq. Control, vol. 45, no. 3, pp. 650–659, May 1998.

[14] Y. B. Ahn and S. B. Park, "Estimation of mean frequency and variance of ultrasonic Doppler signal by using second-order autoregressive model," IEEE Trans. Ultrason., Ferroelect., Freq. Control, vol. 38, no. 3, pp. 172–182, May 1991.

[15] Bae B, Lee H, Lee S, Lee W, Roh Y. Development of a highly attenuative backing for ultrasonic transduces with periodic arrangement of polymeric rods inside the backing. In: Conference proceedings of the IEEE ultrasonic symposium; 2013. p. 1105–08.

[16] P. Zhu, H. Peng, L. Mao, and J. Tian, "Piezoelectric single crystal ultrasonic transducer for endoscopic drug release in gastric mucosa," IEEE Transactions on Ultrasonics, Ferroelectrics, and Frequency Control, vol. 68, no. 4, pp. 952–960, 2021

E-ISSN 2581 – 7957
P-ISSN 2277 – 3916

CVR Journal of Science and Technology, Volume 24, June 2023
DOI: 10.32377/cvrjst2407

A Novel Approach for an IoT based Saline Bottle Level Monitoring System

S. Harivardhagini
Professor, CVR College of Engineering/ EIE Department, Hyderabad, India
Email: harivardhagini@cvr.ac.in

Abstract: The lack of care for people with sufficient skill in hospitals and their heavy duty has become a social problem in the modern world. Development of low-cost health monitoring systems is an essential need for every hospital in the days to come. Various engineering designs are carried for the benefit of hospital facility enhancement. Several health monitoring sensors for humans in bed have been developed. Several sophisticated techniques and equipment have been evolved for treatment of patients in hospitals. However, management and monitoring of the level of saline bottles becomes the fundamental need for good patient care. For patients who require continuous saline, assessment and replacement of saline bottles require manual interface which may not be accurate sometimes i.e., due to the busy schedule, observers may tend to forget to change the saline bottle at the appropriate time. In this paper, a saline monitoring system is designed and prototype is developed which continuously monitors the level of saline in the absence of any hospital staff. The main purpose of this system is to automatically track the saline level of a patient using Arduino UNO R3 and a load cell with HX711. The whole system is remotely controlled by an Android OS smartphone based on Internet of Things (IoT). When the load of the saline bottle reaches a very low level then an alert message will be sent to the nurse and doctor.

Index Terms: Internet of Things (IoT), Arduino UNO R3, Load cell, Saline monitoring

I. INTRODUCTION

There is a continuous growth in the world population, in accordance to this the need for smart health care also becomes essential. Due to the advent of new sensors, microcontrollers and computers, medical care has made tremendous progress. A culmination of medicine and engineering has led to the growth of the medical care stream. This paper elaborates on the design of a low cost indigenously developed sensor which includes a GSM (Global system for mobile communication) modem. This will enable easy monitoring of saline flow from different places. The Arduino microcontroller is used for providing coordination action. The level of the saline bottle is directly proportional to its weight and in order to measure it a LOAD SENSOR and HX711 are placed at the neck of the saline bottle. The weights are categorized as high, medium and low and the output obtained from the sensor is processed to check the same. This information is further transmitted through GSM technology to a distant mobile cell for other actions.

The main objective of the setup is to create an easy, low cost, accessible and authentic method for monitoring saline levels. As the saline goes below the threshold level, it is necessary to change the saline bottle.

The motivation of this novel technique is from the aspect of automating the whole system with minimal human intervention. The main advantage is during the peak hours or nighttime when the need for the nurses to visit the patient's bed frequently reduces drastically as alert notifications will be received periodically. Apart from saving the lives of the patients, the stress of continuous monitoring by the nurses or doctors gets reduced.

This system can automatically monitor the saline flow rate by using an Arduino UNO R3 microcontroller. Wireless data is sent to nurses or doctors' computers or a mobile using GPRS SIM800L and display the results. The hardware devices include - Power Supply, GSM module, Load Sensor, HX711 etc. All these devices are fixed into Arduino to monitor saline. Here a load cell is used, which measures the weight of saline and then generates analog signals, later converted to voltage that can be transmitted to HX711. HX711 receives analog signals from the load cell and it amplifies those signals and transfers them to the microcontroller. GSM module is used when the level of saline goes below threshold value immediately the information including the weight of the saline bottle is sent to the receiver section through this module. An Arduino UNO micro controller is attached to the saline stand so that it can easily monitor the level of saline. When the level of saline goes below threshold then the information will be displayed on LCD and Android App by fetching all the information from the server. It also informs nurses or doctors via generating alert messages on application. The main hardware parts are described as follows.

A. Arduino Uno

The Arduino Uno is a microcontroller board based on the ATmega328. It has 14 digital input/output pins (of which 6 can be used as PWM outputs), 6 analog inputs, a 16 MHz ceramic resonator, a USB connection, a power jack, an ICSP header, and a reset button. It contains everything needed to support the microcontroller; simply connect it to a computer with a USB cable or power it with an AC-to-DC adapter or battery to get started.

B. Load Cell

A load cell is a transducer which transforms force or pressure into electrical output. The magnitude of this electrical output is directly proportional to the force being applied. Load cells have strain gauge, which deforms when pressure is applied on it. And then strain gauge generates electrical signal on deformation as its effective resistance changes on deformation. A load cell usually consists of four strain gauges in a Wheatstone bridge configuration. Load cells come in various ranges like 5kg, 10kg, 100kg and more, here we have used Load cell, which can weigh up to 40kg.

Received on 30-03-2023, Revised on 15-04-2023, Accepted on 20-05-2023.

C. HX711

HX711 module is a Load Cell Amplifier breakout board for the HX711 IC. It permits the user to easily measure weights by reading the load cell. This module uses 24 high precision A/D converter chip HX711. It is specially designed for the high precision electronic scale design, with two analog input channels, the internal integration of 128 times the programmable gain amplifier. The input circuit can be configured to provide a bridge type pressure bridge (such as pressure, weighing sensor mode), is of high precision, low cost is an ideal sampling front-end module.

Figure 1 shows the block diagram of the saline system.

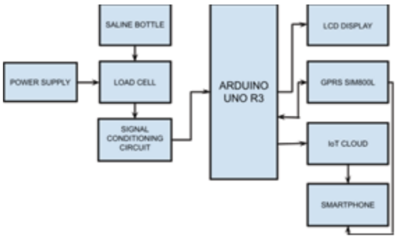

Figure 1. Block Diagram of Saline system

II. LITERATURE SURVEY

A. Literature Survey 1

International Journal of Pharmaceutical Applications Volume: 3, Issue 1, 2017. “Design and Development of Versatile Saline Flow Rate Measuring System and GSM Based Remote Monitoring Device”. The paper [1] elaborates on an automatic saline monitoring system. This uses a low-cost indigenous sly developed sensor. It also uses a GSM (Global system for mobile communication) modem. This facilitates the doctor or nurse to monitor remotely. The coordinating action is provided by the 8051 microcontrollers.

B. Literature Survey 2

The 4th Joint International Conference on Information and Communication Technology, Electronic and Instrumentation Engineering (JICTEI) “Saline Level Monitoring System Using Arduino UNO Processor”. This paper [2] describes that ECG sensor based advanced wireless patient monitoring system the concept is a new innovative idea. This system aims to provide health care to the patient. The ECG of a patient is sensed with the help of a 3 lead electrode system. A AD8232 helps in amplifying small bio signals and is sent to the Arduino which later processes it along with saline level. The level of the saline bottle is detected through IR sensors. The outputs are displayed through a mobile application.

C. Literature Survey 3

International Journal of Engineering Applied Sciences and Technology (IJAST), Volume: 5, issue: 05, 2020. “Design and development of saline monitoring system using flow sensor”. This journal [3] explains how weight or force sensors can be used for monitoring of saline water level and it prevents backflow of the blood into the saline bottle which doesn’t cause any harm to the patient’s health. The main aim of this journal is to overcome drawbacks in manually controlled saline system and to provide greater accuracy than manual saline flow rate control system.

D. Literature Survey 4

International Journal of Research in Engineering and Technology; Volume: 04 Issue: 09, September-2015 “Low-Cost Saline Level Monitoring System Using Wireless Bluetooth Module and Cc2500 Transceiver". This paper [4] describes how the medical field is integrated with engineering technologies to solve this problem. Using sensors, PLC, microcontrollers interfacing is made easy. This paper mainly focuses on providing advanced saline level monitoring systems.

E. Literature Survey 5

Journal of Mechanical and Mechanics Engineering, MAT Journals 2020 Volume-6, Issue-3 (September-December 2020). This paper [5] highlights the basic information regarding strain gauge-based load cells, classification of these load cells and throws light on some of the new ways of designing these load cells. The force measurement system and its salient features have been briefly discussed. So, from this paper we got to know the usage of load cells and we used load cells as the weight sensor in this project.

F. Literature Survey 6

Paper on Patient Health and Saline Level Monitoring System using IoT, Devendra P Gadekar, Dr. Y P Singh, Efficiently Identification, Volume & Issue: Volume 08, Issue 11 (November 2019). The anesthesiologist can monitor several patients in parallel. In case of any anomaly in the measured data, the doctor is alerted by a notification sent by the Android app. In this proposed system [6], it is possible to automatically monitor the salt flow rate using the microcontroller. Wireless data is transmitted to nurses or doctors. The results are displayed in the form of saline droplet rate, number of droplets coming from the saline bottle.

G. Literature Survey 7

General Application Research on GSM Module, published in 2011 International Conference on Internet Computing and Information Services, Date Added to IEEE Xplore: 01 November 2011. This research paper [7] describes that the GSM network is the most worldwide mobile communication network nowadays. Based on the SIEMENS MC35 GSM module, general techniques of communication with GSM network are depicted, including the initialization of terminal equipment, sending and reading short messages (SMS), sending SMS to group users, and the management on phonebook of SIM card, furthermore, a flexible solution on real-time reading SMS is proposed. Finally, application cases are given for the GSM module. So, we are using the GSM module in our project to send messages to the end user.

H. Literature Survey 8

Working principle of Arduino and using it as a tool for study and research, International Journal of Control, Automation, Communication and Systems. This paper [8] explores the working principle and applications of an Arduino board. This also explores how it can be used as a tool for study and research works. Main advantages are fast processing and easy interface. Today, with an increasing number of people using open-source software and hardware devices day after day, technology is forming a new dimension by making complicated things look easier and interesting. These open sources provide free or virtually low costs, highly reliable and affordable technology. This paper provides a glimpse of the type of Arduino boards, working principles, software implementation and their applications.

I. Literature Survey 9

Online Integrated Development Environment (IDE) in Supporting Computer Programming Learning Process during COVID-19 Pandemic, IJID (International Journal on Informatics for Development), Volume: 9, No. 1, 2020. In this journal [9] they described that they should install a text editor called Integrated Development Environment (IDE) to support it. There are various online IDEs that support computer programming. However, students must have an internet connection to use it. After all, many students cannot afford to buy internet quotas to access online learning material during the COVID-19 pandemic. According to these problems, this study compares several online IDEs based on internet data usage and the necessary supporting libraries' availability. In this study, we only compared eleven online IDEs that support the Python programming language, free to access, and do not require logging in. Based on the comparative analysis, three online IDEs have most libraries supported. So, we thought of using IDE software and code on this platform.

J. Literature Survey 10

International Journal of Internet of Things and Web Services. Nuba Shittain Mitu, Vassil T. Vassilev, Myasar Tabany (2021). Low Cost, Easy-to-Use, IoT and Cloud-Based Real-Time Environment Monitoring System Using ESP8266 Microcontroller. This paper [10] proposes a low-cost, Easy-to-use, IoT and cloud-based system solution for environmental data monitoring in real-time through the combination of Internet of Things (IoT) and Cloud Computing technology via Arduino IDE. This paper presents a low implementation cost Data Collection Circuit (DCC) using AT-Arduino commands-based microcontroller ESP8266 and custom IoT device for environment data collection from any physical circumstances. This paper has the scope to introduce the NoSQL, scalable, serverless, real-time database that is Google's firebase, to store the sensor data for real-time monitoring and management of the database.

III. WORKING

In the proposed system saline is automatically monitored by using the Internet of Things. The hardware devices include a Saline bottle, Load Sensor, signal conditioning circuit, power supply, LCD display, GPRS SIM800L, Arduino UNO R3 etc. Here a load cell is used to measure the weight of saline which generates analog signals that can be transmitted to signal conditioning circuit. A signal conditioning circuit receives analog signals from the load cell, and it amplifies those signals, converts the analog signal to digital and transfers them to the Arduino UNO R3 microcontroller. When the weight of saline goes below threshold value then this value is sent over the receiver section of the Arduino UNO R3 then it transmits the signal to GPRS SIM800L. Here weight is directly proportional to level. GPRS SIM800L will receive commands from the microcontroller and transmit alert messages accordingly to the user's smartphone. The information about the saline level will be displayed on LCD and graphical representation is seen in the Android App by fetching all information from the IoT cloud. Figure 2 indicates the flowchart of the saline system.

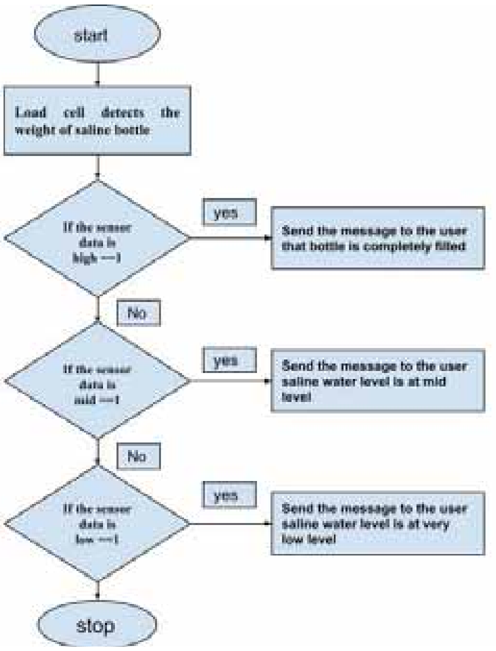

Figure 2. Flow chart of Saline system

IV. PROTOTYPE

The prototype model is built with the following set up. It consists of a power supply which is given to the hardware components by the transformer which converts 220V AC to 0-12V AC. A fully activated Micro SIM card in the socket is inserted. The Tx pin and Rx pin are connected on the Arduino. It will be using software serial to talk to the module. Once the system gets connected to the server or a network the push button of the Arduino UNO R3 must be pressed. The input to the load cell is given through the weight of saline bottle. As the saline weight varies, the signals generated from the sensor will get amplified and converted into digital signals due to HX711 which works as a signal conditioning circuit. The digital signal is transferred to the Arduino UNO R3 microcontroller. When the weight of saline goes below threshold value then the level is low as they both are directly proportional, this value is sent over the receiver section of the Arduino UNO R3 then it transmits the signal to GPRS SIM800L. GPRS SIM800L will receive commands from the microcontroller and transmit alert messages accordingly to the user's smartphone. The information about the saline level will be displayed on LCD, Continuous data about the level of saline bottle can be seen in the excel sheet and graphical representation is seen in the Android App i.e., ThingSpeak by fetching all information from the IoT cloud. Figure 3 shows the prototype of the system.

Figure 3: Prototype of the saline system

V. RESULTS

The weight of the saline bottle indirectly indicates the amount of saline present in it. Three levels (HIGH MEDIUM and LOW) are fixed to indicate the level of the saline present in the bottle. When the weight of the saline bottle is between 350 g – 500 g then the condition is considered HIGH. When the level of the saline bottle is between 200 g – 350 g then the condition is considered as MEDIUM. The weight below 200 g is considered LOW. The above-mentioned conditions are explained clearly in the following sections.

A. Condition 1

The weight of the saline bottle is well above the set threshold level (424.08 g) indicating HIGH condition. Figure 4 shows the case of weight of the saline bottle is high hence the level of the liquid in the saline bottle is high as they both are directly proportional.

Figure 4. Level of the liquid in the saline bottle is HIGH.

Figure 5 shows the alert message which has been sent to the user's phone saying "**ALERT, SALINE STATUS IS HIGH LEVEL, WT:424.08 g**". Figure 6 indicates the graphical representation of weight of saline bottle and time.

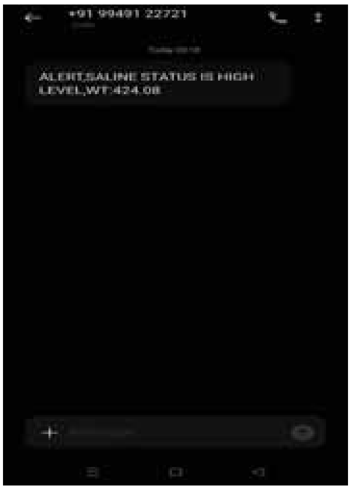

+91 99491 22721

ALERT,SALINE STATUS IS HIGH LEVEL,WT:424.08

Figure 5. Alert message indicating the liquid in the saline bottle is HIGH.

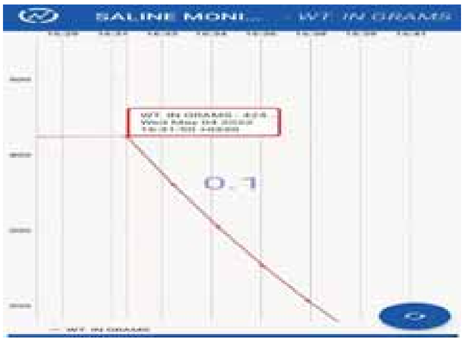

Figure 6. Graphical representation of the weight of the bottle in HIGH condition

B. Condition 2

The weight of the saline bottle is medium (254.08 g) hence the level of the liquid in the saline bottle is medium as they both are directly proportional. Figure 7 shows the level of Saline bottles. Figure 8 indicates the corresponding alert message indicating "**ALERT, SALINE STATUS IS MEDIUM LEVEL, WT:254.08 g**" and Figure 9 indicates the graphical representation of the same.

Figure 7. Level of the liquid in the saline bottle is MEDIUM.

+91 99491 22721

ALERT,SALINE STATUS IS MEDIUM LEVEL,WT:254.08

Figure 8. Alert message indicating the liquid in the saline bottle is MEDIUM.

Figure 9. Graphical representation of the weight of the bottle in MEDIUM condition

C. Condition 3

The weight of the saline bottle is low (143.56 g) indicating the LOW condition. Figure 10 indicates the corresponding alert message indicating **"ALERT, SALINE STATUS IS LOW LEVEL, WT:143.56 g"** and Figure 11 indicates the graphical representation of the same.

+91 99491 22721

ALERT,SALINE STATUS IS LOW LEVEL,WT:143.56

Figure 10. Alert message indicating the liquid in the saline bottle is LOW.

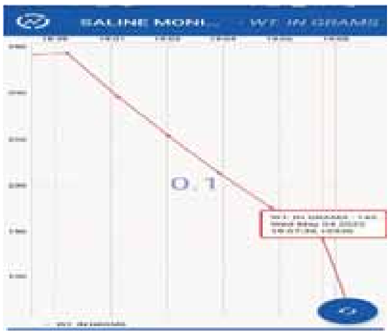

Figure 11. Graphical representation of the weight of the bottle in LOW condition

Continuous data indicating the level of saline bottle can be seen in the excel sheet which is taken from the ThingSpeak application as shown in figure 12.

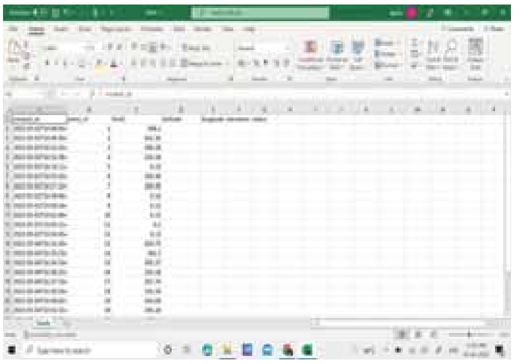

Figure 12. Excel sheet indicating the data.

VI. CONCLUSIONS

IoT based saline level monitoring system, makes the efforts on the part of nurses minimal. Human intervention is reduced as the system is automated. As the saline reaches different levels, alert notifications are sent to the mobile of nurses or doctor; this enables them to visit the patient less frequentlyto check the level of saline in the bottle since an alert notification will be sent to the nurses, doctors, caretakers when saline reaches the critical level. It will save the life of the patients. This will reduce the stress in continual monitoring by the doctor or nurse at an affordable cost. This automatic saline level monitoring system provides more flexibility to doctors, thereby the patients care is enhanced. Hence it saves lots of time for a doctor or nurse who is on duty. This proposed system can automatically monitor the saline flow rate by using an Arduino UNO R3 microcontroller. It can wirelessly send the data to nurses or doctors' computers or a mobile using GPRS SIM800L and display the results. The system is loyal, remunerative and comfortable for nurses. It can be reused for the next saline bottle. It is beneficial for nurses as well as doctors at rural hospitals. Nurses can easily monitor saline levels from a distance.

REFERENCES

[1] C. C. Gavimath, Krishnamurthy Bhat, C. L. Chayalakshmi, R. S. Hooli, “Design and Development of Versatile Saline Flow Rate Measuring System and GSM Based Remote Monitoring Device” International Journal of Pharmaceutical Applications Volume: 3, Issue 1,2017.

[2] Ashika A. Dharmale, Revati R. Mehare, Ankita R. Bharti, Shweta R. Meshram, Prof. Swapnil V. Deshmukh, “IOT Based Saline Level Monitoring & Automatic Alert System" International Journal of Advanced Research in Computer and Communication Engineering Vol. 8, Issue 4, April 2019.

[3] Tanvi Kulkarni, Mr. Avinash Devare, Sayli Zende, Shubhada Yadav, Ajay Biradar, “Design and Develop A Model For Saline Monitoring System” International Journal of Engineering Applied Sciences and Technology (IJEAST), Volume: 5, issue: 05, 2020.

[4] Sakshi D. Ambadkar, Shobha S. Nikam, “NRF Transceiver based Saline Level, Health Monitoring & Control System", International Journal of Research in Engineering and Technology; Volume: 04 Issue: 09, September-2015.

[5] Vijay A. Kamble1, Vasudev D. Shinde, Jayant K. Kittur, “Overview of Load Cells” Journal of Mechanical and Mechanics Engineering, Volume-6, Issue-3, September-December, 2020.

[6] Devendra P Gadekar, Dr. Y P Singh, “Paper on Patient Health and Saline Level Monitoring System using IoT”, Efficiently Identification, Volume & Issue: Volume 08, Issue 11 November 2019.

[7] Ma Yuchun, Hu Yinghong, Li Zhuang, “General Application Research on GSM Module”, International Conference on Internet Computing and Information Services, 2011.

[8] Leo Louis, “Working Principle of Arduino and using it as a tool for study and research”, International Journal of Control, Automation, Communication and Systems.

[9] Kartikadyota Kusumaningtyas, Eko Dwi Nugroho, Adri Priadana, “Online Integrated Development Environment (IDE) in Supporting Computer Programming Learning Process during COVID-19 Pandemic”, IJID (International Journal on Informatics for Development), Volume: 9, No. 1, 2020.

[10] Nuba Shittain Mitu, Vassil T. Vassilev, Myassar Tabany, “Low Cost, Easy-to-Use, IoT and Cloud-Based Real-Time Environment Monitoring System Using ESP8266 Microcontroller”, International Journal of Internet of Things and Web Services. 2021.

E-ISSN 2581 – 7957
P-ISSN 2277 – 3916

CVR Journal of Science and Technology, Volume 24, June 2023
DOI: 10.32377/cvrjst2408

LabVIEW based Rainwater Harvesting System

Gopisetty Ramesh
Sr. Asst. Professor, CVR College of Engineering/EIE Department, Hyderabad, India
Email: ramesh.g@cvr.ac.in

Abstract: Today, there is a lack of water resources to meet water demands. Rainwater is a natural source of water to human beings and living things, which is not being used productively. The productive use of rainwater is called Rainwater Harvesting. The collected water may be used for drinking, gardening, household purposes etc. Our proposed solution is to monitor and control the quality and quantity of water using LabVIEW programming software and accordingly take further steps. The collected water goes through the threshold values of quality measurement i.e., pH value, Turbidity & Conductivity, while measuring the level of harvested water in the sump. If the harvested water is qualified, it can be used for household purposes and if it is not qualified, the harvested water sinks into the ground to increase the groundwater level. The aim of this project is to increase the groundwater level, productive usage of rainwater, reduce the water bill and it has less maintenance and is cost efficient as well. The future scope is to purify the water using filters and convert it into drinking water and irrigation purposes.

Index Terms: LabVIEW, Harvesting, pH Sensor, Arduino

I. INTRODUCTION

Rain-water harvesting is a method that is used to preserve rainy water for different uses and in future needs as well. Rainwater Harvesting is a technique of collecting and storing rainwater and to be used for various purposes while it can be used in future as well.

Rainwater harvesting systems were used long back to at least 4,000 years ago [1], the ability to estimate rainfall based on historical data continues to be the topic of much discussion [5]. The difficulty in estimating rainfall is increased when attempting to derive an optimal design of RWH, a system which is largely dependent upon the ability to model supply, demand, and storage effectively. We modify the non-parametric, stochastic rainfall generator of [2] increasing the daily data collection time frame from 50 years to 64 years while retaining the assumption that daily rainfall probabilities and distributions are contingent upon knowledge of a 30 days centered moving average around the previous day's information. We gather daily rainfall data from the United States National Oceanic and Atmospheric Administration.

As an additional extension over previously submitted work, we also evaluate the possibility of non-stationarity, the idea that water variability is non-constant over time, which recent studies indicate to be a serious problem [7]. In this study, we were concerned only with the stationarity or non-stationarity of supply rather than the larger analysis of regional water availability of primary interest is the required roof surface area and cistern volume to design a system capable of supporting all of a small family's water needs with 100% reliability in a semi-urban region of American countries and based on analyses of supply, demand, efficiency, occupancy, and other distributions. The results of the analyses are summarized in a response chart and a fitted multiple regression equation, another useful extension, which is also potentially useful for water planners in this region of American countries. The significance of this study is important. First, the study extends previous non-parametric rainfall generators longitudinally. Second, the study evaluates non-stationarity of rainfall as part of a potential rainfall estimator.

Third, it provides a mechanism for determining the optimal roof surface area and cistern size for the construction of an RWH that is 100% reliable. Fourth, the conclusions from the study informed the real-world construction of an author's RWH. This study also expands and improves a paper currently under journal consideration in several major ways. First, we extend the analysis of rainfall generators to explore for non-stationarity of rainfall in the geographic region, a unique contribution. Second, we provide separate surface response plots for given family sizes, which are more useful to RWH system planners. Third, we provide curve fitting models via regression that allow planners to have estimates of what building requirements are likely to be needed. Fourth, we evaluate the portability of models across family sizes. None of this work has been published or presented previously by the authors. Rainwater harvesting in urban and rural houses is shown in figure 1.

Received on 24-03-2023, Revised on 10-04-2023, Accepted on 08-05-2023.

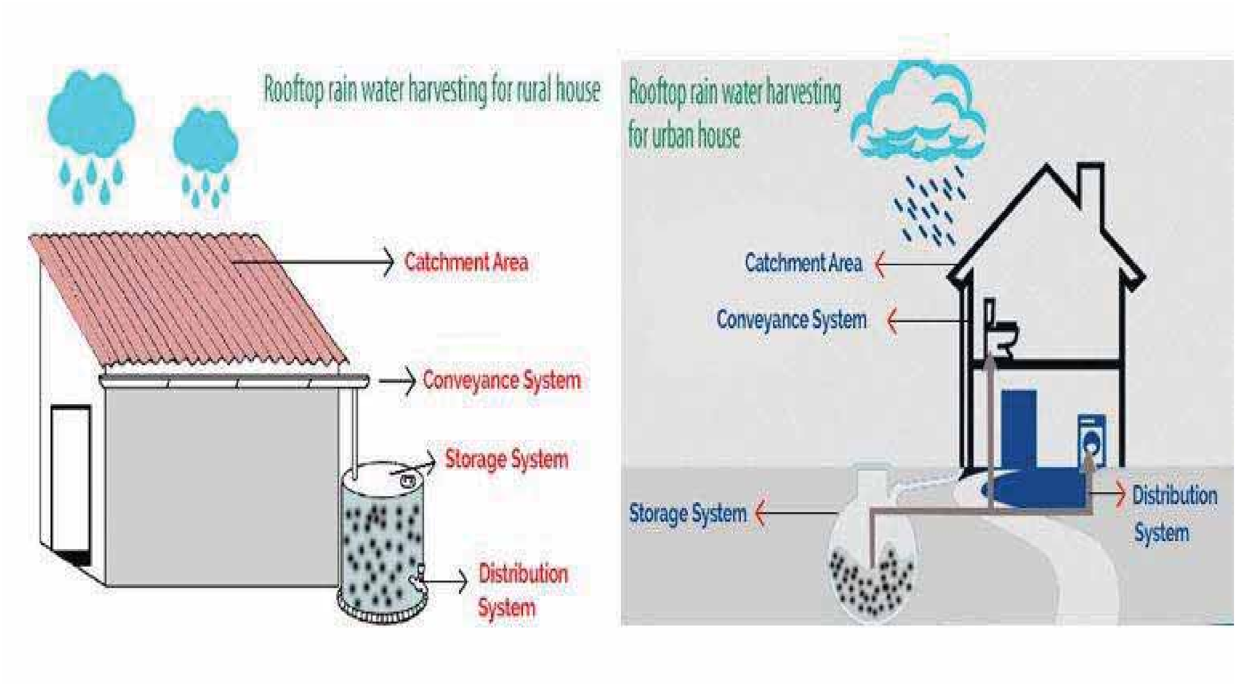

Figure 1. Rainwater Harvesting in Urban and Rural House

II. LITERATURE REVIEW

[12] Rain-water harvesting is a technique of collecting and storing rainwater from rooftops, the earth surface or rock and earth catchment area using normal techniques such as jars and pots as well as more complex techniques such as underground check dams and sumps. The techniques usually found in Asian and European countries arise from practices employed by ancient civilizations within these regions and still serve as a major source of drinking water supply in rural areas and urban areas. Commonly used systems are constructed of three principal components: catchment area, collecting device, and transport system.

[10] Issues are dedicated to rainwater harvesting, available through ITDG Publishing, Photo-manuals by Eric Nissen-Petersen. A range of manuals on how to build several tank types including cylindrical water tanks with dome, an under-ground tank, smaller water tanks and jars, installation gutters and splashguards.

Domestic Water Supply Using Rainwater Harvesting, by [11], Director of the Development Technology Unit, University of Warwick. Rain-water harvesting is a technique of collecting and storing water drops during the rainy season and for use in times when there is small rain to no rain availability. In certain regions of the world rain-water harvesting can be the difference between having a plentiful crop and dried up vines. There are several objectives behind rainwater harvesting.

Increase the availability of water during drought season. Many eco-systems have wet and dry seasons. Because the dry seasons can consist of weeks or months of little to no rainfall, it is important to collect the water during the rainy season and have it available for use during the dry season. Rainwater harvesting enables you to store rain when it is prevalent to be used when there is no rain.

III. IMPLEMENTATION

RWH is a method of capturing and storing water during rainy periods for use in times when there is little to no rain available. In certain regions of the world, rainwater harvesting can be the difference between having a plentiful crop and dried up vines. There are several objectives behind rainwater harvesting.

Increase the available water level during hot Seasons. Many eco-systems have wet and dry seasons. The hot season is a period of weeks or months and little to no rain, it is important to collect it during the rainy season and have it available for use during the hot season. RWH enables storage of water when it is prevalent to be used when there is no rain.

Prevent overuse of Aquifers. As cities and towns grow the need for water increases. Many municipalities rely upon aquifers deep below the ground for this water supply. The problem is it takes a long time to replenish an aquifer if it is quickly drained. By harvesting rainwater for later use, the demand on aquifers is reduced, which enables them to remain full.

Save Money and Pumping water up from underground can be a cost effective method. It is estimated that for every one-meter pumping of water level, there is a consumption of 0.4 Kilo watt. Hour of electric power consumption. So, by having water nearer to the surface, or at the surface in reservoirs, less electric power is required to collect the water so less money is spent.

The block diagram of the harvesting system is shown in figure 2. Block diagram of LabVIEW based rainwater harvesting system shown in figure 3.

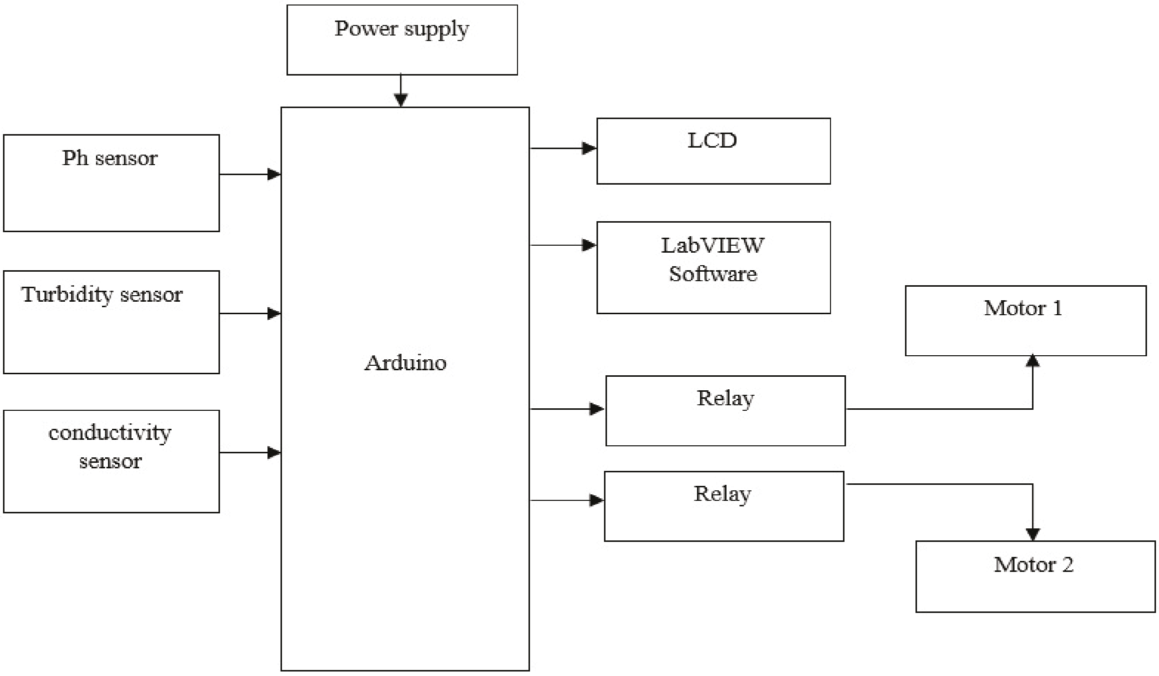

Figure 2. Block diagram of the system

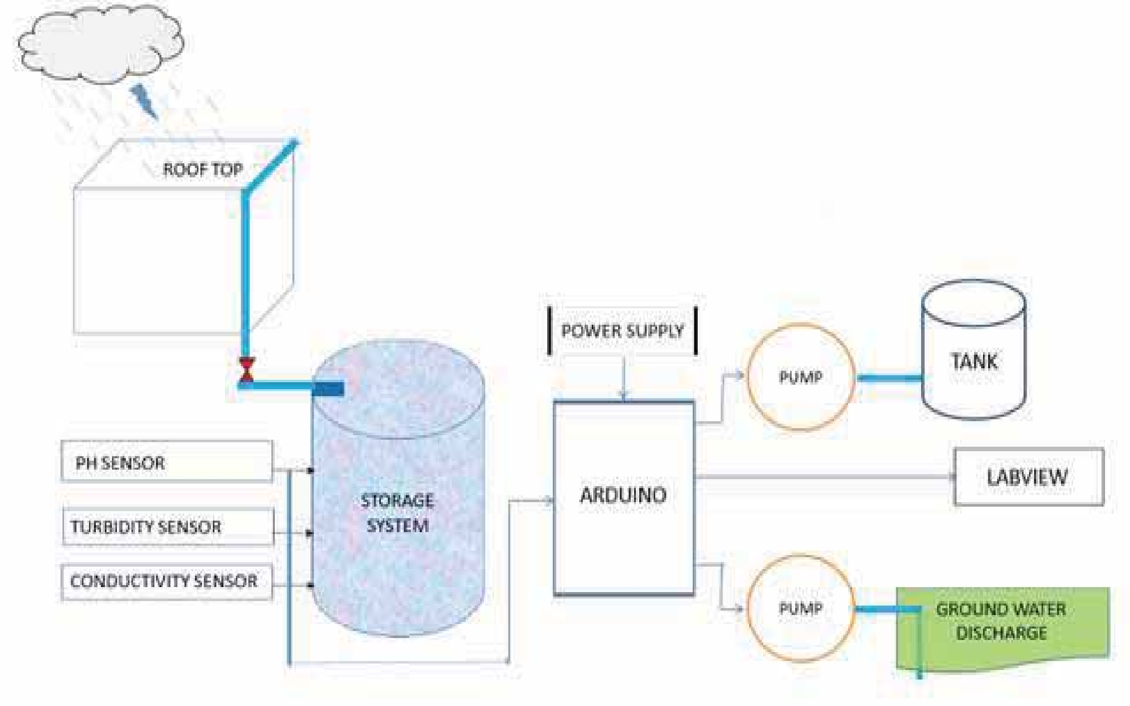

Figure 3. Block Diagram of Rainwater Harvesting Using LabVIEW

IV. RESULTS

Harvesting and collection of rainwater is used to solve the problem of water crisis globally. The use of a rainwater harvesting system provides more advantages for any water crisis and domestic applications like drinking purpose, irrigation etc. This technique can be a boost to an incredible solution in areas where there is enough rainfall but not enough supply of ground-water. It will not only provide the most sustainable and efficient means of water management.

For this, the Government agencies should come out with an appropriate incentive structure and logistic assistance to make it a real success. Rain-water harvesting is something that hundreds of families across the world should participate in rather than pinning hopes on the administration to fight the water crisis. This water conservation technique is a simple and cost-effective process with numerous benefits that can be easily practiced in homes, apartments, parks and across the world. As we all know, charity begins at home, likewise, a contribution to society's welfare must be initiated from one's home. The hardware implementation of the system is shown in figure 4 and figure 5 shows the graphical user interface of the system using LabVIEW software.

Below are the results of the system:

1. Rainwater harvesting system is monitored and controlled using LabVIEW software.
2. Water level control and monitoring is done through wireless technology.
3. Water quality analysis includes pH, turbidity, and conductivity of water is monitored.
4. With the above analysis, water is sent either to the tank or it is discharged to the ground for drinking and gardening purposes.

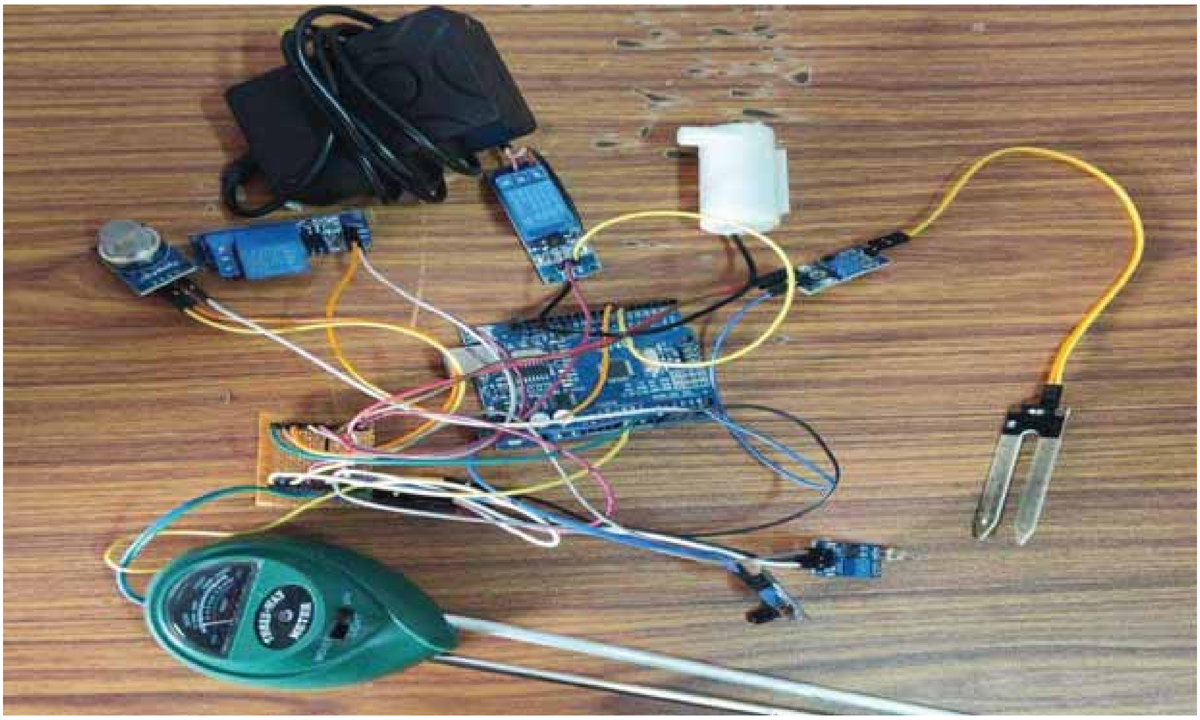

Figure 4. Hardware Setup of the system

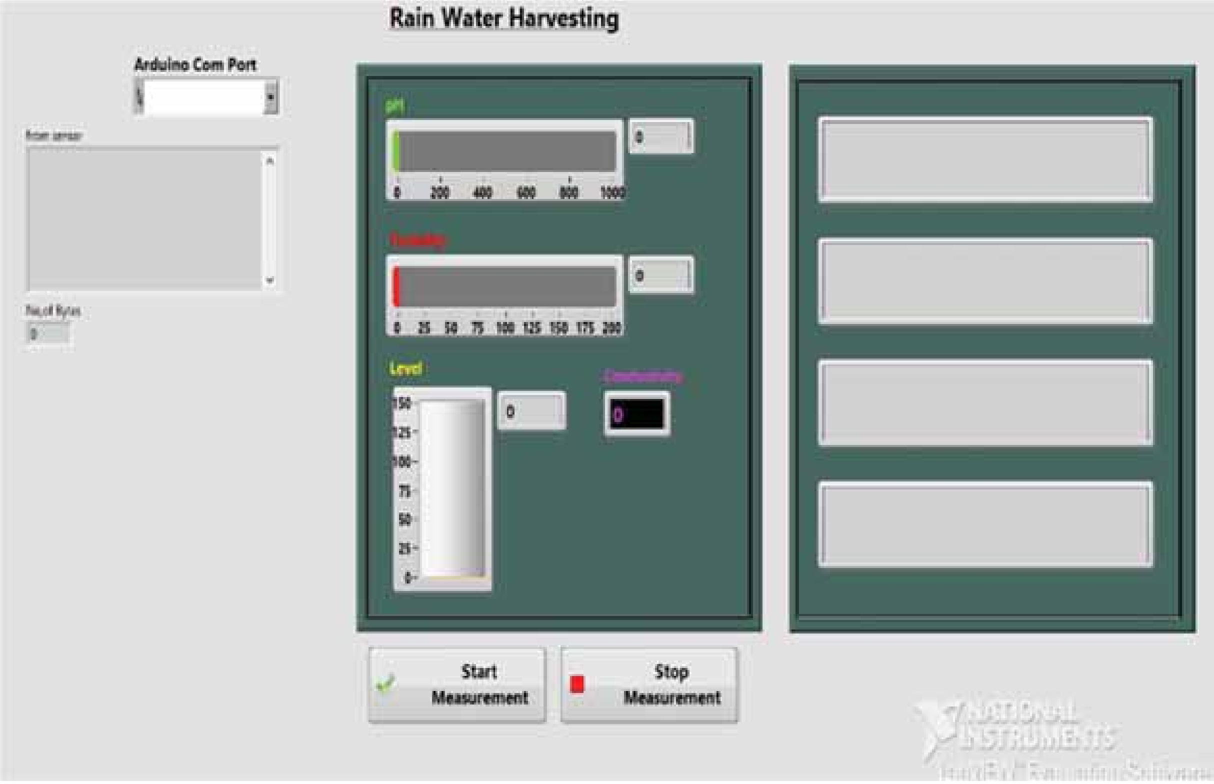

Figure 5. LabVIEW display of the system.

V. CONCLUSIONS

The Rainwater Harvesting System Using LabVIEW mainly aims to improve the quality of ground water resources and to meet the increasing demand for water during dry seasons.

Nowadays, rainwater is being used as the primary source of drinking water in several rural areas and semi urban areas. Because rainwater is free from pollutants and contains salts, minerals, and other natural contaminants. In areas where there is excess rainfall, the surplus rainwater can be used to increase ground water level through artificial recharge techniques.

In urban areas, water harvesting is usually done with the help of some infrastructure or the simplest method for a rainwater harvesting system is storage tanks. In this, a catchment area for the water is directly linked with cisterns, tanks and reservoirs. Water can be stored here until needed or used daily. The roofs of homes or apartments are the best catchment areas provided, they are large enough to store daily water needs. Other than that, large bowls and tarps can also fulfill the function.

REFERENCES

[1] Abdulla, F.A., & A. W. Al-Shareef. 2019. “Roof Rainwater Harvesting Systems for Household Water Supply in Jordan.” Desalinization 243:195-207.

[2] Basinger, M., F. Montalto, and U. Lall. 2018. “A Rainwater Harvesting System Reliability Model based on Nonparametric Stochastic Rainfall Generator.” Journal of Hydrology 392:105- 118.

[3] Evans, C.A., P.J. Coombes, and R.H. Dunstan, RH. 2016. “Wind, Rain and Bacteria: The Effect of Weather on the Microbial Composition of Roof-Harvested Rainwater.” Water Research 40: 37-44.

[4] Guo, Y. and B.W. Baetz. 2017. “Sizing of Rainwater Storage Units for Green Building Applications.” Journal of Hydrologic Engineering 12(2): 197-205.

[5] Lall, U., and A. Sharma. 2014. “A Nearest Neighbor Bootstrap for Resampling Hydrologic Time Series.” Water Resources Research 32(3): 679-693.

[6] Magyar, M.I., V.G. Mitchell, A.R. Ladson, and C. Diaper. 2017. “An Investigation of Rainwater Quality and Sediment Dynamics. Water Science & Technology 56(9) 21-28.

[7] Milley, P.C.D., J. Betancourt, M. Falkenmark, R. Hirsch, Z.W. Kundzewicz, D.P. Lettenmaier, and R.J. Stouffer. 2008. “Stationarity is Dead: Whither Water Management?” Science Magazine, 319: 573- 574.

[8] National Geographic. 2020. “Water Footprint Calculator Methodology and Tips. Accessed 10 March.

[9] National Oceanic and Atmospheric Administration. 2012a. NNDC Climate Data Online. Accessed 7 March.

[10] John Gould “Rainwater catchment systems: reflections and prospects” pp: 2-5, volume 18, January 2010.

[11] Ibrahim, Gaylan Rasul Faqe; Rasul, Azad; Ali Hamid, Arieann; Ali, Zana Fattah; Dewana, Amanj Ahmad "Suitable Site Selection for Rainwater Harvesting and Storage Case Study Using Dohuk Governorate". April 2019.

[12] Duke, Katie. "Ownership of Rainwater and the Legality of Rainwater Harvesting in British Columbia". Appeal. Retrieved 2016-03-29, 2014.

E-ISSN 2581 – 7957
P-ISSN 2277 – 3916

CVR Journal of Science and Technology, Volume 24, June 2023
DOI: 10.32377/cvrjst2409

Extensive Content Feature based Image Classification and Retrieval using SVM

A. Srinivasa Reddy
Assoc. Professor, CVR College of Engineering/CSIT Department, Hyderabad, India
Email: srinivas.asr@gmail.com

Abstract: **The classification and retrieval of picture advances in the field of image retrieval, particularly content-based image retrieval, are presented in this work. Scaling Invariant Feature Transform (SIFT) and developed K-Means clustering approach can be used to first arrange the features extracted based on the bag of visual words (BOW). The two stages of our retrieval method are retrieval and classification. The k-Nearest Neighbor (kNN) and Support Vector Machine (SVM) techniques were used to classify the photos based on their attributes and results were compared. This will categorize the images into different groups to improve the precision and recall rate. Following image classification, similar images matching the query image are pulled from the appropriate class.**

Index Terms: **Bag of visual Words, Support Vector Machines, k-Nearest Neighbor, *Scaling Invariant* Feature Transform, classification, retrieval, classification.**

I. INTRODUCTION

Searching for digital images in huge databases is known as the image retrieval problem. Content-based image retrieval, also known as query by image content (QBIC) applies computer vision techniques to this problem for a scientific overview of the CBIR field [1,2]. "Content-based" refers to a search that examines the contents of the image rather than its associated metadata, such as its keywords, tags, or descriptions. Colors, shapes, textures, and any other information that can be inferred from the image itself are all examples of "content" in this context. CBIR is preferable since searches that only employ metadata rely on the accuracy and comprehensiveness of the annotations.

Toshikazu Kato, an engineer at the Japanese Electrotechnical Laboratory, is credited with coining the phrase "content-based image retrieval" in 1992 to describe research involving the automatic retrieval of photos from a database based on the colours and forms present. The methods, devices, and algorithms are derived from statistics, pattern recognition, signal processing, and computer vision, among other disciplines.

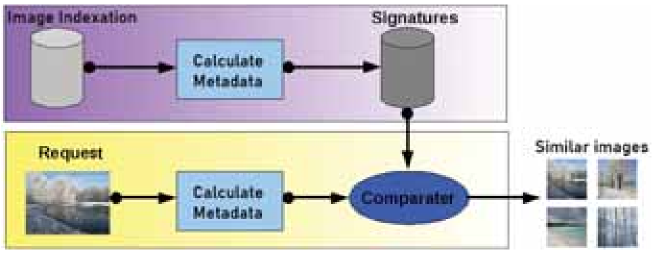

Figure 1. General CBIR scheme

The image metadata or keywords that are related to the visual content or properties of the picture file are what the annotation-based retrieval is dependent on. An automatic image annotation process assigns significant words to an image while taking into account its content. This method is predicated on the idea that zooming is significant enough to allow for the indexing, retrieval, and comprehension of enormous image data collections. Breast density texture characterisation effectively makes use of the two-dimensional principal component analysis in order to characterise the texture effectively while allowing for dimensionality reduction. The retrieval function is performed using a support vector machine [3]. A novel approach to interactive image segmentation-based content-based picture retrieval with relevance feedback has been developed [4]. It is based on the random walker algorithm.

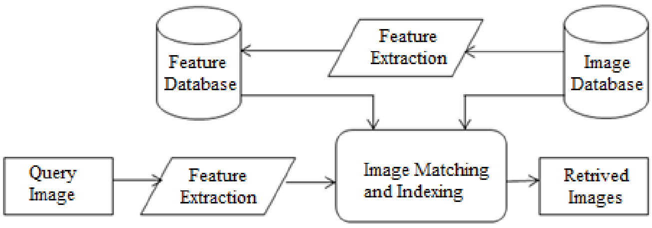

Figure 2. CBIR Model

The technique used to extract components from given images is a critical step in CBIR, and how well it works depends on how highlights are isolated from the images. Two images' similarity is calculated as a percentage of the discrepancies between their element vectors. The goal of CBIR [5,6] is to recover images from a query image that have photos with comparable visual elements, which has proven to be a challenging task in the realm of computer vision and artificial intelligence. The regular CBIR can be expanded by the creative method, much like how the content-based recovery is. Here, only visual highlights are used; access to substantive information is not available.

With the use of machine learning (ML), which is a form of artificial intelligence (AI), software programmes can predict outcomes more accurately without having to be explicitly instructed to do so. To forecast new output values, machine learning algorithms use historical data as input. Support vector machines (SVMs) [3,7] are a group of supervised learning techniques for classifying data, performing regression analysis, and identifying outliers. Support vector machines' benefits include efficiency in high-

Received on 20.08.2022, Revised on 19-10-2022, Accepted on 10-12-2022.

dimensional environments. Still useful in situations where the number of dimensions exceeds the number of samples.

II. LITERATURE REVIEW

Stefanos Vrochidis et al. [1] mentioned that “to address the demand for content-based patent picture search and retrieval, we first explore the possible advantages, the needs, and the obstacles associated with patent image retrieval. Then, we present a framework that includes cutting-edge image analysis and indexing algorithms. To successfully facilitate content-based image retrieval in the patent domain, the proposed system applies document image pre-processing, image feature, and textual information extraction. We put in place a patent picture search engine to gauge the potential of our idea. Results from a variety of interaction modes, comparisons with other systems, and a quantitative assessment of our engine show that image processing and indexing technologies are at a stage of development where they are ready to be included into practical patent retrieval applications”.

Srinivasa Rao et al. [2] stated that “There are Moment Invariants (MI) and Zernike Moments (ZM)-based Content Depending Picture Retrieval (CBIR) systems that use invariant image moments based on shape. The shape features of an image can be effectively represented by MI and ZM. However, their use in CBIR is limited by the MI's non-orthogonality and the ZM's poor reconstruction. Therefore, a CBIR system based on orthogonal moments must be effective. Legendre Moments (LM) can compactly express the features of an image's shape and are orthogonal and computationally faster. This paper proposes a CBIR system for grayscale images utilizing Exact Legendre Moments (ELM). The suggested CBIR system outperforms the MI and ZM moment-based approaches in terms of retrieval effectiveness and retrieval time. Using the Support Vector Machine (SVM) classifier also increases the efficiency of classification. Over the traditional CBIR technique, better retrieval outcomes are obtained using the Stacked Euler Vector (SERVE) in conjunction with Modified Moment Invariants (MMI)”.

Srinivasa Reddy A. et al. [3] discussed that “One of the methods for detecting tumors in any part of the body is magnetic resonance imaging (MRI). The brain tumor is becoming one of the leading causes of mortality for many people. A brain tumor is among the deadliest malignancies, so it is important to find it quickly and get the right therapy to save a life. Due to the development of tumor cells, the detection of these cells is a challenging issue. Comparison of the MRI treatment for a brain tumor is crucial. Using basic imaging techniques, it is quite challenging to see the aberrant brain structures. To solve a problem, automated methods for classifying and detecting brain tumors are suggested in this work”.

Nidhi Singh [4] et al. proposed that “It addresses the issue of content-based picture retrieval in dynamic environments. Systems that evaluate photos in real-time cannot function in a situation where new or additional images are constantly being added or stored. The authors of this research suggest a system that may choose the best features to evaluate recently acquired photos, increasing retrieval efficiency and accuracy. Here, a better algorithm is suggested. After segmentation, the process entails creating feature vectors that will be used to compare query photos to database images for similarity. The framework has been trained on several database pictures. When compared to the performance of traditional methods of content-based picture retrieval, the suggested algorithm's performance on a variety of real photos is found to be rather satisfactory”.

III. CONTENT BASED IMAGE RETRIEVAL

In 1992, T. Kato coined the phrase "content-based picture recovery" to describe his work with database-based automatic image retrieval. In the CBIR, images are retrieved based on colour and shape [1,2,4]. Since then, the method of utilizing linguistic image qualities to extract desired photographs from a large collection has been referred to as CBIR. Among the fields where methods, tools, and calculations are applied are insights, design recognition, signal preparation, and computer vision. As it is based on the visual analysis of contents that are present in the query image, content-based image retrieval (CBIR), a framework, can get around the issues outlined above. Numerous uses of the CBIR technology have been developed, including fingerprint identification, biodiversity information systems, digital libraries, crime prevention, medical research, and history.

While CBIR does have relatively high accuracy on common benchmark datasets, some jobs, such datasets for trademarks, still have low accuracy. Unsolved issues include partial similarity, semantic similarity, domain variance, and resistance against adversarial attacks.

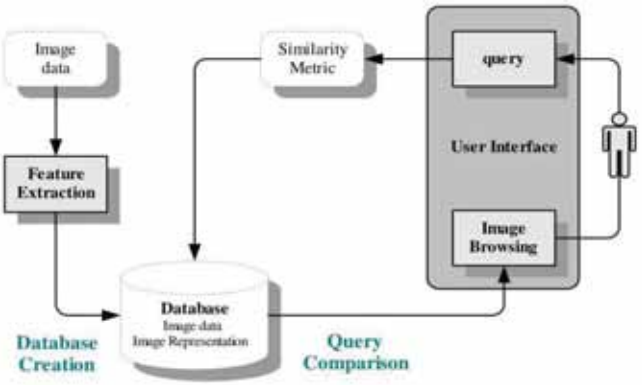

Figure 3. Architecture of CBIR

Using an image distance measure is the most popular technique for comparing two images in content-based image retrieval. An image distance measurement examines how similar two photos are in terms of their shape, colour, texture, and other attributes. For instance, 0 denotes a perfect match with the query in terms of the dimensions considered. A score greater than 0, as one might guess, denotes varying degrees of similarity between the photos. Then, you can arrange search results according to how close they are to the image you are looking for.

The semantic gap is the discrepancy between the low-level features provided by CBIR systems and the user's required semantic categories. The semantic gap between the low-level visual features (color, shape, texture, etc.).

A. Color

It is possible to calculate distance measurements based on colour similarity by creating a colour histogram for each image that shows the percentage of pixels that have a particular value. One of the most popular methods is examining photos based on the colours they contain because it can be done regardless of the size or orientation of the image. Research has, however, also tried to break down colour proportion by region and by the spatial relationships between various colour zones.

B. Texture

Measures of texture look for visual patterns in images and how those patterns are defined spatially. Depending on how many textures are found in the image, Texel's - which represent textures - are divided into a variety of sets. These sets not only specify the texture but also the location of the texture within the image. Additional techniques for categorizing textures include, Matrix of co-occurrence, Wavelet transform, and laws texture energy.

C. Shape

Shape does not refer to the shape of an image but to the shape of a particular region that is being sought out. Shapes will often be determined first applying segmentation or edge detection to an image. Other methods use shape filters to identify given shapes of an image. Shape descriptors may also need to be invariant to translation, rotation, and scale. Some shape descriptors include Fourier transform and Moment invariant.

D. Image Retrieval

In the context of image retrieval, the terms Accuracy, Recall and Precision are described in terms of a set of recovered images, a collection of relevant images, or a list of all online pictures that are pertinent to a particular image, and a set of pictures acquired by a web search engine for a query.

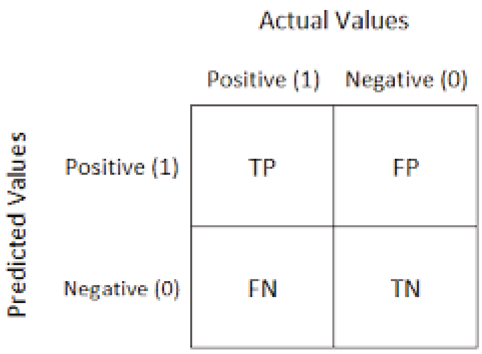

		Actual Values	
		Positive (1)	Negative (0)
Predicted Values	Positive (1)	TP	FP
	Negative (0)	FN	TN

Figure 4. Confusion Matrix

True Positive:	Actual-Yes	Predicted-Yes
True Negative:	Actual-No	Predicted-No
False Positive:	Actual-No	Predicted-Yes
False Negative:	Actual-Yes	Predicted-No

Accuracy

Accuracy reveals how frequently the ML model was overall correct.

$$\text{Accuracy} = (TP+TN) / (TP+TN+FP+FN) \qquad (1)$$

Precision

The model's precision measures how well it can forecast a particular category.

$$\text{Precision} = TP / (TP+FP) \qquad (2)$$

Recall

How frequently the model was able to identify a particular category is indicated by recall.

$$\text{Recall} = TP / (TP+FN) \qquad (3)$$

IV. SUPPORT VECTOR MACHINE

Support vector machines (SVMs) are a collection of supervised learning techniques used to classify images and identify outliers. The SVM algorithm's objective is to establish the best line or decision boundary that can divide n-dimensional space into classes, allowing us to quickly classify fresh data points in the future.

A hyperplane is the name given to this optimal decision boundary. SVM selects the extreme vectors and points that aid in the creation of the hyperplane. Support vectors, which are used to represent these extreme instances, form the basis for the SVM method. Consider the diagram below, where a decision boundary or hyperplane is used to categorise two distinct categories.

SVM comes in two varieties:

Linear SVM: Linear SVM is used for data that can be divided into two classes using a single straight line. This type of data is called linearly separable data, and the classifier employed is known as a Linear SVM classifier.

Non-linear SVM: Non-Linear SVM is used for non-linearly separated data. If a dataset cannot be classified using a straight line, it is considered non-linear data, and the classifier employed is referred to as a Non-linear SVM classifier.

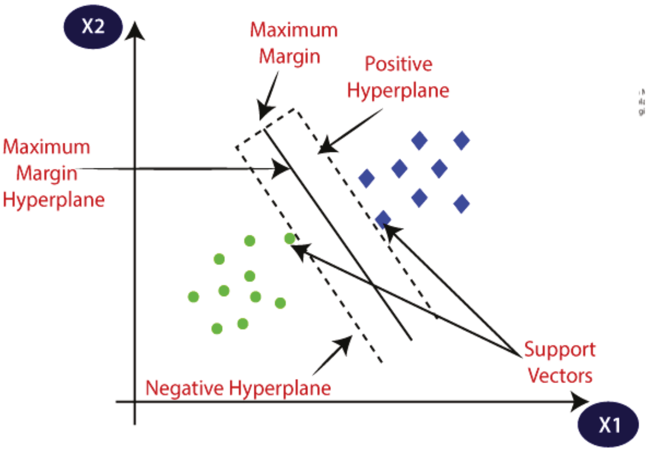

Figure 5. Architecture of SVM

In n-dimensional space, there may be several lines or decision boundaries used to divide classes; however, the optimal decision boundary for classifying the data points must be identified. The hyperplane of SVM is a name for this optimal boundary.

V. PROPOSED METHODOLOGY

A computer system for browsing, searching, and retrieving images from a database of digital images is called an image retrieval system. The two methods used for searching and retrieving images from an image database are context-based image retrieval and content-based image retrieval. Content-based image retrieval is a system for retrieving different images from an image database. Most web image retrieval solutions now use text-based image retrieval. A keyword-based search is used in the text-based approach. We use a high-level feature as a label for getting the image based on the names in context-based image retrieval. Our recommended approach consists of two essential components, namely: Process of feature extraction and retrieval.

There are two types of feature extraction: textual feature extraction and visual feature extraction. An example of a visual feature is Bag of Visual Words. text-based features such as filenames, notes, and keywords. By using our recommended technique, the features are extracted from the Bag of Visual Words (BoW). The BoW includes feature description, code book production, and point of interest detection. This graphic piece could be a representation of an image in a histogram. Scaling Invariant Feature Transform (SIFT) and the newly created K-means clustering algorithm can be used to frame the BoW.

A better multi-texton approach can be used to extract the texture. Following the feature extraction, the retrieval technique will be used. The two stages of our retrieval procedure are categorization and retrieval. Applying the kNN algorithm will be the primary method of classifying the photos based on their attributes. To improve the precision and recall rate, this will divide the photos into several classes. The performance of the recommended picture retrieval is assessed based on the precision, recall, and accuracy values after the classifications of the similar images, which are obtained from the pertinent class in accordance with the provided query image.

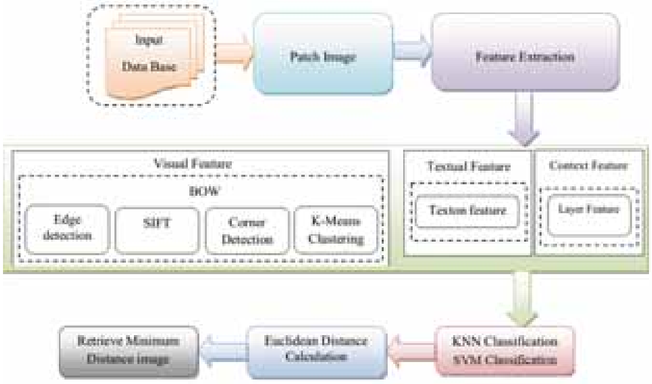

Figure 6. Architecture of Proposed method

A. Feature Extraction

By removing picture features, content-based images retrieval (CBIR) was launched. In general, the features are divided into visual elements like colour and texture, to mention a few, as well as text-based features like annotations and keywords. A lot of information about a picture's content can be found elsewhere outside the image itself. The context of an image can be thought of as all information about the image that isn't related to its visual qualities. The context for retrieval fundamentally alters in this case of a considerably larger collection of photographs because the feature space is suddenly more heavily loaded with images. A high level, layer-based feature is the context feature.

B. Texture Images

Unevenness is visible as tone or intensity fluctuations over a neighborhood in an intensity image. A recurrent array of a specific essential model comes from the relative change in most instances. Large-scale fundamental models are mostly responsible for the coarser texture. The basic models of minute size always represent the finer texture in a similar way. The spotlight has been shone on a feast of creative techniques meant to coerce the texture features in this way. There are many different types of texture feature extraction techniques, such as spectral texture feature extraction techniques and spatial texture feature extraction techniques, depending on the domain from which the feature is extracted.

C. Multi-Texton Features

Textons are generally portrayed as a collection of blobs or embryonic patterns that exhibit a consistent character across the image, while a specific definition of textons is not yet possible. The pre-attentive distinction is somewhat diminished if the texture pieces are stretched out very far in one orientation. The texton-gradients at the texture boundaries are improved if the stretched-out elements are not jittered in orientation. Because the texture gradients only exist at the texture boundaries, the texture discrimination can be increased with a small element dimension like this. This, together with the block's simplicity of expression, is why textons detection is used in this page.

D. Feature Extraction from Visuals

The visual search is a type of conceptual function that invites attention and traditionally permits an active scan of the visual scene for the goal amid other objects or features (the distractors). We first extort the Bag of visual words as the feature extraction from the photos (BOW). Additionally, we implement this functionality using the SIFT and K-Means techniques.

A group of mathematical approaches known as edge detection are focused on locating the locations in digital images where there are sharp brightness variations or, more precisely, breaks. Edges are likely integrated by the detection of brief linear edge segments and the accumulation of edges into prolonged edges. There are numerous techniques to position the edges, including the Laplacian Roberts, Sobel, and gradient.

The k-Nearest Neighbors algorithm is widely regarded as a non-parametric method for classification and regression. The most common distance function is the Euclidean distance, which is how people typically think about distance in the actual world:

$$d_{Euclidean}(x, y) = \sqrt{\sum_i (x_i - y_i)^2} \tag{4}$$

When measuring the distance, some characteristics with high values, like income, can outweigh the influence of other features that are assessed on a smaller scale. When dealing with continuous data, min-max normalization or Z-score standardization can be used successfully.

Min–max normalization:

$$X^* = \frac{X - min(X)}{range(X)} = \frac{X - min(X)}{max(X) - min(X)} \tag{5}$$

Z-score standardization:

$$X^* = \frac{X - mean\,(X)}{SD\,(X)} \tag{6}$$

$$F = 2 * \left(\frac{precision * recall}{precision + recall}\right) \tag{7}$$

VI. RESULTS AND DISCUSSION

Based on the assessment criteria, such as Precision, Recall, and Accuracy, the performance of our proposed image retrieval and classification job is assessed. The outcomes of linked recovered photos are created for the test images made available.

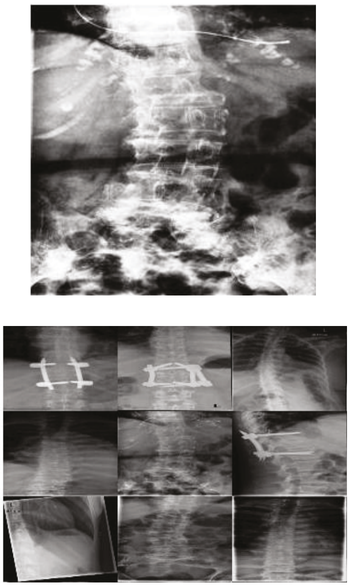

Figure 7. Backbone Input and Retrieved Images

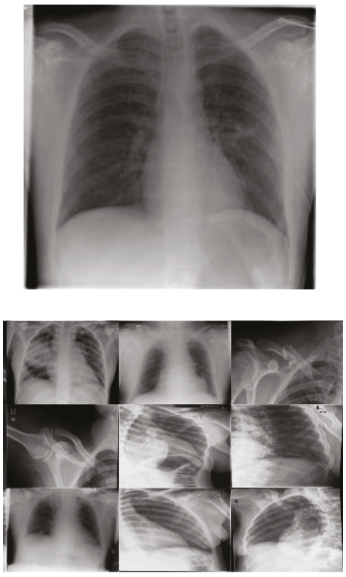

Figure 8. Chest Input and Retrieved Images

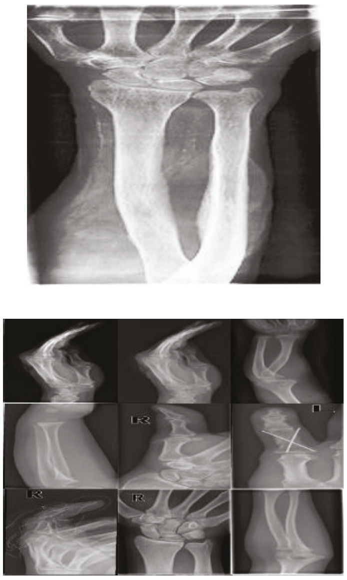

Figure 9. Hand Input and Retrieved Images

TABLE I.
PRECISION

	Hand Bone	Back Bone	Chest Bone
SVM	94.2	93.7	93.3
Naïve Bayes	82.4	87.5	86.6
KNN	92.8	90.5	91.8

TABLE II.
RECALL

	Hand Bone	Back Bone	Chest Bone
SVM	92.1	91.7	90.3
Naïve Bayes	87.2	85.5	87.3
KNN	90.5	89.2	88.7

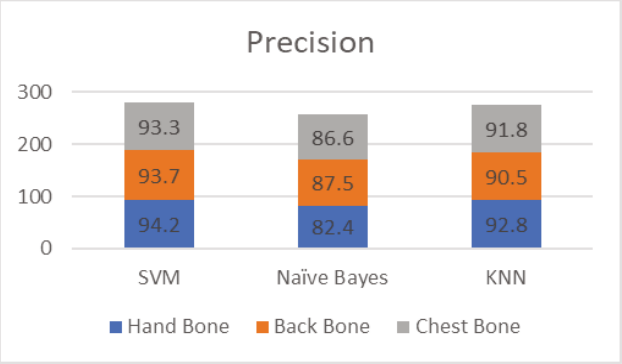

Figure 9. Preciosion for SVM, NB, and KNN

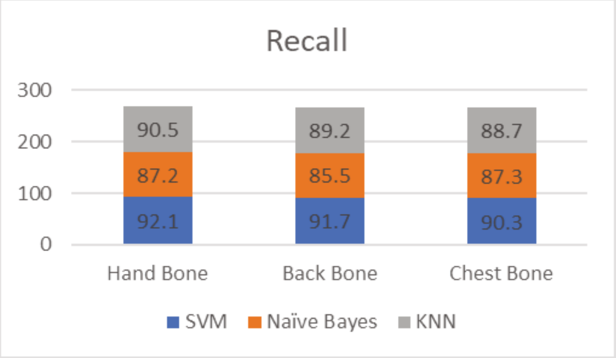

Figure 10. Recall for SVM, NB, and KNN

VII. CONCLUSIONS

The two steps implemented are feature extraction and picture retrieval. The evaluation results of our recommended SVM method have shown that it is the most effective. We have applied the SVM algorithm on average to get 93% accuracy. Additionally, a comparison between the Naïve Bayes and KNN was done. Our suggested SVM image retrieval and classification algorithm outperforms the competition, according to analysis from the comparison. The MATLAB platform was used to implement our method. The proposed method achieves greater precision values when compared to existing methods. The same can be implemented on Google Colab environment for more accurate results while considering more data sets.

REFERENCES

[1] Stefanos Vrochidis, Symeon Papadopoulos, Anastasia Moumtzidou, Panagiotis Sidiropoulos, Emanuelle Pianta and Ioannis Kompatsiaris, "Towards content-based patent image retrieval: A framework perspective", Elsevier Journal of World Patent Information, pp.94-106, 2010.

[2] Ch.Srinivasa Rao, S.Srinivas Kumar and B.Chandra Mohan, “Content-based Image Retrieval Using Exact Legendre Moments And Support Vector Machine”, The International Journal of Multimedia and Its Applications, Vol.2, No.2, May 2010.

[3] A. Srinivasa Reddy, P. Chenna Reddy, MRI brain tumor segmentation and predict ion using modified region growing and adaptive SVM, Soft Comput. 25(2021) 4135–4148.

[4] Nidhi Singh, Kanchan Singh and Ashok K. Sinha, "A Novel Approach for Content Based Image Retrieval", Elsevier Journal of Procedia Technology, pp.245-250, 2012.

[5] A. Srinivasa Reddy, Effective CNN-MSO method for brain tumor detection and segmentation, Materials Today: Proceedings, Volume 57, Part 5, 2022, Pages 1969-1974.

[6] Sahith, R. and Reddy, P. V. P. (2019). Decision tree based machine learning algorithms to classify rice plant diseases. International Journal of Innovative Technology and Exploring Engineering, 9(1): 5365–5368.

[7] Reddy, A.S. and P.C. Reddy. Novel Algorithm based on Region Growing Method for Better Image Segmentation. in 2018 3rd International Conference on Communication and Electronics Systems (ICCES). 2018. IEEE.

[8] G Malleswari, "Significance of Genetic Algorithms in Image Segmentation", International Journal of Signal Processing, Image Processing and Pattern Recognition,9(4), 177-184.

[9] G. Malleswari and A. S. Reddy, "Diverse Convolutional Neural Network Models for Feature Extraction from Brain Tumor Images," 2023 7th International Conference on Computing Methodologies and Communication (ICCMC), Erode, India, 2023, pp. 405-410.

[10] A. S. Reddy and G. Malleswari, "Adaptive Energy Routing Protocol using Spider Optimization in Wireless Sensor Networks," 2023 International Conference on Computer Communication and Informatics (ICCCI), Coimbatore, India, 2023, pp. 1-6.

E-ISSN 2581 – 7957
P-ISSN 2277 – 3916

CVR Journal of Science and Technology, Volume 24, June 2023
DOI: 10.32377/cvrjst2410

Improved Bandwidth Allocation based on History in BWA Networks

M. Deva Priya
Assoc. Professor, Sri Eshwar College of Engineering/CSE Department, Coimbatore, Tamilnadu, India
Email: devapriya.m@sece.ac.in

Abstract: **WiMAX is a wireless technology that supports several applications. To efficiently assign resources to different kinds of traffic, Bandwidth Allocation (BA) module is included in MAC layer. The key goal is to reduce delay and make efficient use of available frame space, thereby reducing Information Element (IE) overheads. In this paper, Bandwidth Allocation based on History (BAH) is proposed for allocating bursts in WiMAX networks. BAH scheme focuses on assigning bandwidth depending on Expended as well as Fairness levels. Performance of the propounded mechanism is analyzed based on Throughput, Packet Loss Ratio (PLR) and Average Delay.**

Index Terms: **WiMAX, bandwidth, Expended and Fairness levels,**

I. INTRODUCTION

Worldwide Interoperability for Microwave Access (WiMAX), IEEE Std 802.16-2005 is a telecommunication protocol which offers fixed as well as mobile access to internet [1]. Broadband Wireless Access (BWA) technology is based on IEEE 802.16 standard [2]. WiMAX network includes comparatively reduced cost in contrast to DSL, GSM or Fiber-Optics [3]. WiMAX replaces cellular technologies like GSM and CDMA. It involves 2 modes namely, Point-to-Multipoint (PMP) or mesh mode based on applications [4]. It offers increased coverage as well as bandwidth supporting last-mile access to the Internet.

WiMAX supports real-time as well as non-real time communications. Real-time traffic flows include Unsolicited Grant Service (UGS) as well as real-time-Polling Services (rtPS). Non-real time services include non-real-time-Polling Services (nrtPS) as well as Best Effort (BE) services [5]. Traffic from a Mobile Subscriber Station (MSS) should be scheduled and essential bandwidth must be assigned to every flow dynamically [6]. Every MSS shares a dynamic Burst Profile (BP) with the Base Station (BS). BPs are determined depending on Quality of Service (QoS) demands as well as channel conditions.

BS allocates bandwidth depending on diverse factors like demanded bandwidth, QoS and available resources. Grants are represented using an Uplink (UL)-MAP. MSS forwards BW-REQs to the BS using any one of ensuing methods.

- ✓ It may forward a BW-REQ in the granted slot assigned through polling.
- ✓ When polled by BS, it may use contention request interval based on broadcast or multicast poll.
- ✓ It may piggyback BW-REQ on packets containing data.

The BW-REQs are incremental [7]. When an MSS is in short of bandwidth, it sends incremental requests. BS adds the demanded bandwidth to the requirement observed for MSS [8]. An MSS establishes connections with BS for connection-based BW-REQs. The fundamental schemes for sending BW-REQs in WiMAX include:

- ✓ **Contention-based Random Access:** The MSS forwards a BW-REQ during contention period.
- ✓ **Contention-free based Polling Access:** BS preserves details of registered MSSs and every MSS forwards a BW-REQ only after polling.
- ✓ **Grouping mode:** Random access scheme is linked with polling. On polling a group, MSSs contend for sending BW-REQs. This is appropriate when BS do not have sufficient bandwidth to independently poll every MSS.

In this paper, Bandwidth Allocation based on History (BAH) scheme is proposed which assigns bandwidth to flows in present round depending on requests' Arrival Rate (λ), Expended as well as Fairness levels of assigned bandwidth.

II. RELATED WORK

Gakhar et al (2006) [9] have proposed a dynamic resource reservation scheme which varies the quantity of resources reserved depending on actual amount of active connections. Park et al. (2008) [10] have proposed a dynamic bandwidth allocation mechanism for handling real-time services by predicting the quantity of requested bandwidth depending on backlogged traffic and rate mismatch amid packet arrival and service rates. De Rango & Malfitano (2009) [11] have proposed Greedy Choice with Bandwidth Availability aware Defragmentation (GCAD-CAC) which preempts accepted calls on arrival of calls with high priority. Defragmentation of gaps between data sub-frames takes place. Lakshmanan et al (2009) [12] have considered bandwidth allocation and call admission based on possibility of handover as well as call arrival at the MSS. Chuck & Chang (2010) [13] have performed bandwidth recycling for reclaiming unused bandwidth from MSs without altering the present bandwidth reservation, thus ensuring QoS. Antonopoulos et al. (2010) [14] have designed a call admission mechanism based on bandwidth reservation for peak hour traffic to offer increased priority to VoIP calls.

Nasser et al. (2011) [15] have proposed Utility Optimized QoS (UOQoS) mechanism for mobile WiMAX which focuses on bandwidth utilization as well as acceptance of fresh as well as handover calls by linking a utility function to every connection. Sheu et al (2011) [16] have proposed

Received on 06-04-2023, Revised on 27-04-2023, Accepted on 04-05-2023.

Greedy Weighted Algorithm (GWA) to assign bandwidth for video multicast in relay networks so as to circumvent duplicate bandwidth allocation. Bounded GWA (BGWA) is also propounded. Gupta et al (2012) [17] have designed Efficient Bandwidth Management (EBM) to deal with efficient bandwidth allocation to increase bandwidth in ensuing time frame if there is inadequacy in the present time frame and vice-versa. Sheu et al. (2013) [18] have proposed approximation based resource allocation mechanism that focusses on improving utilization of DL bandwidth by sorting requests and dynamically assigning bandwidth.

Pillappaiah et al (2013) [19] have classified users depending on priority and dependency or independency of networks for resource allocation. Chern & Xu (2013) [20] have designed a mechanism wherein, bandwidth is reserved for every connection and Weighted Fair Queuing (WFQ) algorithm is used for scheduling the requests. Based on lengths of queues and connection classes, weights are assigned. Furqan & Hoang (2013) [21] have proposed WiMAX Fair Intelligent Congestion Control (WFICC) which finds the network load depending on borrowing of bandwidth and degradation of highly provisioned connections.

El Bouchti et al (2014) [22] have propounded a scheme for dynamically allocating bandwidth and admitting calls for polling services by using game theory. Non-cooperative 2-person common-sum game is framed, where BS and a fresh connection acts as players. Accepting or declining a connection along with quantity of bandwidth assigned to a connection is considered. Queuing model based on Adaptive Modulation and Coding (AMC) in physical layer is involved in analyzing the QoS of rtPS and nrtPS services.

El-Hammani et al (2017) [23] have focused on link variations while designing call admission schemes for handling real-time traffic. Diverse scenarios for splitting bandwidth as well as handling mobility are considered. Low and high mobility classes are focused on.

Niyato & Hossain (2018) [24] have designed a fuzzy logic-based admission controller for OFDMA-based networks. Factors like peak traffic rate, quality of channel, traffic load are considered for estimating intensity of traffic arrival, allocating available radio resources and admitting or blocking connections. A queueing model is used and packet-level QoS obtained aids in establishing inference rules for resource-allocation. Ahmed et al (2019) [25] have proposed a 2-level scheduling scheme for Base Station (BS) UL scheduler to ensure Quality of Service (QoS) to several traffic classes. It guarantees effectual and reasonable transmission of multimedia.

Ibrahim et al (2022) [26] have dealt with the additional bandwidth which is not utilized. It is recycled so as to improve QoS and conserve the present bandwidth reservation. Bandwidth may be available with the subscribers in addition to that of Downlink (DL) and UL. A suitable scheduling mechanism related to Round Robin (RR) is proposed. Idle bandwidth is reused.

Hindumathi et al (2023) [27] have concentrated on using optimized bandwidth and rejecting ongoing calls in addition to freshly connected calls. A unique and appropriate utility function is assigned to every connection. The proposed framework guarantees high-quality service to both real-time and non-real-time traffic. 2-level scheduling scheme is proposed for BS schedulers involved at UL so as to render service with improved quality to diverse traffic flows.

III. PROPOSED MODEL

The proposed BAH scheme allocates bandwidth to every flow in the present round by taking the consistency of assignment and bandwidth usage in previous round into consideration.

A. Bandwidth Allocation based on History (BAH)

BAH dynamically allocates bandwidth to flows depending on diverse factors from former round. It considers the ensuing factors:

- ✓ Traffic Arrival Rate (λ_{Pres})
- ✓ Bandwidth assigned in former round (B_{Alloc}^{Prev})
- ✓ Fairness level (F_{Prev})
- ✓ Expended level (E_{Prev})
- ✓ Available bandwidth (B_{Avail}^{Prev})
- ✓ Extra bandwidth (B_{Add}^{Prev})

BAH computes the Fairness level by taking the quantity of demanded and assigned bandwidth for every flow in previous round into consideration. Service flows request for some amount of bandwidth (B_{Req}^{i}). BAH module focuses on allocating a portion of whole volume of demanded bandwidth. Let bandwidth required by every flow be 'B_{Need}^{i}'. The amount of bandwidth demanded is the difference between requested and assigned bandwidth.

$$B_{Need}^{i} = B_{Req}^{i} - B_{Alloc}^{i} \tag{1}$$

Available bandwidth (BW_{Avail}^{i}) is evenly distributed to degraded flows as assigned to every MSS during handover. Every flow gets a share depending on the need.

$$\gamma = \frac{B_{Avail}^{T}}{\sum_{i=1}^{n} B_{Need}^{i}} \tag{2}$$

where,

n - Number of degraded flows

B_{Need}^{i} - Quantity of bandwidth needed by every flow

B_{Add}^{i} - Extra bandwidth which is allotted to every flow for upgrading

Every flow gets the share.

$$B_{Add}^{i} = \gamma * BW_{Need}^{i} \tag{3}$$

The additional bandwidth assigned to every flow in former round, '$B_{Add}^{i,Prev}$' is computed as:

$$B_{Add}^{i,Prev} = \frac{B_{Need}^{i}}{\sum_{i=1}^{n} B_{Need}^{i}} * B_{Avail}^{O,Prev} \tag{4}$$

For a flow (i),

$$\delta_i = \frac{B_{Need}^{i}}{\sum_{i=1}^{n} B_{Need}^{i}} \tag{5}$$

Where,

δ_i - Ratio of demanded bandwidth to total need

Then,

$$BW_{Add}^{i,Prev} = \delta_i * BW_{Avail}^{O,Prev} \tag{6}$$

Depending on quantity of bandwidth required by every flow, 'δ_i' varies. Overall Fairness level (F^{O}_{Pres}) is computed as,

$$\beta_i = \frac{B^{i}_{Add,Prev}}{B^{i,Prev}_{Need} * \delta_i} \tag{7}$$

$$F^{O}_{Pres} = \sum_{i=1}^{n} \frac{B^{i,Prev}_{Alloc}}{B^{i,Prev}_{Req}} * \beta_i \tag{8}$$

$$F^{O}_{Pres} = \sum_{i=1}^{n} \frac{B^{i,Prev}_{Req} - B^{i,Prev}_{Need}}{B^{i,Prev}_{Req}} * \beta_i \tag{9}$$

$$F^{O}_{Pres} = \sum_{i=1}^{n} 1 - \frac{B^{i,Prev}_{Need}}{B^{i,Prev}_{Req}} * \beta_i \tag{10}$$

When less quantity of bandwidth is needed, fair bandwidth allocation contributes to increased Fairness level.

Besides Fairness level, overall Expended level is the level of use of assigned bandwidth. It is the proportion of throughput got in former round to assigned bandwidth.

$$E^{O}_{Pres} = \sum_{i=1}^{n} \frac{Th^{i}_{Prev}}{B^{i,Prev}_{Alloc} + B^{i,Prev}_{Add}} \tag{11}$$

$$B^{i}_{Tot} = B^{i}_{Alloc} + BW^{i}_{Add} \tag{12}$$

$$E^{O}_{Pres} = \sum_{i=1}^{n} \frac{Th^{i}_{Prev}}{B^{i}_{Tot}} \tag{13}$$

Sum of Fairness as well as Expended levels is given by,

$$D = F_{Pres} + E_{Pres} \tag{14}$$

As already mentioned, bandwidth is assigned to each flow in present round in terms of Fairness as well as Expended levels.

If bandwidth is assigned more than the essential, then these levels will have high values. In that case, assigned bandwidth is directly based on Arrival Rate (λ_{PREV}) of former round. A portion of available bandwidth is assigned for a flow 'N' depending on demanded additional bandwidth.

$$B^{Next}_{Alloc} = \left(\frac{\lambda_{Pres}{}^{N}}{\lambda_{Pres}{}^{O}}\right) \tag{15}$$

If bandwidth allocated to a flow is less than demanded, then both levels represent minimum values. The possible maximum bandwidth should be assigned.

$$B^{Next}_{Alloc} = \left(\frac{((1+D)\lambda_{Pres})^{N}}{((1+D)\lambda_{Pres})^{O}}\right) * BW^{O,Pres}_{Avail} \tag{16}$$

If bandwidth is not justly allocated, then Fairness level shows a lesser value. It is assigned depending on Fairness level.

$$B^{Next}_{Alloc} = \left(\frac{((1+F_{Pres})\lambda_{Pres})^{N}}{((1+F_{Pres})\lambda_{Pres})^{O}}\right) \times B^{O,Pres}_{Avail} \tag{17}$$

If bandwidth is not properly used, then Expended level indicates a lesser value. Bandwidth is assigned depending on Expended level.

$$B^{Next}_{Alloc} = \left(\frac{((1+E_{Pres})\lambda_{Pres})^{N}}{((1+E_{Pres})\lambda_{Pres})^{O}}\right) \times B^{O,Pres}_{Avail} \tag{18}$$

Variance of CD (VCD) varies with the number of connections currently established. Connections are accepted only when VCD is less than the threshold. After repeated iterations, it was decided to set the threshold to 0.8.

IV. RESULTS AND DISCUSSION

The system is implemented using Ns2. Parameters involved in simulation are shown in Table 1.

TABLE I.
SIMULATION PARAMETERS

PARAMETER	VALUE
MAC	IEEE 802.16e
Routing Protocol	DSDV
Frame Length	0.004
Queue length	50
Packet Size	1492 bytes
Number of MSSs	50
Start Time/ Stop Time	20 sec / 120 sec

The proposed BAH scheme yields better results. The performance of BAH is compared with Bandwidth Allocation scheme Without History (BAWH) depending on Dynamic QoS-based Bandwidth Allocation (DQBA).

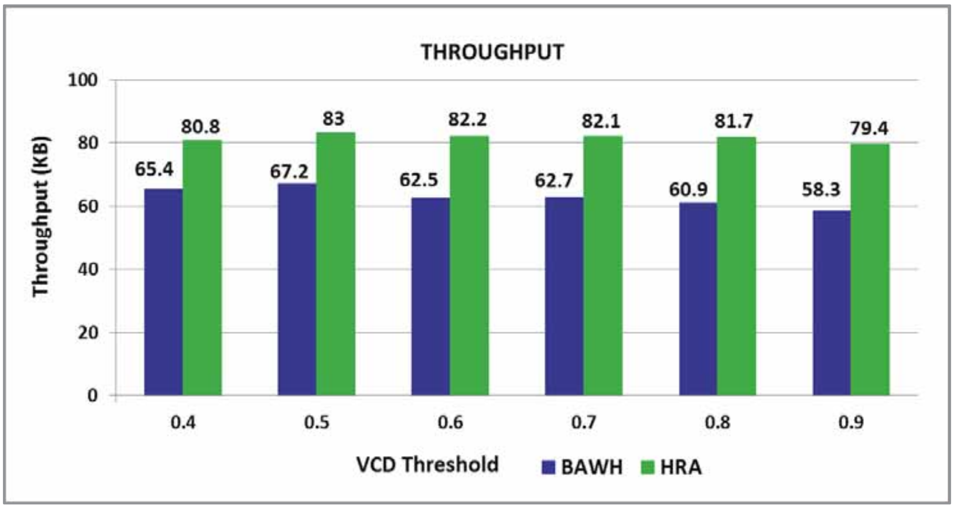

Figure 1. Throughput

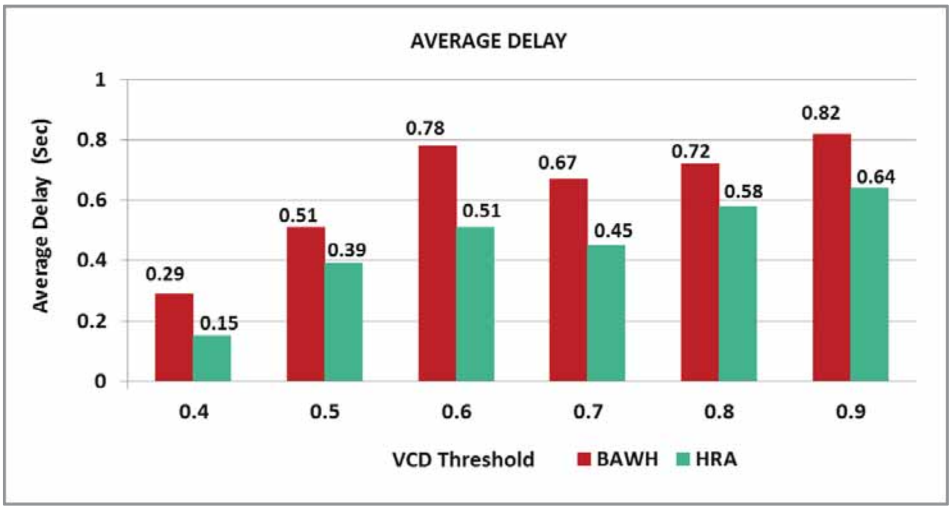

Figure 2. Average Delay

Fig. 1 shows the Throughput. BAH offers 18.7% better Throughput when compared to BAWH.

Fig. 2 shows the Average Delay. BAH involves 39.34% reduced Average Delay in contrast to BAWH.

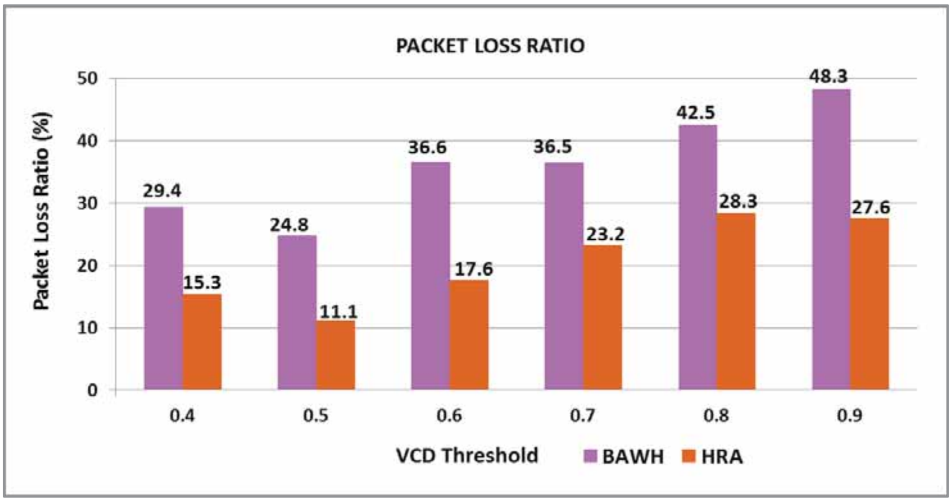

Figure 3. Packet Loss Ratio

Fig. 3 shows the Packet Loss Ratio (PLR). Similarly, BAH involves 15.8% less PLR in contrast to BAWH.

V. CONCLUSIONS

The proposed Bandwidth Allocation based on History (BAH) accepts calls only when the new incoming call does not affect the current QoS. This avoids QoS degradation to a better extent when compared to present mechanisms. The proposed scheme offers improved outcomes based on Throughput, Packet Loss Ratio (PLR) and Average Delay.

REFERENCES

1. IEEE Standard for Local and Metropolitan Area Networks, IEEE Std 802.16-2005, Dec. 2005, Part16: Air Interface for Fixed and Mobile Broadband Wireless Access Systems.
2. Qassem, Y., Al-Hemyari, A., Ng, C., Noordin, N., & Rasid, M. (2009). Review of network routing in IEEE 802.16 WiMAX mesh networks. Australian Journal of Basic and Applied Sciences, 3(4), 3980-3996.
3. Priya, M. D., Valarmathi, M. L., Bharathi, K. J., & Deepa, M. (2013). BAC: Bandwidth based Admission Control Scheme for Gateway Relocation in IEEE 802.16e Networks, 4(1), pp. 699-705
4. Ohrtman, F. (2005). WiMAX handbook. McGraw-Hill Professional Publishing.
5. Guice, R. J., & Munoz, R. J. (2004). IEEE 802.16 commercial off the shelf (cots) technologies as a compliment to ship to objective maneuver (stom) communications. Naval Postgraduate School Monterey CA.
6. Chu, G., Wang, D., & Mei, S. (2002). A QoS architecture for the MAC protocol of IEEE 802.16 BWA system. In IEEE International Conference on Communications, Circuits and Systems and West Sino Expositions, 1, 435-439.
7. Ohrtman, F 2005, WiMAX Handbook, McGraw-Hill, Inc. ISBN: 0-07-145401-2.
8. Guice, R.J., & Munoz, R.J. (2004). IEEE 802.16 Commercial Off The Shelf (COTS) technologies as a compliment to Ship To Objective Maneuver (STOM) communications, Published Thesis, Naval Postgraduate School.
9. Gakhar, K., Achir, M., & Gravey, A. (2006). Dynamic resource reservation in IEEE 802.16 broadband wireless networks. In14th IEEE International Workshop on Quality of Service, pp. 140-148.
10. Park, E. C., Kim, H., Kim, J. Y., & Kim, H. S. (2008). Dynamic bandwidth request-allocation algorithm for real-time

services in IEEE 802.16 broadband wireless access networks. In IEEE INFOCOM 2008-The 27th Conference on Computer Communications, pp. 852-860.

11. De Rango, F., & Malfitano, A. (2009). Bandwidth availability aware defragmentation based CAC algorithm for IEEE 802.16 distributed mesh networks. In IEEE International Symposium on Performance Evaluation of Computer & Telecommunication Systems, Vol. 41, pp. 146-153.
12. Lakshmanan, M., Mohammed, V. N., & Nandakumar, S. (2009). QoS provisioning for mobile and fixed wireless real time multimedia services. In IEEE International Conference on Internet Multimedia Services Architecture and Applications (IMSAA), pp. 1-6.
13. Chuck, D., & Chang, J. M. (2010). Bandwidth recycling in IEEE 802.16 networks. IEEE Transactions on Mobile Computing, 9(10), 1451-1464.
14. Antonopoulos, A., Skianis, C., & Verikoukis, C. (2010). Traffic-aware connection admission control scheme for broadband mobile systems. In IEEE Global Telecommunications Conference GLOBECOM 2010, pp. 1-5.
15. Nasser, N., Miller, R., Esmailpour, A., & Taha, A. E. M. (2011). Utility optimized bandwidth allocation in WiMAX networks. In 7th IEEE International Wireless Communications and Mobile Computing Conference, pp. 540-545.
16. Sheu, J. P., Kao, C. C., Yang, S. R., & Chang, L. F. (2011). A resource allocation scheme for scalable video multicast in WiMAX relay networks. IEEE Transactions on Mobile Computing, 12(1), 90-104.
17. Gupta, A., & Chandavarkar, B. R. (2012). An Efficient Bandwidth Management algorithm for WiMAX (IEEE 802.16) wireless network: EBM allocation algorithm. In 7th IEEE International Conference on Industrial and Information Systems (ICIIS), pp. 1-5.
18. Sheu, J. P., Ko, C. H., & Ma, C. (2013). An approximation downlink bandwidth allocation scheme for IEEE 802.16 OFDMA system. In IEEE Wireless Communications and Networking Conference (WCNC), pp. 327-332.
19. Pillappaiah, S., Sarkar, M., Nagaraj, S., & Paolini, C. (2013). Auction based resource allocation in WiMAX. In 9th IEEE International Wireless Communications and Mobile Computing Conference (IWCMC), pp. 288-293.
20. Chern, H., & Xu, B. (2013). The bandwidth allocation by queue length (BA-QL) for WiMAX network. In 3rd IEEE International Conference on Information Science and Technology (ICIST), pp. 1076-1080.
21. Furqan, F., & Hoang, D. B. (2013). Wireless Fair Intelligent Admission Control-WFIAC. In 27th IEEE International Conference on Advanced Information Networking and Applications (AINA), pp. 1001-1008.
22. El Bouchti, A., Haqiq, A., & Benjelloun, A. (2014). Non-cooperative game for admission control and bandwidth allocation in WiMAX networks. In 4th edition of the IEEE International Conference on the Innovative Computing Technology (INTECH 2014), pp. 225-230.
23. El-Hammani, S., Ibrahimi, K., Bouyakhf, E. H., & El-Azouzi, R. (2017). Mobility management schemes for real-time traffic and resource allocation in IEEE 802.16 e mobile network. International Journal of Communication Systems, 30(1), e2926.
24. Niyato, D., & Hossain, E. (2018). Resource allocation and admission control using fuzzy logic for OFDMA-based IEEE 802.16 broadband wireless networks. In WiMAX (pp. 249-280). CRC Press.
25. Ahmed, Z., Hamma, S., & Nasir, Z. (2019). An optimal bandwidth allocation algorithm for improving QoS in WiMAX. Multimedia Tools and Applications, 78(18), 25937-25976.
26. Ibrahim, A. A., Salsabil, S. I., & Lawal, I. A. (2022). Effective Utilization of An Unused Bandwidth in IEEE 802.16 Network. Journal of Telecommunication, Electronic and Computer Engineering (JTEC), 14(2), 15-22.
27. Hindumathi, V., Veeramalla, S. K., & Vasudeva Reddy, T. (2023). Adaptive Resource Allocation in WiMAX Networks for Improved Quality of Service (QoS). In Intelligent Data Engineering and Analytics: Proceedings of the 10th International Conference on Frontiers in Intelligent Computing: Theory and Applications (FICTA 2022) (pp. 625-633). Singapore: Springer Nature Singapore.

E-ISSN 2581 – 7957
P-ISSN 2277 – 3916
CVR Journal of Science and Technology, Volume 24, June 2023
DOI: 10.32377/cvrjst2411

Implementing a Linear Regression Gradient Descent Model for Admission Process Framework

Ajeet K. Jain[1] and K. Venkatesh Sharma[2]
[1]Asst. Prof., Keshav Memorial Institute of Technology/ CSE Department, Hyderabad, India
Email: jainajeet123@gmail.com
[2]Professor, CVR College of Engineering/CSE Department, Hyderabad, India
Email: venkateshsharma.cse@gmail.com

Abstract: **Machine Learning (ML) is the fundamental learning paradigm in the scientific community having a wide range of applications in vivid domains. The hidden underlying patterns in data can be easily identified with use of popular ML algorithms. The meaningful pattern provides insight information extracted from the data. In so doing, human incapability hinders the process of recognising meaningful patterns in the given data sets. Such fine exemplary thoughts are given to machines with suitable algorithms and it can detect not only the finer patterns, but also provides meaningfulness of data spread in the domain. The area of ML is a blend of mathematics, probability, statistics and allied sciences in an articulated way and thus endows the ability to "learn *and adapt*". A generalized Gradient Descent (GD) based model is proposed which can be implemented on any dataset. The model is tested to forecast a student's admission on his (her) GRE score. Proposed model reflects good accuracy and the Pearson Correlation coefficient suggests the pertinent relationship among different attributes. The model also focuses the underlying mathematical derivation to a minimum to comprehend.**

Index Terms: **Linear Regression, Gradient Descent, RMS Error, MSE, ERM, Pearson Correlation**

I. INTRODUCTION

Linear regression finds a relationship between a dependent variable for a given set of independent variables—also known as a relationship involving *explanatory variables* and some real estimated *outcome*. The traditional straight-line equation $\mathbf{y = m\,x + b}$; is used to estimate '**y**' for a given set of '**x**' with bias matrix **'b'** and the domain X consists of $\mathbb{R}^{\mathbf{d}}$ and the label set $\mathbf{y} \in \mathbf{Y}$ is the set of real numbers for a given **d** [1]. A linear function $\boldsymbol{h} : \mathbb{R}^d \mapsto \mathbb{R}$ that suitably estimates the relationship between given variables—for instance, predicting probability of getting the admission as a function of GRE score. [2] This, when combined with standard GD mechanism, can provide a fairly good idea how the blending works in ML for a given application domain and the generalized model is shown in Figure 1.

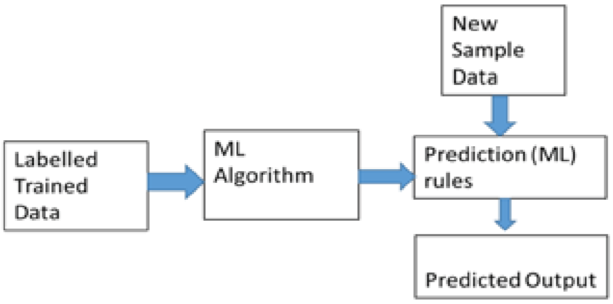

Figure 1. A Generic ML GD model framework

A. Linear Regression

A linear regressor is basically the set of linear functions [2]:

$$H_{reg} = L_d = \{x \mapsto \langle w, x \rangle + b : w \in R^d, b \in R \qquad (1)$$

Here $\boldsymbol{H_{reg}}$ is a regression function; **x** is input space, and b as bias. Intuitively, to lessen the difference between actual and expected values, [3] we define a loss function calculating the discrepancy of values while using a regressor, in Figure 2. The most generally used squared-loss function is given by:

$$l\,(h, (x, y)) = (h(x) - y)^2 \qquad (2)$$

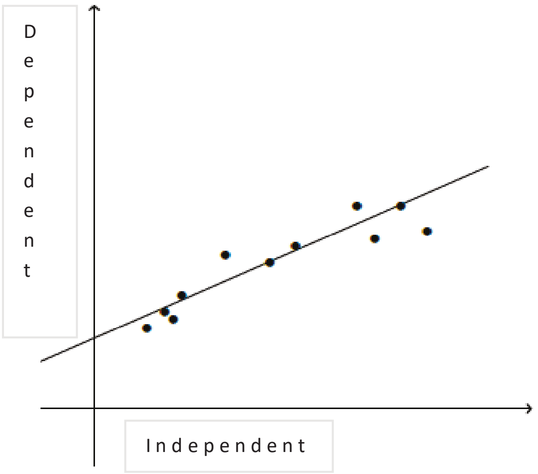

Figure 2. Linear regression showing variables.

Received on 19-01-2023, Revised on 07-03-2023, Accepted on 11-05-2023.

For the observed values, the loss is usually calculated as Mean Squared Error (MSE):

$$Ls(h) = \frac{1}{m}\sum_{1}^{m}(h(xi) - yi)^{2} \qquad (3)$$

[4] where the meaning of all the symbols used are intuitive. Such an algorithm solves the expected risk minimization (ERM) problem for linear regression predictors.

[5] The solution to this equation is to find the derivative, i.e., gradient of the objective function and compare it to zero:

$$\frac{2}{m}\sum_{i=1}^{m}(\langle \mathbf{w}, \mathbf{x}_i\rangle - y_i)\mathbf{x}_i = 0 \qquad (4)$$

This can be simplified in matrix notation form as

Aw = **b** where

$$A = \left(\sum_{i=1}^{m} \mathrm{x}_i \, \mathrm{x}_i^{\top}\right) \quad \text{and} \quad \mathrm{b} = \sum_{i=1}^{m} y_i \mathrm{x}_i . \qquad (5)$$

In other words, in the matrix notation form as:

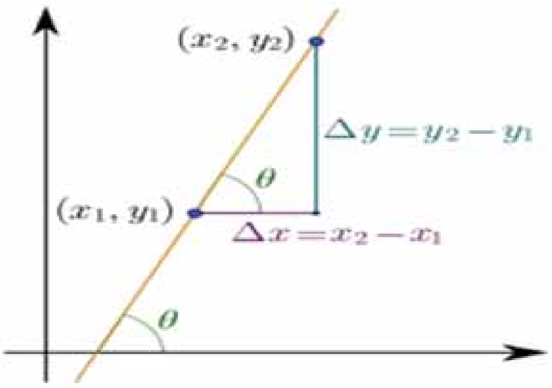

Figure 3. A Gradient vector

The solution to the ERM problem is w = **A** $^{-1}$ **b** when A is invertible**.**

II. GRADIENT

[6] A gradient is a vector generalization of the derivative and we need to calculate its minimum value and moreover, a derivative is a scalar valued. . To be precise, a derivative is defined for functions having a single variable; on the other hand, a function with a number of variables, the gradient definition is a better and intuitive option, as depicted in Figure 3.

[7] More formally, for a given training set **S** and using homogenous description for **L_d** the class of problem towards ERM calculations is to find

$$\text{argmin}L_s(h_w) = \text{argmin } 1/m\sum((w,x_i) - y_i)^2$$

[8] The slope represents the gradient of a graph and directs towards increase or decrease in that direction. To optimize for minimum value, the first-order derivative helps us achieve these using iterations. In order to locate a local minimum using GD optimization, we step proportionally towards negative of the gradient of the function at the current point. [9] On the other hand, when we undertake the steps that are proportional to the estimated gradient, it is termed as gradient ascent [10]. These prevailing methods are robust in use and have found many applications in various domains – as the next section highlights those aspects.

III. GRADIENT DESCENT MODEL

The gradient based method has always been attractive due to its simplicity and robustness in optimization scenarios [1]. For a given machine learning algorithm, a MSE cost (loss) function can evaluate the parameters of the learning model with weights updates. The main focus is to find the set of parameters, i.e., weights which minimize the loss function. [11] This can provide a clue towards reaching local optima. We repeat this process (known as an epoch) until we reach near a valley point, as depicted in Figure 4 where J(w) is a loss unction for the parameter's 'w'. For more on this, one can refer to [1].

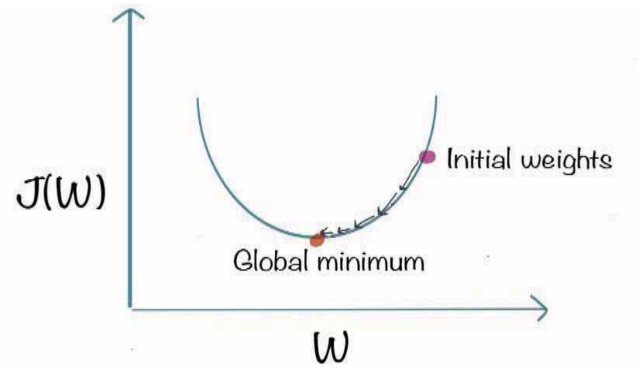

Figure 4. Cost (Loss) function

IV. PEARSON CORRELATION COEFFICIENT ‘R’ (PCC)[1]

In order to find the relationship between the variables, we use the metric of measure as Pearson coefficient – which suggests the strength of the relationship being either ‘*strong*’ or ‘*weak*’ or ‘*none* ’ —we can infer relationships depending upon the value as depicted in Figure 5.

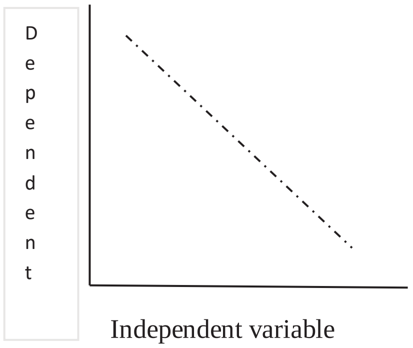

Figure 5(a) r = -1; A perfect negative relationship

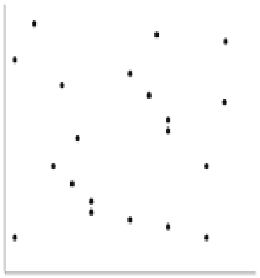

Figure 5 (b). r= 0
No coorelation

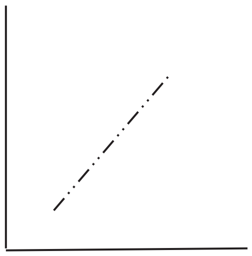

Figure 5 (c) . r = +1
A perfect positive relashion

The scatter plots for various values of ‘r’ suggest the relationships—meaning that in a negative correlation as one variable increases, the other variable decreases; and on other hand, a positive correlation shows that both the variables increase or decrease together.

V. FRAMEWORK

The gradient descent method offers some interesting challenges with good convergence speed, as:

(i) Selecting an optimal value of learning rate is many times not obvious—a smaller value leads to slower convergence whereas a bigger value hinders convergence and causes the loss function to fluctuate around the minimum or even tends to diverge.

(ii) Following the Occam Razor principle in the proposed method, simply start from a lower value and keep judging the accuracy trend and a suggested way would be to keep trying with a learning rate schedule, so that reproducibility of the algorithm is guaranteed. The schedules are to be defined in advance and are sometimes unable to adapt to a dataset's characteristics. This is the preferred way implemented in the work.

(iii) Further, the same learning rate applies to all parameter updates. If the data is sparse with features having different frequencies, it would be wise not to update all of them to the same extent but perform a larger update for rarely occurring features. This adaptivity works well with sparsity of data.

(iv) Most challenging task is to avoid non-convex error functions getting trapped into their numerous local minima sub-optimally—as this difficulty arises not from local minima but from saddle points where one dimension slopes up and other slopes down. These saddle points’ plateau makes the algorithm hard to escape as the gradient is becoming close to zero in all dimensions.

VI. IMPLEMENTATION

The test case implements GD in order to minimize a cost function J (w) parameterized by a model parameter. The gradient (derivative) shows the incline or slope of the cost function. Hence, to minimize the cost function, we move in the direction opposite to the gradient [12].

For a given dataset from Kaggle web site, predicting graduate admission process using GD technique.

The dataset contains several parameters which are considered important during the application for Masters Programs.

The parameters included are:

- GRE Scores (out of 340)
- TOEFL Scores (out of 120)
- University Rating (out of 5)
- Statement of Purpose and Letter of Recommendation Strength (out of 5)
- Undergraduate GPA (out of 10)
- Research Experience (either 0 or 1)
- Chance of Admit (ranging from 0 to 1)

STEPS:

- Import the **csv** file from Kaggle ((https://www.kaggle.com/datasets/mohansacharya/graduate-admissions?select=Admission_Predict_Ver1.1.csv)
- Pre-process data and remove missing or null values.
- Apply gradient descent algorithm.
- Analyse algorithm performance using metrics.

The data set file used is available from Kaggle website and read into the Python environment and using appropriate commands, it shows all the columns under the heading. The corresponding box plot depicts the minimum, average and maximum GRE Score for the admission criterion along with a chance of admission.

Pseudo code for Gradient Descent Model

```
Steps:

Initialize weights 'w' at random
compute gradients $G = \nabla_{w} J(w)$ of loss function wrt parameters, i.e., $G_i = \partial J(w) \partial w_i$
Update weights proportional to G, i.e.
 $w = w - \eta \cdot G$
until J(w) stops reducing or other pre-defined termination criteria is met.
```

Towards this process, the Pearson coefficient method is being applied to know about those attributes having strong and weak relationship, thus profiling the user about the anticipated chances.

Finally, a min-max scaling is applied on the data to reveal the chances of admission.

This implementation is an extension of the standard gradient method making it quite obvious about the results to interpret and thus augmenting the process of knowing the chances. For instance, doing research and making a publication with a professor stands a higher chance, and so are the other factors too. The following screenshots depict various plots. The curve fitted emphasizing the admission process. The relationship plot shows various intriguing parameters and their relative values.

```
df=pd.read_csv('ap.csv')
```

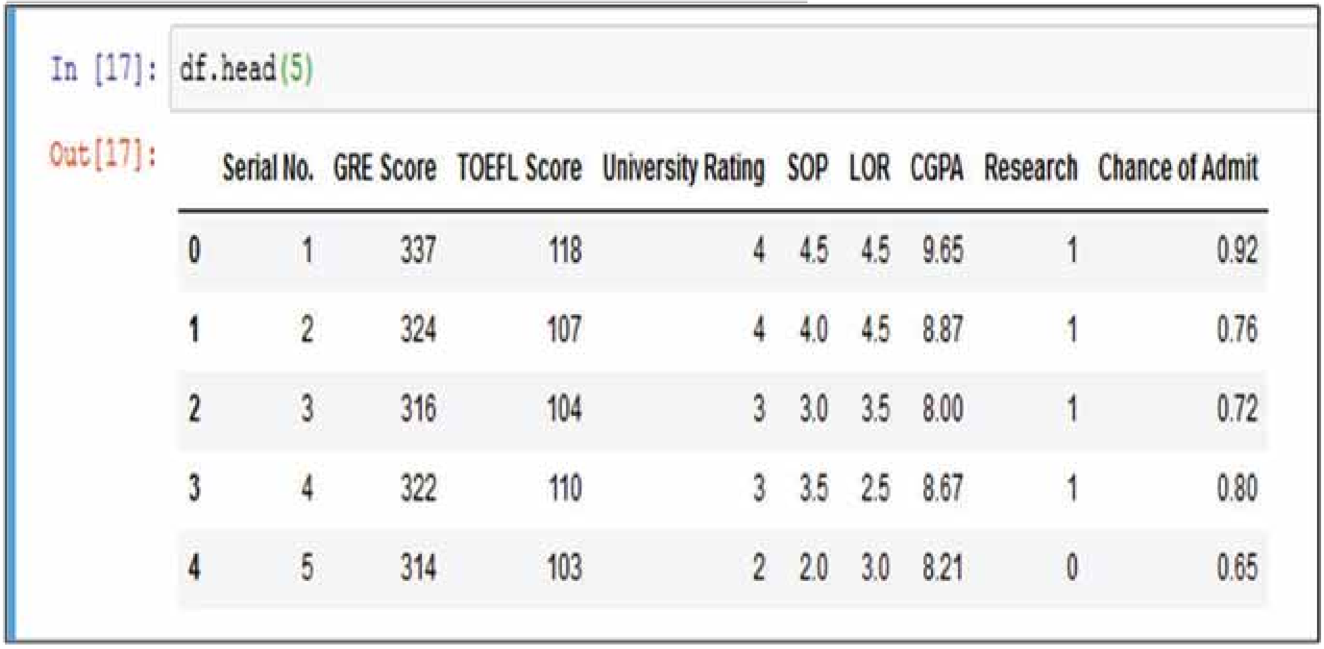

```
In [17]: df.head(5)
```

Out[17]:

	Serial No.	GRE Score	TOEFL Score	University Rating	SOP	LOR	CGPA	Research	Chance of Admit
0	1	337	118	4	4.5	4.5	9.65	1	0.92
1	2	324	107	4	4.0	4.5	8.87	1	0.76
2	3	316	104	3	3.0	3.5	8.00	1	0.72
3	4	322	110	3	3.5	2.5	8.67	1	0.80
4	5	314	103	2	2.0	3.0	8.21	0	0.65

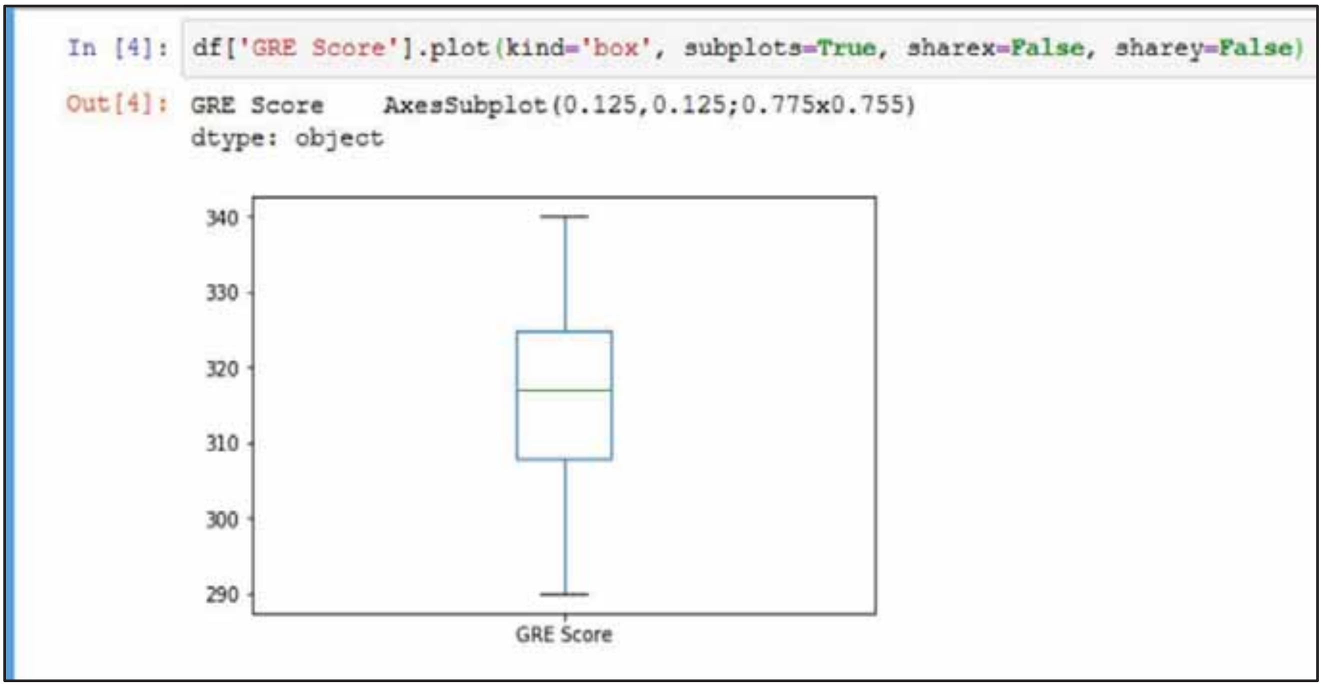

```
In [4]:  df['GRE Score'].plot(kind='box', subplots=True, sharex=False, sharey=False)

Out[4]:  GRE Score    AxesSubplot(0.125,0.125;0.775x0.755)
         dtype: object
```

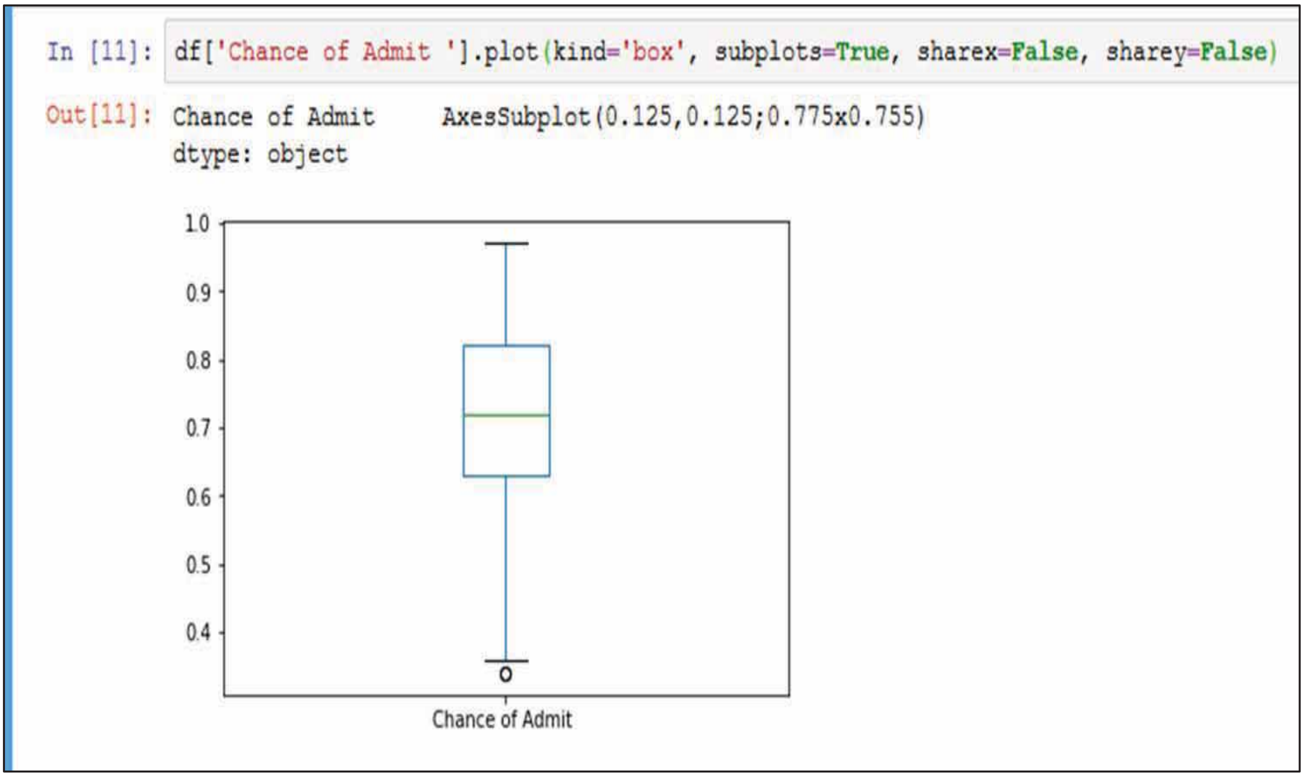

```
In [11]:  df['Chance of Admit '].plot(kind='box', subplots=True, sharex=False, sharey=False)

Out[11]:  Chance of Admit     AxesSubplot(0.125,0.125;0.775x0.755)
          dtype: object
```

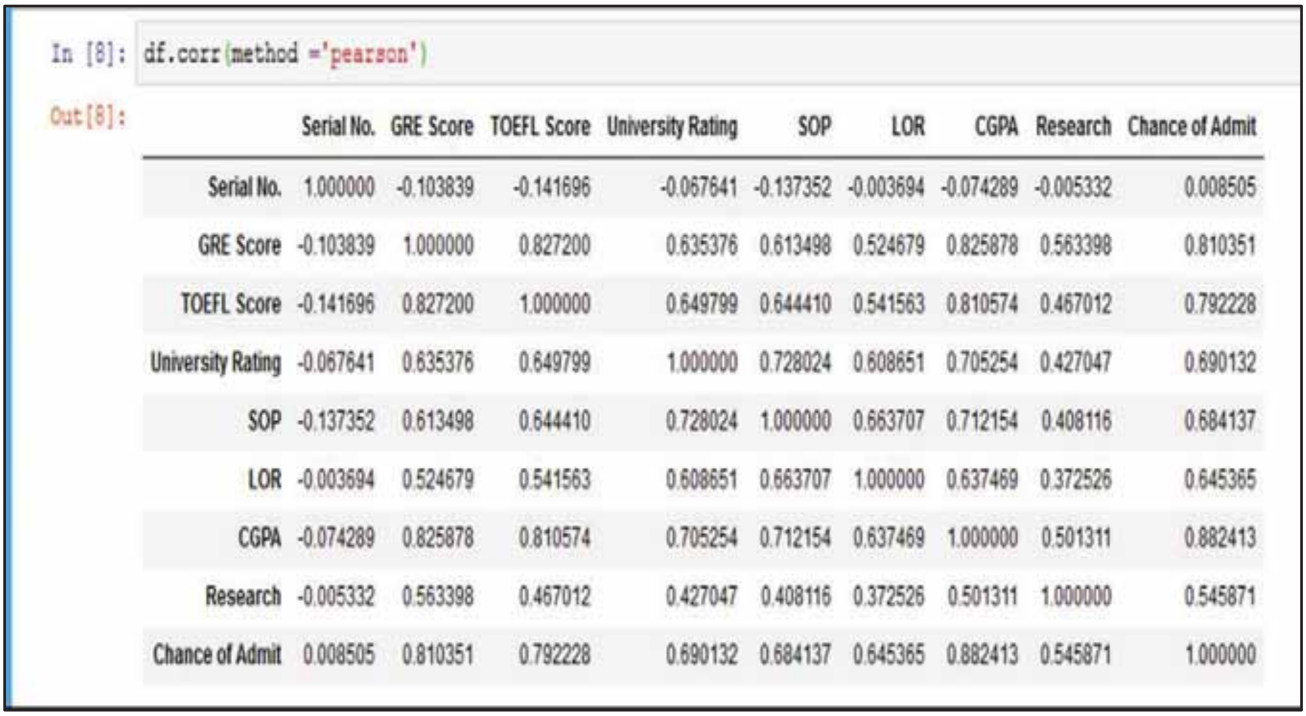

```
In [8]: df.corr(method ='pearson')
Out[8]:
```

	Serial No.	GRE Score	TOEFL Score	University Rating	SOP	LOR	CGPA	Research	Chance of Admit
Serial No.	1.000000	-0.103839	-0.141696	-0.067641	-0.137352	-0.003694	-0.074289	-0.005332	0.008505
GRE Score	-0.103839	1.000000	0.827200	0.635376	0.613498	0.524679	0.825878	0.563398	0.810351
TOEFL Score	-0.141696	0.827200	1.000000	0.649799	0.644410	0.541563	0.810574	0.467012	0.792228
University Rating	-0.067641	0.635376	0.649799	1.000000	0.728024	0.608651	0.705254	0.427047	0.690132
SOP	-0.137352	0.613498	0.644410	0.728024	1.000000	0.663707	0.712154	0.408116	0.684137
LOR	-0.003694	0.524679	0.541563	0.608651	0.663707	1.000000	0.637469	0.372526	0.645365
CGPA	-0.074289	0.825878	0.810574	0.705254	0.712154	0.637469	1.000000	0.501311	0.882413
Research	-0.005332	0.563398	0.467012	0.427047	0.408116	0.372526	0.501311	1.000000	0.545871
Chance of Admit	0.008505	0.810351	0.792228	0.690132	0.684137	0.645365	0.882413	0.545871	1.000000

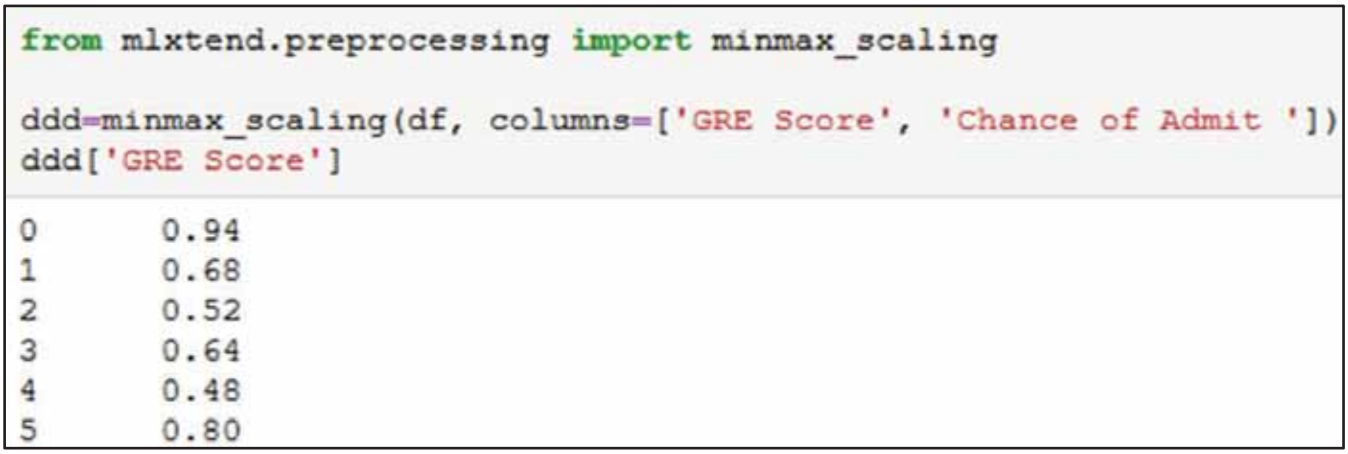

```
from mlxtend.preprocessing import minmax_scaling

ddd=minmax_scaling(df, columns=['GRE Score', 'Chance of Admit '])
ddd['GRE Score']
```

```
0       0.94
1       0.68
2       0.52
3       0.64
4       0.48
5       0.80
```

OUTPUT

```
208.62459057697134
203.67659693403385
198.85546802208228
194.15794742163806
189.58086230330625
185.1211212820759
180.77571232669354
176.5417007227052
172.41622708778274
168.39650543799877
164.47982130373626
160.6635298939625
156.9450543076261
153.32188379096428
149.79157203954514
146.35173554389624
143.00005197759614
139.73425862674856
136.55215085976465
```

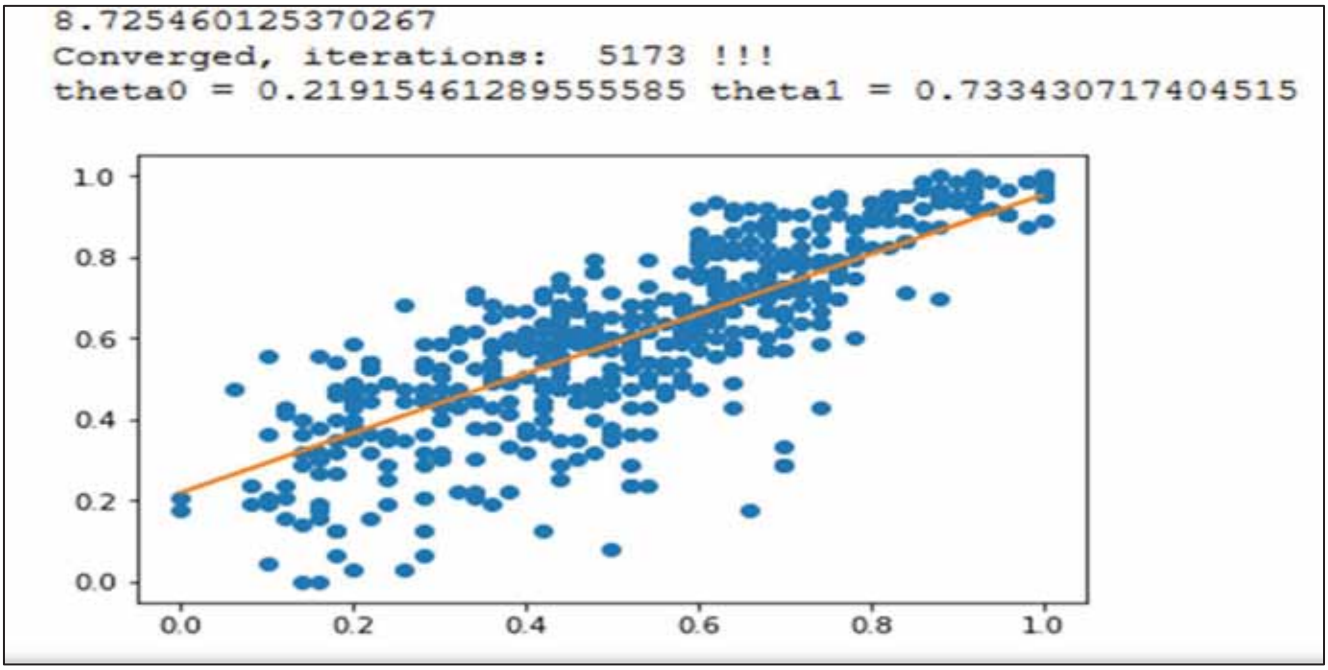

```
8.725460125370267
Converged, iterations:  5173 !!!
theta0 = 0.21915461289555585 theta1 = 0.733430717404515
```

VII. CONCLUSIONS

The GD model has been implemented in the work on the principle of Occam Razor: "*simplest things which work first, are better* ". The model takes gradient based approach to fit the regressor on Kaggle[2] dataset and it can be best suited on any linearly predictable scenario. It captures the parameters which play the critical role for a student's chances for admission process as it reveals the internal relationship amongst parameters. Further, the model is able to predict the outcome as a percentage of the chance of a GRE score. The Pearson correlation coefficient 'r' has a strong bearing on the underlying parameters- as it is evident from the program run and various plots. As the linear regressor is one of the most suitable models fit for such type of data, there are improvements also possible-like using Stochastic GD for better performance and efficiency with a niche fit. Moreover, the model can further be extended to undertake features of multiple dependencies as well by way of looking at the extracted features of the data set and fitting it intuitively.

REFERENCES

[1] Ajeet K. Jain, Dr. PVRD Prasad Rao and Dr. K Venkatesh Sharma; "Deep Learning with Recursive Neural Network for Temporal Logic Implementation", International Journal of Advanced Trends in Computer Science and Engineering, Volume 9, No.4, July – August 2020 https://doi.org/10.30534/ijatcse/2020/383942020

[2] Ajeet K. Jain, Dr. PVRD Prasad Rao and Dr. K Venkatesh Sharma;"A Perspective Analysis of Regularization and Optimization Techniques in Machine Learning", Chapter submitted to Computational Analysis and Understanding of Deep Learning for Medical Care: Principles, Methods, and Applications", CUDLMC 2020.

[3] Haykin Simon 2016, Neural Network and Machine Learning, 3rd Ed. Pearson Edn. 2010

[4] CholletFrancois 2018, Deep Learning with Python, Manning Pub., 1st Ed. 2018

[5] Frassord Davi, Linear regression with numpy 2016 (GitHub); www.github /Frossard.htm

[6] Lachlan Miller, Machine Learning: Cost Function, Gradient Descent and Univariate Linear Regression, www.github/lachlanmiller.htm

[7] Ravidran B 2019, NPTEL Course, Introduction to Machine Learning

[8] Karl Gustav Jensson 2108, Introduction to Machine Learning.ML, NPTEL

[9] Gupta A and Biswas G P 2020, Python Programming, Problem solving, packages and libraries, 1st Ed.TMH

[10] Potter Merle C, Potter, J.L. Goldberg and Edward F. Aboufadel 2010 Advanced Engg. Mathematics, Oxford University Press, 3rd Ed.

[11] Charu C. Agrawal, Neural Networks and Deep Learning, 1st Ed. Springer 2018

[12] Bishop, C.M., Neural Network for Pattern Recognition, 1995.

E-ISSN 2581 – 7957
P-ISSN 2277 – 3916

CVR Journal of Science and Technology, Volume 24, June 2023
DOI: 10.32377/cvrjst2412

Real Time Video based Vehicle Detection, Counting and Classification System

K. Sai Keerthan[1], R Vishal[2], T. Tanay[3], M. Vasavi [4]
[1]UG Scholar, CVR College of Engineering/CSE Department, Hyderabad, India
Email: saikeerthankothawadla@gmail.com
[2] UG Scholar, CVR College of Engineering/CSE Department, Hyderabad, India
Email: vishalrambathri02@gmail.com
[3] UG Scholar, CVR College of Engineering/CSE Department, Hyderabad, India
Email: tanaychowdary@gmail.com
[4]Sr.Asst.Professor, CVR College of Engineering/CSE Department, Hyderabad, India
Email: m.vasavi@cvr.ac.in

Abstract: **City planners have wrestled with traffic challenges for a long time. Better techniques for simplifying the process and analyzing traffic are currently being developed. Both the quantity of vehicles at a specific location over a specific time period and the kind of vehicles can be taken into account for traffic analysis. Such devices have been created for decades, but the bulk of them use sensors to identify the moving cars, such as a couple of proximity sensors to determine the direction of the driving vehicle and to count the number of moving vehicles.**

These systems are highly effective and have matured, however they are not very cost-efficient. The problem is that such systems demand routine maintenance and calibration. Creating a vision-based vehicle counting and categorization system is the aim of this project. In order to do feature extraction and be able to identify and count the vehicles, this system takes still pictures from video. The cars are then categorized by comparing the contour regions to the predetermined values. The comparison of two classification algorithms is the work's significant contribution. Utilizing both the Bag of Features (BoF) approach and contour comparison (CC), classification has been achieved.

Index Terms: **Background learning, Foreground extraction, Vehicle classification, YOLO algorithm, COCO dataset.**

I. INTRODUCTION

There is a greater need for effective management and monitoring of road traffic as a result of the growth of road networks, an increase in the number of vehicles, and, most importantly, the size of vehicles. Intelligent traffic surveillance systems are crucial for modern traffic management, but conventional approaches like wireless sensor networks, inductive loops, and EM microwave detectors are expensive, heavy, and difficult to install without causing traffic disruptions. Instead, video-based surveillance systems can be an effective alternative. Video surveillance systems are now more accessible and efficient because of advancements in storage capacity, processing power, and video encryption techniques.

The videos that these surveillance systems stores are normally examined by humans, which takes time. The need for more reliable, automatic video-based surveillance systems is essential. Although the primary function of a traffic surveillance system are to detect, monitor, and categorize cars, they can also be used to carry out more complicated operations like lane recognition and driver behavior recognition. Systems for monitoring traffic can be used for a number of things, such as identifying people, detecting unusual behavior, detecting accidents, detecting car theft, monitoring parking places, and detecting accidents. Hardware and software are the two main components of a traffic monitoring system.

The hardware component is a stationary camera installed on the side of the road that records the video stream, and the processing and analysis is handled by software component. These systems may be portable and include a CPU built into the camera for instantaneous processing and evaluation, or they may be nothing more than cameras that send the video stream to a processing hub. A variety of techniques have been employed to develop systems that can recognize, count, and categorize cars and may be used for traffic monitoring in intelligent transportation systems. These systems are discussed in this section along with details on their creation.

For traffic monitoring, computer vision technology is widely used. A crucial element of ITS is the development of computer vision technologies over video-based traffic monitoring for spotting moving cars in video feeds. Vehicle tracking and detection using computer vision technologies has been the subject of extensive research. In 2005, Hasegawa and Kanade unveiled a technique for identifying and categorizing moving objects according to their type and color. A series of photographs of a particular place were made available during this process, and vehicles were located using these images. Using Python and OpenCV, Nilesh et al. (2013) created and constructed a system for identifying and counting moving automobiles. Using background subtraction, picture filtering, image binary, and segmentation techniques, it can identify and count moving objects like cars in real time or from recorded movies. Using Python and OpenCV, as well as an adaptive background subtraction technique in conjunction with virtual detector and blob tracking technologies, Da Li et al. (2014) developed a real-time moving vehicle identification, tracking, and counting system. The virtual detector creates a collection of rectangular regions in each input image frame, and the blob tracking technique creates input image frames with the absolute difference between the background image and foreground blobs representing the moving cars. The techniques outlined above have some

Received on 02-04-2023, Revised on 11-04-2023, Accepted on 26-04-2023.

limitations, including how they handle shadows and how they obstruct many vehicles that appear in a single area. In order to create a device that can be used for traffic surveillance in intelligent transportation systems, a variety of approaches have been used.

II. LITERATURE SURVEY

For a system that counts vehicles in real time using video, Tursun, M., and Amrulla, G. [10] developed an efficient virtual loop technique. To determine how many vehicles pass through, they deployed sophisticated traffic monitoring cameras placed along roads. This technology counts in three phases by monitoring the movement of the vehicle inside a tracking area known as the virtual loop. Lei, M., et al. [11] suggested yet another car counting mechanism based on video. Automatic feature estimation and Gauss shadow elimination were the two main methods used in this system, which employed surveillance cameras positioned at relatively high elevations to gather the traffic video feed.

The visual angle and the system's capacity to eliminate shadow and ghost effects are what affect the accuracy rate. The system's fundamental flaw is its inability to categorize vehicle types. Bas et al. [12] The authors introduced a method for counting vehicles through video analysis. The approach utilizes an adjustable bounding box size for tracking and detecting vehicles, based on an estimation of camera distance. A boundary is often defined in a picture for both inbound and outbound directions in order to identify the Region of Interest (ROI). The system is unable to monitor moving cars as they change directions, despite advancements to deal with specific weather situations.

N.C. Mithun et al. [13] The authors suggested a system for detecting and classifying vehicles that relies on time spatial images and the use of virtual detecting lines spread out. A two-step K closest neighbor (KNN) approach is used to classify automobiles using shape-invariant and texture-based criteria. Experiments reveal that the suggested method has higher accuracy and a lower error rate than earlier methods since it accounts for different illumination settings. A system for recognizing and classifying automobiles at busy urban crossroads was proposed by Habibu Rabiu. [14]. The system uses background elimination, the Kalman filter method, and a Linear Discriminant Analysis classifier to accurately classify cars in order to detect and track them.

The most crucial stage of a video-based traffic monitoring system is the initial phase which is vehicle recognition since it has a significant impact on other algorithms like tracking and classifying the vehicles. For this reason, it's crucial to accurately recognize and separate from the background moving item. Foreground detection uses many techniques, such as frame n differencing [15]. The most basic foreground identification and segmentation technique is frame differencing, it relies on the intimate association of the series of moving images.

Collins [16] proposed a more accurate frame differencing technique that computes the foreground by comparing the differences between numerous frames as opposed to simply the initial one. Gibson [17] created the optical flow field method, a different technique. Wu, K., et al. postulated that mode velocity within a picture is represented by optical flow [18]. The Optical Flow approach treats the Detecting Area Image as a vector field of velocity, with each vector representing the momentary change in a pixel's position relative to its surroundings. Another technique for identifying foreground objects is the average model. [19]. The background value of a pixel in the average model is the average grey value of that pixel over a set of frames.

Friedman, N., and S. Russell [20] GMM was suggested by Stauffer, C., and W.E.L. Grimson [21, 22] improved for tracking in real-time. The backdrop is assumed to be more apparent than any foreground areas in the Gaussian Mixture Model. A nonparametric background model based on kernel density estimation was proposed by Elgammal [23]. The kernel density estimation method chooses the data with the highest probability density as the background after evaluating video data samples using kernel functions. Images are portrayed by the bag of features model as random groupings of local features. The bag of words representation used in text-based information retrieval served as the model for the term "bag of features."

III. IMPLEMENTATION

The system is made to perform vehicle detection, recognition, and tracking in video frames. It then divides the identified vehicles into three separate size groups. The system is made up of three modules: Vehicle categorization, Foreground extraction, and Background learning.

Background Learning:

Background Learning is used to create a background model of the video scene by analyzing the pixels in each frame of the video over a period of time. This background model is then used to identify any changes in the scene, which could indicate the presence of a moving object.

The first module in the vehicle detection system is responsible for learning about the background in the video feed. This is important for identifying the moving objects or foreground. The module extracts frames from the video and uses image processing algorithms to learn about the static backgrounds in the scene. For instance, in a traffic scenario captured with a stationary camera, the background would include static objects such as buildings and road signs. By analyzing the differences between the background and foreground, the system can accurately detect and track vehicles in the video feed. The use of image processing algorithms allows the system to learn about the background and identify changes in the foreground in real-time.

Foreground Extraction:

Foreground Extraction uses the background model to subtract the background from each frame of the video, leaving only the foreground pixels, which correspond to the moving objects in the scene. This module is used to isolate the vehicles in the video frames.

The second module in the vehicle detection system comprises three steps: background subtraction, image enhancement, and foreground extraction. First, the background is subtracted to make the foreground objects visible. This is done by assigning binary 0 to the pixels that correspond to static objects in the scene. Next, to acquire accurate foreground object contours, picture enhancing techniques like noise filtering, dilation, and erosion are used.

These techniques help to improve the quality of the foreground objects and remove any artifacts or noise. Finally, the module outputs the foreground extraction, which is a set of contours representing the moving vehicles in the video frames. These contours will then be used in the subsequent module for vehicle classification based on their size and shape.

Vehicle Classification:

Once the foreground extraction module is applied in the vehicle detection system, proper contours of the vehicles in the video frames are obtained. From these contours, features such as contours aspect ratio, area, size, and solidity are extracted. These features are then used to classify the vehicles based on their size and shape. For example, the system could classify vehicles into small, medium, and large categories based on their total length and area. Alternatively, it could classify vehicles based on their shape, such as car vs. trucks using aspect ratio as a classification parameter. The extraction of these features is crucial in accurately identifying and categorizing the vehicles in real-time.

IV. WORKING

Steps for execution:

1. Importing the necessary libraries and setting up the vehicle detection, counting, and categorization system are the first steps in the code.
2. The pre-trained object identification model is then loaded using the YOLOv3 method.
3. The video stream is then captured and examined using OpenCV frame by frame.
4. The vehicles in each picture are recognized using the object detection model.
5. The monitored vehicles are recognized using a centroid tracker approach, which gives each one a unique ID and monitors its movement over time.
6. Following that, the system counts the number of vehicles passing through a certain Region Of Interest (ROI) and classifies them based on type (car, bus, truck, etc.).
7. A pre-trained machine learning model that recognizes the type of vehicle based on image features is used to do the categorization.
8. The system then updates the count and classification data for each car, displaying it on the output video stream.

The completed video stream is finally exported to a file for additional use. Overall, the system uses deep learning and computer vision algorithms to provide real-time vehicle recognition, counting, and categorization for a video stream.

Details of each Step:

1. **Import required libraries**: First, the necessary libraries, including argparse, NumPy, and OpenCV, are imported.
2. **Initialize the camera**: The OpenCV function named Video Capture is then used to initialize the camera.
3. **Initialize required variables:** There are fixed variables for frame count, width, height, and font.
4. **YOLOv3 network should be loaded:** The pre-trained YOLOv3 model is loaded using the cv2.dnn.readNet function.
5. **Describe the classes and colors:** Both the categories of objects that the model can recognize, and the colors connected to them are specified.
6. **Specify the output layers**: The output layers of the YOLOv3 network have been identified.
7. **Start an endless loop**: The camera's frames are started to be recorded in an endless loop.
8. **Image preprocessing:** Scaling and normalizing the pixel values are two steps in the preprocessing of the recorded frame.
9. **Perform network inference:** To find objects, the preprocessed image is passed via the YOLOv3 network.
10. **Postprocess the detections:** Postprocessing removes low confidence and non-vehicle detections from the YOLOv3 network's detections. The threshold for low confidence detections is set to 0.3. This means that any detected object with a confidence score below 0.3 will be considered as a low confidence detection and ignored.
11. **Count vehicles:** The number of detected vehicles for the current frame is counted and shown on the output.
12. **Vehicle classification:** The aspect ratio of each vehicle (car, truck, or bus) determines its classification.
13. **13. Define bounding boxes and labels for each vehicle:** Each detected vehicle has bounding boxes and labels placed around it, and on the output, each vehicle's type is indicated.
14. **Show the results**: The show function in OpenCV is used to display the result frame on the screen.

V. DATASET AND CLASSES

The dataset used is COCO. The COCO (Common Objects in Context) dataset is a widely used benchmark dataset in computer vision. It includes over 200,000 diverse images with 80 objects categories, annotated with masks, bounding boxes, category labels. The dataset is popular for training and evaluating object detection algorithms like YOLO. It has also spurred competitions and challenges, driving advancements in the field of computer vision. Overall, the COCO dataset serves as a standard resource for benchmarking object algorithms and promoting research in the field.

The total number of classes in the provided code depends on the implementation and dataset used to train the YOLO model. In this code, the number of classes is set to 80, which is a common value used for the COCO dataset. The COCO dataset is widely used for object detection tasks and includes 80 different object classes.

However, based on the COCO dataset used for training, which includes 80 object categories, the classes could potentially include a wide range of common objects and vehicles, such as:

Person, Bicycle, Car, Motorcycle, Bus, Truck, Traffic Light, Stop sign, Pedestrian, Motorbike, Caravan, etc.

In the provided code, if a vehicle is not part of the classes defined in the COCO dataset, the YOLO model may classify it as a generic class like "object", "unknown", or "other". As a result, the code could potentially detect and count vehicles that are not included in the COCO dataset, but it will not provide specific class labels for those vehicles. The model's behavior for unclassified vehicles may vary depending on the implementation and configuration of the YOLO algorithm being used. It's important to consider the limitations of the dataset and model when using the code for vehicle detection and classification tasks.

VI. RESULTS

Figure 1. It shows the first step for executing the project where a command is passed in the command prompt to start the GUI.

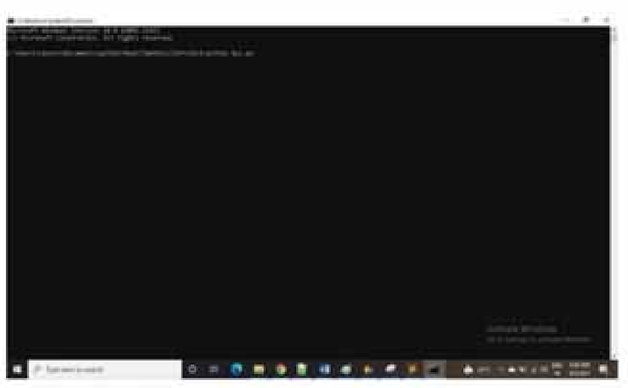

Figure 1. Command prompt in which command executed.

Figure 2. Graphical User Interface is opened after the command executed in the command prompt which displays the option of choosing the video to process in the project. We should click on the button "Upload A Video" located in the bottom of the window, which then displays the window of folder to select a video.

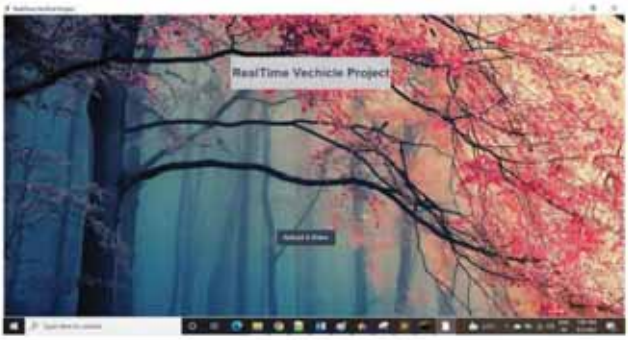

Figure 2. Graphical User Interface

Figure 3. Display of GUI after the selection of the video to be analyzed in the project. We should click on the "Get RealTime Vehicle Reading" option to start analyzing the video and start detecting and counting of the vehicles in the video.

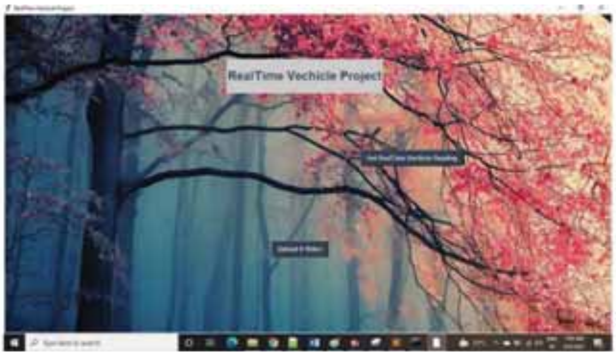

Figure 3. GUI after selection of the video to be processed.

Figure 4. After clicking on the "Get RealTime Vehicle Reading" option, it displays all the background details of the execution like number of frames per second captured and the count of the vehicle in the command prompt.

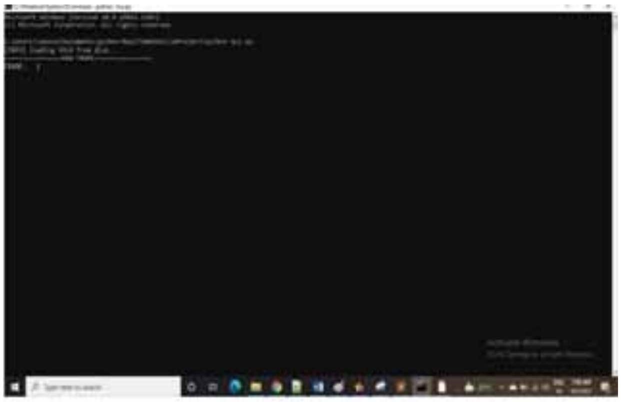

Figure 4. Background details of the execution.

Figure 5. Finally, it displays a video which consists of the traffic, the count of the vehicles moving on the road and the classification of vehicle captured from the input video.

Figure 5. Output video with the count of vehicles

VII. CONCLUSIONS

The proposed fix makes use of the OpenCV bindings and is written in Python. Various sources of traffic camera footage are being utilized. The user selects the area of interest to be looked into using a straightforward interface, and image processing methods are then applied to count the number of vehicles and categorize the cars. We developed a video-based vehicle monitoring system for real-time traffic data collection. Python, OpenCV, and the Background Subtraction Yolo algorithm were used to create the system. In the suggested model we studied the traffic flow in the day and night. Additionally, we evaluated the various shadows cast by moving autos.

REFERENCES

[1] I. Alam, M. F. Ahmed, M. Alam, J. Ulisses, D. M. Farid,Shatabda, and R. J. F. Rossetti, "Pattern mining from historical traffic big data," in IEEE Technologies for Smart Cities (TENSYMP 2017). IEEE, July 2017, pp. 1–5.

[2] I. Alam, D. M. Farid, and R. J. F. Rossetti, "The prediction of traffic flow with regression analysis," in Emerging Technologies in Data Mining and Information Security, ser. Advances in Intelligent Systems and Computing, A. A., D. P., M. J., B. A., and D. S., Eds. Springer, Singapore, 2019, vol. 813, pp. 661–671.

[3] A. Talebpour, H. S. Mahmassani, and S. H. Hamdar, "Effect of information availability on stability of traffic flow: Percolation theory approach," Transportation Research Procedia, vol. 23, pp. 81–100, 2017.

[4] A. Csikos, T. Charalambous, H. Farhadi, B. Kulcs ´ ar, and H. Wymeersch, ´ "Network traffic flow optimization under performance constraints," Transportation Research Part C: Emerging Technologies, vol. 83, pp. 120–133, 2017.

[5] M. Zhou, X. Qu, and X. Li, "A recurrent neural network based microscopic car following model to predict traffic oscillation," Transportation Research Part C: Emerging Technologies, vol. 84, pp. 245– 264, 2017.

[6] F. B. Ghorghi and H. Zhou, "Traffic control devices for deterring wrongway driving historical evolution and current practice," Journal of Traffic and Transportation Engineering, vol. 4, pp. 280–289, 2017.

[7] A. Abadi, T. Rajabioun, and P. A. Ioannou, "Traffic flow prediction for road transportation networks with limited traffic data," IEEE Transactions on Intelligent Transportation Systems, vol. 16, no. 2, pp. 653–662, 2015.

[8] S.-Y. Cheung, and P.P. Varaiya, "Traffic surveillance by wireless sensor networks: Final report", PhD diss., University of California at Berkeley, 2006.

[9] S. Oh, S. Ritchie, and C. Oh, "Real-time traffic measurement from single loop inductive signatures", Transportation Research Record: Journal of the Transportation Research Board, (1804), pp. 98-106, 200

[10] M. Tursun, and G. Amrulla, "A video based real-time. vehicle counting system using optimized virtual loop method", IEEE 8th International workshop on Systems Signal Processing and their Applications (WoSSPA), 2013.

[11] M. Lei, D. Lefloch, P. Gouton, K. Madani, "A video based real-time vehicle counting system using adaptive background method", IEEE International conference on Signal Image Technology and Internet Based Systems (SITIS'08), pp. 523-528, 2008.

[12] Bas, Erhan & Tekalp, A. & Salman, F.. (2007). Automatic Vehicle Counting from Video for Traffic Flow Analysis. 392 - 397. 10.1109/IVS.2007.4290146.

[13] N.C. Mithun, N.U. Rashid, and S.M. Rahman, "Detection and classification of vehicles from video using multiple time-spatial images", IEEE Transactions on Intelligent Transportation Systems, vol 13, no 3, p. 1215-1225, 2012.

[14] H. Rabiu, "Vehicle detection and classification for cluttered urban intersection", International Journal of Computer Science, Engineering and Applications, vol 3, No.1, p. 37, 2013.

[15] M. Seki, H. Fujiwara, and K. Sumi, "A robust background subtraction method for changing background", Fifth IEEE Workshop on Applications of Computer Vision, 2000.

[16] R.T. Collins, et al., "A system for video surveillance and monitoring", VASM final Report, Robotics Institute, Carnegie Mellon University, 2000, pp.1-68.

[17] J.J. Gibson, "The perception of the visual world", 1950.

[18] K. Wu, et al., "Overview of video-based vehicle detection technologies", 2011.

[19] G. Yang, "Video Vehicle Detection Based on Self Adaptive Background Update", Journal of Nanjing Institute of Technology (Natural Science Edition), vol 2, p. 13, 2012.

[20] N. Friedman, and S. Russell, "Image segmentation in video sequences: A probabilistic approach", Proceedings of the Thirteenth conference on Uncertainty in artificial intelligence, 1997, Morgan Kaufmann Publishers Inc.

[21] C. Stauffer, and W.E.L. Grimson, "Learning patterns of activity using real-time tracking", IEEE Transactions on pattern analysis and machine intelligence, 2000. Vol 22, no. 8, pp. 747-757, 2000.

[22] C. Stauffer, and W.E.L. Grimson, "Adaptive background mixture models for real-time tracking", IEEE Computer Society Conference Computer Vision and Pattern Recognition, 1999.

[23] A. Elgammal, D. Harwood, and L. Davis, "Nonparametric model for background subtraction", European conference on computer vision, Springer, 2000.

E-ISSN 2581 – 7957
P-ISSN 2277 – 3916

CVR Journal of Science and Technology, Volume 24, June 2023
DOI: 10.32377/cvrjst2413

MLO Mammogram Pectoral Muscle Masking with Adaptive MSER

Ch. Sarada
Sr. Asst. Professor, CVR College of Engineering/CSE Department, Hyderabad, India
E-mail: Chintala.sarada@cvr.ac.in

Abstract: **Breast cancer claims the lives of many people every year. Breast cancer diagnosis is a difficult process that requires competent radiologists. Manual detection of breast cancer disease takes a large amount of time, as does manual treatment of disease. As a result, automated detection is required, which aids in early treatment and in some circumstances, saves lives. These technical advancements are beneficial for early treatment due to resource availability and computing capability. A mammogram is a technique for detecting breast cancer masses early. To identify masses from MLO mammograms, several image processing-based computer-aided diagnostic techniques have been developed. In computer aided diagnosis systems, the presence of Pectoral Muscle in MLO Mammograms has a considerable detrimental influence on mass detection from MLO Mammograms. Masking the Pectoral muscle improves mass detection from an MLO mammogram. Locating the Pectoral muscle is tough since the intensity of this tissue is equivalent to that of a malignancy. The primary goal of this research is to develop a Most Stable Extremal Region (MSER) based method to locate and mask Pectoral muscle from the Mediolateral Oblique Mammogram. The empirical analysis suggests that the proposed novel procedure is straightforward and gives promising results in locating and masking Pectoral muscle. The suggested technique enhances accuracy by 96.27% compared to 95% for state-of-the-art solutions. Python and MATLAB are used to create the new system.**

Index Terms: **MLO Mammogram, Pectoral muscle, Most Stable Extremal Region (MSER), Image processing.**

I. INTRODUCTION

Depending on the type of breast tissue being discussed, a woman's breasts can be fatty, fibrous, or glandular. The lobules and ducts of the breast are examples of glandular tissue. From the skin to the chest wall, there is a layer of connective tissue called fibrous tissue. Connective tissue includes the fibrous tissue that makes up ligaments and scar tissue. The transition from glandular to connective tissue is facilitated by the deposition of fatty tissue. Fibroglandular tissue [1] is the term used by medical professionals to describe any type of tissue that is not fatty. Milk is made in the mammary lobes, and then transported to the nipple via ducts. Thick breasts typically have glandular or fibrous tissue as their primary composition. These types of tissues appear white, thick, and denser than fatty tissue. Organs and tissues of the breast are shown in Fig.1. The breast is a dense-tissue organ that needs to be observed.

It is true that cancer is fatal, but early detection increases the likelihood of a long and healthy life. Due to its principal sites of proliferation in the milk glands and ducts, breast cancer is particularly deadly for women.

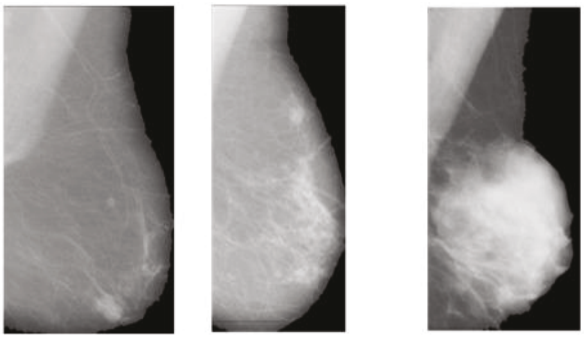

Fatty tissue Glandular tissue
Dense tissue

Figure1. Different tissue type breast organs

Mammography is the name for the imaging technology used to create Mammogram pictures of a woman's breast organ. As Mammograms allow radiologists to detect abnormal lumps, they are the primary tool used in the diagnosis of Breast Cancer. Mammograms can be taken from two different angles: the mediolateral oblique (MLO) and the cranial-caudal (CC). The MLO view is the better as it observes the lateral side of the breast, which is typically affected by pathological abnormalities because it captures larger areas of the upper-outer quadrant of the breast. The connection between CC and MLO is depicted in Fig. 2. The CC view is a top-down view. This is a view of the MLO from a very specific angle [1].

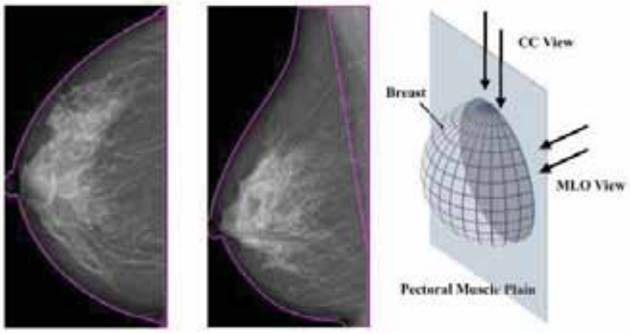

(a) (b) (c)

Figure 2. (a)CC View (b) MLO View (c) Corresponding projection model

Breast mass is a typical early indicator of breast cancer. The process of detecting masses is being sped up with the use of numerous computer-aided diagnosis approaches based on Digital Image Processing. The presence of Pectoral muscle makes the challenge of developing a computer-aided diagnosis system to detect Mass even more difficult, as its

Received on 17-02-2023, Revised on 06-04-2023, Accepted on 27-04-2023.

properties, such as grey level, are similar to those of Mass. The position of the Pectoral muscle on an MLO mammography is shown in Fig.3.

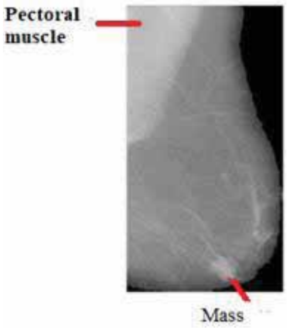

Figure 3. Mammogram with Pectoral Muscle

The presence of Pectoral muscle raises the likelihood of a false positive diagnosis of breast cancer, even if a breast mass is a frequent sign of the disease. This work seeks to implement a Digital Image Processing system based on Most Stable Extremal Regions (MSER) to detect and mask the Pectoral muscle in MLO Mammograms to help with Mass detection.

Section II explains existing Pectoral mask systems, Section III discusses the proposed system, Section IV provides the ensuing analysis, and Section V summarizes the new strategy to detect and mask the Pectoral muscle.

II. LITERATURE SURVEY

S. Marijeta et al. [2] employed mammography contrast improvement and K-means to identify and hide the Pectoral muscle. The K-means technique is used to find the Pectoral muscle area after trimming the original MLO mammography and boosting pixels in the mass. The limits of the Pectoral muscle are determined through cubic multinomial fitting. The Mini-MIAS database analysis of simulated mammograms shows the procedure to be reliable. With 19.25% of instances being deemed acceptable and 12.42 % being deemed poor, this approach is 68.42% accurate.

P. S. Vikhe et al. [3] describe a Pectoral covering technique for detecting the Pectoral area in mammograms using a grey level-based approach. By enlarging the Pectoral region and choosing its boundary points, the method locates the Pectoral muscle's border. With the Least Squares Error method, the initial arbitrary limits are smoothed out. The success percentage of the suggested strategy is 96%.

Wavelets based Pectoral muscle masking strategy is proposed by M. Mughal et. al [4]. In which the Pectoral border line is found by using two-dimensional multilevel wavelets. The approach has a success rate of 76.63%, with 14.59% of results considered good and 7.76% considered poor. However, the suggested solution is only partly automated.

The Pectoral covering approach is proposed by Saeid Asgari Taghanaki et al. [5] using the area-developing strategy and the Shape principles. The separation of the Pectoral muscle is accomplished using a method based on geometrical principles. It doesn't matter whether your pecs are large or rounded for this technique. Finding the Pectoral muscle's edge is necessary for segmentation, but if the texture is too complicated for edge detection techniques based on colour and brightness, this may be challenging. This approach is based on geometric principles, so it would work with a variety of Pectoral muscle shapes. The Pectoral area is located using a modified region development approach with automated seed finding, which allows for a broad range of muscle forms and orientations. It succeeded in delivering precise results in 67% cases, acceptable results in 22% of the cases and 10% of instances are inappropriate.

Samuel Rahimeto and colleagues [6] employed Ostu's multi-thresholding to locate the bright area that corresponds to the observed Pectoral muscle. This is accomplished by determining the ideal threshold value. Overall, Pectoral muscle area is detected accurately in 93.36 percent of the cases.

The Bounding Box method is developed by Enas Mohammed Hussein Saeed and colleagues [7] based on Region Growing technique with the aim of accurately localising the Pectoral muscle. To solve the problem of Pectoral muscle masking, this study employs a practical solution that combines the Bounding Box (BB) and Region expanding procedures. In this research, pre-processing the mammography pictures is done in two steps. Using a medium filter and a threshold binary picture, first the label and noise are removed. To enhance outcomes while depleting Pectoral muscles, the second phase is combining the bounding box and region growth processes into a unified system.

Pascal Vagssa and his associates proposed a Hough transform-based method to localise the Pectoral muscle [8]. The researcher's conclusions had a 93.8% accuracy rate and a 6.2% error rate. One of the few limitations of this strategy is that the 512x512 pixel region of interest exercised in the upper left corner of the mammography may not be ideal for all Mammogram images.

A strategy for masking Pectoral tissue in mammograms has been developed by G Vaira Suganthi et al. [9], J Sutha, M Parvathy, and C Durga Devi by employing active contour and grey level thresholding methods to define the border between Pectoral and breast tissue. The proposed method accuracy is 92.55 percent. The maximum intensity of each line is used in the suggested approach for determining Pectoral boundaries, which may work for certain images only.

III. PROPOSED SYSTEM

The Pectoral muscle can be seen in MLO Mammogram. The issue with Pectoral muscle is that it has comparable qualities as Mass. As a result, the computer aided diagnosis system could detect the Pectoral region, or a portion of it as a Mass. So, in a computer-aided diagnosis system, it is always recommended to cover the Pectoral region before testing for breast tumours to avoid false positives. In the proposed system, the MSER based approach is used to locate the Pectoral muscle regions. Fig. 4 shows proposed procedure to locate and mask the Pectoral muscle. Cropping the huge image contour to remove artefacts from original MLO Mammogram is the first step in the procedure. In step 2, the resultant Mammogram orientation is set to the right.

The Pectoral area is located, pruned and covered in the third phase of the recommended technique. All phases are detailed in subsections.

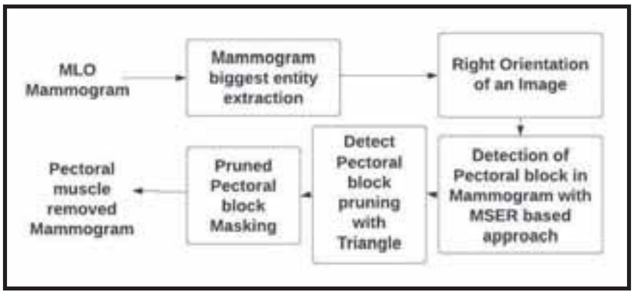

Figure 4. Top level diagram of proposed system

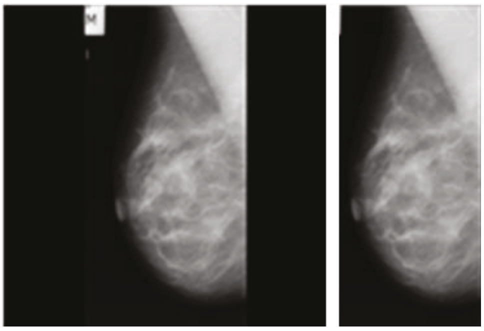

(a) (b)

Figure 5. (a) Initial Image (b) Trimmed Image

A.Mammogram Biggest Entity Extraction

Extra black margins and artefacts such as labels would be present in the original MLO Mammogram. The original Mammogram must be cleaned of these artefacts and extra black margins so that the resulting Mammogram is free of artefacts and contain the exact Mammogram part, resulting in faster processing.

The Mammogram biggest entity extraction procedure extracts largest object from the original Mammogram. This is achieved in two steps. Firstly, the Cropping process crops out the breast region in accordance with the Otsu's [10] method. The threshold is in accordance with the Otsu's method. The limit value follows the Otsu formula. Ostu's global thresholding technique finds the threshold by reducing the weighted variance within the class. The image's histogram is analysed, and the components are ranked by minimising the variation between them. Once the cut-off for an Otsu has been determined, morphological techniques like morphology close and open operations are used to filter out insignificant details and partition the breast area from the rest of the body. Cropping of an example MLO Mammogram result is shown in the figure 5.. Detailed steps for extracting largest Object from MLO Mammogram is described in the following algorithm 1.

```
Algorithm 1: LargestObjectExtraction(Image)
Step 1. Filter the image using a Gaussian filter to get
                          rid of the fuzziness.
Step 2. Utilize Otsu's and morphological techniques to
         identify the greatest contour.
Step 3. Find the perimeter of the biggest rectangle.
Step 4: Use the rectangle drawn in Step 3 to crop the image.
Step 5: Return the altered Image.
```

The Pectoral region-part will be situated in the top left or right corner of the retrieved biggest picture once the largest object has been extracted from the original mammography. The next step in finding the Pectoral area is to rotate the extracted Mammogram to the right. As a result, before applying the Pectoral muscle region identification technique, all left-oriented images are rotated to the right. The total intensity of the top left and top right corners of cropped Mammogram is computed and compared to ensure that the cropped mammography is oriented correctly. The cropped mammogram has to be reoriented if the overall intensity of the left top-left corner is lesser than that of the right top-right corner. In such a case, a horizontal mirror image is created from the cropped picture to get the right oriented image. Algorithm 2 shows the steps involved in the setting of orientation.

```
Algorithm 2: ImageRigthOrientation(Largeobjectimage)
step1.Set ImageHeight, ImageWidth =
                         Largeobjectimage.shape
step 2. Set BoxHeight equal to 10% of ImageHeight
step 3. Set BoxWidth equal to 10% of ImageWidth
step 4. Set leftcornersum=0
step 5. Set rightcornersum=0
step 6. Determine the average brightness of the image's
                                     top left corner
          6.1. For m=0 to BoxHeight
             6.1.1. For  n=0 to BoxWidth
                       compute ltcornersum=ltcornersum+
                                     TrimmedImage(m , n)
          6.2. leftcornermean= leftcornersum/ (BoxHeight
                                     * BoxWidth)
step 7.  Determine the average brightness of the image's
            top right corner
          7 1. For m= 0 to BoxHeight
             7.1.1. For  n=ImageWidth - BoxWidth to
                                                ImageWidth
                     Compute rightcornersum=rightcornersum+
                                     largeobjectimage(M , N)
          7.2. rightcorrnermean= rightcornersum/
                         (BoxHeight * BoxWidth)
step 8. if leftcornermean < rightcornermean
          Determine Mirror image of Largeobjectimage
          8.1. For m= 0 to BoxHeight
             8.1.1. For n=0 to BoxWidth
                   MirredImage (m, width - n) =
                         Largeobjectimage (M,   N)
step 9. Return MirredImage
```

Sample output of right orientation process is shown in the Fig. 6

.

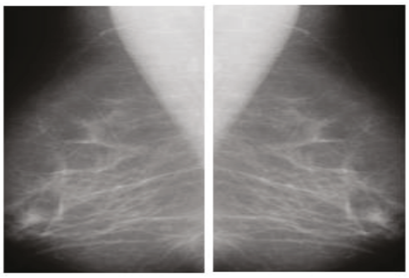

(a) (b)

Figure 6. (a) Left-oriented MLO Mammogram (b) After right Orientation

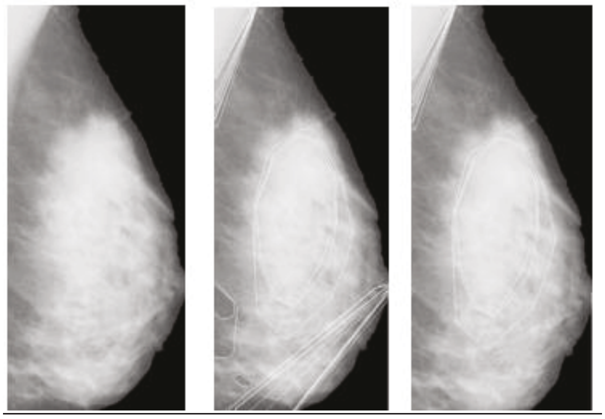

(a) (b) (c)

Figure 7. (a) Input Image (b) both MSER$^-$ & MSER$^+$ outcomes for the Input Image shown (a) (C)Only MSER+ outcomes with a smaller number of thresholds

C.Detection of Pectoral Muscle with MSER Technique

Once the raw Mediolateral Oblique Mammogram data has been processed, the resulting picture is clean, properly cropped, and orientated to the right. Here, we present a Maximally Stable Extremal Region (MSER)-based technique for identifying Pectoral muscle regions in pre-processed pictures.

A new approach based on the Maximally Stable Extremal Regions (MSER) technology is created and developed to locate the Pectoral muscle. This system is developed specifically for identifying the Pectoral region. The innovative method consists of two main stages.

The first step, known as adaptive MSER, involves making adjustments to the current MSER, and the second, detecting the greatest Pectoral area based on the first step's output, is known as the detection stage.

In the first stage, the fundamental MSER method [11] finds a set of stable connected components throughout the whole range of grayscale values from 0 to 255, inclusive. In the process, every intermediate step involves thresholding the image to produce a series of monochrome photographs. A single extreme feature will be all white, while the other will be entirely in black color.

Black-to-white (MSER-) and white-to-black (MSER+) MSER operations create redundantly coupled components. A more detailed example is shown in Fig.7. above. The polygon in each line of Fig. 7(b) represents the MSER stable linked components.

Adaptive MSER is a kind of MSER that is optimised to find stable related components and eliminate duplicates more quickly. Instead of handling the whole grayscale range, the adaptive MSER just deals with the range from white to black (MSER+) (MSER) with. The improved MSER version produced the results seen in Fig.7(c) when fed the data from Fig.7(a). Eleven threshold values are used here to classify related parts. By default, we set the threshold for Pectoral muscle intensity at 50 relative to the value of the observation. However, the number of grayscale levels varies according to an image's average intensity. If a Mammogram's typical intensity is 110, for instance, the lowest acceptable intensity would be 90 (110 minus 20). To account for MSER zones whose values are always within 20 of the mean, we subtract the mean from the MSER value. Using these threshold values, we can analyse data and extract stable linked components from a reduced set of images, as compared to standard MSER. The streamlined MSER only generates necessary images without producing duplicates. Using the height of the calculated region, these images are further filtered to retain just the Pectoral region. The Pectoral area is what you'll find in the top left corner. Since the maximum height of the Pectoral region is equal to the maximum height of the Image minus 150, the height of the top left corner of the calculated Pectoral area must be less than the height of the image minus 100.

```
Algorithm 3: PectoralMSER (RightOrientedImagee)
step 1. set ImageeHeight, ImageeWidth ←
            RightOrientedImagee.shape
step 2. This step is to find linked regions from intensity thresh
=255 to MI-20, where MI is the average intensity of the upper-
left corner of the clipped Mammogram Image
 2.1. For Thresh=255 to MI-20
   2.1.1. For m=0 to ImageeHeight
            For n=0 to ImageWidth
              if RightOrientedImagee [m, n]<=Thres
               if RightOrientedImagee [m, n] is a
            CRegionImagee Neighbour
                 CRegionImagee [m, n] =
                            RightOrientedImagee [m, n]
  2.2. Attach linked regions found in
            CRegionImagee to the component tree
step 3. From the linked component tree, select only linked
components which are related to Pectoral region
step 4. Calculate Variation for regions selected
         according to the previous step
  4.1. $Variation_{Threshold} =( Area_{Threshold+\Delta} - Area_{Threshold-\Delta})/ Area_{Threshold}$
  4.2. Attach computed $Variation_{Thresh}$ to
        Variation_Listt along with the corresponding
                            connected region information
step 5. Choose connected components with local minimum
from the Variation_Listt
  5.1. PectoralRgns={r |r ∈Variation_listt & it is the
            local minimum}
step 6. Choose the largest connected component from the
Vairation_Listt and take it as a
                    PectoralRegion
  6.1. PectoralRgnArea=0
  6.2. PectoralRgn= -1
  6.3. For Rgn in PectoralRgns
    6.3.1. if Area(Rgn )> PectoralRgnArea
             PectoralRgnArea=Area (Rgn)
            PectoralRgn = Rgn
step 7. Prune the PectoralRgn with width-height triangle
step 8. Return PectoralRgn
```

Second-stage processing involves filtering all related areas detected in stage one down to only those in the Pectoral region. The Pectoral region is then found to include the most interconnected areas.

The algorithm 3 gives steps involved in adaptive MSER-based methods to identify the Pectoral area. Step 2 of this algorithm finds every linked component in a given MLO Mammogram. At step 3, connected components associated with the pectoral muscle are filtered. The variation for each threshold is determined in step 4 and only components with a local minimum are chosen. The component with the greatest area is chosen as the pectoral muscle region from the filtered list of components. The chosen largest area component is then trimmed and masked. Fig. 8 shows output of a sample MLO Mammogram.

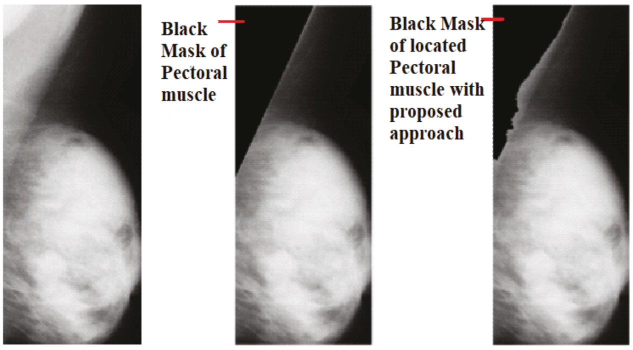

(a) (b) (c)

Figure 8. (a) Pre-processed Image, (b) Black mask of Pectoral tissue ground truth (c) Black mask of Pectoral tissue computed by MSER Based technique

Key aspects of MSER are maximum area variation, minimum area and maximum area. To ensure that only very small regions are rejected by the adaptive MSER, the minimum area to exclude is set to fifty, while the maximum area at discard is set to. This maximum area function would be helpful in cases when MSER specifies the whole Breast as the region. The Max Area variation has been essential since it determines the maximum intensity fluctuation between extreme places. Dimensions of stable regions are unchanging across a broad range of delta () thresholds. Standard values for delta () are 0.1 and 1.0. The MaxArea variation feature is applied to one of the values determined via experimental research [0.25,0.5, 0.75].

The following are the detailed steps for determining Pectoral regions based on Maxarea variation.

1. First, count filtered regions with Maxarea variation 0.25. if filtered regions are discovered. Use Filtered Regions. Otherwise proceed.
2. Count filtered areas with Maxarea variation 0.5. If higher than zero, follow the filtered regions; otherwise, continue.
3. Step Third, counts filtered areas with Maxarea variation 0.75.
   If count>0, utilise filtered regions; otherwise, move to the next step.
4. No regions are considered if all stages have zero regions.

Fig. 9 shows MaxArea changes cases.

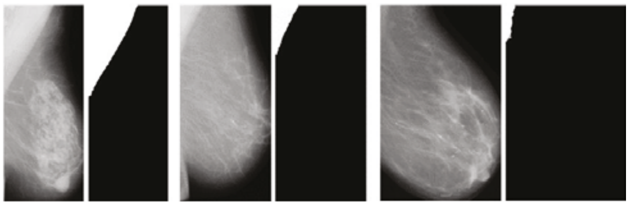

(a) (b) (c)

Figure 9. MSER regions with (a) change of 0.75 (b) change of 0.5 (c) change of 0.25

One problem with the direct MSER based approach is that if any Mass region is very adjacent to the Pectoral region, and then it includes that Mass part also as the part of the computed Pectoral region. The following figure shows the concerned sample.

(a) (b) (c)

Figure 10. (a) input Image (b)Actual Pectoral (white mask) (c) Computed Pectoral with MSER based approach(white)

This problem is resolved by pruning the detected Pectoral region using the Pectoral width-height triangle. Here, Pectoral width and height of detected Pectoral region is computed. Using this data, a triangle is constructed and pruned. The detected Pectoral region for the sample given in the above figure after pruning and corresponding Mammogram with Pectoral region mask is shown below.

Figure 11. (a) Detected pectoral part before trimming(white) (b) Pectoral region after trimming(white mask)

The MSER-based technique is very effective at detecting the Pectoral area. It is able to identify the pectoral area, which may be of varying shapes.

IV. PERFORMANCE METRICS AND RESULTS ANALYSIS

The recommended technique is validated using the Mini-MIAS database. There are 322 MLO Mammography images overall in this database. The database's mammogram IDs are mdb001, mdb002, through mdb322. While some Pectorals are parabolic in shape, the majority are triangular. According to the background tissue, there are three different kinds of images in Mini-MIAS: fatty, fatty-glandular, and dense-glandular. In dense tissue, Pectoral muscle detection is difficult. Every picture captured by Mini-MIAS is analysed. Classification performance is evaluated using a variety of metrics, including Global Pixel Accuracy (GPA), Following is the formula used.

$$GPA = (TP + TN) / (TP + FP + TN + FN)$$

Pectoral regions (both detected and ground-truth) were used in the assessment of performance. The FP value indicates the total number of Pectoral area pixel assignments that should have been made to the background but were instead made to the foreground, whereas the FN value indicates the total number of background pixel assignments made to the Pectoral area. In this scenario, TP is the aggregate of all reliable forecasts for pectoral muscle pels. The TN value is the estimated total number of non-Pectoral pels with correct classifications.

In 275 pictures, the system found Pectoral muscle area with an accuracy score > 97% or above, which is deemed accurately segmented. There are 32 pictures where computed Pectoral area accuracy is nearly good that were declared as acceptable since the false positives and false negative rates were less than four percent. In 12 photos, Pectoral area finding is incorrect. So, the total number of instances with good Pectoral area finding is 307 (275 + 32). In the three photos, there is no pectoral muscle. So, the total number of images where Pectoral detected and covered correctly are 310. The mean values of the metric measures of the 298 Images is 99.128 ± 0.654. The Pectoral masking analysis summary of Mini-MIAS is shown in Fig.12. The accuracy achieved is (310/322) 96.2% which is a good improvement over many surveyed approaches. The suggested method is compared to the current literature in the table below. There is evidence that the suggested approach is an improvement above the state-of-the -art.

TABLE I.
COMPARATIVE ANALYSIS OF PROPOSED APPROACH WITH EXISTING LITERATURE TO DETECT AND COVER THE PECTORAL MUSCLE.

Comparitive analysis of proosed method accuracy with existing literature					
Author	**Methodology used**	**% of Images accuratly segmented, acceptable and unacceptable cases**			
		Accuratly segmented cases %	**Acceptable Cases %**	**Unacceptable cases %**	**Overall accuracy acchieved(accurate+ acceptable)**
S. Marijeta et.al	K-Means and Cubic polynomial	68.32	19.25	12.42	87.57
M. Mughal et al.	Wavelet-based approach	77.63	14.59	7.76	85.39
Saeid Asgari Taghanaki	Geometry rule-based approach	67 exact +18 Optimal	5	10	90
Samuel Rahimeto et al.	Ostu's muti-thresholding	not given	not given	not given	93.36
Woong Bae Yoon, Ji Eun Oh et al.	Hough Transform	not given	not given	not given	92.2
Pascal Vagssa et al.	Hough Transform	not given	93.8	6.2	93.8
G Vaira Suganthi et al.	Intensity Thresholding	not given	not given	not given	92.55
Proposed	**Stable Connected**	**85.400**	**10.800**	**3.800**	**96.200**

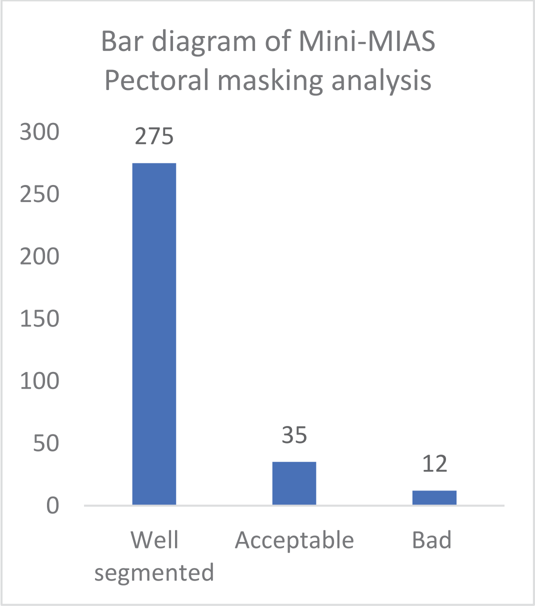

Figure 12. Mini-MIAS Pectoral masking analysis

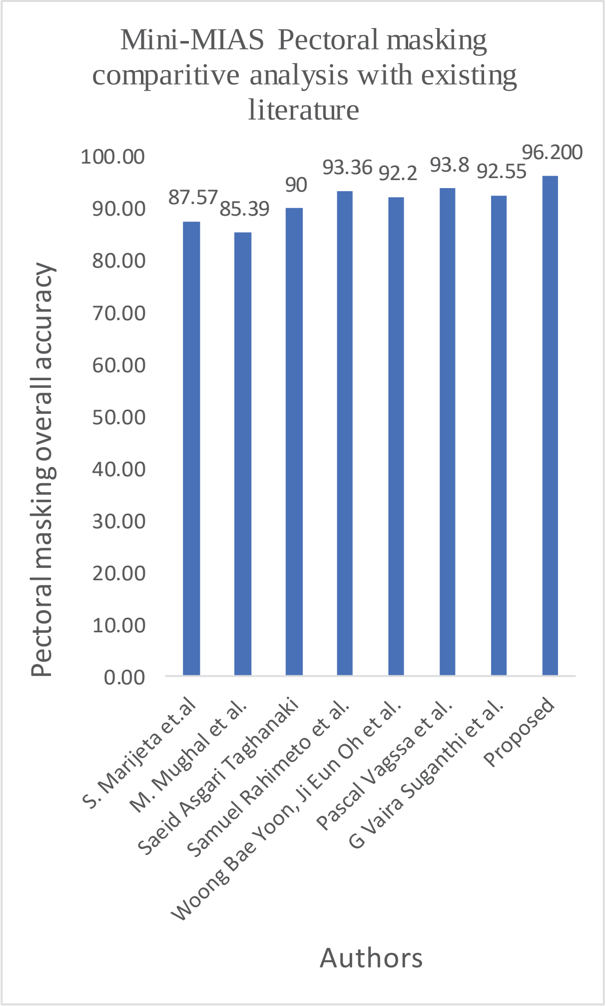

Figure 13. Bar diagram of comparative analysis of proposed approach for detection and covering of Pectoral muscle with existing literature.

The Fig.13 clearly shows us that the proposed approach can detect and cover the Pectoral muscle region with very good accuracy.

V. CONCLUSIONS

In this work, the design and development of new techniques to identify and cover Pectoral muscle is explored. The suggested solution outperformed the state-of-the-art methods in about 96.2% of Mini-MIAS cases, leading to favourable findings. The proposed approach cannot detect Pectoral region if the Mammogram is dense, so, it can be extended to detect the Pectoral regions in dense Mammograms also.

REFERENCES

[1] https://www.mskcc.org/cancercare/types/breast/anatomy-breast.

[2] S. Marijeta, A. Gavrovska, M. Milan, I. Reljin and B. Reljin "Breast Region Segmentation and Pectoral Muscle Removal in Mammograms," Telfor Journal, Vol. 8, No. 1, 2016.

[3] Vikhe, P.S., Thool, V.R. “Detection and Segmentation of Pectoral Muscle on MLO-View Mammogram Using Enhancement Filter,” J Med Syst 41, 190 (2017). https://doi.org/10.1007/s10916-017-0839-8.

[4] Stefanoyiannis AP, Costaridou L, Skiadopoulos S, Panayiotakis G. “A digital equalisation technique improving visualisation of dense mammary gland and breast periphery in mammography,” Eur J Radiol. 2003;45(2):139-149. doi:10.1016/s0720-048x(02)00057-8.

[5] Raju, Rajeswari & Maul, Tomas & Bargiela, Andrzej. “New image processing pipelines for membrane detection,” Journal of the Institute of Industrial Applications Engineers” 3. 15-23. 10.12792/JIIAE.3.15.

[6] Rahimeto, S., Debelee, T.G., Yohannes, D. et al. “Automatic pectoral muscle removal in mammograms. Evolving Systems,” 12, 519–526 (2021).https://doi.org/10.1007/s12530-019-09310-8.

[7] Enas Mohammed Hussein Saeed, Hayder Adnan, "Pectoral Muscles Removal in Mammogram Image by Hybrid Bounding Box and Region Growing Algorithm,”.

[8] Vagssa P., Doudou N.M., Jolivo T., Videme O., Kolyang D.T. 2020. “Pectoral muscle deletion on a mammogram to aid in the early diagnosis of breast cancer,” International Journal of Engineering, Science and Technology, Vol. 12, No. 3, pp. 57-65. doi: 10.4314/ijest.v12i3.6.

[9] Suganthi G. V, Sutha J, Parvathy M, Devi C. D. “Pectoral Muscle Segmentation in Mammograms,” Biomed Pharmacol J 2020;13(3).

[10] https://learnopencv.com/otsu-thresholding-with-opencv/.

[11] Fredrik Kristensen and W. James MacLean “Real-Time Extraction of Maximally Stable Extremal Regions on an FPGA”.

E-ISSN 2581 – 7957
P-ISSN 2277 – 3916

CVR Journal of Science and Technology, Volume 24, June 2023
DOI: 10.32377/cvrjst2414

Over The Top (OTT) Platform using Reactjs

Md. Ashraf[1], G. Rithwik[2], T Sai Sriram[3], M Vasavi [4]
[1]UG Scholar, CVR College of Engineering/CSE Department, Hyderabad, India
Email: mohammadashraf1399968@gmail.com
[2] UG Scholar, CVR College of Engineering/CSE Department, Hyderabad, India
Email: rithwikmaharaj@gmail.com
[3] UG Scholar, CVR College of Engineering/CSE Department, Hyderabad, India
Email: saisriramthota@gmail.com
[4]Sr.Asst. Professor, CVR College of Engineering/CSE Department, Hyderabad, India
Email: m.vasavi@cvr.ac.in

Abstract: **Televisions used to be a household necessity. It's now little more than a fixture taking up space. TV viewing has become far too common. We have to pay for a slew of channels, just to get repeat episodes, stale content, and obnoxious advertising in between. By 2023, 34.9 million American households are predicted to terminate their cable contracts. The desire for content is voracious during the lockdown. Binge-watching was a weekend activity before the coronavirus took over the country. However, with the introduction of multiple digital channels, binge-watching has become the new norm. Video live streaming applications have undeniably altered the television industry and are in high demand in the market. This project proposes an Ott platform for the ui/ux.**

Index terms**: Firebase, stripe payment, react js, design, authentication.**

I. INTRODUCTION

With improved networks, better internet access, and mobile devices capable of multimedia services, Indian subscribers are becoming more and more prevalent on over-the-top (OTT) platforms. The growth of new subscribers coming from Tier I and Tier II cities is responsible for this increase in OTT consumption in India.

All media and entertainment outlets' focus. Numerous media and entertainment outlets have started their own platforms or are attempting to work with other platforms to stream their content in response to the growing demand. In India, the OTT market is anticipated to grow significantly during the next five years. Disney+ Hot star, Amazon Prime Video, and Netflix currently have the largest user bases for over-the-top services in India. However, there are a number of local OTTs supported by production houses. With improved networks, better internet access, and mobile devices capable of multimedia services, Indian subscribers are becoming more and more prevalent on over-the-top (OTT) platforms. The growth of new subscribers coming from Tier I and Tier II cities is responsible for this increase in OTT consumption in India.

Such as Sony LIV, Voot , Zee5, Eros Now, and AL Balaji, which are vying for market share against these big competitors globally. People have stayed at home as a result of the COVID-19 pandemic and the ensuing lockdown, increasing the number of subscribers for these OTT platforms. Additionally, since the lockdown caused by the coronavirus hampered the theatrical experience, producers are moving new releases to OTT platforms. With improved networks, better internet access, and mobile devices capable of multimedia services, Indian subscribers are becoming more and more prevalent on over-the-top (OTT) platforms. The growth of new subscribers coming from Tier I and Tier II cities is responsible for this increase in OTT consumption in India [2].

A digital media service that is given directly to audiences over the Internet is known as an OTT (over-the-top) media platform. OTT avoids the businesses that formerly acted as a controller or distributor of this content, including cable, radio, and satellite television channels. It has also been applied to cell phones with no carriers, who charge for all communications as data in order to prevent monopolistic competition. Another term for OTT is a new breed of contemporary television networks that, like traditional satellite or cable TV providers, deliver live broadcasts of linear specialty channels over the open Internet as opposed to a closed, exclusive network of private network of proprietary equipment like setup box.

Over-the-top (OTT) is the video content that is provided over all types of devices which include the traditional closed TVs. When using OTT, customers don't want to pay a TV cable organization to watch content, as most of it is accessible via the internet. With improved networks, better internet access, and mobile devices capable of multimedia services, Indian subscribers are becoming more and more prevalent on over-the-top (OTT) platforms. The growth of new subscribers coming from Tier I and Tier II cities is responsible for this increase in OTT consumption in India [1].

Almost all industries have been adversely impacted by the COVID-19 epidemic in various ways. During these times, the OTT platforms have gone through changes and advanced to the next stage. The use of has increased across all age groups, not just among young people. worldwide entertainment has been satisfied through these platforms which made the OTT wider acceptance.

The mechanism through which internet users watch content like as films and web series directly is known as the Ott platform. The purpose of this platform is to create a web-based interface for the OTT streaming website. This website will be simple to use, making it enjoyable for consumers to watch.

The main objectives of this website are to create an intuitive web interface that allows users to search for films, read a detailed description of the film, and watch the film.

Received on 16-04-2023, Revised on 02-05-2023, Accepted on 11-05-2023.

II. LITERATURE SURVEY

The proliferation of internet-enabled digital devices that can support digitized information has led to an increase in the consumption of digital content internationally, according to the Deloitte research "Digital Media: Rise of on-demand Content." This tendency is visible in India on a variety of channels, including audio, visual, news, music, etc. It states that an Indian teenager, on

The average person devotes 14% of their time and over 17% of their monthly budget to entertainment. An internet user in India consumes 6.2 hours of content on a daily average, with 21% of that time going towards audio-visual entertainment. a change in consumer behavior about a preference for OTT material and convenient access to huge libraries

Manoj Kumar Patel (2020): According to the findings, OTT platforms are evolving and have a significant advantage over traditional entertainment channels. The study claims that the rise of OTT will undoubtedly increase in 8 India due to its cost effectiveness and continual development of content richness, based on an online survey with 95 percent of the primary stakeholders aged 20 to 40 years. Finally, the author believes that the rapid rise of streaming media in India is due to the freedom it offers customers to access information at any time, regardless of location.

Prof. Ripal Madhani and Dr. Vidya Nakhate (2020): The study compares viewing behavior across traditional television channels and over-the-top video platforms in Maharashtra. The article examines the behavioral characteristics of traditional and OTT viewers for a total of 110 persons utilizing a structured questionnaire. In conclusion, the survey find that consumers prefer OTT platforms to traditional television channels because they offer greater convenience in terms of time and locate lower data costs, and instant access to high-quality content.

Meghan McAdams (2019): “Understanding the Modern Media Streaming Landscape: What is OTT.” Due to their involvement with so many channels, % of OTT users are experiencing "subscription fatigue." It was also observed that the potential for comparable specialist offers would not be affected by the emergence of expansive platforms like Disney Plus.

2019: Brett Hutchins According to him, the growth of media sort websites and the market for coverage rights will be disrupted by live streaming services. Tensent Amazon Prime Video, and DAZN are establishing new standards for the availability and curation of sports media, emphasizing a significant change in the media platforms that broadcast live content as well as the global market for sports broadcast rights.

P Singh (2019): P Singh's study, "New Media as a Change Agent of Indian Television and Film: A Study of Over-the-Top Platforms," examines how these new digital platforms are influencing Indian television and film as well as how young people use them to view videos.

According to study, young people enjoy viewing OTT web series and films. The typical OTT watcher watches for two hours, with midnight viewing being the most common. Young people choose over-the-top (OTT) over traditional television due to the service's accessibility to international programming.

Paramveer Singh (2019): According to 2019 research, Jio, Netflix, and Hot star are the most widely used services among young people in India. Youth are more likely to use these sites' free trials, watch at night, and favor web series over films. Over-the-top applications, according to the respondents, are altering Indian media consumption practices.

Drs. Priya Grover and Sabyasachi Dasgupta (2019): According to the study "UNDERSTANDING ADOPTION FACTORS OF OVER-THE-TOP VIDEO SERVICES AMONG MILLENNIUM CONSUMERS," Indian viewers are lured to OTT content and are willing to pay for simple, limitless access to content that is not time- or location-restricted. It again highlights the unfavorable correlation between OTT's pricing strategy and its level of popularity. In addition to their viewing habits and media choices, another aspect that makes it tough for Indian viewers to choose is data consumption.

Valliappan Raju and Muhammad Farooq (2019): the report demonstrates how OTT services have an impact on telecom companies in the era of transformational marketing. This paper focuses on how the emergence of Over-the-Top (OTT) services like WhatsApp, Messenger, and Telegram, which offer many new features like sharing pictures, videos, file transferring, video calling, group conversations, and so on, has caused a revenue loss for telecom's traditional voice and information sectors. According to the survey, customers are purchasing fixed internet contracts and using OTT for communication, which is reducing the revenue generated by voice and SMS for telecom providers. The analysis found that, on the plus side, OTT services had previously been the primary reason for income decreases.

III. IMPLEMENTATION

1. For creating a website where we are using a backend as Firebase, so we need to create an account in firebase.
2. For design purpose we are using react JS for the better user experience while using the website
3. To implement Firebase Authentication in your ReactJS app so that users can login and register. Firebase provides. Various authentication methods, including email/password authentication, google and other sign-ins.
4. We are using a fire store for storing our data. It is best in the business, by this we can easily retrieve and store data.
5. When you’re creating an Ott platform the biggest concern is payment mode it should be more secured so, we are using one of the best payment gateway applications know as stripe payment method [3].
6. We are using video.js or hls.js to implement the streaming functionality. You can store video files in

Firebase Storage and use the streaming libraries to play the videos on the platform.

7. For testing we are using postman for some api testing and basic user interface testing we are just doing manual testing for this project.

VI. RESULTS

Sign up page: Figure 1: This page is used for user to sign up to the application, we are using email id as user identity for Login after the giving the mail user will verify it and verify it and add other personal details.

Figure 1. Sign up page.

Sign in page: Figure 2: This page is used for user to login to the platform and use the website, could be able to login and if we not signed up there is a option for it, once click Login it will check in database whether the user exist if not will throw an error.

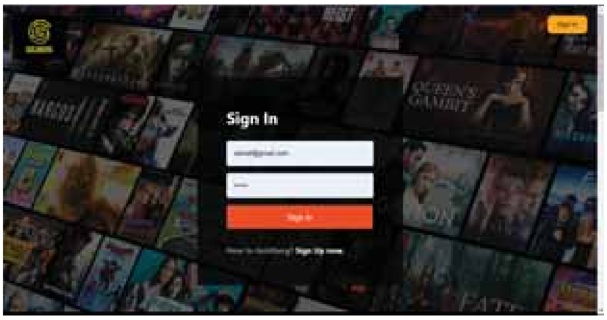

Figure 2. Sign in page

Home page: Figure 3: After the login we will reach the home page, here we display all the movie/Tv series.

Poster will be displayed we are fetching these details from firebase DB, depending upon user selection user can watch the movie/series, after clicking on a movie /tv series user will redirect the streaming page.

When you click on any of the movie/series you will redirect to description page of the movie, if you click on play button.

You will reach the stream page where user could watch the movie/tv series.

We use row module so that users could scroll movies from home page.

Figure 3. Home page

Sign out: Figure 4: from the page and edit the details and user as other facility of shifting the profiles to other profiles here you can choose your payment mode there are total three kind of payment modes here depending which ever you choose you will redirect to payment link where you could enter your details of your credit/debit card and also you can could able to sign out from this page after clicking on sign out page

You can change your profile photo if you want to form your computer by browsing the pic, but the pic should be at limited in size.

Figure 4. Sign out page.

Payment page: Figure 5: This the page where user will enter his/her credit card details for payment process as we are using payment process it will redirect stripe payment page here is sample of the payment page.

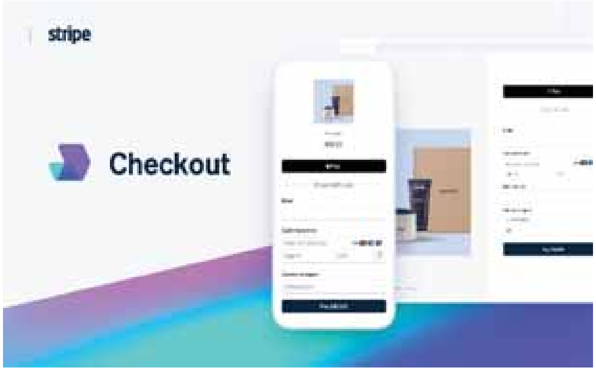

Figure 5. Payment page

V. CONCLUSIONS

React JS is a popular and widely-used JavaScript library for building user interfaces, and it is well-suited for building complex web applications such as OTT platforms. An OTT platform built with React JS can offer a seamless user experience, with fast loading times and intuitive navigation. To ensure the success of the project, it is important to carefully plan the architecture and design of the platform, as well as to thoroughly test and optimize the performance of the application. Overall, building an OTT platform using React JS can be a challenging and rewarding project that requires a combination of technical skills and creativity.

Growing demand [4] for online video content: With the increasing popularity of video streaming services and the rise of mobile devices, the demand for online video content is expected to continue to grow. Improved user experience: OTT platforms using React JS can offer a seamless user experience, with fast loading times and intuitive navigation, which is essential for engaging and retaining users. Ongoing development and innovation: The React JS community is constantly developing new features and tools to improve the performance, scalability, and functionality of the library, which means that OTT platforms built with React JS can benefit from ongoing development and innovation.

React.js has proven to be a great option for creating OTT (Over-The-Top) systems, in conclusion. React.js's component-based architecture, which is effective and modular, has a number of benefits that make it a good choice for creating OTT platforms that are both reliable and user-friendly.

First of all, React.js offers a high level of maintainability and reusability. Developers can more quickly and easily handle updates and modifications by decomposing the user interface into reusable components. Teams can work efficiently together because of its modularity, with many developers working on various components at the same time.

Second, React.js provides outstanding performance. Faster page loads and better user experiences are made possible by its virtual DOM (Document Object Model), which enables efficient rendering by ensuring that only the required components are updated when changes are made.

This is vital for OTT platforms because they transmit a lot of media content and need to ensure seamless playback.

Redux or React Router are only two examples of the numerous modules and tools in the extensive React.js ecosystem that improve development possibilities. Developers can design complex features like user authentication, personalized recommendations, and content management systems using these technologies, which offer state management, routing, and other crucial functionalities.

Additionally, the React.js community offers fantastic help. Developers can discover a wide range of online resources, tutorials, and forums thanks to the huge and active community. React.js is kept current with the newest ideas and best practices thanks to this active community, which encourages the development of OTT platforms.

In conclusion, React.js provides a great foundation for creating OTT platforms, offering performance, reusability, a wide range of tools, and strong community support. By utilizing these benefits, developers may produce interactive features, responsive and engaging user interfaces, and effective content delivery systems, all of which contribute to an outstanding user experience in the realm of online streaming.

React.js-based OTT platforms have a bright future because of the evolving and growing need for online streaming services. Here are some crucial aspects for advancement and development:

React.js can be used by OTT platforms to give more personalized content recommendations based on user preferences, watching history, and behavior. React.js can be combined with machine learning and AI algorithms to deliver more accurate and pertinent suggestions, increasing user engagement and retention.

Advanced Search and Filtering: React.js can be used to create advanced search and filter options that make it simple for users to locate and discover content based on different factors like genre, language, actors, or release dates. The user experience can be further improved by implementing sophisticated search features, such as voice search or predictive search.

React.js may continue to develop to optimize efficiency and scalability for massive OTT platforms, which brings us to point three. The framework can take advantage of technologies like static site generation or server-side rendering (SSR) to speed up initial page loads and overall performance. React.js may also easily adjust to handle growing user traffic and content catalogue growth.

Seamless Multi-Platform Experience: React.js makes it possible to create user interfaces that are responsive and can change fluidly to fit different devices and screen sizes. OTT platforms can employ React.js to create a uniform and understandable user experience across many platforms as mobile devices, smart TVs, and other connected devices become more prevalent.

Integration with Emerging Technologies: To improve the OTT platform experience, React.js may integrate with emerging technologies. Immersive viewing experiences can be provided, for instance, by incorporating virtual reality (VR) or augmented reality (AR) capabilities. Voice-controlled playback and navigation can be made possible by integration with voice assistants or smart home gadgets.

Accessibility and Inclusivity: React.js offers outstanding assistance with creating inclusive and accessible online applications. OTT platforms can concentrate on enhancing accessibility features like keyboard shortcuts, audio descriptions, and closed captioning.

REFERENCES

[1] "What is OTT (Over the Top) and Why is it Important?", Trigger Digital, July 2019, [online] Available: https://www.trigger.digital/blog/2019/8/7/what -is-Ott-over-the-top-and-w

[2]] A. Liptak, "The MPAA says streaming video has surpassed cable subscriptions worldwide", Verge, March https://www.theverge.com/2019/3/21/18275670/mpaareport-streamingvideo-cable-subscription-worldwide.

[3] "Cable broadcasting subscriptions data", 2020 https://www.ncc.gov.tw/chinese/news.aspx?site_content_sn=1966&is_history=0..

[4] C. L. Yeh, "OTT Industrial Policy White Paper", pp. 2326, 2016, [online]Available:https://drive.google.com/file/d/0B1WuxrQ1cL3UeGRKc mFqUmlTaVk/view.

E-ISSN 2581 – 7957
P-ISSN 2277 – 3916

CVR Journal of Science and Technology, Volume 24, June 2023
DOI: 10.32377/cvrjst2415

Automatic Non-Contact Temperature Detection for Health Monitoring

Janardhan Gurram[1], A. V. Shree Anurag [2], Nupur Kumari [3]
[1]Sr. Asst. Professor, CVR College of Engineering/EEE Department, Hyderabad, India
Email: janumtech009@gmail.com
[2]UG Student, CVR College of Engineering/EEE Department, Hyderabad, India
Email: shreeanurag.av@gmail.com
[3]UG Student, CVR College of Engineering/EEE Department, Hyderabad, India
Email: nupursgh24@gmail.com

Abstract: **COVID-19 has made a significant impact on temperature measurement of the human body for primary diagnosis of COVID. Non-contact temperature detection using MLX90614 sensor has been widely used in practice to avoid spread of diseases due to the contact. The thermal gun used to measure temperature is required to be operated by operating personnel. In this paper an automated non-contact temperature detection system is developed and tested. The paper also includes sending the temperature data with a timestamp. The kit developed for the measurement of temperature includes height adjustment mechanism and buzzer alert to indicate higher temperature and make surrounding people know about it. The project proposed in the paper has been developed as a kit with a stand and wheels for easy porting. The project is funded by NexGen IEDC.**

Index Terms: **MLX90614 sensor, non-contact temperature detection, Ultrasound sensor.**

I. INTRODUCTION

With the outbreak of COVID across the world, it became the primary diagnosis of temperature in public places like educational institutes, shopping malls and including workplaces. The general mechanism of measuring the temperature is, by using a thermal gun for which operating is mandatory which puts the operating person at high risk of spread of the disease. To avoid manual intervention in measuring the temperature, an automated non-contact temperature detection kit is prepared with a high reliability and precision measurement. The device is designed with better user experience and calibrated with consideration of real time temperature measurement.

A. Temperature measurements

The human body temperature measurement is done by placing the thermometer probe under the tongue in the mouth and holding it for three minutes till the beep from the device. Rectal thermometers are used for infant babies to measure the temperature as it is difficult to make the babies hold the thermometer for a longer time. Color changing plastic strips are available to measure the temperature and it is not highly accurate [1].

Temperature measurement became the greatest concern for primary diagnosis.

II. PROPOSED SYSTEM

Due to the advent of various non-contact temperature detection products are available in the market with decent accuracy but it requires manual intervention. The product proposed, designed and developed does not need human presence to measure the temperature.

A. Literature Survey

Giovanni Battista Dell Ísola, Elena Cosentini , Laura Canale , Giorgio Ficco and Marco Dell' Isola, MDPI, 2021, To address this issue, researchers have developed an uncertainty evaluation and screening decision rule to guide the use of non-contact temperature measurement devices. This rule considers the uncertainty associated with the measurement, as well as the prevalence of COVID-19 in the population being screened [2]. It recommends a screening decision based on a combination of the measured temperature and the estimated uncertainty of the measurement.

In addition to this decision rule, it is important to use non-contact temperature measurement devices in conjunction with other measures, such as symptom screening and social distancing, to prevent the spread of COVID-19. These devices should also be regularly calibrated and maintained to ensure accurate and reliable measurements.

Overall, non-contact body temperature measurement can be a useful tool in preventing the spread of COVID-19, but it should be used in conjunction with other measures and with an understanding of its limitations and uncertainties. The uncertainty evaluation and screening decision rule can help guide the use of these devices in a way that maximizes their effectiveness while minimizing the risk of false positives or false negatives [3].

G Teran, J Torrez-Llanos, T E Teran-Miranda, C Balderrama, N S Shah, P Villarroel, Child Care Health Dev. 2012 Jul, 'Clinical accuracy of a non-contact infrared skin thermometer in pediatric practice, to address this issue, researchers have developed an uncertainty evaluation and screening decision rule to guide the use of non-contact temperature measurement devices. This rule considers the uncertainty associated with the measurement, as well as the prevalence of COVID-19 in the population being screened.

Received on 24.03.2023, Revised on 18-04-2023, Accepted on 28-04-2023.

It recommends a screening decision based on a combination of the measured temperature and the estimated uncertainty of the measurement [4].

In addition to this decision rule, it is important to use non-contact temperature measurement devices in conjunction with other measures, such as symptom screening and social distancing, to prevent the spread of COVID-19. These devices should also be regularly calibrated and maintained to ensure accurate and reliable measurements.

Overall, non-contact body temperature measurement can be a useful tool in preventing the spread of COVID-19, but it should be used in conjunction with other measures and with an understanding of its limitations and uncertainties. The uncertainty evaluation and screening decision rule can help guide the use of these devices in a way that maximizes their effectiveness while minimizing the risk of false positives or false negatives [5] .

A. Proposed System

The MLX90614 human body temperature sensor can measure temperature using infrared technology by detecting the obstacle at which temperature is to be measured. The temperature sensor uses the output of an HCSR04 ultrasonic sensor that detects the object or person whose temperature is to be found. The LCD screen, which is a flat-panel display [6], uses the light-modulating properties of liquid crystals combined with polarizers in order to display characters effectively on the screen to display messages such as “Please Proceed”, “Calculating temperature, do not remove your hand”, etc.

The Raspberry Pi 4 can be used to measure temperature using the MLX90614 infrared thermometer sensor. This sensor is a non-contact temperature measurement device that uses infrared radiation to measure the temperature of an object or surface without physically touching it [7].

To use the MLX90614 sensor with the Raspberry Pi 4, you will need to connect it to the GPIO pins on the board. The MLX90614 communicates using the I2C protocol, which is supported by the Raspberry Pi. You will need to enable I2C communication in the Raspberry Pi configuration settings and install the necessary Python libraries for interfacing with the sensor.

Once the sensor is connected and the software is set up, you can use Python code to read the temperature measurements from the MLX90614 sensor. The sensor can measure temperatures ranging from -70°C to +380°C with an accuracy of ±0.5°C.

You can also use machine learning techniques to analyze the temperature data collected by the sensor. For example, you can train a machine learning model to detect anomalies in the temperature readings, which could indicate a malfunctioning system or a potential safety hazard.

Overall, the Raspberry Pi 4 and the MLX90614 sensor can be used together to measure temperature and apply machine learning techniques for advanced analysis. This can be useful in a wide range of applications, such as industrial monitoring, environmental sensing, and medical research.

in order to ensure that the concentric hollow rods stay in place at various height levels [8].

Power the Sensor using a regulated +5V through the VCC and Ground pins of the sensor. The current consumed by the sensor is less than 15mA and hence can be directly powered by the on board 5V pins (If available). The Trigger and the Echo pins are both I/O pins and hence they can be connected to I/O pins of the microcontroller.

To initiate the measurement process of the ultrasonic distance sensor, the trigger pin must be set to a high state for a duration of 10 microseconds before being turned off. This action will generate an ultrasonic wave with a frequency of 40Hz from the transmitter.

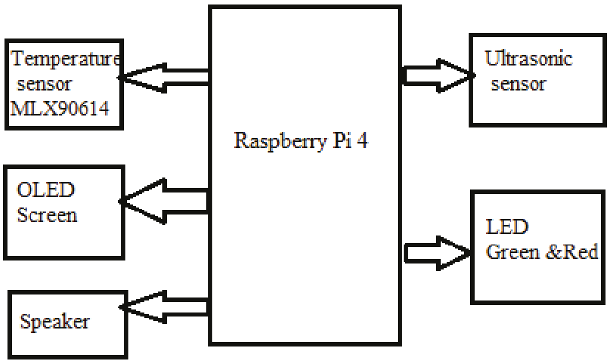

Figure 1. Block diagram of proposed system

The receiver will then wait for the wave to bounce off an object and return to the sensor. When the wave returns, it causes the Echo pin to go high for a specific duration, which is equivalent to the time taken for the wave to return to the sensor after reflection. The microcontroller unit or micro processing unit measures the duration during which the Echo pin remains high, providing information on the time taken for the wave to return [5]-[8]. This information is then used to calculate the distance, as discussed in the preceding section.

Figure 1 presents the block diagram of the proposed system's architecture, illustrating the controller, the temperature sensor MLX90614, and the ultrasound sensor acting as a distance sensor to detect obstacles in the path of the infrared radiation. Figure 2 demonstrates the circuit connections between the different components in the proposed system. Finally, Figure 3 displays the product schematic of the proposed automated non-contact system.

Obstacle sensor recognizes the obstacle or person’s entry detects the temperature if the person puts his/her hand near to the MLX90614 sensor and records the temperature. If the temperature is greater than a preset value then it objects the person’s entry into the place giving an alarm by raising a red colored indication otherwise, it will allow the person into the premises and is shown in flowchart in Figure. 4.

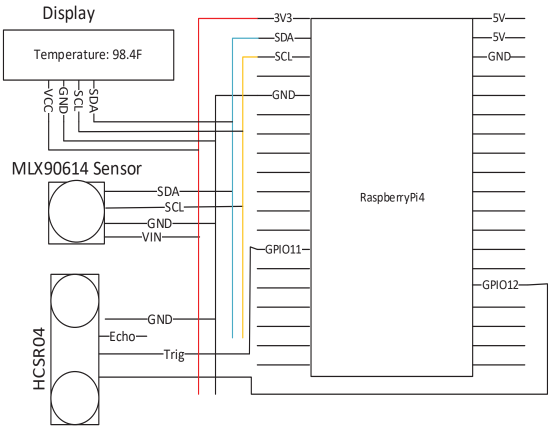

Figure 2. Circuit connection of proposed system

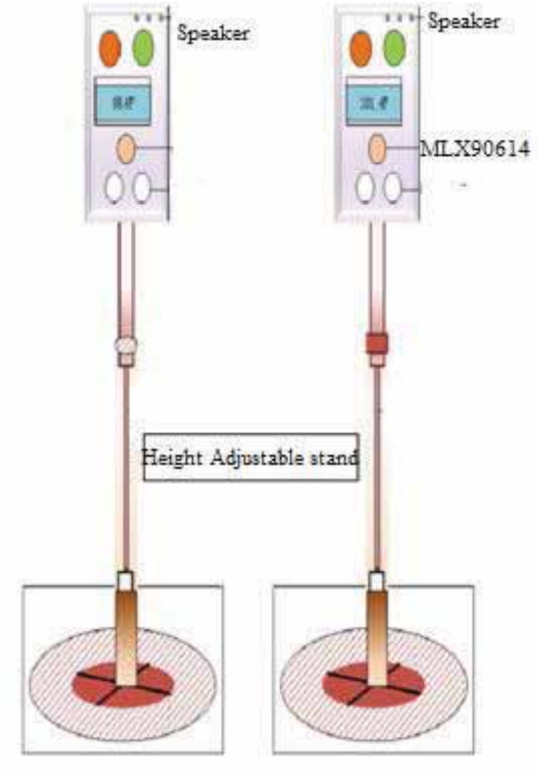

Figure 3. Product structure

Figure3. shows the structure and with a height adjustable mechanism so that a customized height with reference to children and adults height.

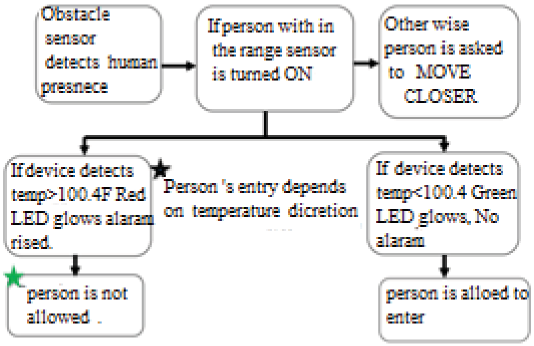

Figure 4. Flowchart of operation of proposed system

TABLE I.
MODULES /SENSORS USED IN THE PRODUCT

S.no	Sensor/Module	Model	Operating Voltgae	Operating range
1.	Infrared Temperature Sensor	MLX90614 ESF-DCI	3V to 5V	-45°c to 85°c 1 - 20cm
2.	Raspberry Pi 4 Model B	Broadcom BCM2711, Quad core	5V	5V/2.5A DC power input
3.	LCD Display	HD44780	5V	20x4 size
4.	Obstacle Sensor	HC SR04	5V	2cm to 80cm
5.	Speaker	SR-887	5V	AUX Line-In speaker

TABLEI. indicates the modules and sensors used in the automated non-contact temperature detection system.

The MLX90614 is a non-contact infrared thermometer that measures temperature. It contains both an IR-sensitive thermopile detector chip and a signal conditioning ASIC integrated into the same TO-39 can. The MLX90614 features a low noise amplifier, a 17-bit ADC, and a powerful DSP unit, enabling it to achieve high accuracy and resolution in temperature measurement [9].

The HCSR04 is an ultrasound sensor that can be used to measure distances non-invasively. It operates by sending out ultrasonic waves from the transmitter and detecting the waves that bounce back to the receiver. The time taken for the wave to travel to the object and back to the receiver is used to calculate the distance between the sensor and the object [10].

The HCSR04 has four pins: VCC, Trig, Echo, and GND. The VCC pin is connected to a power supply, typically 5V. The Trig pin is used to initiate the measurement process by sending out a high pulse of at least 10 microseconds [6]. The Echo pin is used to measure the time duration for which the pin remains high, which corresponds to the time taken for the wave to return. The GND pin is connected to ground.

A 16x4 LCD character display is a type of alphanumeric display module that can show up to 16 characters per row and 4 rows of characters. These displays are commonly used in various applications such as medical instruments, industrial equipment, and consumer electronics [11].

The LCD display module typically consists of a controller chip, a display driver, and a backlight. It can be interfaced with a microcontroller or other electronic circuits through various communication interfaces such as parallel or serial. The display can be customized to show different fonts, sizes, and styles of characters [6].

III. MECHANICAL DESIGN

A. *Casing for Components*

The electronic components of the device are enclosed in a 21.5x22x22 cubic cm metal box. Device view and dimensions are cited in Figure.7.

As shown in the image, the place at which a person is required to show their hand is very clearly indicated through yellow colored protrusion. Highlighting this area ensures that a person has no confusion whatsoever, regarding where they should place their hand. Within the highlighted cylindrical protrusion, obstacle sensor and IR temperature sensor are present.

The inside of the metal enclosure is outfitted with insulating fiberglass, which ensures that no short circuit condition is possible.

The PCB is held in place within the casing through screws, and a separate slot is created for the power source inside the enclosure. Panel dimensions are shown in figure. Two slots, one for power line-in/charging and other for battery percentage indicator are present. System is operated (ON/OFF) through a switch fitted in the back panel, through a push button. The casing is painted with rust resistant, triple coat blue paint for aesthetics and surface corrosion protection.

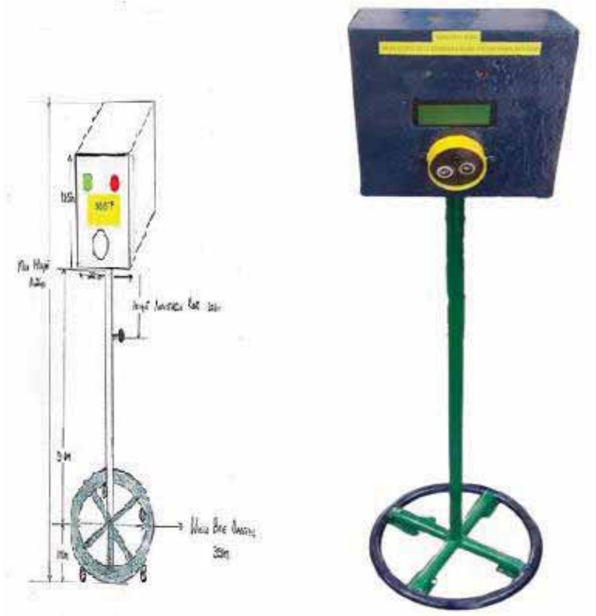

Figure.7. Mechanical Design

IV. METHODOLOGY

The automated non-contact temperature detection using MLX90614 sensor is mentioned in the following steps.

1. When a person stands at the designated area in front of the device, and shows his palm as instructed on the device screen, the obstacle sensor detects the presence of a person.
2. The obstacle sensor triggers the high accuracy IR temperature sensor to take a reading of the person's body temperature.
3. The temperature sensor takes multiple readings, and the device averages out the readings to arrive at the exact and accurate temperature of the person.
4. If the person's body temperature is detected to be above a pre-set temperature (100.4 F in this case), this means that the person has a fever.
5. In this case, the device immediately displays a message asking the person to stop, and a red bulb glow, signifying abnormal temperature.
6. At the same time, a siren is heard along with a voice message, to indicate to the people around that a potential threat to health has been detected.
7. However, if a person's temperature is detected to be within normal limits, then a message flashes on the screen, advising him/her to proceed.
8. Along with the message, a green bulb lights up, and a voice is heard asking the person to proceed.
9. Thus, our device is user friendly, as the user is directed through both messages on the screen, as well as through green and red-light bulbs in a visual and auditory manner.
10. This ensures that even illiterate people can use the device with no difficulty.

The temperature is measured using a commercial thermal gun and is compared with an automated non-contact temperature device that is designed and developed at the NewGen center at CVR College of Engineering. Table II. compares the temperature measurement using both methods. The temperature sensor of this device has been calibrated by keeping a medical grade, high accuracy Intext non-contact-based thermometer as reference.

Subject's body temperature was measured using our device first, and the standard thermometer next. The results are tabulated as cited in TABLE II. There is close to zero variation between the temperature reading taken by our device, and the medical grade thermometer. In a similar manner, the obstacle sensor was also tested, and its readings (in terms of distance of an object from the sensor) were found to be accurate,

The sensor calibration process was carried out, to ensure highly accurate readings at every instance.

TABLE II.
TEMPERATURE COMPARISON

S. No.	MLX90614 Sensor (Observed) Temperature measured(F)	High accuracy Contact Thermometer based Thermometer (Expected)(F)	Error value (F) (Observed-Expected)
1.	96.8	96.7	0.1
2.	97.3	97.2	0.1
3.	96.4	97.0	-0.6
4	98.6	98.9	-0.3
5.	97.7	97.7	0
6.	96.9	96.6	-0.3

Figure 7. Temperature measurement comparison

V. CONCLUSIONS

The need for a Non-Contact Temperature Detection System in the present society where COVID-19 has become a part of our life. The technology, working, circuit diagram as well as the design of the device have been illustrated in detail. The calibration of the temperature sensor, compared with standard temperature sensor has been done, and it has been found to be highly accurate. The mechanical design and integrity of the device casing has been discussed to be resilient. Thus, this device can provide a one stop Non-Contact Temperature solution to be used in all public places. Adding the features mentioned in the future scope section of this document will extend the usability of the device even further. Owing to the accuracy, easy-to-use, as well as the time pertinent nature of our device, our project can be a useful tool in the arsenal in the fight against COVID-19. Face mask detection can be incorporated by implementing Machine Learning algorithms.

REFERENCES

[1] https://medlineplus.gov/ency/article/003400.htm

[2] A. Shajkofci, "Correction of Human Forehead Temperature Variations Measured by Non-Contact Infrared Thermometer," in IEEE Sensors Journal, vol. 22, no. 17, pp. 16750-16755, 1 Sept.1, 2022, doi: 10.1109/JSEN.2021.3058958.

[3] J. -W. Lin, M. -H. Lu and Y. -H. Lin, "A Thermal Camera Based Continuous Body Temperature Measurement System," 2019 IEEE/CVF International Conference on Computer Vision Workshop (ICCVW), Seoul, Korea (South), 2019, pp. 1681-1687, doi: 10.1109/ICCVW.2019.00208.

[4] A. Sharma and A. R. Yadav, "Image processing based body temperature estimation using thermal video sequence," 2017 International Conference on Computing Methodologies and Communication (ICCMC), Erode, India, 2017, pp. 846-852, doi: 10.1109/ICCMC.2017.8282585..

[5] Dell'Isola, G.B.; Cosentini, E.; Canale, L.; Ficco, G.; Dell'Isola, M. Noncontact Body Temperature Measurement: Uncertainty Evaluation and Screening Decision Rule to Prevent the Spread of COVID-19. *Sensors* 2021, *21*, 346. https://doi.org/10.3390/s21020346

[6] Teran CG, Torrez-Llanos J, Teran-Miranda TE, Balderrama C, Shah NS, Villarroel P. Clinical accuracy of a non-contact infrared skin thermometer in paediatric practice. Child Care Health Dev. 2012 Jul;38(4):471-6. doi: 10.1111/j.1365-2214.2011.01264.x. Epub 2011 Jun 8. PMID: 21651612.

[7] Ian Sinclair, *Sensors and Transducers*, Third Edition, Elsevier Publications, 1 January 2011, ISBN-10:9380931085

[8] Simon Monk, Raspberry Pi Cookbook, Second Edition, 6 August 2016, ISBN-10 : 9789352133895

[9] https://www.melexis.com/en/documents/documentation/datasheets/datasheet- mlx90614

[10] https://www.ncbi.nlm.nih.gov/pmc/articles/PMC7284737/

[11] https://www.raspberrypi.org/documentation/hardware/raspberrypi/bcm2711/rpi_DAT A_2711_1p0_preliminary.pdf

E-ISSN 2581 – 7957
P-ISSN 2277 – 3916

CVR Journal of Science and Technology, Volume 24, June 2023
DOI: 10.32377/cvrjst2416

Design and Analysis of a Switched Capacitor Inverter for EV

G. Harshavardhan[1] and G. Prasanthi[2]
PG Scholar, JNTUA College of Engineering Mechanical Engg, Department, Ananthapuramu, India.
Email: harsheee14@gmail.com
Professor, JNTUA College of Engineering/Mechanical Engg, Department, Ananthapuramu, India.
Email: prasanthi.mech@jntua.ac.in

Abstract: **This paper focuses on the switched-capacitor converter configurations for a wide range of applications, which have numerous stages which are designed for different voltage levels. A single-phase switching capacitor multilevel boost inverter topology configuration with fifteen levels is discussed using fewer switches and a voltage boost gain. The main goal of this work is to develop a 15L multilevel inverter that can provide AC output voltage with minimal harmonic distortion. The output THD decreases to zero as even the level number approaches infinity.**

Index Terms: **Multilevel inverter (MLI), Cascaded H-bridge, 15 level inverter, reduced switches.**

I. INTRODUCTION

The desire for more powerful machinery, which can now produce megawatts of power, has just started to grow in the industry. The medium voltage is typically coupled to a megawatt-sized regulated AC drives network. Currently, it is not possible to link a medium voltage grid directly to a single semiconductor switch. A new family of multilevel inverters has been developed to function at greater voltage levels.

Multilevel inverters use power semiconductor and capacitor voltage sources to produce voltages with stepped waveform. Power semiconductors can only withstand lower voltages, but switch commutation enables capacitor voltage addition, producing a high output voltage. Due to their versatility and flexibility to work at many voltages, multilevel inverters are currently utilised extensively. Several dc voltage sources are used by the multilevel inverter to generate the required output. By using a switching frequency and more dc sources, an inverter's voltage output waveform gets closer to having a symmetrical Frequency [1]. Due to the numerous dc sources, it has little switching losses, low voltage stress, high efficiency, minimal output of Electro Magnetic Interference (EMI), and capacity to operate at high voltage. In addition, multilevel inverters would undergo more procedures. The multilevel approach is based on an inverter with three levels [2–5]. The use of multilevel inverters in power electronic applications is growing because they can satisfy the growing need for power rating and power quality, as well as a reduction in harmonic distortions and electromagnetic interference. Pulse width modulated (PWM) and switching frequency of Multilevel inverters are a variety of ways that make them preferable to two-level inverters [6]. The following are the advantages of a multilevel inverter that stand out the most: a) It is possible to generate reduced dv/dt stress and less distortion in the output voltage. b) There is negligible distortion in the current input drawn. c) There is an incredibly low common mode voltage. d) The switching frequency is incredibly low. The configuration of a multilevel inverter consists of capacitor voltage sources and devices for transmitting power. It is suitable for high voltage applications and voltage waveforms because it can measure the output voltage with greater harmonics to acquire high voltages with maximum device rating. Capacitor-clamped inverters, Diode-clamped inverters, and Cascaded H-bridge inverters are the three primary varieties of multilevel inverters. At each level, fewer cascaded H-bridge inverters, switches, and capacitors are needed.

A cascaded H-bridge with switches and capacitors creates a discrete input voltage in multilevel inverters [11]. One H-bridge cell may deliver voltages at zero, one, and two volts DC. This multilevel inverter's main advantage is that it has fewer parts than the other two types. Compared to the other two types, the inverter is less expensive and lighter. To develop original switching methods, soft switching might be used [7]. Multilevel cascade inverters are utilized to eliminate THD harmonics, the transformer required for standard multilevel inverters, the clamping diodes required for diode-clamped inverters, and the flying capacitors required for flying capacitor inverters all need to be considered. This is the situation if each cell needs a lot more isolated voltage than the other two types [8]. As switching device counts and Total Harmonic Distortion are reduced, the proposed Multilevel Inverter Topology provides greater advantages than current topologies [9] – [10], Switching losses are decreased as a result and improving output effectiveness. We are developing a multilevel inverter with fewer switches, more efficiency, and lower losses. The widespread use of pulse width modulation (PWM) techniques is due to their easy usage, long lifespan, and minimal computational needs [12].

II. CONVENTIONAL MULTILEVEL INVERTER

A number of levels of dc voltages, which are frequently produced from capacitor voltage sources, are combined to create a minute sinusoidal voltage in the fundamental design of the converter with many levels. The synthesized output

Received on 11-03-2023, Revised on 13-04-2023, Accepted on 05-05-2023.

waveform includes more steps as the level count rises, creating a staircase wave that resembles the desired waveform. The output wave's harmonic distortion lowers and approaches zero when more levels are added to the waveform. The quantity of levels rises, and so does the voltage that can be increased by introducing more levels of voltage. It is possible to determine the output voltage while operating in the positive half-cycle.

A. Cascaded multilevel inverter

An inverter with cascading multilevel is shown in Figure 1 below. A number of H-bridge inverter modules make up the device. This multilevel inverter's primary goal is to produce the required voltage from a number of dc sources, including batteries, fuel cells, and solar cells. It shows how a cascaded single-phase inverter with SDCSs is built from the ground up. Each SDCS is as seen in Figure 1 below, coupled to an H-bridge inverter. The ac terminal voltages of various level inverters are used to connect them in series. Contrary to the diode clamp or flying capacitor inverter, the cascaded inverter does not require any voltage-balancing capacitors or voltage-clamping diodes.

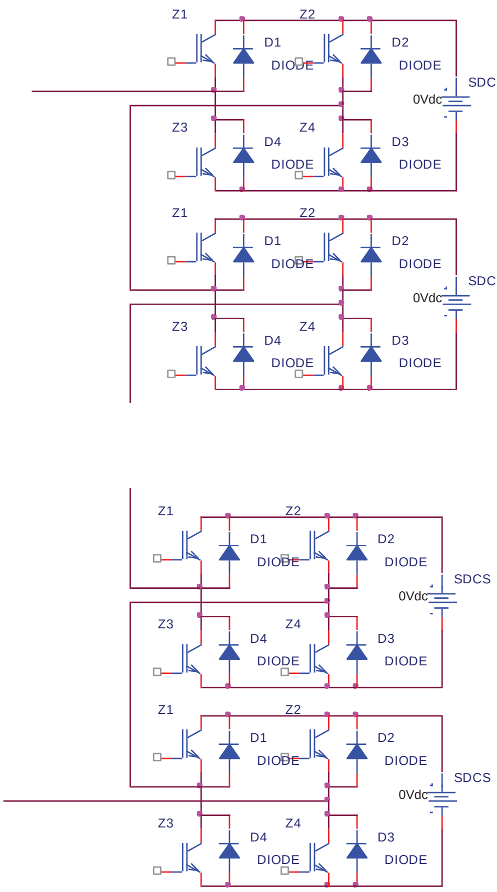

Figure 1. Cascaded Multilevel Inverter.

B. Proposed method

The various topologies of multilevel inverters as they are described in the literature have a lot in common. Their main disadvantage is the circuit complexity of multiple inverter setups, which calls for numerous power switches. Generators or series-connected coordinated power switches are not necessary for the multiple energy supply converters to reach high energies with low harmonics thanks to their distinctive structural design. A multilevel inverter's primary job is to combine various dc power values to create the intended voltage. The enormous power required by large electric drives can be conveniently provided by multilevel inverters. The intended waveform resembles a staircase waveform because as the number rises, the synchronized result pattern has more phases. Just as the level count increases as more levels are introduced to the waveform, the harmonic component of the output wave decreases to zero.

The voltage that can be covered by adding additional inverters rises with the number of levels, so the active devices never have voltage-sharing issues. Utility applications do not use electric motor drives, which employ several inverters. In static var correction, no active power is transferred between the converter and the system, but in motor drives, the converter must manage a bidirectional real power flow. Due to the switching between a number of smaller voltage levels, multilevel PWM drives have a lower dv/dt. Switching losses and the voltage's overall harmonic distortion is still significant. The converter that generates uniformly balanced voltages across the capacitors in the dc link has numerous levels of clamped diodes. As we move to the simpler H-Bridge multilevel inverter, both power devices and circuit complexity will reduce, leading to a reduction in circuit losses. If the trend of technology to make multilevel inverters more affordable is also considered, they can compete with the standard arrangement.

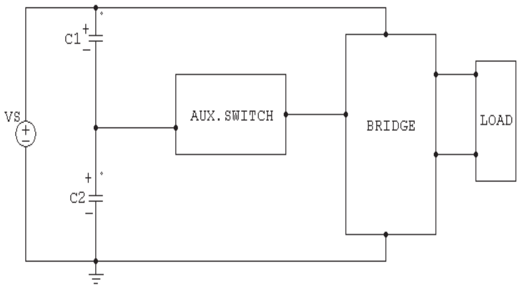

Figure 2. Block diagram of MLI.

A new converter topology is presented in this study which is depicted as a block diagram in Figure 2 (burdensome power stage and complex firing regulating circuit). Using a controller, the firing control circuit was created, and it was used in the design of the seven-level bridge converters shown below.

In this design, the inclusion of an H-Bridge stage and an auxiliary bidirectional switch significantly reduces the complexity of the power circuit.

Standard sinusoidal pulse width modulation is utilized to give switching pulses to the H Bridge circuit (for the generation of positive and negative cycles). The switching pulses for the frontend MOSFETs are produced using the binary priority encoder's logic, which was previously explained. These pulses are generated when the reference signal crosses the carrier signals. Each switch receives a delay along with the generated pulses. The carrier waves roughly have a frequency of 5 KHz, whereas the Reference Sine waves have a frequency of 50 Hz. Regarding component count and layout complexity, the power stage's innovative converter architecture provides a major improvement. The second-best architecture, the asymmetric cascade arrangement, requires fewer diodes and capacitors and fewer primary switches than the simplified H-bridge multilevel inverter. The FPGA has the ability to conduct all required modulation in the modulator circuit functions, which are demonstrated in Figure 3 below, providing yet another substantial reduction in price and circuit complexity.

The circuit design of the 15-level multi-inverter shown the H-bridge in Figure 3. It is composed of Six auxiliary switches, and four main switches for 15-level output voltage capacitors which are needed.

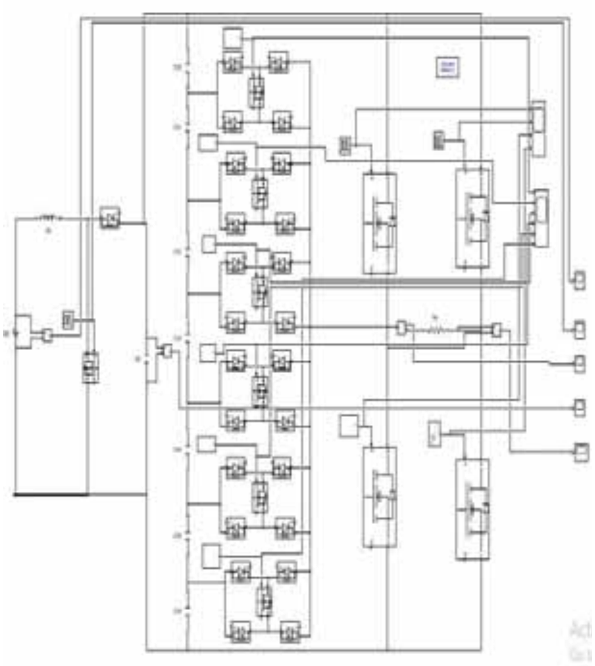

Figure 3. MATLAB Circuit Diagram.

To demonstrate how this streamlined H-bridge multilevel inverter architecture may reduce the number of components, the total number of components was calculated, reducing the number of controlled power switches from the required twelve to just seven, implementing a 13-level simplified H-bridge multilevel inverter and three previously established ones, the diode clamped and capacitor stages, which are considered to be the conventional multi-level stages. Clamped configuration and a new and highly improved multi-level stage with reduced switches achieve approximately requirements for primary switches that are reduced by 40%. The voltage and current ratings of the auxiliary switch are less than those of the regulated switches.

Auxiliary Devices (Capacitors & Diodes): Compared to the diode-restricted configuration, the new configuration needs fewer capacitors and diodes.

Furthermore, since the primary dc power supply is connected to three capacitors in parallel, there is no substantial, during normal operation, capacitor voltage swing range of the previous multilevel.

C. Simulation

In Figure 4 shows the firing pulses to the switches, Figure 5 shows the experimental setup, and Figure 6 shows the cascaded 15-level output waveform.

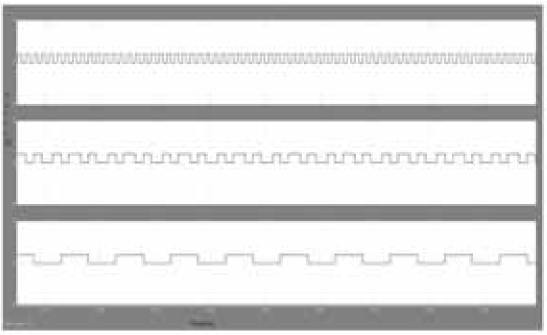

Figure 4. The Firing Pulses to the Switches.

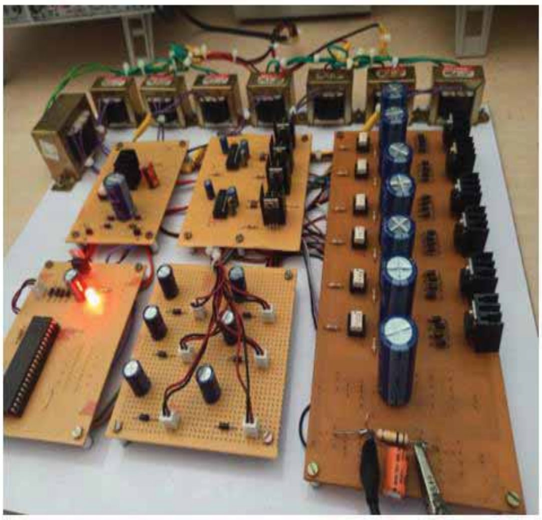

Figure 5. Experimental Setup of Cascaded 15-Level Inverter.

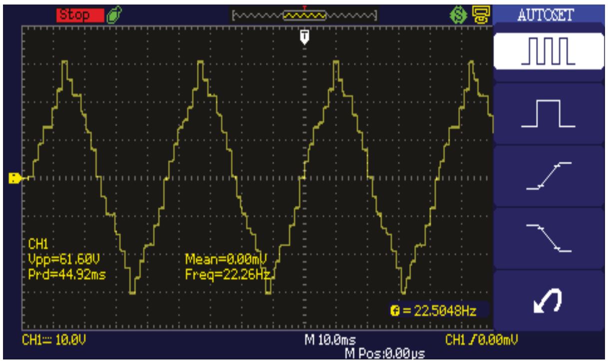

Figure 6. Output waveform

III. CONCLUSIONS

To investigate different operating models, an MLI topology with a single phase, and 15 Switches for level lowering are used. An FPGA IP Core Processor-based Hardware prototype is used to verify the simulation results. A cutting-edge SPWM modulation technique is suggested. The inverter can expand while still providing a high output voltage and lowering overall expenses by raising the level with the fewest switches possible. This research proposes an Asymmetric cascaded multilevel inverter with fifteen levels. It generates a high-frequency sinusoidal waveform. A cascaded multilevel inverter's efficiency can be increased by reducing switching losses, and overall harmonic distortion must be decreased.

REFERENCES

[1] Nabae; I. Takahashi; H. Akagi. ―A new neutral point-clamped PWM inverter‖, IEEE Trans. on Industry Applications, vol. 17, no. 5,pp. 518- 523, 1981.

[2]] C.Bharatiraja, R.Latha, Dr.S.Jeevananthan,S.Raghu and Dr.S.S.Dash,"Design And Validation Of Simple Space Vector PWM Scheme For Three-Level NPC - MLI With Investigation Of Dc Link Imbalance Using FPGA IP Core‖, Journal of Electrical Engineering, vol. 13, edition 1, pp 54-63, 2013.

[3] Rodriguez, J.; Jih-Sheng Lai ; Fang ZhengPeng."Multilevel inverters: a survey of topologies, controls,and applications‖, IEEE Transactions on IndustrialElectronics, vol. 49, no. 4, pp 724-738.

[4] P.Jamuna; Dr.C.ChristoberAsirRajan "New Asymmetrical Multilevel Inverter Based Dynamic Voltage Restorer‖ Journal of Electrical Engineering, vol. 13, edition 1, pp 244-252, 2013.

[5] Nikhil; V.K.; Joseph, K.D. "A Reduced Switch Multilevel Inverter for Harmonic Reduction", Power and Energy Engineering Conference (APPEEC), Asia-Pacific, pp 1-4, 2012.

[6] Al-Judi; A.; Bierk, H.; Nowicki, E."A modified cascaded multilevel inverter with reduced switch count employing bypass diodes IEEE Conference on Vehicle Power and Propulsion, pp. 742-747, 2009

[7] Ebrahim B., Mohammad F., Farshid N."Symmetric and asymmetric multilevel inverter topologies with reduced switching devices, Elsevier Journal of Energy Conversion and Management, Electric Power Systems Research Vol. 86, pp.122-130,2012.

[8] E. Babaei,"A cascade multilevel inverter topology with reduced number of switches, IEEE Trans. Power Electron. Vol 23 no. 6, 2657– 2664, 2008.

[9] M. Calais, V. G. Agelidis, Multilevel converters for single-phase grid connected photovoltaic systems, an overview, in Proc. IEEE Int. Symp. Ind. Electron, vol. 1, pp. 224–229, 1998..

[10] S. B. Kjaer; J. K. Pedersen; F. Blaabjerg. ,"A review of single-phase grid connected inverters for photovoltaic modules, IEEE Trans. Ind. Appl., vol.41, no. 5, pp. 1292–1306, Sep./Oct. 2005.

[11] P. K. Hinga; T.; Ohnishi; T. Suzuki, "A new PWM inverter for photovoltaic Power generation system, Rec. IEEE Power Electron. Spec. Conf., pp.391–395, 1994

[12] Boost, M.A.; Ziogas, P.D.," State-of-the-art carrier PWM techniques: a critical evaluation ,IEEE Transactions on Industry Applications, vol. 24, no. 2,Mar 1998 pp 271-280

E-ISSN 2581 – 7957
P-ISSN 2277 – 3916

CVR Journal of Science and Technology, Volume 24, June 2023
DOI: 10.32377/cvrjst2417

Synthesis and Characterization of Encapsulated PCM

Panuganti Leelavathi
Asst. Professor, KLR College of Engineering and Technology/ Mechanical Engg. Department, Kothagudem, India.
Email: panugantileelavathi054@gmail.com

Abstract: **The purpose of this research was to develop and examine the TES properties of a unique organic PCM that has been encapsulated (Encapsulated PCM). The methyl palmitate PCM core and the melamine-formaldehyde shell of the microcapsules were synthesized by a simple in-situ polymerization process. According to the results of the microstructural examination, it can be assumed that the as-prepared microcapsules were of spherical shape, and the presence of carbon, oxygen, and nitrogen elements proves that the encapsulated PCM was successfully formed. The improvements in chemical stability, surface roughness, and average particle size (490.2 nm) have allowed for greater storage stability. Having a high latent heat of fusion of 70 kJ/kg, the microcapsules have a high thermal storage capacity of 88%. The operational temperature range of the pure PCM was significantly lower than the microcapsules' thermal stability of 130 °C. Moreover, the Micro PCM met the thermal insulation standards due to its low observed thermal conductivity of 0.1587 W/m K. During the thermal cycling test, microcapsules showed incredible chemical stability (up to 200 heating/cooling cycles) and thermal reliability (reliability index = 92.9%). The results of the tests suggest that the encapsulated PCM with the improved characteristics can be a good candidate for low temperature thermal energy storage.**

Index Terms: **PCM, Encapsulation.**

I. INTRODUCTION

In recent decades, researchers have paid more attention to the process of microencapsulation, in which a functional component is enclosed in a membrane or polymeric shell material. Cell transplantation, food processing, drug delivery, pharmaceutical products, cosmetics, adhesives, self-healing coatings, fermentation, pesticides, textile printing and dyeing, energy storage, and so on are just some of the major application domains where microencapsulation is well established and being implemented.

With its energy storage qualities by virtue of their solid-liquid phase transition behaviour, phase change materials (PCMs) have become highly desirable in recent years for use in thermal energy storage (TES). The organic PCMs in the form of microcapsules are chosen over the inorganic PCMs and the eutectic PCMs for use in thermal energy storage (TES).

This is because phase change materials (PCMs) can undergo the process of phase transition within the shell material without any leakage. Also, the relatively small size of the microcapsules would greatly enhance the influence of surface energy. In addition, the PCM's thermal-physical and physico-chemical characteristics can be shielded from disturbances caused by physical, chemical, and sudden changes in the process/environmental conditions by microencapsulation.

On the other hand, organic PCM has some drawbacks, such as poor heat conductivity, problems with handling and leakage during phase transformation, and interactions with other materials, etc. Thermo-physical property improvements in PCMs have been examined in the past with the goal of improving their TES capacities.

PCMs, on the other hand, would degrade if left unprotected from the elements. In a similar manner, extended exposure to extreme temperatures may affect the thermo-physical properties of Encapsulated PCMs. In this regard, the cycling stability test of a storage unit is essential for ensuring its long-term functioning. In a standard thermal cycling test, the latent heat storage system goes via at least one melt-freeze cycle per day [1].

Melt-freeze cycles of Encapsulated PCM, however, are performed in a lab setting under controlled conditions during an accelerated thermal cycle test. If the PCM is not well encapsulated, it could escape and undergo heat and/or chemical interaction with the surrounding matrix materials, losing its essential properties in the process.

Methyl Palmitate was used as the PCM and melamine-formaldehyde was used as the shell material in the reported fabrication of encapsulated PCM. When the MEPCM was put through 100 thermal cycles, there was reportedly no substantial thermal drop in enthalpy or leakage of the PCM from shell material.

Notably, melamine's great mechanical strength makes it a viable candidate as a shell material to prevent leakage problems in the PCM. Melamine also extinguishes itself if it catches fire. Furthermore, melamine has a propensity to decrease water content, which can improve the fluidity and workability of the surrounding materials in specific contexts [2].

In this context, a variety of synthesis methods are available for the manufacture of the MPCMs, and they can be roughly divided into:

Each of the aforementioned approaches to synthesis has advantages and potential uses in certain contexts. The in-situ polymerization approach for manufacturing MPCMs has gained traction in recent years, expanding their use across the board of TES applications. Because in-situ polymerization is one of the most efficient techniques because the reactants are not mixed in with the PCM and the whole process occurs in a single, unbroken stream.

Numerous recent studies have demonstrated the encapsulation of various PCMs using different shell

Received on 06-02-2023, Revised on 21-02-2023, Accepted on 15-04-2023.

materials, giving credence to the effectiveness of the in situ polymerization technique.

Urea formaldehyde (UF) and melamine formaldehyde are two of the most common candidate shell materials (MF). Cross-linked microcapsules consisting of a PCM core and a UF or MF shell can be manufactured with ease using a condensation polymerization procedure.

Microcapsules with interesting compositions, such as paraffin/melamine-UF, Methyl Palmitate/poly(styrene-co-divinylbenzene-co) acrylamide, n-eicosane with a poly(methyl methacrylate-co-methacrylic acid), and n-dodecane/MF shell, have been produced and effectively used to store.

The ratio of the mass of the microcapsules after encapsulation to the mass of the PCM before encapsulation is a fundamental determinant of the quality of any microencapsulation procedure. Furthermore, the quality of the microencapsulation is determined by crucial factors such as (a) the mean diameter of the particle, (b) the thickness of the shell, (c) the type of the precursors, surfactants, reagents, solvents, pH regulators, etc., and their proportions, (d) the reaction time, and so on.

Although there have been many studies on the synthesis of MPCMs with respectable encapsulation quality and properties, these studies have been restricted to medium and palmitate. The white powder was then separated from the supernatant and collected. After being washed twice with acetone, this powder was used to create the final encapsulated PCM.

II. EXPERIMENTAL PROCEDURE

2.1. Preparation of Encapsulated PCM

Encapsulated PCM was made by encapsulating Methyl palmitate PCM in a melamine formaldehyde shell using a simple in-situ polymerization technique. Different methods of PCM encapsulation have been tested. Trials revealed that adjusting the cross-linking agent concentration influenced microcapsule formation. Furthermore, the production of microcapsules was greatly aided by the process taking place in acidic conditions.

Although it was not possible to completely prevent agglomeration/coalescence, good control over encapsulated PCM formation was achieved by lowering the copolymer percentage, fine-tuning the hydrophilic-lipophilic balance (HLB) scale of surfactant molecules, and adjusting the pH value for the reaction. As a result of these measurements, the response was adjusted as follows: Equal parts of Tween 20 and Span 60 were used as surfactants in the O/W mix. An additional 50 ml of Methyl palmitate PCM was added, and the whole thing was mixed at a speed of 8000 rpm to 8500 rpm in a high-speed shear mixer.

Oil in water emulsion had a pH value between 5.8 and 7. The shell precursor, on the other hand, was made by dissolving 30 mm of formaldehyde solution into 100 milliliters of dimethyl-dimethyl-siloxane (DDW).

high temperature energy storage applications. Even fewer studies have been done on the topic of encapsulated organic PCMs with MF or UF shell material for low temperature energy storage applications [2].

This study considered Methyl palmitate, or lauryl alcohol, a saturated 12-carbon organic fatty alcohol that can be prepared from the fatty acids found in coconut oil. Methyl palmitate is used in a wide variety of industries, from the cosmetics and lubricant oil industries to flavor enhancers, perfumes, construction, agriculture, and the pharmaceutical industry. Despite Methyl palmitate's widespread application, our research shows that its capacity as a storage medium for energy is still relatively unexplored. Consequently, this research is unique in its investigation of the energy-storage characteristics of Methyl Palmitate as PCM for use at low temperatures.

To be more specific, this study aimed to develop a simple method for synthesis of encapsulated PCM with Methyl palmitate in the center and melamine-formaldehyde on the exterior. Following synthesis, the microcapsules were studied for microstructural, chemical, and thermal energy storage capabilities. The effects of 200 thermal cycles on the chemical stability and thermal reliability of encapsulated PCM were also investigated. The findings are shown and explained in detail.

III. RESULTS AND DISCUSSION

3.1. FESEM Results of the encapsulated PCM

The as-synthesized microcapsules' surface morphology was examined using FESEM with an EDS detector. The FESEM images in Fig. 1 demonstrate that the microcapsules were roughly spherical in shape and displayed a modest degree of surface roughness. Encapsulated PCM capsules were primarily formed due to interfacial tension between the PCM, polymer, and surfactant.

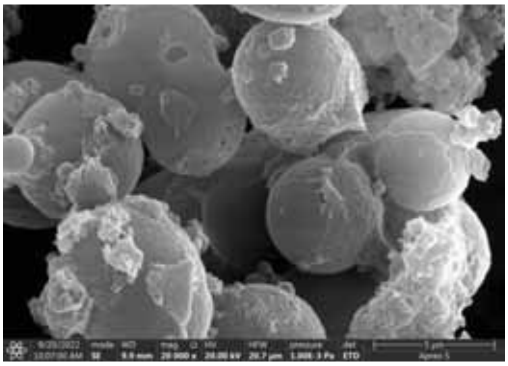

Figure1. FESEM images of Encapsulated PCM

3.2. Particle size distribution of the Encapsulated PCM

From Fig. 2, the microcapsules ranged in size from far under 60 nm to well over 980 nm. Capsules with a first peak averaged 119.6 nm in diameter and a second peak averaged 550.1 nm in diameter at 65.9% and 34.1% intensity, respectively. To be precise, we calculated a Z-average microcapsule diameter of 380 nm across both peaks. Furthermore, this provided strong backing for the study's simple synthesis of Encapsulated PCM, which formed at the micro/nano scale. In addition, as shown in Fig. 1 (b) and because of the smaller particle size, it was predicted that the surface energy would increase as the radius of curvature between two adjacent particles was decreased [4].

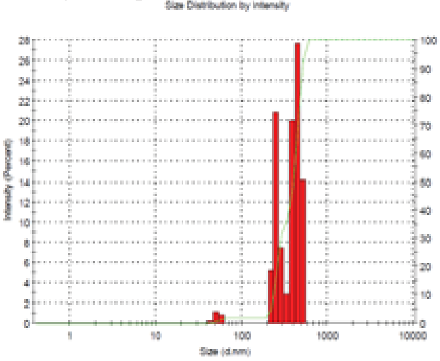

Figure 2. Particle size distribution of the Encapsulated PCM.

3.3. Crystal structure of the Encapsulated PCM

In Fig. 3, we see the XRD pattern of the Encapsulated PCM, which exhibits a broad and massive peak at 21.24Â°, indicating that the material is mostly amorphous. This might be because of the Encapsulated PCM's disordered molecular structure, which caused the lattice parameter to shift.

Physical interaction between the PCM and the shell material or a lack of incident electrons diffracted along that lattice direction of the Encapsulated PCM may explain the lack of a highly crystalline structure [5].

Encapsulated PCM's lack of crystalline ability and weak peak intensity may have been caused, at least in part, by the sample powder's coarse grain structure. Encapsulated PCM's amorphous structure was predicted to have a high internal energy, and the powdered form of the microcapsules being manufactured showed a promising dispersal performance. Additionally, the shell stability and resistance against cracking were characterized by the low peak intensity, but at the expense of a decrease in the encapsulating properties.

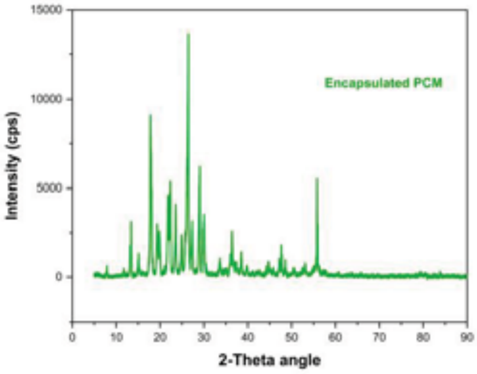

Figure 3. XRD pattern of the Encapsulated PCM.

3.4. FTIR Analysis of Encapsulated PCM

As can be seen in Fig. 4, the FTIR spectrum of Methyl palmitate PCM has a very strong and broad peak at 3360 cm-1, which corresponds to the O-H stretching frequency. It was the C-H stretching vibration of the aliphatic chain that contributed to the peaks at 2925 and 2855 cm^{-1}.

Medium bending vibration of methylene/methyl (at 1459 cm^{-1} and C-O stretching of alcohol (at 1066 cm-1) are responsible for the peaks in the infrared spectrum. The in-plane rocking vibration of the methylene group was blamed for the 728 cm^{-1} peak. The N-H bending vibration of the amine group was observed as a peak at 3145 cm^{-1} in the FTIR spectra of the melamine.

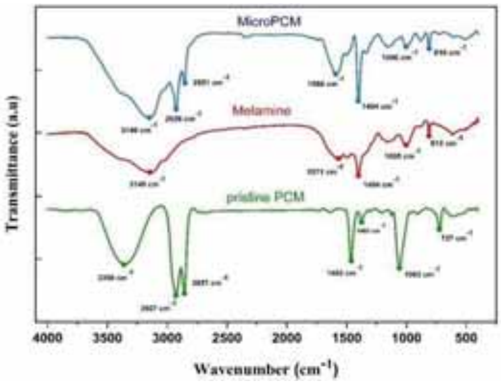

Figure 4.Chemical Compatibility test results

The N-H bond in-plane bending vibration was attributed to the prominent peak at 1560 cm^{-1}. Similarities between the 810 cm^{-1} peak and the stretching vibration of triazine rings were found. Table 1 provides a concise summary of the FTIR analysis results. The absorption peaks of PCM and the melamine-formaldehyde shell can be seen in the FTIR spectra of the Encapsulated PCM, with no evidence of a shift. This not only confirmed that the PCM was successfully encapsulated in the melamine-formaldehyde shell material, but also demonstrated there was no chemical contact between the core and the shell material [6].

3.5. Phase change and latent heat properties of the Encapsulated PCM

Results from a DSC study comparing the phase change behaviour of pure PCM and Encapsulated PCM are shown in Fig. 5. As can be seen from the data, the pure Methyl palmitate PCM showed a single-peak congruent phase change both during cooling and melting. It's interesting to see that the pure PCM goes straight from an isotropic liquid to a triclinic solid as it freezes [7].

Encapsulated PCM showed unusual behaviour during its phase transformation, with dual peaks appearing during the cooling process and a single peak appearing during melting, just like pure PCM. It was at an onset temperature of 20 °C that the Encapsulated PCM's two peaks, the rotator and stable crystal phase, were activated.

The occurrence of the dual crystallization peak can be attributed to (a) the containment of the Methyl palmitate PCM within a closed shell, and the transition of the core PCM inside the shell from the heterogeneously nucleated liquid phase to the rotator phase and then to the Beta phase at temperatures of 20 °C and 14.21 °C, respectively, as the temperature of the Encapsulated PCM [8].

The DSC results (Fig. 5) indicated that peaks contributed 46.9% and 51.4%, respectively, to the latent heat of crystallization at approximately 20 °C and 14 °C.

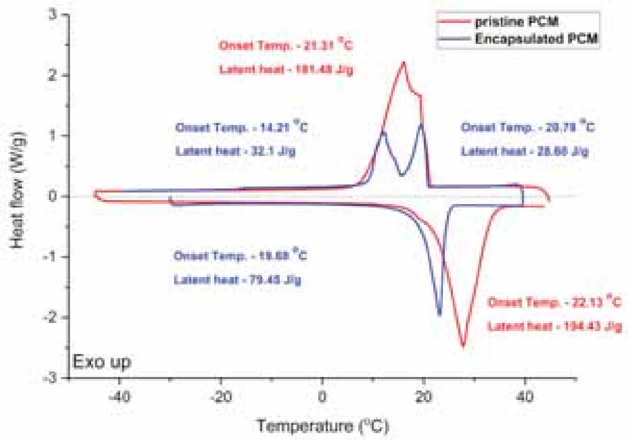

Figure 5. DSC graphs of PCM and Encapsulated PCM.

However, the nucleation kinetics of the PCM inside the shell material was also significantly affected by the degree of supercooling (the difference between the onset temperatures of melting and cooling processes).

Keeping in view the enthalpies associated with both the melting and freezing processes, we can calculate the Encapsulated PCM's encapsulation efficiency (EE) to be 36.9 %, as shown in Eq. (1). As a result, this is favored as a more appropriate parameter than the encapsulation ratio for gauging the PCM's performance in the MF shell. Latent heat enthalpies of encapsulated PCMs may be changed by adjusting the core-to-shell ratio.

To this end, we used Eq. (3) to calculate the thermal energy storage capacity (ε) of the Methyl palmitate PCM contained within the MF shell material, and discovered that the Encapsulated PCM displayed a very high i.e. 88.7%. This showed that almost complete the Methyl Palmitate PCM enclosed could efficiently store and release the energy via phase transformation [9].

$$R = \frac{\Delta H_{m,\ NP}}{\Delta H_{m,\ PCM}} \times 100 \qquad \text{-----}\ (1)$$

$$EE = \frac{\Delta H_{m,NP} + \Delta H_{c,NP}}{\Delta H_{m,PCM} + \Delta H_{c,PCM}} \times 100\% \qquad \text{-----}\ (2)$$

$$\varepsilon = \frac{\frac{\Delta Hm,NP + \Delta Hc,NP}{R}}{\Delta Hm,PCM + \Delta Hc,PCM} \times 100\% \qquad \text{-----}\ (3)$$

where, $\Delta H_{m,\ PCM}$ and $\Delta H_{c,\ PCM}$ are the latent heat of melting and freezing of pure PCM and $\Delta H_{m,\ micro\text{-}PCM}$ and $\Delta H_{c,\ micro\text{-}PCM}$ are the latent heat of melting and freezing of Encapsulated PCM, respectively.

The pure PCM's behavior during solid-to-liquid and solid-to-solid phase transitions within the shell material may be a factor in the Encapsulated PCM's lowered latent heat. Some researchers suggest that the lower PCM content of the shell material may also contribute to the reduced latent heat enthalpy [10].

As indicated in Table 4, significant thermal properties of the encapsulated PCM were in good agreement with those of other MPCMs of related types. The Encapsulated PCM created in this study has demonstrated promising phase transition characteristics, significant latent heat potential, and excellent thermal energy storage capacity, according to the DSC results.

3.6. Thermal stability of the Encapsulated PCM

As can be seen in Fig. 6, TGA was used to test the thermal stability of both pure PCM and Encapsulated PCM. The findings of the tests, which were conducted using the tangential approach, showed that the single-step mass loss/degradation of the pure PCM began at 100 °C and was finished at 184 °C, with a mass loss of 99% leaving the residual contents behind in the crucible. The Encapsulated PCM was broken down into two stages: This mass loss was primarily attributable to the evaporation of water and other molecules from the microcapsules' outer surfaces during the first step of their decomposition [11].

When the temperature was raised even higher, cracks appeared in the MF shell material, exposing the PCM contained within to the high heat and leading to its decomposition at 130°C. The FESEM picture of the broken microcapsules following full disintegration of the PCM is shown in the Fig. 6 to support this finding.

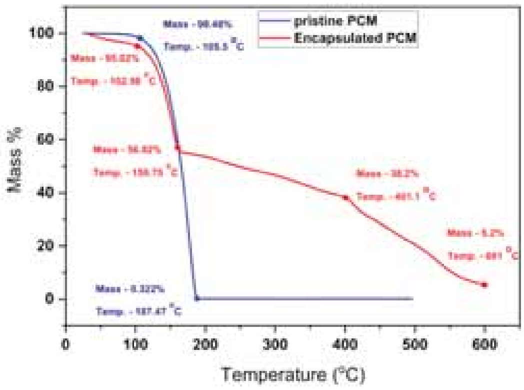

Figure.6. TGA graphs of PCM and the Encapsulated PCM.

At 160 °C, all the PCM in the shell dissolved, resulting in a 39% mass loss. A sudden mass loss was detected between 387.9 °C and 415.8 °C, and the decomposition proceeded up to 610 °C. The second step of decomposition began at about 188 °C and was associated with the loss of the shell material (MF) [12, 13].

The TGA results show that the Encapsulated PCM had great thermal stability, since the decomposition temperature was much higher than the PCM's operational temperature range (21°C to 26°C), making it ideal for low temperature TES applications [14].

3.7. Thermal conductivity of the Encapsulated PCM

Encapsulated PCM and pure PCM were found to have thermal conductivities of 0.1789 and 0.1587 W/m K, respectively. Based on the test results, it indicates that Encapsulated PCM had a somewhat lower thermal conductivity than pure PCM. Since the outer MF polymeric shell material has very low thermal conductivity, it is possible that its presence contributes to this marginal reduction [15].

One positive effect of Encapsulated PCM's low thermal conductivity was that it made for an effective heat insulator. However, the PCM's melting and freezing behaviour within the shell would have been slightly changed due to the shell material's insulating tendency towards heat transfer, as a result of the shell's poor thermal conductivity. This may also have contributed to the lowered latent heat enthalpy of the Encapsulated PCM. Nonetheless, the Encapsulated PCM has proven to be thermally stable and to be a good heat insulator [16].

IV. CONCLUSIONS

1. Microstructural analysis clearly showed that Encapsulated PCM formed into spherical capsules with a slightly rough exterior. The elemental composition of the Encapsulated PCM has been further verified by the presence of carbon, nitrogen and oxygen.
2. The particle size study found that the microcapsules had a Z-average size of 380 nm, which provided strong support to the development of the micro/nano sized Encapsulated PCM particles with desirable surface energy features.
3. The XRD findings highlighted the Encapsulated PCM's amorphous form. However, it was anticipated that the microcapsules would have a lot of energy on the inside, which would make their shells more resistant to cracking.
4. Minor peak changes seen in the FTIR spectra might be attributable to physical amalgamation between the PCM (core) and the MF (shell) during synthesis, confirming their chemical stability.
5. The Encapsulated PCM showed impressive phase change behaviour, with a huge latent heat potential. However, the Encapsulated PCM still showed good phase transition characteristics as applicable for thermal energy storage despite the presence and phases during the crystallization process and a relatively low supercooling degree.
6. A high thermal energy storage capability (ε) of 87 % was demonstrated by the Encapsulated PCM, characterizing its efficiency in storing and releasing the energy during phase change.
7. The operating temperature limits of pure PCM for the TES application were far lower than those of the Encapsulated PCM, which remained thermally stable up to 131°C. The Encapsulated PCM was able to insulate against heat because of its low thermal conductivity as well.
8. For low-temperature thermal energy storage applications, as-synthesized Encapsulated PCM with the aforementioned advantages can be a promising and practical option.

REFERENCES

[1] Sayanthan Ramakrishnan, Xiaoming Wang, Jay Sanjayan, John Wilson, Thermal performance of buildings integrated with phase change materials to reduce heat stress risks during extreme heatwave events, Applied Energy (2016).

[2] Marine Auzeby, Shen Wei, Chris Underwood, Chao Chen, Haoshu Ling, Song Pan, Bobo Ng, Jess Tindall, Richard Buswell, Using phase change materials to reduce overheating issues in UK residential buildings, Energy Procedia 105 (2017) 4072 – 4077.

[3] R. Parameshwaran, K. Deepak, R. Saravana, S. Kalaiselvam, Preparation, thermal and rheological properties of hybrid nanocomposite phase change material for thermal energy storage, Applied Energy 115 (2014) 320–330.

[4] Nurten Sahan, Halime Paksoy, Determining influences of SiO2 encapsulation on thermal energy storage properties of different phase change materials, Solar Energy Materials & Solar Cells 159 (2017) 1–7.

[5] E. M. Anghel, A. Georgiev, S. Petrescu, R. Popov, M. Constantinescu, Thermo-physical characterization of some paraffins used as phase change materials for thermal energy storage, J Therm Anal Calorim(2014).

[6] V.V. Tyagi, A.K. Pandey, D. Buddhi, R. Kothari, Thermal performance assessment of encapsulated PCM based thermal management system to reduce peak energy demand in Buildings, Energy and Buildings (2016).

[7] Amirreza Fateh, Felix Klinker, Michael Brutting, Helmut Weinlader, Francesco Devia, Numerical and experimental investigation of an insulation layer with phase change materials (PCMs), Energy and Buildings.

[8] Pramod B. Salunkhe, D. Jaya Krishna, Investigations on latent heat storage materials for solar water and space heating applications, Journal of Energy Storage 12 (2017) 243–260.

[9] Hussein Akeiber, Payam Nejat, Muhd Zaimi Abd. Majid, Mazlan A. Wahid, Fatemeh Jomehzadeh, Iman Zeynali Famileh, John Kaiser Calautit, Ben Richard Hughes, Sheikh Ahmad Zaki, A review on phase change material (PCM) for sustainable passive cooling in building envelopes, Renewable and Sustainable Energy Reviews 60 (2016) 1470–1497.

[10] Pau Gimenez-Gavarrell, Sonia Fereres, Glass encapsulated phase change materials for high temperature thermal energy storage, Renewable Energy 107 (2017) 497-507.

[11] Seunghwan Wi, Jungki Seo, Su-Gwang Jeong, Seong Jin Chang, Yujin Kang, SuminKim, Thermal properties of shape-stabilized phase change materials using fatty acid ester and exfoliated graphite nanoplatelets for saving energy in buildings, Solar Energy Materials & Solar Cells 143 (2015)168–173.

[12] M. Amin, N. Putra, E.A. Kosasih, E. Prawiro, R. Achmad Luanto, T.M.I. Mahlia, Thermal properties of beeswax/graphene phase change material as energy storage for building applications, Applied Thermal, Engineering (2016).

[13] M. Fuensanta, U. Paiphansiri, M.D. Romero-Sanchez, C. Guillem, A.M. Lopez-Buendıa, K. Landfester, thermal properties of a novel nanoencapsulated phase change material for thermal energy storage, Thermochimica Acta (2013).

[14] Yalin Zhu, Shuen Liang, Hui Wang, Ke Zhang c, Xiaorong Jia a, Chunrong Tian, Yuanlin Zhou, Jianhua Wang, Morphological control and thermal properties of Nanoencapsulated n-octadecane phase change material with

organosilica shell materials, Energy Conversion and Management 119 (2016) 151–162.

[15] Yalin Zhu, Shuen Liang, Keping Chen, Xia Gao, Pianpian Chang, Chunrong Tian, Jianhua Wang, Yigang Huang, Preparation and properties of nanoencapsulated n-octadecane phase change material with organosilica shell for thermal energy storage, Energy Conversion and Management 105 (2015) 908–917.

[16] Ahmet Sari, Cemil Alkan, Alper Bicer, Ayse Altunta, Cahit Bilgin, Micro/nanoencapsulated n-nonadecane with poly(methyl methacrylate) shell for thermal energy storage, Energy Conversion and Management 86 (2014) 614–621.

E-ISSN 2581 – 7957
P-ISSN 2277 – 3916

CVR Journal of Science and Technology, Volume 24, June 2023
DOI: 10.32377/cvrjst2418

A Numerical Study of the Effect of Viscous Dissipation on the Heat and Mass Transfer of a Rotatory Nano Fluid

Alfunsa Prathiba[1] and P. Johnson Babu[2]
[1]Sr. Asst. Professor, CVR College of Engineering/H&S(Mathematics)Department, Hyderabad, India
Email id: alphonsaperli@gmail.com
[2]Asst. Professor, St Joseph's Degree and P.G College/ Department of Physics and Electronics, Hyderabad, India
Email id: johnson.life@gmail.com

Abstract: **Viscosity dissipation is the non-reversible conversion of mechanical energy into thermal energy that occurs when a fluid performs work on neighbouring layers as a result of the impact of shear forces. Thus, the purpose of this research is to address the viscous dissipation effect on boundary layer flow of rotating incompressible Cu-Water nanofluid over an elongating surface. The model equations are transformed into a set of nonlinear ordinary differential (ODE) equations using a similarity transformation prior to getting computationally analysed using the Lobatto III A method using MATLAB. The influence of various parameters such as Eckert number, rotation porosity parameter etc on the flow properties has been analysed. The analysis discloses that with the amplification of the rotation parameter, Eckert number, nanoparticle volume fraction, and the porosity the temperature of the fluid experiences an improvement. Moreover, the velocity in the secondary direction decreases with an increase in the rotation parameter.**

Keywords: **Boundary layer, rotatory flow, viscous dissipation, porous medium, Lobatto III A method.**

I. INTRODUCTION

Viscous dissipation refers to the irreversible conversion of mechanical energy into kinetic energy that occurs as a result of fluid particle interactions. It is of importance in numerous applications such as the substantial temperature increase is found in high-velocity polymer manufacturing flows including as extrusion or injection moulding. The thin boundary layer surrounding fast aircraft experiences aerodynamic heating, which boosts skin temperature [1]. Viscosity dissipation and spontaneous convection flow were initially studied by Gebhart [2]. He found that in natural convection flows with significant gravitational effects or a liquid with a large Prandtl number, internal produced energy cannot be ignored. Hussanan et al [3] defined viscous dissipation as "the work done by a fluid on neighbouring layers due to the impact of shear forces". Nur Syamila Yusof et al.,[4] studied "the steady-state flow of a non-Newtonian fluid (Casson fluid) across an exponentially porous, slippery Riga plate with thermal radiation and magnetic field effects". They discovered that increasing the thermal and velocity slip parameters reduces the temperature. Using the Lobatto III A approach, Mohamad Shoaib et al [5] explored "heat and mass transfer in 3D radiative flow of hybrid nanofluid across a rotating disc". They discovered that temperature distribution is related to Brinkman number [5].

Heat transfer is crucial in many fields including biomedical, material science, oceanographic, nanotechnology, inorganic chemistry, and many more [6]. It is used in several technical advancements such as liquid distillation, heat exchange, and atomic controller refrigeration. In fluid mechanics, viscosity causes resistance to fluid motion, converting mechanical energy into heat energy. Thus, it is termed as internal energy shift [7]. Irfan Anjum Badruddin et al used the Finite element approach to explore the influence of viscous dissipation and heat radiation on natural convection in a porous material enclosed inside a vertical annulus tube and found that the average Nusselt number rises near the cold plate owing to increasing Ec values [8].

Nanofluid (NF) is a mixture of base fluid (water, ethanol etc) and nanoparticles. It is well known that the presence of nanomaterials alters the transporting characteristics and heat transfer efficiency in NF. The heat transmission qualities of a nanofluid are based on the mass fraction and thermophysical parameters of nanoparticles as well as the base fluid. These fluids are included in applications such as, oil exploration, metal extrusion, fiberglass polymer processing, continuous casting, plastic foil elongating and geothermal energy extraction. The thermal capacity of a NF with a permeable medium may be increased. Using nanoparticles in base liquids like oil, water, and ethylene glycol is a great way to improve heat transfer rate [9]. Research conducted on heat transfer intensification via NF can be identified in the series of the work.

In multiple procedures: such as temperature distribution, geothermal, enzymatic, nuclear reactor designs and earth sciences, there is the incorporation of convective flow in view of a porous media [10]. Permeable porous space is quite strong in subterranean systems, energy accumulating units, the circulation of water in supplies, photovoltaic reception, and so on. A large number of rotational "flows near stretchable or inextensible limits" are now being studied by academics. Zaimi et al. [11] constructed self-similar solutions for rotating viscoelastic fluid flow through an impermeable stretchable surface. Bakar et al [12] analysed "forced convection stagnation-point flow in a Darcy-Forchheimer porous medium towards a shrinking sheet". Ullah et al. [13] investigated the "effect of velocity slip on MHD Casson fluid in a porous medium with nonlinear stretching". Many researchers have engaged themselves in analysing the flow properties under various conditions in the presence of porous

Received on 09-02-2023, Revised on 29-03-2023, Accepted on 11-04-2023.

medium due to its immense industrial and geophysical applications [14]–[18].

Due to its numerous useful applications in a wide range of engineering systems, boundary layer flows with internal heat generation over stretching sheets continue to be studied [1]. To best of the knowledge of the author the impact of internal energy on the rotary $Cu + H_2O$ flow in the presence of porous medium was not addressed by the researchers. Thus, the relevance of viscous dissipation to the thermal performance across a spinning sheet is underlined in this research.

II. MODELLING OF THE FLOW

Considering a steady, laminar, incompressible $Cu + water$ NF rotating flows over an expanding sheet in the presence of internal energy as shown in Figure 1**.** The fluid is assumed to flow in the $z > 0$ plane with the sheet elongating with a constant flow speed of $U_0 = bx$,where is $b > 0$ is invariant. The velocity components in the cartesian plane are assumed to be u, v, w in the $x, y \,\&\, z - direction$.The angular velocity of the flow is treated as Ψ.Further the flow is consistent with both ambient \ wall temperature and concentration.

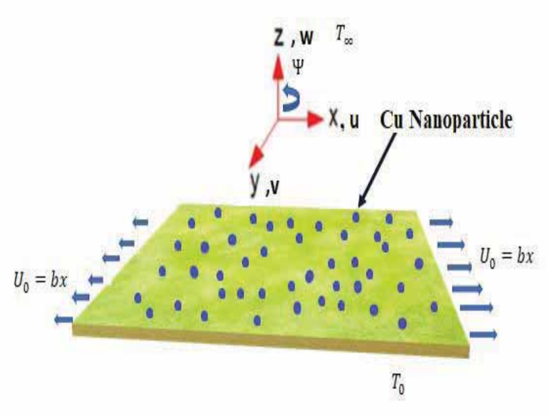

Figure 1. The physical model of the problem

"The **Maxwell-Garnetts and Brinkman models** are used to measure nano liquid thermal conductivity and dynamic viscosity". These models characterize spherical nanoparticles with a volume fraction of $< 10\%$ .Using the given hypotheses the boundary-layer flow governing equations are[19]

$$\frac{\partial u}{\partial x} + \frac{\partial v}{\partial y} + \frac{\partial w}{\partial z} = 0 \tag{1}$$

$$u\frac{\partial u}{\partial x} + v\frac{\partial u}{\partial y} + w\frac{\partial u}{\partial z} = \frac{\mu_{nf}}{\rho_{nf}}\frac{\partial^2 u}{\partial z^2} + 2\Psi v - \frac{\nu_{nf}}{k_p}u \tag{2}$$

$$u\frac{\partial v}{\partial x} + v\frac{\partial v}{\partial y} + w\frac{\partial v}{\partial z} = \frac{\mu_{nf}}{\rho_{nf}}\frac{\partial^2 v}{\partial z^2} - 2\Psi u - \frac{\nu_{nf}}{k_p}v \tag{3}$$

$$u\frac{\partial T}{\partial x} + v\frac{\partial T}{\partial y} + w\frac{\partial T}{\partial z} = \frac{k_{nf}}{(\rho Cp)_{nf}}\frac{\partial^2 T}{\partial z^2} + \frac{\mu_{nf}}{(\rho Cp)_{nf}}\left[\left(\frac{\partial u}{\partial z}\right)^2 + \left(\frac{\partial v}{\partial z}\right)^2\right] \tag{4}$$

$$u\frac{\partial C}{\partial x} + v\frac{\partial C}{\partial y} + w\frac{\partial C}{\partial z} = D_{nf}\frac{\partial^2 C}{\partial z^2} \tag{5}$$

The end constraints are,

$$\begin{gathered} u = U_0 \;\; ; \; v = 0 \;\; ; w = 0 \;\; ; T = T_0 \;\; ; \\ C = C_0 \quad at \quad z = 0 \\ u \to 0; v \to 0; w \to 0; \;\; T \to T_\infty \;\; ; C \to C_\infty \\ as \;\; z \to \infty \end{gathered} \tag{6}$$

μ_{nf} the dynamic viscosity[20] , ρ_{nf} the density[21] , k_{nf} the thermal conductivity[22], $(\rho Cp)_{nf}$ the heat capacitance[23], D_{nf} is the mass diffusivity[24] of the NF which are given by

$$\mu_{nf} = \frac{\mu_f}{(1-\phi)^{\frac{5}{2}}}, \qquad \rho_{nf} = (1-\phi)\rho_f + \phi\rho_s \tag{7}$$

$$k_{nf} = k_f\left[\frac{k_s + 2k_f - 2\phi(k_f - k_s)}{k_s + 2k_f + \phi(k_f - k_s)}\right] \tag{8}$$

$$(\rho C_p)_{nf} = (1-\phi)(\rho C_p)_f + \phi(\rho C_p)_s \tag{9}$$

$$D_{nf} = \frac{D_f}{1-\phi}, \tag{10}$$

The subscripts in the above equations indicate the properties of the NF, base fluid(water), solid Cu nanoparticle. The thermophysical properties required for the flow analysis are given below,

TABLE I.
PROPERTIES OF WATER AND SOLID COPPER NANO PARTICLE [25]

Properties	Base Fluid **(Water)**	Nano Particles **(Cu)**
$\boldsymbol{Thermal\ Conductivity(k)(Wm^{-1}K^{-}}$	0.613	400
$\boldsymbol{Density(\rho)(kgm^{-3})}$	997.1	8933
Specific heat $\boldsymbol{(Cp)(Jkg^{-1}K^{-1})}$	4179	385
$\boldsymbol{\beta\ (1/K)}$	36.2x 10^{-5}	1.67x10^{-5}

III. MATHEMATICAL TECHNIQUE

Let us consider the following similarity transformations [19], [22], [26]

$$\left.\begin{aligned} &\eta = \sqrt{\frac{a}{\nu}}z\,, u = axF'(\eta), v = axG(\eta),\\ &w = -\sqrt{a\nu}F(\eta), \Theta(\eta) = \frac{T-T_\infty}{T_0-T_\infty},\\ &\Phi(\eta) = \frac{C-C_\infty}{C_0-C_\infty} \end{aligned}\right\} \quad \textbf{(11)}$$

Substituting these into the equations to**,** equation ***(1)*** is satisfied and the remaining equations **(*2*)-(*5*)**, along with the boundary conditions**(*6*)**, transform into highly non-linear ODE, which can be given as

$$\frac{\mu_{nf}}{\mu_f}\frac{\rho_f}{\rho_{nf}}F^{'''} = (F')^2 - FF^{''} - 2R_0G + k_1F' \quad \textbf{(12)}$$

$$\frac{\mu_{nf}}{\mu_f}\frac{\rho_f}{\rho_{nf}}G^{''} = F^{'}G - G^{'}F + 2R_0F' + k_1G \quad \textbf{(13)}$$

$$\frac{k_{nf}}{k_f}\frac{(\rho C_p)_f}{(\rho C_p)_{nf}}[\Theta^{''}] = -(Pr\,(F\Theta^{'} + Ec((F^{''})^2 + (G^{'})^2)) \quad \textbf{(14)}$$

$$\Phi'' + \frac{Sc}{(1-\phi)}F\Phi' = 0 \quad \textbf{(15)}$$

With the BCs,

$$\begin{gathered} F'(\eta) = 1, G(\eta) = 0, F(\eta) = 0,\\ \Theta(\eta) = 1, \Phi(\eta) = 1 \ \ at\,\eta = 0\\ F'(\eta) \longrightarrow 0, G(\eta) \longrightarrow 0,\\ \Theta(\eta) \longrightarrow 0, \Phi(\eta) \longrightarrow 0 \ \ as\,\eta \longrightarrow \infty \end{gathered} \quad \textbf{(16)}$$

The parameters involved in the above equations are [19],[27]

$$Eckert\ number:\ Ec = \frac{\rho_f U_0^2}{(\rho C_p)_f(T_\infty - T_0)}\,,$$

$$Porosity\ parameter: k_1 = \frac{\nu_f}{bk_p}$$

$$Rotational\ parameter: R_0 = \frac{\Psi}{b}$$

$$Prandtl\ number: Pr = \frac{\upsilon_f}{\alpha_f}\,,$$

$$Schmidt\ number: Sc = \frac{\upsilon_f}{D_f}$$

The expression for the local drag force coefficients [19] $C_{fx}\,and\,C_{fy}$, heat transfer coefficient Nu_x and the mass transfer coefficient Sh_x can be defined as

$$C_{fx} \equiv \frac{\tau_{xz}}{\frac{1}{2}\rho U_0^2}, C_{fy} \equiv \frac{\tau_{yz}}{\frac{1}{2}\rho U_0^2},$$

$$Nu = \frac{xq_w}{k(T_0 - T_\infty)}, and$$

$$Sh_x = \frac{xq_m}{D_M(C_0 - C_\infty)}$$

In which τ_{xz}, τ_{yz} signify the tensors of shear stress and $q_w\,, q_m$ represent "the heat and mass flux at the sheet walls". Applying the transformations**,** the above expressions transform into,

$$\begin{aligned} Re_x^{\frac{1}{2}}C_{fx} &= \frac{\mu_{nf}}{\mu_f}F''(0)\\ Re_x^{1/2}C_{fy} &= \frac{\mu_{nf}}{\mu_f}G'(0)\\ Re_x^{-1/2}Nu_x &= -\frac{k_{nf}}{k_f}\Theta'(0)\\ Re_x^{-1/2}Sh_x &= -\frac{D_{nf}}{D_f}\Phi'(0) \end{aligned} \quad \textbf{(17)}$$

IV. SOLUTION METHODOLOGY

The non-dimensional ODEs are set into a linear format using the relations,

$$\begin{aligned} f_1 = F, f_2 = F', f_3 = F'', F''' = f_3' &\\ = -A_1A_2[f_1f_3 + 2R_0g_1 &\\ - (f_2)^2 + k_1f_2] & \end{aligned} \quad \textbf{(18)}$$

$$\begin{aligned} g_1 = G, g_2 = G', G'' = g_2' &\\ = A_1A_2[-f_1g_2 + 2R_0f_1 &\\ + f_2g_1 + k_1g_1] & \end{aligned} \quad \textbf{(19)}$$

$$\begin{aligned} \theta_1 = \Theta(\eta), \theta_2 = \Theta'(\eta)\,, \theta_3 = \Theta'_2 &\\ = -\frac{Pr * k_f}{k_{nf}}\Big[A_3f_1\theta_2 &\\ + Ec[f_3^2 + g_2^2]\Big] & \end{aligned} \quad \textbf{(20)}$$

$$\Phi_1 = \Phi, \Phi_2 = \Phi', \Phi_3 = -\frac{Scf\Phi'}{(1-\phi)} \quad \textbf{(21)}$$

$$Here, A_1 = \frac{\mu_f}{\mu_{nf}}\ , \boldsymbol{A_2} = \frac{\rho_{nf}}{\rho_f}, \boldsymbol{A_3} = \frac{[\rho C_p]_{nf}}{[\rho C_p]_f} \quad \textbf{(22)}$$

Along with the modified BCs

$$f_1 = 0, f_2 = 1, g_1 = 0, \Theta_1 = 1, \Phi_1 = 1\ as\,\eta = 0$$

$$f_2 \rightarrow 0, g_1 \longrightarrow 0, \Theta_1 \longrightarrow 0, \Phi_1 \longrightarrow 0\ as\,\eta \longrightarrow 0$$

The set of equations **(*12*)-(*15*)**, along with the prescribed conditions **(16)**, has been solved using the bvp4c solver which performs the finite difference code that implements the three-stage Lobatto IIIA formula of fourth-order [28]. The system is solved with absolute and relative accuracy of order 10^{-6}.

The MATLAB BVP4C implements Lobatto IIIa collocation RK method [29]– [33] . The validation of the code was verified by comparing the results by determining the values of $C_{fx}\,, C_{fy}\,and\,Nu_x$ for the base fluid and matched with the formerly available papers in **TABLE 4** and TABLE 3

TABLE II.
COMPARISON OF THE VALUES OF $Re_x^{1/2}C_{fx}$ and $Re_x^{1/2}C_{fy}$ FOR BASE FLUID WHEN $\phi = Ri = A = B = Sc = 0$

	Nor Azizah Yacob et al[34]		**N. A. Salleh,.et al**[35]		**Present findings**	
R$_0$	$-\frac{\mu_{nf}}{\mu_f}F''(0)$	$-\frac{\mu_{nf}}{\mu_f}G'(0)$	$-\frac{\mu_{nf}}{\mu_f}F''(0)$	$-\frac{\mu_{nf}}{\mu_f}G'(0)$	$-\frac{\mu_{nf}}{\mu_f}F''(0)$	$-\frac{\mu_{nf}}{\mu_f}G'(0)$
0.0	**1.00000**	**0.00000**	**1.000000**	**0.000000**	**1.00000**	**0.000000**
0.5	**1.13838**	**0.51276**	**1.138381**	**0.512760**	**1.138411**	**0.512802**
1.0	**1.32503**	**0.83809**	**1.325029**	**0.837098**	**1.325031**	**0.837121**
2.0	**1.6524**	**1.28726**	**1.652352**	**1.287259**	**1.652392**	**1.287301**

TABLE III.
COMPARISON OF CALCULATED VALUES OF $Re_X^{-0.5}Nu_X$ FOR BASE FLUID.

	Nadeem et al. [36]	**N. A. Salleh,.et al** [35]	**Current findings**
R$_0$	$\frac{-k_{nf}}{k_f}\Theta'(0)$	$\frac{-k_{nf}}{k_f}\Theta'(0)$	$\frac{-k_{nf}}{k_f}\Theta'(0)$
0.00	1.770948	1.770948	1.77094791
0.50	1.725631	1.725631	1.72563892
1.00	1.660286	1.660286	1.66028591
2.00	1.533487	1.533487	1.53348701

V. RESULTS AND DISCUSSION

To analyse the predominance of the parameters such as Eckert number, porosity etc involved in the governing ODEs of the rotary NF flow over a linearly stretching sheet in the presence of internal energy and porous medium the Lobatto IIIA collocation method has been utilised . The results obtained have been graphed, tabulated, and discussed below.

The values of parameters throughout the analysis have been considered as $Ec = 0.2, k_1 = 0.5, Sc = 0.5, R_0 = 0.2, \phi = 0.02$, except for the modifications required in the corresponding figures.

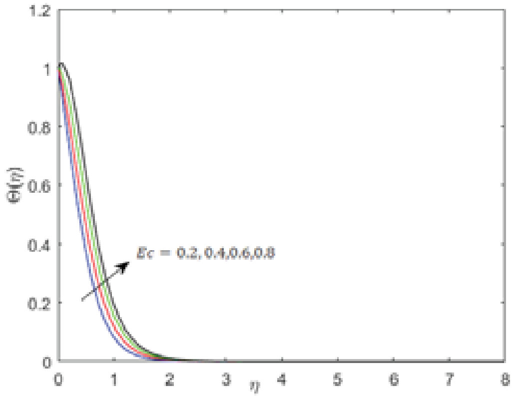

Figure 2. Effect of Eckert number on the Temperature profile

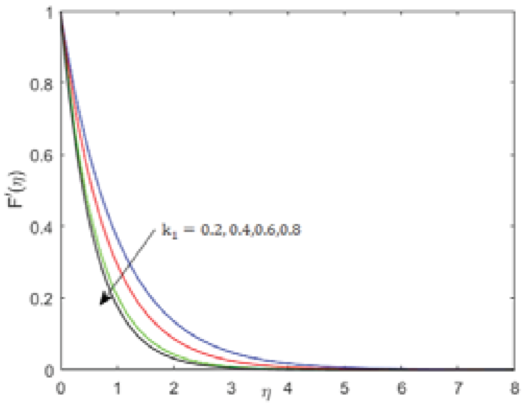

Figure 3. The Predominance of k_1 (porosity parameter) value on PVG

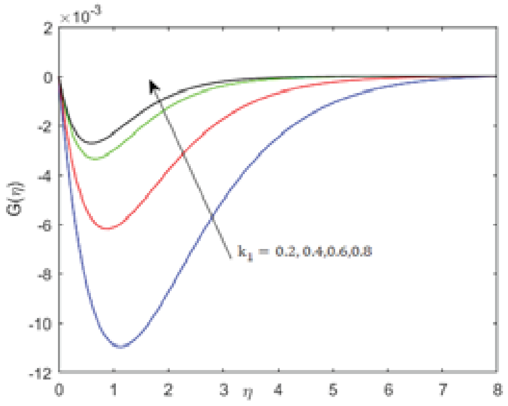

Figure 4. Impact of k_1 on the SVG

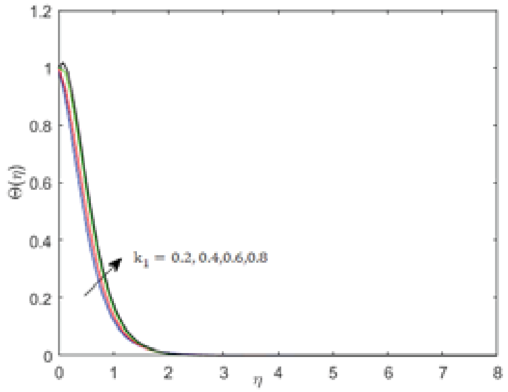

Figure 5. Effect of k_1 on $\Theta(\eta)$

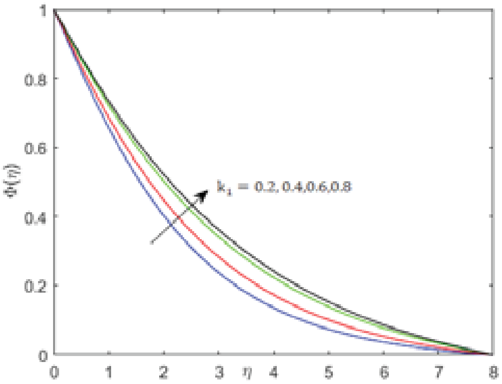

Figure 6. Effect of k_1 on $\Phi(\eta)$

Figure 3-Figure 6 demonstrates the porosity parameter's role on the physical properties of the NF flow. Higher porosity increases the impulse and speeds the flow, whereas it decelerates the flow for small pore size by increasing the "viscous drag of the porous channel" [37]. Thus, the improvement in values of k_1 leads to the enlargement of the temperature, SVG, and concentration profiles whereas the impact is opposite on PVG. And also, we observe that the increase in the porosity leads to the increase in both temperature and concentration profiles.

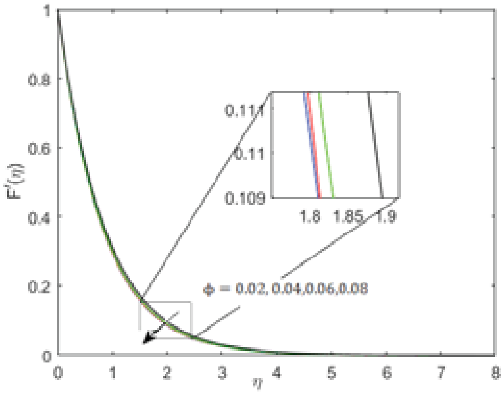

Figure 7. Influence of ϕ on primary velocity $F'(\eta)$

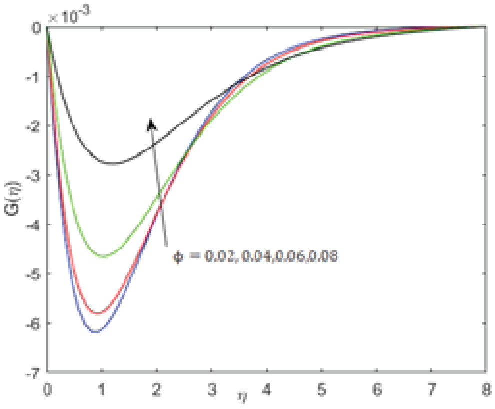

Figure 8. Development of secondary velocity profile with improvement in ϕ

The predominance of the solid Cu – "nanoparticle volume fraction" on flow properties of fluid flow is displayed in Figure 7-Figure 10**.** From the graphs, it is evident that the addition of the nanoparticle into the base fluid enhances the temperature and decreases the mass diffusivity of the flow. We notice the improvement in the secondary velocity profiles and fall in PVG due to the increase in ϕ.

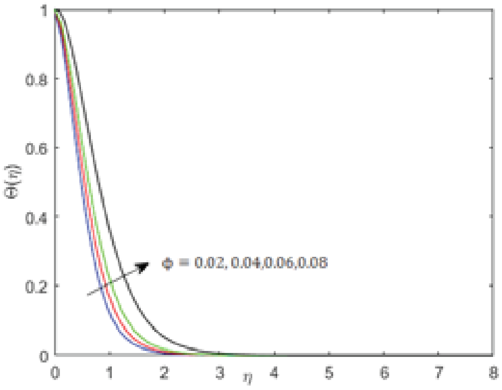

Figure 9. The upshoot of temperature with change in ϕ

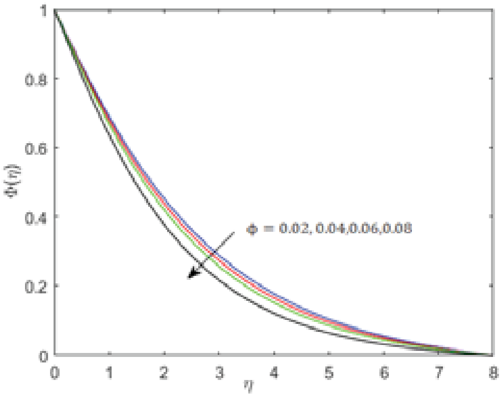

Figure 10. The variation in the concentration profile with ϕ

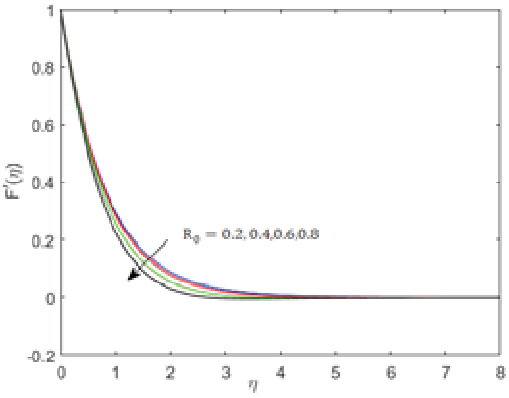

Figure 11. Impact of R_0 on $F'(\eta)$

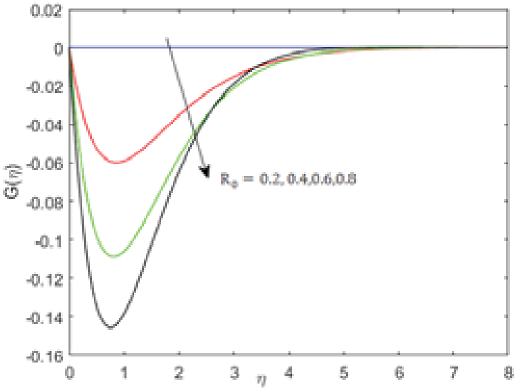

Figure 12. The change in $G(\eta)$ with changes in R_0

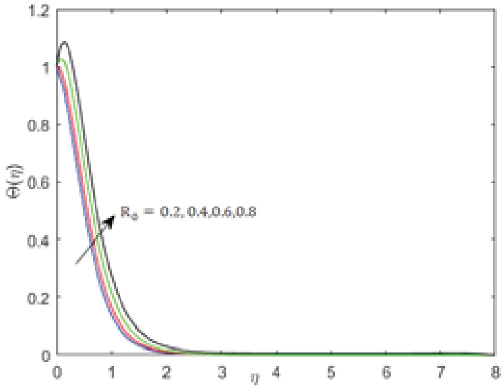

Figure 13. Impact of R_0 on $\Theta(\eta)$

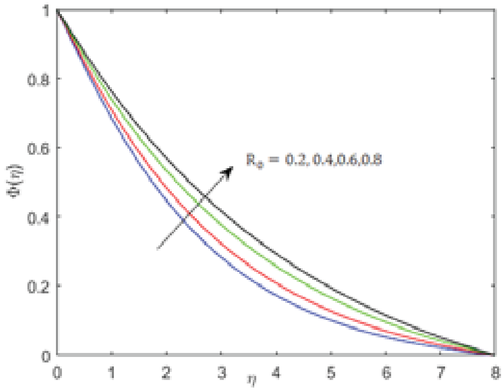

Figure 14. The influence of R_0 on $\Phi(\eta)$

Figure 11-Figure 14 shows the influences of the rotation parameter on the velocity, concentration, and temperature BLs of the NF fluid flow. The statistics display that the increase in the R_0 value improvises the concentration and the temperature of the flow but leads to the downfall of the speed of the fluid. Increasing the rotation generally causes the particle motion close to the boundary to slow down. These factors contribute to the rise in temperature and concentration profiles.

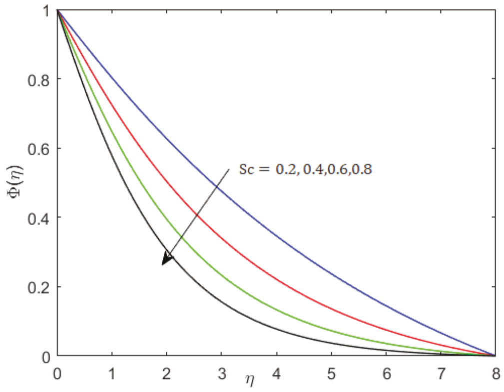

Figure 15. The outcome of Sc's effect on $\Phi(\eta)$

Schmidt number is the ratio of the shear component for diffusivity viscosity/density to the mass-transfer diffusivity. This equation materially connects the hydrodynamic and the mass-transfer BLs. Thus, from Figure 15 we understand that the rise in Sc diminishes the concentration profile.

TABLE 4. displays the numerical values of the physical quantities of industrial interest for various values of the parameters involved in the modified flow governing equations. From the table, we observe that the improvement in Ec leads to the fall in local Nusselt number due to the reason that the rise Ec results in the fall in thermal BL. The enlargement of the values of k_1 and R_0 lead to the fall local Sherwood number values, whereas we observe the opposite behaviour when the ϕ and Sc values increase as seen from the tabulated value. The primary and secondary skin friction values improve with k_1 and decay for the rise in the values of ϕ and R_0

TABLE IV.

CALCULATED VALUES OF $\frac{1}{(1-\phi)^{2.5}}F''(0)$, $\frac{1}{(1-\phi)^{2.5}}G'(0)$, $-\frac{k_{nf}}{k_f}\Theta'(0)$ AND $-\frac{1}{(1-\phi)}\Phi'(0)$ FOR DIFFERENT VALUES OF THE PHYSICAL PARAMETERS SUCH AS Ec, Sc, R_0, ϕ and k_1

R_0	Ec	Sc	ϕ	$k_1{'}$	$Re_x^{1/2}C_{fx}$	$Re_x^{1/2}C_{fy}$	$Re_x^{-1/2}Nu_x$	$Re_x^{-1/2}Sh_x$
0	0.5	0.5	0.5	0.5	-1.111816	0	0.41709	0.345995
0.2					-1.288031	-0.171253	0.364229	0.334726
0.4					-1.303946	-0.193361	0.290194	0.329548
0.6					-1.34511	-0.370777	0.098932	0.317088
0.8					-1.400148	-0.52773	-0.156678	0.302363
0.2	**0.2**	0.2	0.02	0.5	-1.288196	-0.019665	1.296906	0.327212
	0.4				-1.288196	-0.019665	0.674597	0.327212
	0.6				-1.288196	-0.019665	0.052309	0.327212
	0.8				-1.288196	-0.019665	-0.570017	0.327212
0.2	0.5	0.5	**0.02**	0.5	-1.224904	-0.018701	0.402254	0.330155
			0.04		-1.288197	-0.019665	0.36346	0.334671
			0.06		-1.354621	-0.020648	0.32121	0.339555
			0.08		-1.424474	-0.021652	0.275239	0.344818
0.2	0.5	0.5	0.02	**0**	-1.052069	-0.026512	0.78951	0.366961
				0.5	-1.288197	-0.019665	0.36346	0.334671
				1	-1.662988	-0.014328	-0.343836	0.295102
				1.5	-1.821711	-0.012902	-0.651519	0.281863
0.2	0.5	**0.2**	0.02	0.5	-1.288197	-0.019665	0.36346	0.201807
		0.4			-1.288197	-0.019665	0.36346	0.289629
		0.6			-1.288197	-0.019665	0.36346	0.379276
		0.8			-1.288197	-0.019665	0.36346	0.465216

VI. CONCLUSIONS

The 3D rotational flow of $Cu + water$ NF across an elongating sheet is studied to examine the effects of viscous dissipation and porosity on fluid flow parameters. We utilised the Lobatto IIIa fourth-order approach in MATLAB to evaluate the data. We next analysed the data mathematically and visually. The following are the paper's main takeaways:

- The SVG amplifies with the boost in ϕ , and k_1 whereas the PVG displays the opposite effect.
- With the amplification of the rotation parameter, nanoparticle volume fraction, internal energy and k_1 the temperature of the fluid experiences an improvement
- The local Nusselt number declines with an increase in the Eckert number.
- The surge in the Schmidt number improves the rate of diffusivity and decreases the concentration of the species.

REFERENCES

[1] M. Gnaneswara Reddy, P. Padma, and B. Shankar, "Effects of viscous dissipation and heat source on unsteady MHD flow over a stretching sheet," *Ain Shams Eng. J.*, vol. 6, no. 4, pp. 1195–1201, Dec. 2015, doi: 10.1016/j.asej.2015.04.006.

[2] B. Gebhart, "Effects of viscous dissipation in natural convection," *J. Fluid Mech.*, vol. 14, no. 2, pp. 225–232, Oct. 1962, doi: 10.1017/S0022112062001196.

[3] A. Hussanan, M. Z. Salleh, I. Khan, and S. Shafie, "Analytical solution for suction and injection flow of a viscoplastic Casson fluid past a stretching surface in the presence of viscous dissipation," *Neural Comput. Appl.*, vol. 29, no. 12, pp. 1507–1515, 2018, doi: 10.1007/s00521-016-2674-0.

[4] N. S. Yusof, S. K. Soid, M. R. Illias, A. S. Abd Aziz, and N. A. A. Mohd Nasir, "Radiative Boundary Layer Flow of Casson Fluid Over an Exponentially Permeable Slippery Riga Plate with Viscous Dissipation," *J. Adv. Res. Appl. Sci. Eng. Technol.*, vol. 21, no. 1, pp. 41–51, 2020, doi: 10.37934/araset.21.1.4151.

[5] M. Shoaib *et al.*, "Numerical analysis of 3-D MHD hybrid nanofluid over a rotational disk in presence of thermal radiation with Joule heating and viscous dissipation effects using Lobatto IIIA technique," *Alexandria Eng. J.*, vol. 60, no. 4, pp. 3605–3619, 2021, doi: 10.1016/j.aej.2021.02.015.

[6] T. Salahuddin, N. Siddique, M. Arshad, and I. Tlili, "Internal energy change and activation energy effects on Casson fluid," *AIP Adv.*, vol. 10, no. 2, 2020, doi: 10.1063/1.5140349.

[7] T. M. Ajayi, A. J. Omowaye, and I. L. Animasaun, "Viscous Dissipation Effects on the Motion of Casson Fluid over an Upper Horizontal Thermally Stratified Melting Surface of a Paraboloid of Revolution: Boundary Layer Analysis," *J. Appl. Math.*, 2017, doi: 10.1155/2017/1697135.

[8] I. A. Badruddin, Z. A. Zainal, Z. A. Khan, and Z. Mallick, "Effect of viscous dissipation and radiation on natural convection in a porous medium embedded within vertical annulus," *Int. J. Therm. Sci.*, vol. 46, no. 3, pp. 221–227, 2007, doi: 10.1016/j.ijthermalsci.2006.05.005.

[9] X. Q. Wang and A. S. Mujumdar, "Heat transfer characteristics of nanofluids: a review," *Int. J. Therm. Sci.*, vol. 46, no. 1, pp. 1–19, 2007, doi: 10.1016/j.ijthermalsci.2006.06.010.

[10] M. Tayyab, I. Siddique, F. Jarad, M. K. Ashraf, and B. Ali, "Numerical solution of 3D rotating nanofluid flow subject to Darcy-Forchheimer law, bio-convection and activation energy," *South African J. Chem. Eng.*, vol. 40, no. January, pp. 48–56, 2022, doi: 10.1016/j.sajce.2022.01.005.

[11] K. Zaimi, A. Ishak, and I. Pop, "Stretching surface in rotating viscoelastic fluid," *Appl. Math. Mech.*, vol. 34, no. 8, pp. 945–952, Aug. 2013, doi: 10.1007/s10483-013-1719-9.

[12] S. A. Bakar, N. M. Arifin, R. Nazar, F. M. Ali, and I. Pop, "Forced convection boundary layer stagnation-point flow in Darcy-Forchheimer porous medium past a shrinking sheet," *Front. Heat Mass Transf.*, vol. 7, no. 1, pp. 1–6, 2016, doi: 10.5098/hmt.7.38.

[13] I. Ullah, S. Shafie, and I. Khan, "Effects of slip condition and Newtonian heating on MHD flow of Casson fluid over a nonlinearly stretching sheet saturated in a porous medium, Effects of slip condition and Newtonian heating," *J. King Saud Univ. - Sci.*, vol. 29, no. 2, pp. 250–259, 2017, doi: 10.1016/j.jksus.2016.05.003.

[14] A. Tassaddiq, "Impact of Cattaneo-Christov heat flux model on MHD hybrid nano-micropolar fluid flow and heat transfer with viscous and joule dissipation effects," *Sci. Rep.*, vol. 11, no. 1, pp. 1–14, 2021, doi: 10.1038/s41598-020-77419-x.

[15] K. A. Maleque, "Dufour and soret effects on unsteady MHD convective heat and mass transfer flow due to a rotating disk," *Lat. Am. Appl. Res.*, vol. 40, no. 2, pp. 105–111, 2010.

[16] S. Dero, A. M. Rohni, and A. Saaban, "Triple Solutions and Stability Analysis of Mixed Convection Boundary Flow of Casson Nanofluid over an Exponentially Vertical Stretching / Shrinking Sheet," vol. 1, no. 1, pp. 94–110, 2020.

[17] T. S. Kumar, "Hybrid nanofluid slip flow and heat transfer over a stretching surface," *Partial Differ. Equations Appl. Math.*, vol. 4, p. 100070, Dec. 2021, doi: 10.1016/j.padiff.2021.100070.

[18] A. O. Ajibade, A. M. Umar, and T. M. Kabir, "An analytical study on effects of viscous dissipation and suction/injection on a steady mhd natural convection couette flow of heat generating/absorbing fluid," *Adv. Mech. Eng.*, vol. 13, no. 5, pp. 1–12, 2021, doi: 10.1177/16878140211015862.

[19] W. Owhaib, M. Basavarajappa, and W. Al-Kouz, "Radiation effects on 3D rotating flow of Cu-water nanoliquid with viscous heating and prescribed heat flux using modified Buongiorno model," *Sci. Rep.*, vol. 11, no. 1, p. 20669, 2021, doi: 10.1038/s41598-021-00107-x.

[20] H. F. Oztop and E. Abu-Nada, "Numerical study of natural convection in partially heated rectangular enclosures filled with nanofluids," *Int. J. Heat Fluid Flow*, vol. 29, no. 5, pp. 1326–1336, 2008, doi: 10.1016/j.ijheatfluidflow.2008.04.009.

[21] S. Chaudhary and K. M. Kanika, "Viscous dissipation and Joule heating in MHD Marangoni boundary layer flow and radiation heat transfer of Cu–water nanofluid along particle shapes over an exponential temperature," *Int. J. Comput. Math.*, vol. 97, no. 5, pp. 943–958, 2020, doi: 10.1080/00207160.2019.1601713.

[22] B. C. Rout, S. R. Mishra, and T. Thumma, "Effect of viscous dissipation on Cu-water and Cu-kerosene nanofluids of axisymmetric radiative squeezing flow," *Heat Transf. - Asian Res.*, vol. 48, no. 7, pp. 3039–3054, 2019, doi: 10.1002/htj.21529.

[23] U. Khan, N. Ahmed, M. Asadullah, and S. Tauseef Mohyud-din, "Effects of viscous dissipation and slip velocity on two-dimensional and axisymmetric squeezing flow of Cu-water and Cu-kerosene nanofluids," *Propuls. Power Res.*, vol. 4, no. 1, pp. 40–49, 2015, doi: 10.1016/j.jppr.2015.02.004.

[24] U. Khan, A. Zaib, I. Khan, and K. S. Nisar, "Activation energy on MHD flow of titanium alloy (Ti6Al4V) nanoparticle along with a cross flow and streamwise direction with binary chemical reaction and non-linear radiation: Dual Solutions," *J. Mater. Res. Technol.*, vol. 9, no. 1, pp. 188–199,

2020, doi: 10.1016/j.jmrt.2019.10.044.

[25] W. Owhaib, M. Basavarajappa, and W. Al-Kouz, "Radiation effects on 3D rotating flow of Cu-water nanoliquid with viscous heating and prescribed heat flux using modified Buongiorno model," *Sci. Rep.*, vol. 11, no. 1, pp. 1–16, 2021, doi: 10.1038/s41598-021-00107-x.

[26] T. Hayat, M. Imtiaz, and A. Alsaedi, "Melting heat transfer in the MHD flow of Cu–water nanofluid with viscous dissipation and Joule heating," *Adv. Powder Technol.*, vol. 27, no. 4, pp. 1301–1308, 2016, doi: 10.1016/j.apt.2016.04.024.

[27] H. M. Duwairi and R. A. Damseh, "Magnetohydrodynamic natural convection heat transfer from radiate vertical porous surfaces," *Heat Mass Transf. und Stoffuebertragung*, vol. 40, no. 10, pp. 787–792, 2004, doi: 10.1007/s00231-003-0476-2.

[28] A. S. Oke, "Heat and Mass Transfer in 3D MHD Flow of EG-Based Ternary Hybrid Nanofluid Over a Rotating Surface," *Arab. J. Sci. Eng.*, 2022, doi: 10.1007/s13369-022-06838-x.

[29] L. O. Jay, "Lobatto Methods," *Encycl. Appl. Comput. Math.*, vol. 1, no. 1, pp. 817–826, 2015, doi: 10.1007/978-3-540-70529-1_123.

[30] S. G. Pinto, S. P. Rodríguez, and J. I. M. Torcal, "On the numerical solution of stiff IVPs by Lobatto IIIA Runge-Kutta methods," *J. Comput. Appl. Math.*, vol. 82, no. 1–2, pp. 129–148, 1997, doi: 10.1016/s0377-0427(97)00086-1.

[31] C. Ouyang, R. Akhtar, M. A. Z. Raja, M. Touseef Sabir, M. Awais, and M. Shoaib, "Numerical treatment with Lobatto IIIA technique for radiative flow of MHD hybrid nanofluid (Al2O3-Cu/H2O) over a convectively heated stretchable rotating disk with velocity slip effects," *AIP Adv.*, vol. 10, no. 5, 2020, doi: 10.1063/1.5143937.

[32] A. S. Alhamaly, M. Khan, S. Z. Shuja, B. S. Yilbas, and H. Al-Qahtani, "Axisymmetric stagnation point flow on linearly stretching surfaces and heat transfer: Nanofluid with variable physical properties," *Case Stud. Therm. Eng.*, vol. 24, Apr. 2021.

[33] N. Vedavathi, G. Dharmaiah, K. Venkatadri, and S. A. Gaffar, "Numerical study of radiative non-Darcy nanofluid flow over a stretching sheet with a convective Nield conditions and energy activation," *Nonlinear Eng.*, vol. 10, no. 1, pp. 159–176, 2021, doi: 10.1515/nleng-2021-0012.

[34] N. A. Yacob, N. F. Dzulkifli, S. N. A. Salleh, A. Ishak, and I. Pop, "Rotating flow in a nanofluid with cnt nanoparticles over a stretching/shrinking surface," *Mathematics*, vol. 10, no. 1, 2022, doi: 10.3390/math10010007.

[35] S. N. A. Salleh, N. Bachok, and N. M. Arifin, "Flow and Heat Transfer Towards a Stretching Surface in a Rotating Nanofluid with Suction," *Indian J. Sci. Technol.*, vol. 9, no. 48, 2017, doi: 10.17485/ijst/2016/v9i48/97772.

[36] S. Nadeem, A. U. Rehman, and R. Mehmood, "Boundary Layer Flow of Rotating Two Phase Nanofluid Over a Stretching Surface," *Heat Transf. - Asian Res.*, vol. 45, no. 3, pp. 285–298, 2016, doi: 10.1002/htj.21167.

[37] C. Kang and P. Mirbod, "Porosity effects in laminar fluid flow near permeable surfaces," *Phys. Rev. E*, vol. 100, no. 1, p. 013109, Jul. 2019, doi: 10.1103/PhysRevE.100.013109.

In the next issue (Vol. 25, December 2023)

1.	***Ubiquitous Tracking System: A mobile and versatile GPS-GSM solution for real-time vehicle***	***M. Ashok Sura Rupendra Pilli Sashank Satvika Yannam***
2.	***Crude oil price forecasting – ARIMA model approach***	***Dr. V. Swapna***

Template for the Preparation of Papers for Publication in CVR Journal of Science and Technology

First A. Author[1] and Second B. Author[2]
[1]Designation, Name of Institution/Department, City, Country
Email: first.author@hostname1.org
[2]Designation, Name of Institution/Department, City, Country
Email: second.author@hostname2.org

***Abstract:* These instructions give you basic guidelines for preparing camera-ready papers for CVR College journal Publications. Your cooperation in this matter will help in producing a high-quality journal.**

***Index Terms:* first term, second term, third term, fourth term, fifth term, sixth term**

I. INTRODUCTION

Your goal is to simulate the usual appearance of papers in a Journal Publication of the CVR College. We are requesting that you follow these guidelines as closely as possible. It should be original work. Format must be done as per the template specified. Diagrams with good clarity with relevant reference within the text are to be given. References are to be cited within the body of the paper. Number of pages must not be less than five with minimum number of 4000 words and not exceeding eight pages. The journal is published in colour. Colours used for headings, subheadings and other captions must be strictly as per the template given in colour.

A. Full-Sized Camera-Ready (CR) Copy

Prepare your CR paper in full-size format, on A4 paper (210 x 297 mm or 8.27 x 11.69 in). No header or footer, no page number.

Type sizes and typefaces: Follow the type sizes specified in Table I. As an aid in gauging type size, 1 point is about 0.35 mm. The size of the lowercase letter "j" will give the point size. Times New Roman has to be the font for main text. Paper should be single spaced.

Margins: Top and Bottom = 24.9mm (0.98 in), Left and Right = 16 mm (0.63 in). The column width is 86mm (3.39 in). The space between the two columns is 6mm (0.24 in). Paragraph indentation is 3.7 mm (0.15 in).

Left- and right-justify your columns. Use tables and figures to adjust column length. On the last page of your paper, adjust the lengths of the columns so that they are equal. Use automatic hyphenation and check spelling. Digitize or paste down figures.

For the Title use 24-point Times New Roman font, an initial capital letter for each word. Its paragraph description should be set so that the line spacing is single with 6-point spacing before and 6-point spacing after. Use two additional line spacings of 10 points before the beginning of the double column section, as shown above.

TABLE I.
TYPE SIZES FOR CAMERA-READY PAPERS

Type size (pts.)	Appearance		
	Regular	Bold	Italic
6	Table caption, table superscripts		
8	Tables, table names, first letters in table captions, figure captions, footnotes, text subscripts, and superscripts		
9	References, authors' biographies	Abstract	
10	Section titles ,Authors' affiliations, main text, equations, first letters in section titles		Subheading
11	Authors' names		
24	Paper title		

Each major section begins with a Heading in 10 point Times New Roman font centered within the column and numbered using Roman numerals (except for REFERENCES), followed by a period, two spaces, and the title using an initial capital letter for each word. The remaining letters are in SMALL CAPITALS (8 point). The paragraph description of the section heading line should be set for 12 points before and 6 points after.

Subheadings should be 10 point, italic, left justified, and numbered with letters (A, B, …), followed by a period, two spaces, and the title using an initial capital letter for each word. The paragraph description of the subheading line should be set for 6 points before and 3 points after.

For main text, paragraph spacing should be single spaced, no space between paragraphs. Paragraph indentation should be 3.7mm/0.21in, but no indentation for abstract & index terms.

II. HELPFUL HINTS

A. Figures And Tables

Position figures and tables at the tops and bottoms of columns. Avoid placing them in the middle of columns. Large figures and tables may span across both columns. Leave sufficient room between the figures/tables and the main text. Figure captions should be centered below the figures; table captions should be centered above. Avoid placing figures and tables before their first mention in the

Received on xx-xx-xxxx, Revised on xx-xx-xxxx, Accepted on xx-xx-xxxx.

text. Use the abbreviation “Fig. 1,” even at the beginning of a sentence.

To figure axis labels, use words rather than symbols. Do not label axes only with units. Do not label axes with a ratio of quantities and units. Figure labels should be legible, about 8-point type.

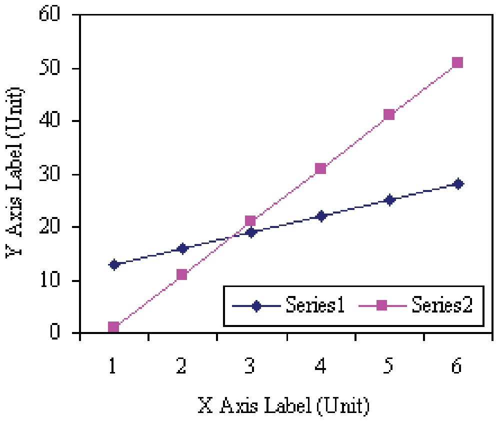

Figure 2. Note how the caption is centered in the column.

All figures, tables and references must be cited in the text.

Please indicate the broad area/specializations into which the research paper falls, in the covering letter/mail to the Editor, so that reviewers with those specializations may be identified.

B. References

Number citations consecutively in square brackets [1]. Punctuation follows the bracket [2]. Use “Ref. [3]” or “Reference [3]” at the beginning of a sentence:

Give all authors’ names; use “et al.” if there are six authors or more. Papers that have not been published, even if they have been submitted for publication, should be cited as “unpublished” [4]. Papers that have been accepted for publication should be cited as “in press” [5]. In a paper title, capitalize the first word and all other words except for conjunctions, prepositions less than seven letters, and prepositional phrases. Good number of references must be given.

Latest references in the area must be included and every refence must be cited in the text of the research article.

C. Footnotes

Number footnotes separately in superscripts $^{1, 2, \cdots}$. Place the actual footnote at the bottom of the column in which it was cited, as in this column. See first page footnote as an example.

D. Abbreviations and Acronyms

Define abbreviations and acronyms the first time they are used in the text, even after they have been defined in the abstract. Do not use abbreviations in the title unless they are unavoidable.

E. Equations0

Equations should be left justified in the column. The paragraph description of the line containing the equation should be set for 6 points before and 6 points after. Number equations consecutively with equation numbers in parentheses flush with the right margin, as in (1). Italicize Roman symbols for quantities and variables, but not Greek symbols. Punctuate equations with commas or periods when they are part of a sentence, as in

$$a + b = c . \tag{1}$$

Symbols in your equation should be defined before the equation appears or immediately following. Use “(1),” not “Eq. (1)” or “equation (1),” except at the beginning of a sentence: “Equation (1) is ...”

F. Other Recommendations

Use either SI (MKS) or CGS as primary units. (SI units are encouraged.) If your native language is not English, try to get a native English-speaking colleague to proofread your paper. Do not add page numbers.

III. CONCLUSIONS

The authors can conclude on the topic discussed and proposed, future enhancement of research work can also be briefed here.

REFERENCES

[1] G. Eason, B. Noble, and I. N. Sneddon, “On certain integrals of Lipschitz-Hankel type involving products of Bessel functions,” Phil. Trans. Roy. Soc. London, vol. A247, pp. 529–551, April 1955.

[2] J. Clerk Maxwell, *A Treatise on Electricity and Magnetism*, 3rd ed., vol. 2. Oxford: Clarendon, 1892, pp.68–73.

[3] I. S. Jacobs and C. P. Bean, “Fine particles, thin films and exchange anisotropy,” in *Magnetism*, vol. III, G. T. Rado and H. Suhl, Eds. New York: Academic, 1963, pp. 271–350.

[4] K. Elissa, “Title of paper if known,” unpublished.

[5] R. Nicole, “Title of paper with only first word capitalized”, *J. Name Stand. Abbrev.*, in press.

[6] Y. Yorozu, M. Hirano, K. Oka, and Y. Tagawa, “Electron spectroscopy studies on magneto-optical media and plastic substrate interface,” *IEEE Transl. J. Magn. Japan*, vol. 2, pp. 740–741, August 1987 [Digests 9th Annual Conf. Magnetics Japan, p. 301, 1982].

[7] M. Young, *The Technical Writer's Handbook*. Mill Valley, CA: University Science, 1989.

[8] T. Ali, B.K. Subhash and R.C. Biradar, “A Miniaturized Decagonal Sierpinski UWB Fractal Antenna”, PIERS C, vol. 84, pp. 161-174, 2018.

ABOUT THE COLLEGE

CVR College of Engineering, an autonomous institution under the UGC, was established in the Year 2001, the first college in Telangana to be promoted by NRI technology professionals resident in the USA. The NRI promoters are associated with cutting-edge technologies of the computer and electronics industry. They also have strong associations with other leading NRI professionals working for world-renowned companies like IBM, Intel, Cisco, Facebook, AT & T, Google, and Apple who have agreed to associate with the College with a vision and passion to make the College a state-of-the-art engineering institution.

All B. Tech Programmes are accredited three or four times by the NBA since 2007. Two UG Programmes namely ECE & EEE are accredited for Six years by the NBA under Tier-I. As of now, all 7 eligible B. Tech Programmes and 2 P.G Programmes are accredited. NAAC reaccredited the college for five years with grade 'A' with effect from 2022. Two M. Tech Programmers of AI and Data Science in 2018-2019 and three B. Tech CSE Programmes (AI & ML, DS & CS) in 2020-2021 are recent additions.

As formulated by the IQAC, many FDPs and workshops are organized by departments. College has MoUs with organizations such as Virtusa, Mitsubishi, NRSC, COMSAT, CADENCE, IIIT. Under innovation activities faculty have published 38 patents so far. Projects from NRSC under the RESPOND programme of ISRO, AICTE-RPS, TEQIP-III from JNTU, MODROBS-AICTE worth Rs.71 Lakhs are some of the recent projects funded by central agencies. Total funds received are Rs. 160 lakhs. Newgen IEDC of Government of India (DST) has sanctioned Rs.287 Lakhs for a period for five years in 2018-19, for Innovative Entrepreneurship Development Programmes by students and staff. 10 Projects were completed in 2019-20, 16 in 2020-21, 20 in 2021-22. An exclusive Innovation Centre of 5000 Sqft. has been created for practical work and counseling.

The college has been creating records year after year. With more than 100 companies visiting CVRCE and 1000+ placements for the 2022 - 2023 academic year, it is the highest among the peer group of colleges. The highest offer is **57 Lakhs** at Deutsche Bank and next being **44 Lakhs** by 4 students at AMAZON and several students received offers higher than **Rs. 25 Lakhs**. More than **100 students** received offers higher than **Rs. 10 Lakhs**. About **200 offers** are higher than **Rs. 7 Lakhs**. With this, CVRCE becomes one of the leading colleges in the state in terms of offers with higher salaries. The placement percentage continues to be 100% since 5 years. The college has made huge progress in a short span of time and is preferred by the students and parents during the EAMCET counseling this year and is among the **top 3 colleges** in the state. College has been consistently in the range of 101-150 by NIRF over last five years. Many students have received special cash prizes in competitions like Hackathon, Mitsubishi etc., worth 1 to 2 Lakhs.

CVR is rated amongst the top 100 engineering institutions in the country by Outlook and holds many more recognitions.

CALL FOR PAPERS:

Papers in Engineering, Science and Management disciplines are invited for Publication in our Journal. Authors are requested to mail their contributions to Editor, CVR Journal of Science and Technology (Email Id: journal@cvr.ac.in). Authors can also submit their papers through our online open journal system (OJS) www.ojs.cvr.ac.in or www.cvr.ac.in/ojs. Papers are to be written using a Standard Template, which may be obtained on request from the Editor. It is also available on the college website www.cvr.ac.in

CVR JOURNAL OF SCIENCE AND TECHNOLOGY

CVR COLLEGE OF ENGINEERING

(UGC Autonomous- Affiliated to JNTU Hyderabad)
Mangalpalli (V), Ibrahimpatnam (M),
R.R. District, Telangana - 501510
http://cvr.ac.in